Measurements of jet mass, top quark mass and top tagging efficiencies in decays of boosted top quarks at CMS

DISSERTATION

zur Erlangung des Doktorgrades
an der Fakultät für Mathematik, Informatik und Naturwissenschaften
Fachbereich Physik

UNIVERSITÄT HAMBURG

vorgelegt von:
DENNIS SCHWARZ

2020

Gutachter:innen der Dissertation:	Prof. Dr. Johannes Haller Prof. Dr. Elisabetta Gallo
Zusammensetzung der Prüfungskommission:	Prof. Dr. Johannes Haller Prof. Dr. Elisabetta Gallo Prof. Dr. Günter Sigl Prof. Dr. Christian Schwanenberger Prof. Dr. Peter Schleper
Vorsitzender der Prüfungskommission:	Prof. Dr. Günter Sigl
Datum der Disputation:	22.02.2021
Vorsitzender des Fach-Promotionsausschusses Physik:	Prof. Dr. Wolfgang Hansen
Leiter des Fachbereichs Physik:	Prof. Dr. Günter Sigl
Dekan der Fakultät MIN:	Prof. Dr. Heinrich Graener

Abstract

Top quarks with high momenta are abundantly produced at the Large Hadron Collider (LHC). They are of relevance for both searches for new physics and measurements of fundamental parameters of the Standard Model of particle physics (SM). At high momenta, top quarks are boosted with high Lorentz factors, such that hadronic decay products collimate, merge into a single jet, and jet substructure techniques become crucial for further analysis. In this thesis, two measurements studying top quarks at high momenta are presented. They make use of proton-proton collision data recorded during the Run 2 data taking period with the Compact Muon Solenoid (CMS) experiment at the LHC, operating at a center-of-mass energy of $\sqrt{s} = 13$ TeV. Both analyses target the lepton+jets decay channel of top quark pair production ($\mathrm{t\bar{t}}$) and use the leptonic leg $\mathrm{t} \to \mathrm{bW} \to \mathrm{b}\bar{\ell}\nu_\ell$ to distinguish signal events from background, while the measurement is performed using the hadronic decay $\mathrm{t} \to \mathrm{bW} \to \mathrm{bq\bar{q}'}$.

The first analysis is a measurement of the differential $\mathrm{t\bar{t}}$ production cross section as a function of the jet mass. The measurement is carried out using data recorded in 2016 corresponding to an integrated luminosity of 35.9 fb^{-1}. Using information from simulated events, the data are unfolded to the particle level. In addition to the measurement of the jet mass itself, the top quark mass is extracted and measured to be $m_\mathrm{t} = 172.6 \pm 2.5$ GeV. This presents a complementary measurement of the top quark mass in a topology very different than threshold production. In addition, the jet mass distribution can be calculated analytically at high top quark momenta, which allows for a direct comparison with data and can help to resolve ambiguities in the definition of the top quark mass scheme.

In the second analysis, the identification of jets that originate from hadronic decays of boosted top quarks, referred to as top tagging, is studied, and the corresponding efficiencies are measured in data and simulation. The measurements are carried out using all three data taking periods in 2016, 2017, and 2018, which correspond to integrated luminosities of 35.9 fb^{-1}, 41.5 fb^{-1}, and 59.7 fb^{-1}, respectively. Top tagging techniques using jet substructure are validated, and the efficiencies are extracted using template fits to data. This enables the efficiency measurement of individual contributions from fully merged, semimerged, and unmerged events, depending on the containment of the top quark decay products in a single jet. As a result, correction factors are derived that account for differences between data and jet substructure modeling in simulation. The correction factors obtained in this measurement are endorsed by the CMS Collaboration for the use in analyses.

Zusammenfassung

Top-Quarks mit hohem Impuls werden in großen Mengen am Large Hadron Collider (LHC) produziert. Sie sind sowohl Teil vieler Suchen nach neuer Physik als auch relevant für Messungen fundamentaler Parameter des Standard Modells der Teilchenphysik. Bei diesen hohen Impulsen haben Top-Quarks große Lorentzfaktoren, sodass ihre hadronischen Zerfallsprodukte kollimieren und mit einem einzelnen Jet rekonstruiert werden. Eine Analyse der Substruktur dieser Jets erlaubt es, ihren Ursprung zu identifizieren. In der vorliegenden Arbeit werden zwei Messungen von Top-Quarks mit hohem Impuls präsentiert. Beide basieren auf Proton-Proton Kollisionsdaten, die während des Run 2 bei einer Schwerpunktsenergie von $\sqrt{s} = 13$ TeV mit dem Compact Muon Solenoid (CMS) Experiment am LHC aufgenommen wurden. Beide selektieren den Lepton+Jets Zerfallskanal von paarweise produzierten Top-Quarks ($\mathrm{t\bar{t}}$) und nutzen den leptonischen Zerfall $\mathrm{t} \to \mathrm{bW} \to \mathrm{b}\bar{\ell}\nu_\ell$ um Signal- von Untergrundereignissen zu trennen, während die Messung am hadronischen Zerfall $\mathrm{t} \to \mathrm{bW} \to \mathrm{bq\bar{q}'}$ durchgeführt wird.

Die erste Analyse ist eine Messung des differentiellen $\mathrm{t\bar{t}}$ Produktionswirkungsquerschnitts als Funktion der Jetmasse. Sie benutzt Daten, die in 2016 aufgenommen wurden und einer integrierten Luminosität von 35.9 fb^{-1} entsprechen. Mit Hilfe von Simulationen werden die Daten entfaltet. Zusätzlich zur Messung der Jetmasse wird die Masse des Top-Quarks mit einem Wert von $m_\mathrm{t} = 172.6 \pm 2.5$ GeV extrahiert. Damit ist dies eine Messung der Top-Quark-Masse in einer kinematischen Region, die sich sehr von $\mathrm{t\bar{t}}$ an der Produktionsschwelle unterscheidet. Zusätzlich lässt sich die Verteilung in der Jetmasse bei hohen Top-Quark-Impulsen analytisch berechnen und erlaubt einen direkten Vergleich mit experimentellen Daten, der die Extraktion einer sauber definierten Top-Quark-Masse ermöglicht.

In einer zweiten Analyse werden Top-Tagging-Algorithmen – also die Identifikation von Jets, die einem hadronischen Zerfall von Top-Quarks mit hohem Impuls entspringen – studiert. Die Tagging-Effizienzen werden sowohl in Daten als auch Simulationen gemessen. Die Analyse basiert auf Daten aus den Jahren 2016, 2017 und 2018, die integrierten Luminositäten von 35.9 fb^{-1}, 41.5 fb^{-1} und 59.7 fb^{-1} entsprechen. Top-Tagging-Algorithmen werden validiert und ihre Effizienzen mit Hilfe eines Template-Fits zu Daten extrahiert. Dies erlaubt die Messung für individuelle Beiträge von Ereignissen, in denen unterschiedliche Anteile des Top-Quark-Zerfalls in einem Jet rekonstruiert werden. Als Ergebnis werden Korrekturfaktoren berechnet, die Unterschiede zwischen Daten und Modellierung von Substruktur in Simulationen ausgleichen. Diese Korrekturfaktoren werden von der CMS Kollaboration für die Nutzung in Analysen empfohlen.

List of own contributions

Measurement of the jet mass distribution and top quark mass

I was the primary and only analyzer of this measurement, which is based on a previous analysis [1, 2]. My work includes studies of various jet clustering algorithms, optimizing the event selection, and calibration of the XCone jets used in the measurement. I performed a measurement of electron trigger scale factors that correct the selection efficiency in simulation and developed an unfolding setup, which resulted in the extraction of the differential top quark pair production cross section as a function of the jet mass and top quark mass. In addition, I was involved in pioneering studies towards a calibration of the jet mass. Furthermore, I was responsible for frequent presentations of the analysis in working meetings and writing of the paper draft. As a contact person, I managed communication during the internal review in the CMS Collaboration as well as in the peer-review of the journal.
The measurement is detailed in Chapter 7 and Section 5.4.3 of this thesis, was published in Physical Review Letters [3], and presented in an article of the CERN Courier [4]. Connected to this measurement, I supervised a Bachelor's Thesis [5] and two Master's Theses [6, 7]. The results of these theses and studies performed in cooperation with Ref. [8] led to the results presented in Section 7.8.

Measurement of top tagging efficiencies

Based on the work of Refs. [9, 2], I extended the measurement to the full data set collected in 2016, 2017, and 2018. In addition, I modified the template fit such that the precision of the measurement was improved significantly and was responsible to frequent updates in working meetings in the CMS Collaboration.
The analysis is presented in Chapter 8 of this thesis, and some results were published in a CMS Detector Performance Summary [10]. As a contact person, I was responsible for creating and editing the document as well as presenting it in the internal review of the CMS Collaboration. This task included collecting the results from other groups studying other tagging algorithms. In addition, my talk on new tagging techniques at the International Conference on High Energy Physics (ICHEP) in 2020 led to a publication of proceedings [11].

Contribution to the online software of the CMS pixel detector

I contributed to the Pixel Online Software, tracking the current status of the AMC13 module, which is responsible for the distribution of timing information and collection of data in the data acquisition system of the CMS pixel detector.

Contents

1 Introduction

The understanding of the fundamental building blocks of our universe is the subject of particle physics research. The theoretical and experimental description of their interactions is inevitably connected to studies of properties of those elementary particles. Decades of research have culminated in the Standard Model of particle physics (SM), describing fundamental interactions and particles in a self-consistent quantum field theory tested to highest precision in a multitude of experiments. Nevertheless, it is known to be an incomplete theory since observed phenomena – e.g. massive neutrinos, gravity, or dark matter – are not included in its current form. However, with the Large Hadron Collider (LHC), increasingly high energies are accessible in the search for new physics. Simultaneously, the properties of known particles and interactions can be measured with extraordinary precision, in search for hints of deviations from the prediction or confirm the theory's validity. The focal point of this thesis is the heaviest known particle – the top quark. Due to its high mass it plays a special role in the SM and especially the electroweak sector. A deep understanding of the top quark and its properties is an essential ingredient for the theoretical framework of particle physics and searches for physics beyond. This work explores top quarks that are produced at very high momentum. Due to challenging experimental conditions, this kinematic regime is yet rather unexplored in the scope of precision measurements. Only with the present experimental setup, consisting of the LHC and particle detectors such as the Compact Muon Solenoid (CMS) experiment, these measurements have become feasible. For many searches and measurements, it is crucial to understand phenomena related to those high-energetic top quarks, since they rely on a precise and efficient reconstruction.

Highly energetic top quarks tend to decay in a collimated shower of particles, which can be reconstructed using a single jet. These jets can be identified using jet substructure observables such as the jet mass, which are sensitive to a jet's origin. At the LHC, multiple non-perturbative effects such as hadronization, color reconnection and contributions from underlying event complicate the modeling of jet substructure in simulation and require a tuning of free parameters to experimental data. Thus, the measurement of the jet mass in hadronic decays provides important data for the understanding of jet formation and jet substructure. In addition, the jet mass distribution is sensitive to the top quark mass and can be derived from first principles, allowing an extraction of this fundamental SM parameter in a well defined mass scheme.

Furthermore, it is measured in a kinematic region, which is very different from common measurements at threshold production and introduces not only an important cross check but offers new possibilities.

In a first analysis, the differential top quark pair production cross section is measured as a function of the jet mass. The measurement is performed using data collected by the CMS detector in 2016, which correspond to an integrated luminosity of 35.9 fb^{-1}. The event selections is optimized for the lepton+jets final state of pair-produced top quarks, where the leptonic top quark decay $\text{t} \to \text{bW} \to \text{b}\bar{\ell}\nu_\ell$ acts as a tag, and the hadronic decay $\text{t} \to \text{bW} \to \text{bq}\bar{\text{q}}'$ enters the measurement. Substantial effort has been made to find a suitable jet definition that ensures a proper reconstruction of the top quark decay into hadrons. A novel jet reconstruction using the XCone algorithm was found to increase the sensitivity of the measurement by a large margin with respect to a previous result [1] at a lower center-of-mass energy. Correcting for detector effects, the jet mass distribution is unfolded to the particle level. The normalized distribution allows for an extraction of the top quark mass. This analysis proves the potential of boosted top quarks for precision measurements of fundamental SM parameters. The final measurement was published in Refs. [3, 12].

Jet substructure is crucial for the identification of a jet's origin. Top tagging algorithms are used to distinguish jets initiated by the hadronic decay of boosted top quarks from those originating from light quarks, gluons, or decays of heavy bosons. Here, a mismodeling of substructure observables in simulation leads to differences in tagging efficiencies compared to data. In order to make tagging algorithms useful for physics analyses, correction factors need to be derived that account for these differences. Thus, detailed studies of the behavior of top tagging algorithms and the measurement of tagging efficiencies are crucial for a large range of physics analyses.

In a second analysis, the top tagging efficiencies are measured in data and simulation. For the first time, the measurements were performed consistently for the full Run 2 data with $\sqrt{s} = 13$ TeV. The data were recorded in 2016, 2017, and 2018 and correspond to integrated luminosities of 35.9 fb^{-1}, 41.5 fb^{-1}, and 59.7 fb^{-1}, respectively. In the analysis, a sample of pair-produced top quarks in the lepton+jets channel is selected, where the muon from the leptonic top quark decay is used to distinguish this process from background. The tagging efficiencies itself are derived using a jet opposite to the muon. In order to extract the tagging efficiencies in data, template fits are performed. A previous measurement [9] based on 2016 data serves as a basis and consistency check. Newly introduced nuisance parameters allow the fit to adjust the tagging efficiency individually for contributions from fully merged, semi-

merged, and not-merged events, depending on the containment of the top quark decay products in a single jet and drastically reduce systematic uncertainties. A total of 414 correction factors, corresponding to jets clustered with the anti-k_{T} [13] and HOTVR [14] algorithms, multiple bins of jet momentum, different tagging working points and three data taking periods were derived and published in Ref. [10].

The thesis is structured as follows. Chapter 2 summarizes the theoretical description of particle physics introducing the SM. A focus is set on the top quark and in particular its mass. In addition, the kinematics of proton-proton collisions as well as the simulation of those events are introduced. The concept of jets and an introduction to jet substructure is given in Chapter 3. Furthermore, the current state of existing measurements is discussed. Chapter 4 details the experimental setup consisting of the LHC and the CMS detector. In the following, the reconstruction of physical objects from detector signals and their calibration are discussed in Chapter 5. All data sets and simulated event samples used in this thesis are described in Chapter 6, focusing on differences between various data taking periods and in the simulation of collision events. The measurement of the jet mass distribution and top quark mass is discussed in detail in Chapter 7. In Chapter 8, the measurement of top tagging efficiencies is described. The thesis closes with a summary of all results in Chapter 9.

2 | Theory

Modern particle physics is capable of describing and testing fundamental processes in an enormous energy range from low-energy experiments up to collisions at high-energy particle colliders. Measurements of fundamental forces and particles have resulted in one of the most precisely tested theories in physics. In this chapter, the fundamental physics of elementary particles is described. A focus is set on the Standard Model of particle physics (Section 2.1), important characteristics of the kinematics in proton-proton collisions (Section 2.2) and the simulation of those (Section 2.3). The top quark, which is of special interest in this thesis is detailed in Section 2.4.

2.1 Standard Model of particle physics

Our current understanding of the dynamics and properties of subatomic particles is formulated as a renormalizable quantum field theory and accumulated in the so-called Standard Model (SM) [15, 16]. The SM includes all fundamental interactions and elementary particles that we know of except gravity. It is capable of predictions over a large span of energy scales and has been successfully tested to high precision with a variety of conceivable measurements. The internal mathematical structure of the SM is based on a local $SU(3)_c \times SU(2)_L \times U(1)_Y$ gauge symmetry, where the groups $SU(3)_c$ and $SU(2)_L \times U(1)_Y$ describe the strong and electroweak interactions, respectively. Prior to electroweak unification, the weak and electromagnetic interactions can be described separately by their respective symmetry groups. The strong, weak, and electromagnetic interactions are mediated by gauge bosons while fermions act as building blocks of matter. Furthermore, the Higgs mechanism makes it possible to consistently include the masses of gauge bosons and fermions in the theory. With the discovery of a scalar Higgs boson in 2012 by the ATLAS and CMS Collaborations [17, 18], every single particle included in the SM has been observed in experimental data.

Fermions are particles with a spin of $1/2$ and are considered the building blocks of matter. There are 12 different fermion flavors – grouped into quarks and leptons – which all have an

anti-partner with opposite electric charge. Three generations of quarks, each containing an up-type and a down-type quark are included in the SM. Starting from the first generation, the three up-type quarks up (u), charm (c), and top (t) all carry an electric charge of $+2e/3$ while all down-type quarks – down (d), strange (s), and bottom (b) – carry $-1e/3$, where e indicates the elementary charge. For both up-type and down-type, the second and third generation particles share all quantum numbers and charges with their first generation partner but are more massive. All quarks carry the charge of the strong interaction, referred to as color charge, and therefore do not only participate in the electroweak but also the strong interaction. In contrast, leptons do not carry color charge but are similarly grouped into generations with increasing masses. Each of the three lepton generations consists of a lepton with electric charge $1e$ (electron e, muon μ, and tau lepton τ) and a corresponding electrically neutral neutrino (ν_e, ν_μ, and ν_τ). Although the discovery of neutrino oscillations [19, 20] requires neutrinos to be massive, they are considered massless in the SM.

Gauge bosons mediate interactions between fermions and have a spin of 1. The strong interaction is mediated by gluons and described in the theory of quantum chromodynamics (QCD). Due to the symmetry group of QCD, invariance is required under local $SU(3)_c$ gauge transformations. As a consequence of the eight generators of the $SU(3)_c$ symmetry group, eight gauge bosons fields, which are identified as gluons, have to be introduced in order to maintain gauge invariance. Each of them corresponds to an unique state of color and anti-color charge, is massless, and electrically neutral. Gluons also couple to other gluons since they carry color charge themselves. The coupling strength of QCD evaluated at $q^2 = (m_Z)^2$ results in a value of $\alpha_s \approx 0.1$ [16], where m_Z is the Z boson mass and q the momentum transfer in an interaction. The coupling strength of QCD decreases with increasing momentum transfer due to the gluon self-coupling. This property leads to the so-called confinement and asymptotic freedom. Confinement describes the fact that colored particles cannot exist freely but form color-neutral bound states. Self-interacting gluons lead to a potential between colored particles, which increases with their distance. Thus, the field energy between separating quarks will reach a level, which is sufficient to create a pair of quark and anti-quark such that ultimately bound states of quarks – hadrons – are formed. This continuous splitting of gluons into pairs of quarks and the formation of hadrons is referred to as hadronization. Since α_s becomes large at small energy scales, perturbation theory collapses, and hadronization cannot be described by analytical calculations. Conversely, with increasing energy the coupling strength of QCD decreases, and quarks behave like free particles (asymptotic freedom).

The weak interaction is represented by the symmetry group $SU(2)_L$ and the weak isospin I,

which acts as the weak charge. The weak interaction maximally violates charge-conjugation and parity (CP) symmetry since the connected $W^{1,2,3}$ bosons only couple to the left-handed (right-handed) component of particles (anti-particles). The weak interaction is the only interaction that allows decays of particles, which are nonetheless only possible within left-handed doublets. In the lepton sector the doublets consist of a charged lepton and the corresponding neutrino and read

$$\begin{pmatrix} \nu_e \\ e \end{pmatrix}_L, \begin{pmatrix} \nu_\mu \\ \mu \end{pmatrix}_L, \begin{pmatrix} \nu_\tau \\ \tau \end{pmatrix}_L. \tag{2.1}$$

Quarks are similarly arranged in left-handed doublets,

$$\begin{pmatrix} u \\ d \end{pmatrix}_L, \begin{pmatrix} c \\ s \end{pmatrix}_L, \begin{pmatrix} t \\ b \end{pmatrix}_L. \tag{2.2}$$

Additionally, the SM allows right-handed singlets for quarks and charged leptons while right-handed neutrinos – due to their vanishing mass – are not part of the SM. All right-handed fermions and the W^3 boson carry $I_3 = 0$ and can thus not participate in particle decays without violating the conservation of the weak isospin. In contrast, left-handed up-type (down-type) quarks and neutrinos (charged leptons) carry $I_3 = +1/2(-1/2)$ and $W^{1,2}$ bosons have a weak isospin of $I_3 = 1$, which allows for transitions within a doublet via the $W^{1,2}$ bosons. However, in the quark sector the mass eigenstates q that we observe as particles are not identical to the flavor eigenstates q′. The mixing of quark mass eigenstates is described by the unitary Cabibbo-Kobayashi-Maskawa (CKM) matrix [21, 22] via

$$\begin{pmatrix} d' \\ s' \\ b' \end{pmatrix} = \begin{pmatrix} V_{ud} & V_{us} & V_{ub} \\ V_{cd} & V_{cs} & V_{cb} \\ V_{td} & V_{ts} & V_{tb} \end{pmatrix} \begin{pmatrix} d \\ s \\ b \end{pmatrix}, \tag{2.3}$$

and allows for (suppressed) transitions between quark generations of mass eigenstates. Note that the choice of rotating the down-type quarks and not up-type quarks is arbitrary. The elements of the CKM matrix, which directly give the transition probability $|V_{ij}|^2$ between two quarks i and j are

$$\begin{pmatrix} V_{ud} & V_{us} & V_{ub} \\ V_{cd} & V_{cs} & V_{cb} \\ V_{td} & V_{ts} & V_{tb} \end{pmatrix} = \begin{pmatrix} 0.9745 \pm 0.0001 & 0.2245 \pm 0.0004 & 0.0037 \pm 0.0001 \\ 0.2244 \pm 0.0004 & 0.9736 \pm 0.0001 & 0.0421 \pm 0.0008 \\ 0.0090 \pm 0.0002 & 0.0413 \pm 0.0007 & 0.99911 \pm 0.00003 \end{pmatrix}. \tag{2.4}$$

The values are not predicted by theory but are measured by various analyses. The precise values

given here are obtained by assuming three quark generations and an unitary matrix.

In the SM the weak interaction is usually considered unified with electromagnetism. This unified electroweak interaction is based on a $SU(2)_L \times U(1)_Y$ symmetry group, where Y indicates a newly-introduced hypercharge. It is defined from the electric charge Q and third component of the weak isospin I_3 via $Y = 2(Q - I_3)$. A total of four bosons – two charged W^1_μ and W^2_μ as well as two neutral W^3_μ and B_μ – arise from requiring gauge invariance under local $SU(2)_L \times U(1)_Y$ transformations. Linear combinations of those boson fields form the observed electroweak bosons $\mathrm{W}^\pm_\mu$, Z_μ, and photon A_μ via

$$\mathrm{W}^\pm_\mu = \frac{1}{\sqrt{2}} \left(\mathrm{W}^1_\mu \mp i \mathrm{W}^2_\mu \right) \tag{2.5}$$

and

$$\begin{pmatrix} \mathrm{A}_\mu \\ \mathrm{Z}_\mu \end{pmatrix} = \begin{pmatrix} \cos\theta_W & \sin\theta_W \\ -\sin\theta_W & \cos\theta_W \end{pmatrix} \begin{pmatrix} \mathrm{B}_\mu \\ \mathrm{W}^3_\mu \end{pmatrix}, \tag{2.6}$$

where θ_W is the Weinberg angle. The Weinberg angle furthermore connects the relation of the weak (α_w) and electromagnetic (α_{EM}) coupling constants via $\alpha_w = \alpha_{\mathrm{EM}} / \sin^2\theta_W$. The gauge bosons connected to the weak interaction are the charged W^+ and W^- as well as neutral Z bosons with masses of $m_{\mathrm{W}} \approx 80.4$ GeV and $m_{\mathrm{Z}} \approx 90.2$ GeV [16], respectively. Because of the large mass of its bosons, the weak interaction only has a short range. The photon (γ) can be interpreted as the gauge boson of the electromagnetic part of the electroweak interaction, which is based on a $U(1)$ symmetry and described in the theory of quantum electrodynamics (QED). Photons are massless and carry no electric or color charge. The coupling strength of QED in the limit of infinitesimal momentum transfer q is $\alpha_{\mathrm{EM}} \approx 1/137$ [16] and rises with q. A smaller value of α_{EM} at small momentum transfer is commonly interpreted as a shielding of electric charge at large distances due to vacuum polarization. The unification of electromagnetism and the weak interaction predicts the observed bosons W, Z, and γ but requires them to be massless in order to retain local gauge symmetry. In contradiction, the masses of W and Z have been measured to be non-vanishing. In order to include massive weak bosons in a consistent way within the SM, the mechanism of electroweak symmetry breaking is introduced.

Electroweak symmetry breaking refers to the mechanism that allows to include mass terms for electroweak bosons in the SM Lagrange density without violating gauge invariance. Up to this point, the SM allows only massless gauge bosons that have two possible transverse polarization states. However, for massive bosons another longitudinal polarization is possible. In order to generate these missing degrees of freedom but retain gauge invariance, a doublet of

complex scalar fields

$$\phi = \begin{pmatrix} \phi^+ \\ \phi^0 \end{pmatrix} \tag{2.7}$$

with a potential of the form

$$V(\phi) = \mu^2|\phi|^2 + \lambda|\phi|^4 \tag{2.8}$$

is introduced, where μ and λ are parameters steering the shape of the potential. For the choice of negative μ^2 and positive λ the potential takes a so-called Mexican hat form (see Figure 2.1) with a minimum at $v = \sqrt{-\mu^2/(2\lambda)}$, which corresponds to the ground state of the SM referred to as vacuum expectation value. Here, the fact that the ground state v is not located at $\phi = 0$ breaks the symmetry in the moment the ground state is taken. Excitations in four directions around the ground state give rise to the three missing degrees of freedom of the longitudinal polarization components of the electroweak bosons W^+, W^-, and Z. The fourth excitation manifests itself in a new scalar particle, the Higgs boson (H), with a mass $m_H = \sqrt{-2\mu^2}$. After inserting the potential $V(\phi)$ into the Lagrange density of the electroweak $SU(2)_L \times U(1)_Y$, terms appear, which are identified as masses for the electroweak bosons. This allows a self-consistent description of the SM without contradicting the observations of massive gauge bosons. The mass terms of W and Z boson then are given by

$$m_W = \frac{1}{2}vg \quad \text{and} \tag{2.9}$$

$$m_Z = \frac{1}{2}v\sqrt{g^2+g'^2}, \tag{2.10}$$

where g and g' are the couplings of $SU(2)_L$ and $U(1)_Y$. Nevertheless, the photon field A remains massless in this mechanism. Fermion masses are implemented by introducing a Yukawa coupling y to the Higgs field. The mass of a fermion f is then determined via the Yukawa coupling y_f and reads

$$m_f = \frac{v}{\sqrt{2}}y_f. \tag{2.11}$$

The values of the fermion masses are not predicted to a certain value in the Higgs mechanism but the Yukawa couplings themselves remain free parameters. Up to this day, all measurements of the observed scalar Higgs boson are in agreement with the properties and couplings predicted by the SM. Despite the undeniable success of the SM, the underlying theory does not offer a complete description of our universe.

Limitations of the Standard Model lie not only in the incompleteness of the theory but also in unknown origins of symmetries, mathematical inconsistencies, or unnatural constructions of

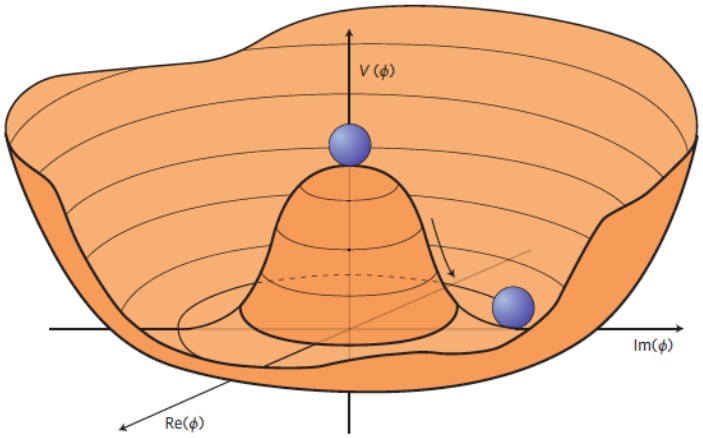

Figure 2.1: The potential $V(\phi)$ for negative values of μ^2 and positive λ in the Higgs mechanism. The ball indicates the symmetric state at $\phi = 0$ and the broken symmetry when the ground state is reached at $v = \sqrt{-\mu^2/(2\lambda)}$. Taken from Ref. [23].

parameters. In fact, it is well known that the SM is incomplete. There are several examples of phenomena, which have been observed in experiments but cannot be described by the SM. Popular examples of this kind are gravity, the neutrino masses, and dark matter. None of which are included in the current status of the theory. Also, the origin of the observed asymmetry of matter and antimatter remains unsolved. In addition, many open questions remain on the internal structure of the theory. In the SM it is unclear why we observe three generations and a total of six flavors for both quarks and leptons. And while there are hints for the unification of the electroweak and strong interaction at large energy scales (which could explain the symmetries between quarks and leptons), no theory introducing another symmetry has been experimentally confirmed. Moreover, most parameters of the SM, e.g. the masses of fermions, cannot be predicted from first principles but have to be measured in experiments. Furthermore, the fine-tuning of the Higgs boson mass [24] is a frequent point of discussion and often considered unnatural. Quantum loop corrections, dominantly from the top quark and electroweak bosons, lead to large corrections in the definition of the Higgs boson mass. If one assumes the validity of the SM up to the Planck scale, these corrections turn out to exceed the bare Higgs boson mass by several orders of magnitude and are therefore considered unnatural. Many extensions of the SM have been developed that introduce new symmetries and particles that would lead to a natural cancellation of those quantum loop effects. Thus, not only the precise determination of SM parameters but also searches for physics beyond the SM are of large interest in particle physics today. At particle colliders, new physics can be probed either by direct searches for hypothetical new particles that are a consequence of an extension to the SM or indirectly by detecting deviations from the prediction in precise measurements of SM

parameters.

2.2 Physics of proton-proton collisions

This thesis presents analyses of collision data obtained from the LHC, which is a circular proton-proton collider. Compared to electron-positron colliders, the initial state particles of hadron colliders are not fundamental. This leads to the fact that the exact kinematic state of the initial particles – quarks and gluons inside the proton – is unknown. However, this mostly applies to the momentum component in beam direction (z-axis) since the transverse components (x and y) of the incoming partons are negligible. Since the z-component of the initial state is unknown, often only the transverse components of the final state particle momenta are used in physics analyses. Therefore, a central observable of final state particles from a proton-proton collision is the transverse momentum

$$p_{\mathrm{T}} = \sqrt{p_x^2 + p_y^2}, \tag{2.12}$$

where p_x and p_y are the transverse components of the momentum p. In addition, the angle from the beam axis θ is often translated to the pseudorapidity η via

$$\eta = -\ln\left[\tan\left(\frac{\theta}{2}\right)\right]. \tag{2.13}$$

In contrast to θ, η is constructed such that differences are invariant under Lorentz transformations in z-direction. In the transverse plane, the angle ϕ is defined. From η and ϕ the angular distance ΔR between two objects i and j is defined as

$$\Delta R = \sqrt{(\Delta\phi)^2 + (\Delta\eta)^2} \quad \text{with} \tag{2.14}$$

$$\Delta\phi = \phi_i - \phi_j \quad \text{and} \tag{2.15}$$

$$\Delta\eta = \eta_i - \eta_j. \tag{2.16}$$

The construction from differences in η and ϕ also makes ΔR invariant under Lorentz transformations in z-direction and thus a suitable observable at hadron colliders.

Another complication of non-fundamental particles is that, in order to predict the cross sections of processes, the probability to find a certain initial state parton has to be known. For every parton inside a proton a parton density function (PDF) $f_i(x, q^2)$ is measured, which gives the

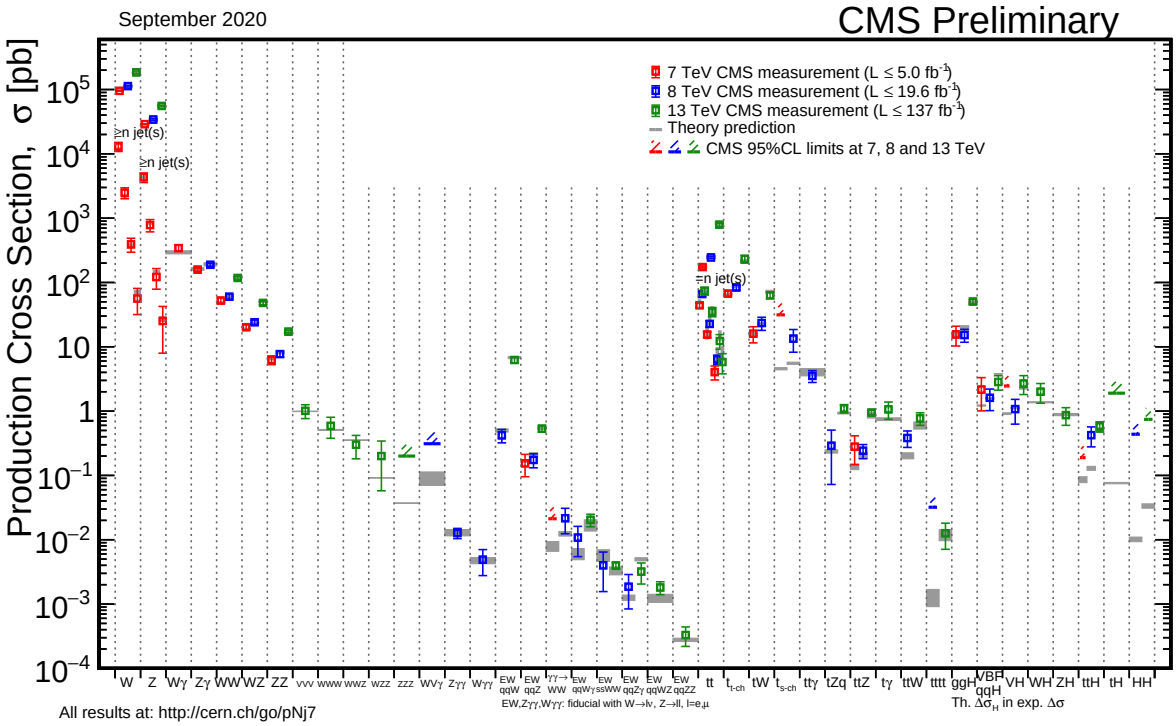

Figure 2.2: Predicted (lines) and measured (markers) production cross sections of a variety of processes predicted by the Standard Model. All presented measurements are performed by the CMS Collaboration. For processes that have not been observed yet, an upper limit is given. Taken from Ref. [25].

probability to find a parton of type i with a certain momentum fraction x of the proton in a process with the momentum transfer q. Subsequently, the production cross section $\sigma_{\mathrm{pp}\to\mathrm{X}}$ of a final state X in proton-proton collisions is calculated via

$$\sigma_{\mathrm{pp}\to\mathrm{X}} = \sum_{i,j} \iint dx_1 dx_2 f_i(x_1, q^2) f_j(x_2, q^2) \sigma_{ij\to\mathrm{X}}, \tag{2.17}$$

where the hard interaction cross section $\sigma_{ij\to\mathrm{X}}$ is folded with the PDFs of all proton constituents that can take part in this process. Up to now, analyses performed by the experiments at HERA [1] using electron-proton collisions provide the most precise measurements of proton PDFs. Nevertheless, these measurements give rise to non-negligible uncertainties, which have to be taken into account in all measurements and searches for new physics at hadron colliders. As Figure 2.2 shows, the production cross sections of several SM processes have been correctly predicted and agree with the measurements performed by the CMS Collaboration.

Moreover, in proton-proton collisions typically a lot more activity than only the main hard

[1] Hadron-Elektron-Ring-Anlage

interaction is observed during a single crossing of two proton bunches. Since only parts of the proton form the initial state of the hard interaction, the proton remnants can result in additional activity in the collision event. This is referred to as the underlying event and consists of mostly low-energy QCD processes. Furthermore, multiple proton-proton collisions can take place within the same or adjacent bunch crossing, which leads to additional particles in the event. These additional collisions are called pileup. Effects from the underlying event and pileup have to be treated carefully, especially when performing jet measurements.

In contrast to electron-positron collisions, the initial state particles carry color charge. Thus, colored final state produced via the strong interaction are connected to the initial state. This has an effect especially on angular distributions and has to be considered in calculations and simulations of proton-proton interactions.

2.3 Simulation of proton-proton collisions

An important tool for the analysis of collision data are simulated events predicting distributions of a variety of kinematic observables. The event simulation is performed in multiple steps starting with the calculation of the matrix element of a specific hard interaction folded with the proton PDFs. This operation is performed by a Monte Carlo (MC) generator such as POWHEG [26, 27, 28, 29] or MADGRAPH5_aMC@NLO [30, 31], which is responsible for the hard scattering process of an interaction. At this stage, the parton level is defined, which includes all particles from the hard interaction. On top of this, particle shower and hadronization processes are simulated using programs such as PYTHIA [32] or HERWIG [33]. It is worth noting that PYTHIA is also capable of and often used for the matrix element calculation of QCD multijet events. The parton shower model is responsible for the simulation of the consecutive branching and splitting of quarks and gluons. This is performed until a cutoff scale – usually in the order of 1 GeV – is reached and perturbative calculations break down. All particles are then handed to the hadronization model capable of simulating the formation of color neutral bound states as it is predicted by QCD. Since calculations at energy scales below the cutoff scale lead to divergences, the hadronization relies on models using tunable parameters, which also introduce underlying event effects. Although these model parameters have no predicted values from perturbative QCD, they can be constrained using specialized measurements in data. All particles with lifetimes longer than 10^{-8} s resulting from decays, the hadronization and parton shower are considered stable and form the particle level or generator level of a simulated event. At this stage, no effects from the detector or additional particles from pileup processes

are considered. Thus, on top of the particle level, the interactions of all stable particles with the detector is simulated using GEANT4 [34, 35], which includes a full description of all detector parts of the CMS experiment. Furthermore, pileup contributions are added at this stage using additional simulated interactions. All stable particles after the detector simulation are referred to as reconstruction level or detector level. Analytical calculations are always carried out on particle or parton level while the data are collected at the detector level. Thus, data have to be unfolded to particle or parton level – meaning corrected for detector and reconstruction effects – in order to be compared to analytical calculations.

2.4 Top quark

The top quark is the heaviest known particle and was discovered in 1995 by the CDF and D0 Collaborations at the Tevatron collider [36, 37]. The most precise single measurements of its mass m_{t} are performed by the ATLAS and CMS Collaborations and result in $m_{\mathrm{t}} = 172.99 \pm 0.85$ GeV [38] and $m_{\mathrm{t}} = 172.25 \pm 0.63$ GeV [39], respectively. A combination with the CDF and D0 Collaborations from 2014 results in $m_{\mathrm{t}} = 173.34 \pm 0.76$ GeV [40]. Because of its large mass, of all known particles the top quark has the largest coupling to the Higgs field and thus plays a special role in quantum loop corrections in the electroweak sector of the SM. This makes the top quark not only an interesting candidate for precision measurements of SM parameters but also makes it crucial to gain understanding of its properties in both direct and indirect searches for new physics.

2.4.1 Production and decay

At a proton-proton collider, top quarks are dominantly produced in pairs of top and anti-top quarks ($\mathrm{t\bar{t}}$) via the strong interaction. Due to the internal structure of the proton, the production channel via gluon-gluon fusion becomes dominant over the quark-anti-quark annihilation with increasing center-of-mass energy $\sqrt{s}$. All leading-order production mechanisms via the strong interaction are shown in Figure 2.3. The total $\mathrm{t\bar{t}}$ production cross section of

$$\sigma_{\mathrm{t\bar{t}}} = 831.76^{+19.77}_{-29.20}\,(\text{scale}) \pm 35.06\,(\text{PDF}+\alpha_s)\ \text{pb} \tag{2.18}$$

is predicted at next-to-next-to-leading order QCD using the Top++2.0 program [41] and assuming a top quark mass of 172.5 GeV in proton-proton collisions at $\sqrt{s} = 13$ TeV. In

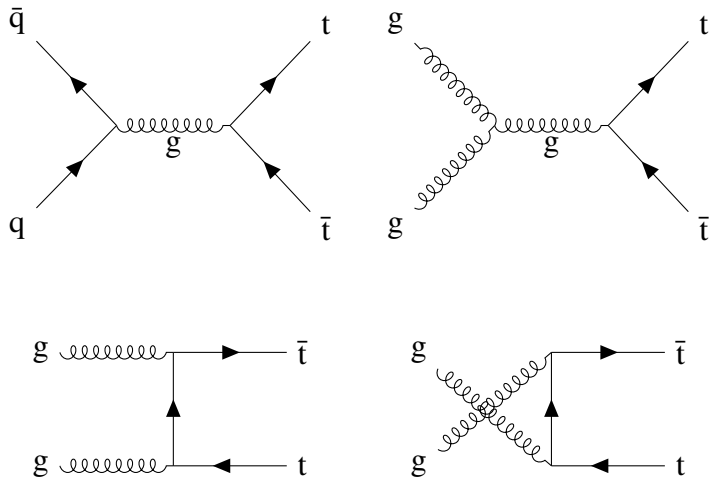

Figure 2.3: Feynman diagrams of the $t\bar{t}$ production mechanisms in proton-proton collisions via the strong interaction. Displayed are the s-channel of quark-anti-quark (upper left) and gluon-gluon (upper right) annihilation as well as the t-channel (lower left) and u-channel (lower right) of $gg \rightarrow t\bar{t}$. Created with TikZ [42].

addition, the top quark can be produced singly via the weak interaction in the *s*-channel or *t*-channel via a W boson and additionally in association with a W boson in the final state. However, this production mechanism is suppressed due to the small coupling strength of the weak interaction.

Top quarks only have a lifetime of about $0.5 \cdot 10^{-34}$ s [16] and therefore do not form color-neutral bound states before they decay. This enables measurements of a bare quark, which is usually not possible for particles charged under color. As indicated in the CKM matrix by the entry V_{tb} (see Equation 2.4), top quarks almost exclusively decay via $t \rightarrow bW$. While the b quark forms hadrons, the W boson further decays into quarks ($W \rightarrow q\bar{q}'$) or a charged lepton and the corresponding neutrino ($W \rightarrow \bar{\ell}\nu_\ell$). The two possible decay modes of the top quark – hadronic and leptonic – are displayed in Figure 2.4 (left and right, respectively). Because of the variety of possible color states in the decay into hadrons, the hadronic decay has a branching fraction of about 67% [16]. Given a pair of top quarks, the full decay can produce three different final states: the all-jets final state, where both W bosons decay into quarks (branching fraction of about 45%), the lepton+jets final state, where one W boson decays into quarks and the other into leptons (branching fraction of about 44%), and the dilepton case with two $W \rightarrow \ell\nu_\ell$ decays (branching fraction of about 11%). In this thesis, the lepton+jets final state is defined to not include top quark decays that contain a τ lepton, which reduces the branching fraction of the lepton+jets channel to about 29%.

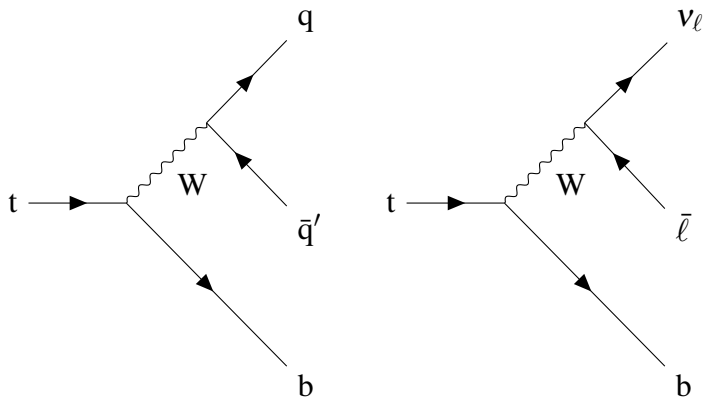

Figure 2.4: Feynman diagrams of the hadronic $t \to bW \to q\bar{q}'b$ (left) and leptonic top quark decay $t \to bW \to \bar{\ell}\nu_\ell b$ (right). Created with TikZ [42].

2.4.2 Top quark mass

The top quark mass m_t is a parameter of large interest in precision measurements of the SM. Considering the uncertainty of less than 1 GeV in direct measurements (Figure 2.5, left) the relative precision already surpasses 0.5%. Also determinations of the top quark mass from cross section measurements start to reach a precision of about 1% (Figure 2.5, right). The top quark mass is of such interest since it is an important parameter in consistency checks of the SM. Due to the large coupling between top quark and Higgs boson, the top quark directly influences the mechanism of electroweak symmetry breaking. This makes the relations of the masses of W boson, Higgs boson and top quark overconstrained, and measurements of those parameters allow for cross checks. The Gfitter group performed a global electroweak fit using combined measurements of m_t and the W mass, which is displayed in Figure 2.6. The overlapping ellipses demonstrate the self-consistency of the SM, considering the latest measurements. With that, the precise measurement of the top quark mass also acts as an indirect search for new phenomena not included in the SM.

A recurring discussion in the determination of the top quark mass is the exact definition of the mass itself. A measurement of the top quark mass is performed by reconstructing an observable in data, which is then compared to predictions of the same observable using different hypotheses of m_t. Here, the prediction can either be obtained from analytical QCD calculations or from simulated events. In so-called direct measurements, the top quark is reconstructed from its decay products via leptons, jets as well as missing transverse momentum, and a sensitive observable is compared to top quark mass hypotheses obtained from simulation. However, this reconstruction relies on parton shower and hadronization models that are not calculable

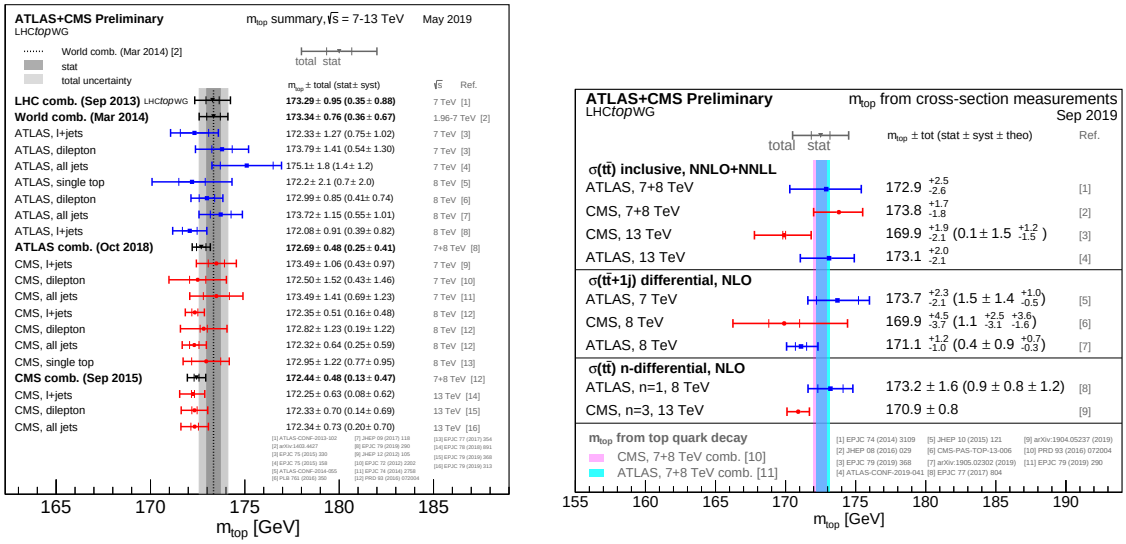

Figure 2.5: A summary of top quark mass results performed by the ATLAS and CMS collaborations for direct measurements (left) and extractions from cross section measurements (right). Taken from Ref. [43].

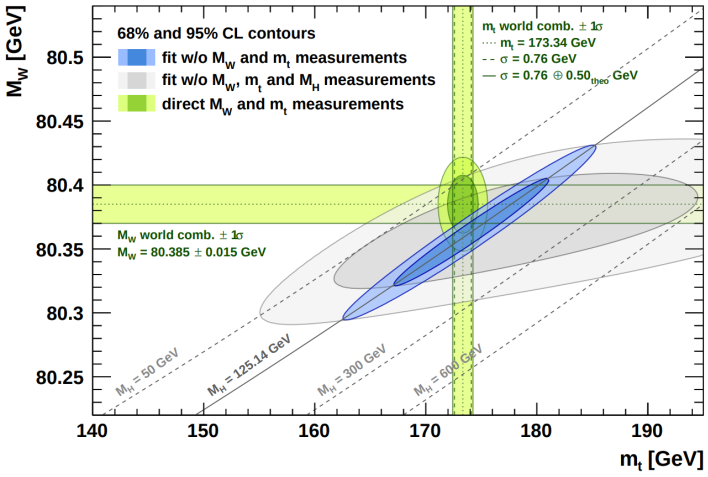

Figure 2.6: Allowed regions in m_{t}-m_{W}-plane obtained by a global electroweak fit. The green bands and ellipses show the direct measurements of the top quark and W boson masses. The grey and blue ellipses show the allowed regions of the electroweak fit excluding and including the Higgs boson mass, respectively. Taken from Ref. [44].

from first principles below a scale of $\Lambda \approx 1$ GeV [45]. Hence, the used observable is not calculable in perturbative QCD, and the top quark mass has to be extracted using simulation. As a consequence, the extracted top quark mass refers to a parameter as it is implemented in the respective event generator. This constitutes a problem since the relation to well defined and renormalizable mass schemes as they are used in field theory is unknown. Especially because direct measurement already reach a precision below the scale of $\Lambda \approx 1$ GeV, it is crucial to

understand the exact relation to mass schemes such as the pole mass $m_{\mathrm{t}}^{\mathrm{pole}}$, $\overline{\mathrm{MS}}$ mass $\overline{m}_{\mathrm{t}}$, or MSR mass $m_{\mathrm{t}}^{\mathrm{MSR}}$ [46, 47], which are all commonly used in analytical calculations connected to the top quark. The pole mass is directly related to the peak position of scattering amplitudes in the production of a top quark. Thus, all self-energy corrections are absorbed into the definition of the top quark mass in this scheme. The $\overline{\mathrm{MS}}$ mass scheme introduces a mass depending on the renormalization scale μ. Very similar to the definition of the strong coupling $\alpha_s(\mu)$, self energy corrections are only absorbed into the top quark mass $\overline{m}_{\mathrm{t}}(\mu)$ above a momentum scale $\mu > m_{\mathrm{t}}$. With this, the $\overline{\mathrm{MS}}$ mass is not affected by non-perturbative effects at small energies and is often referred to as short-distance mass. In contrast, the MSR mass scheme introduces the possibility to evaluate the top quark mass $m_{\mathrm{t}}^{\mathrm{MSR}}(R)$ at scales $R < m_{\mathrm{t}}$, which absorbs all corrections down to the scale R. Further details on the construction and interpretation of the top quark mass in the presented schemes are summarized in Ref. [47].

Since all renormalizable mass schemes can be translated into each other, the remaining issue is the unknown relation to the mass scheme used in event generators. These complications can be avoided by the measurement of an observable that does not rely on simulation but can rather be calculated analytically. A widely considered option are measurements of the $\mathrm{t\bar{t}}$ production cross section, which are sensitive to the top quark mass as well. As shown in Figure 2.5, these pole mass measurements (right) cannot compete with the sensitivity of direct measurements (left) but yet allow the determination of a top quark mass in a well defined and renormalizable mass scheme. The measurement presented in Chapter 7 aims at a differential cross section measurement as a function of the jet mass, which is suitable for analytical calculations.

3 Jets and jet substructure

Particles carrying color cannot be observed as free particles but form color neutral bound states. In combination with radiation of gluons and gluons splitting into pairs of quarks, colored particles result in a jet of hadrons in the detector. These jets are reconstructed using clustering algorithms, which are introduced in Section 3.1. Certain properties of those jets are used to determine their exact origin and are referred to as substructure. For this thesis, the substructure observables jet mass and N-subjettiness play a crucial role and are introduced in Section 3.2. All jet observables described in this chapter are a product of QCD processes. Because low-energy processes that are part of the hadronization process can lead to divergences in analytic calculations, jets are non-trivial objects. This can be addressed by constructing jet observables that are infrared and collinear (IRC) safe, meaning the jet observables are insensitive to low-energy radiation and collinear splitting. All presented jet algorithms are IRC safe by construction. Since both analyses described in this thesis aim at a measurement of jets that reconstruct hadronic top quark decays, a similar focus is set in this chapter.

3.1 Jet clustering algorithms

Jets consist of multiple particles such as hadrons and photons, which are combined to form a single object. For this procedure, dedicated algorithms are needed. All algorithms that are presented in this section are used as implemented in the FASTJET software package [48].

3.1.1 Anti-k_T and Cambridge-Aachen algorithms

Today, iterative jet clustering algorithms are the standard for particle physics analyses. All such algorithms have a similar workflow. The algorithm takes a list of particle candidates as input and creates jets as physics objects from them. As a first step, for each pair of particle

candidates (also referred to as pairs of pseudojets) i and j, the two variables

$$d_{ij} = \min(p_{\mathrm{T},i}^{2n}, p_{\mathrm{T},j}^{2n}) \frac{(\Delta R(i,j))^2}{R^2} \quad \text{and} \tag{3.1}$$

$$d_{iB} = p_{\mathrm{T},i}^{2n} \tag{3.2}$$

are calculated. Here, $p_{\mathrm{T},i}$ is the transverse momentum of the pseudojet i, $\Delta R(i,j)$ is the angular distance between i and j, n is a parameter steering the clustering, and R is a distance parameter. If for any two pseudojets i and j the relation $d_{ij} < d_{iB}$ holds, the four-momenta of i and j are added and form a single pseudojet in the next iteration. Whenever $d_{iB} < d_{ij}$, the pseudojet i is saved in the jet collection and removed from the pseudojet list. This procedure is repeated until the pseudojet list is empty. The two parameters R and n influence the behavior of the clustering. While the distance parameter R defines the maximum distance at which particles still are combined, n affects the order of clustering. With $n = 1$, the algorithm is referred to as k_{T} algorithm [49, 50] and attempts to invert the QCD branching process by clustering low-energy particles first. Nonetheless, this algorithm is not used in the scope of this thesis. If n is set to -1, the algorithm begins clustering particles with high transverse momenta. This option is called the anti-k_{T} (AK) algorithm [13]. If the Cambridge-Aachen (CA) algorithm [51, 52] is used by choosing $n = 0$, the clustering order is not influenced by the particle momenta but only their relative distance, and particles that are very close are clustered first. Figure 3.1 shows the resulting shapes for jets clustered with the anti-k_{T} (left) and Cambridge-Aachen (right) algorithms in the η-ϕ-plane. Not only do AK jets tend to be very circular but also the behavior for close-by jets differs between the algorithms. The anti-k_{T} algorithm produces jets with a circular core and surrounding jets with a crescent moon shape. The Cambridge-Aachen algorithm behaves purely geometric and assigns particles to a jet by their distance only. For the use in analyses performed by the CMS Collaboration, jets are usually clustered using the anti-k_{T} algorithm with a radius parameter of $R = 0.4$ (AK4 jets) or $R = 0.8$ (AK8 jets).

3.1.2 HOTVR algorithm

The Heavy Object Tagger with Variable R (HOTVR) algorithm [14] is an iterative clustering algorithm that – in contrast to the beforehand mentioned algorithms – adjusts its distance parameter R to the p_{T} of the jet [53]. This method addresses the fact that decay products of a Lorentz-boosted particle are collimated. Since the boost of a particle gets larger with its momentum, the decay products of a high-p_{T} object are in average closer than for lower momenta. Thus, a jet that should reconstruct all the decay products of a high-p_{T} object can

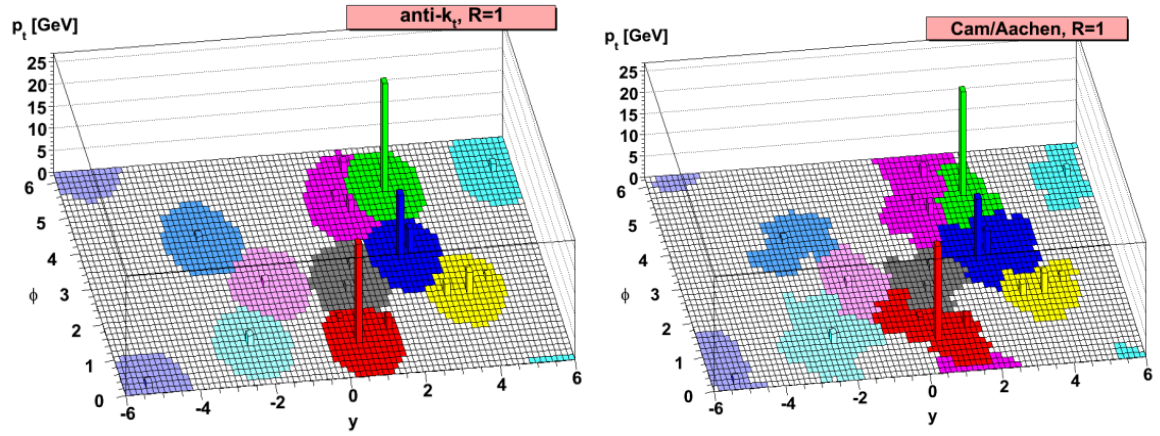

Figure 3.1: Jet areas for anti-k_{T} (left) and Cambridge-Aachen jets (right) in the η-ϕ-plane. The transverse momentum of a particle candidate inside a jet is indicated by the vertical bars. Taken from Ref. [13].

have a relatively small area. The reduction of the distance parameter R is beneficial in those cases since effects caused by pileup and underlying event drastically increase with the area of a jet. The clustering procedure is similar to the Cambridge-Aachen algorithm above but with a modification of $R \to R_{\mathrm{eff}}$, where

$$R_{\mathrm{eff}} = \begin{cases} R_{\mathrm{min}} & \text{for} \quad \rho/p_{\mathrm{T}} < R_{\mathrm{min}} \\ R_{\mathrm{max}} & \text{for} \quad \rho/p_{\mathrm{T}} > R_{\mathrm{max}} \\ \rho/p_{\mathrm{T}} & \text{else} \end{cases}. \tag{3.3}$$

Thus, R_{eff} is given by ρ/p_{T}, where $\rho = 600\,\mathrm{GeV}$ is a scaling parameter. R_{eff} can take values between a minimum $R_{\mathrm{min}} = 0.1$ and a maximum $R_{\mathrm{max}} = 1.5$. Furthermore, the mass jump [54, 55] condition is introduced to eliminate low-energy radiation inside the jet. The mass jump criterion

$$\theta m_{ij} > \max\left(m_i, m_j\right) \tag{3.4}$$

is designed such that the combined invariant mass m_{ij} of two pseudojets i and j is sufficiently increasing in comparison to the individual jet masses m_i and m_j. The criterion is set up with a default strength of $\theta = 0.7$. If the criterion does not hold and no mass jump is observed, the two pseudojets are not combined, and the pseudojet with smaller mass is removed. This veto is only applied if

$$m_{ij} > \mu = 30\,\mathrm{GeV}. \tag{3.5}$$

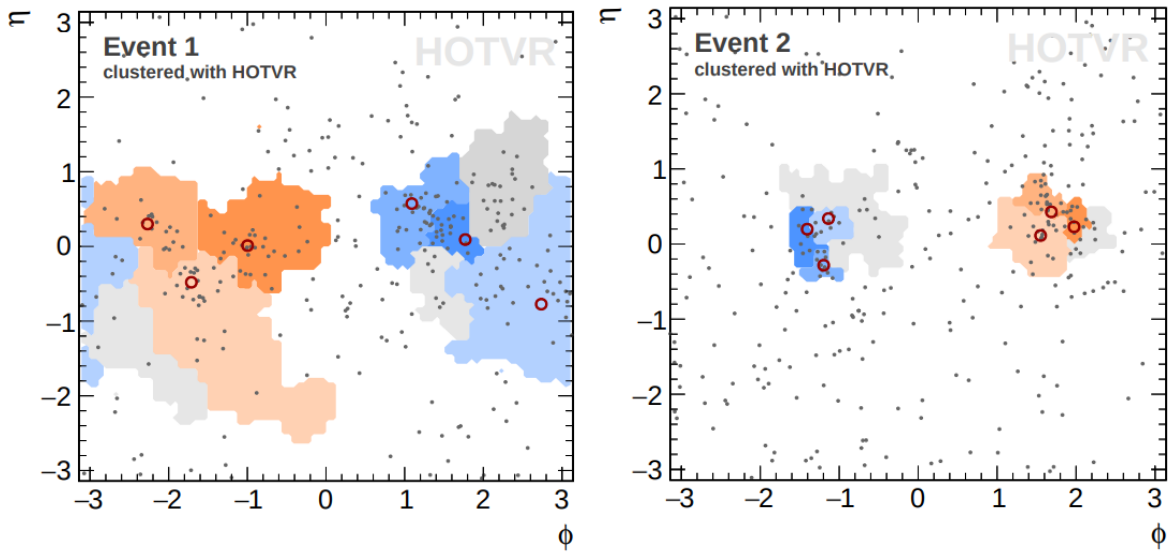

Figure 3.2: The jet area in the η-ϕ-plane for HOTVR jets with low (left) and high (right) momenta in a $t\bar{t}$ sample in the all-jets final state. Grey dots indicate stable particles, the top quark decay products are highlighted with red circles. The jet areas are shown subdivided into subjets in orange and blue for two HOTVR jets. The grey areas indicate pseudojets that were rejected by the mass jump or p_T veto. Taken from Ref. [14].

In addition, the p_T of both pseudojets has to be larger than a threshold of

$$p_{T,sub} > 30\,\text{GeV} \tag{3.6}$$

in order to be combined. Every pseudojet not passing this requirement is removed. If a mass jump is found and the p_T criterion holds, the two pseudojets are combined and enter the next iteration of the clustering process. Furthermore, the two initial pseudojets are stored as subjets. The resulting jet shapes for $t\bar{t}$ events in the all-jets channel are displayed in Figure 3.2 for small (left) and large (right) transverse momenta. All stable particles are shown as grey dots, the top quark decay products are shown as red circles. The orange and blue areas represent the subjets of the two HOTVR jets in the event and the grey areas are subjets that were rejected due to the mass jump or p_T veto. In both presented examples all of the decay products of the top quark end up in the jet despite their very different jet areas that were adapted to the jet p_T. This behavior allows a stable performance of HOTVR jets in various kinematic regions.

3.1.3 XCone algorithm

In contrast to the jet clustering algorithms mentioned previously, XCone [56] is an exclusive algorithm, meaning it always returns a fixed number of jets N that is specified prior to the clustering. Furthermore, the XCone algorithm is defined as a cone algorithm. In contrast to the iterative algorithms, jet axes are defined first, and the momenta of all particle candidates inside a radius R are summed up in order to form a jet. In the XCone algorithm, a cone is defined as the area around an axis in a radius given by the distance parameter R, which is an input to the algorithm. At first all possible IRC-safe axes are found by running a generalized k_{T} clustering algorithm. The N requested axes in a given event are chosen such that the so-called N-jettiness variable of the event is minimized. The N-jettiness $\tilde{\tau}_N$ is a measure of how compatible an event is with a hypothesis of N jets. It is defined as

$$\tilde{\tau}_N = \sum_i \min\{\rho_{\mathrm{jet}}(p_i, n_1), ..., \rho_{\mathrm{jet}}(p_i, n_N), \rho_{\mathrm{beam}}(p_i)\}, \tag{3.7}$$

where the sum runs over all particles i with the four-momenta p_i. The distance measures $\rho_{\mathrm{jet}}(p_i, n_A)$ and $\rho_{\mathrm{beam}}(p_i)$ are defined between i-th particle and A-th axis and between i-th particle and beam axis, respectively. After requiring XCone to find N jets, it finds the N infrared and collinear safe axes in an event that minimize the N-jettiness. Subsequently, all particles within an angular distance R around an axis are clustered to a jet. This way, all isolated XCone jets are circular. If two jet axes end up closer then the predefined distance R, particle candidates are assigned to the jet that is closer in angular distance. Figure 3.3 shows the jet area of XCone jets using simulated $\mathrm{t\bar{t}}$ events for large jets (left) and small jets (right). While the result with large jets and $N = 2$ (one large jet per top quark) gives a result very similar to clustering the same event with the anti-k_{T} algorithm, it is very different in the case of smaller jets with $N = 6$ (one jet per top quark decay parton). While XCone still correctly identifies and reconstructs the jets from the $\mathrm{t\bar{t}}$ decay, anti-k_{T} does not. Also the feature of non-isolated XCone jets is visualized, where the boundaries between jets become straight lines, ensuring the unambiguous assignment of particle candidates to a jet. Since the definition of XCone jets is based on the N-jettiness, which is well-understood and theoretically accessible, they are a promising choice for a measurement aiming at a comparison to analytical QCD calculations.

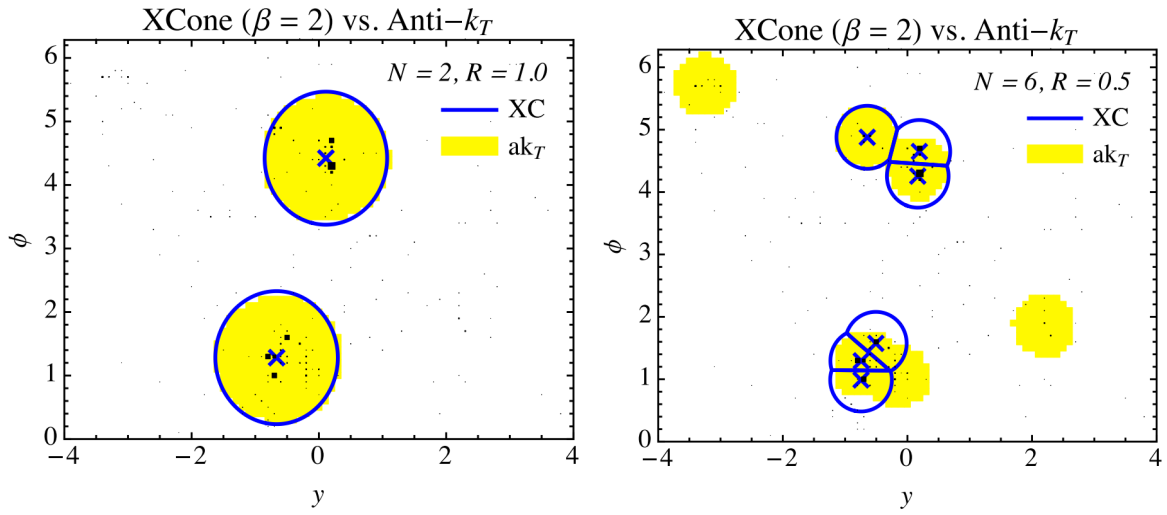

Figure 3.3: Comparison of the jet areas after clustering jets with the XCone algorithm (blue lines) and anti-k_T algorithm (yellow areas) for large jets with $R = 1.0$ and $N = 2$ (left) as well as small jets with $R = 0.5$ and $N = 6$ (right). Both algorithms give similar results with large jets but show very different shapes in the case of small jets. Taken from Ref. [56].

3.2 Jet substructure

Both analyses presented in this thesis set a focus on top quarks with high transverse momenta. While a top quark at rest decaying via $t \to bq\bar{q}'$ would result in three separate jets, the decay products merge into a single large jet if the top quark carries large momentum. At the LHC, top quarks with large momenta are produced in large quantities and are part of the decay chain of many searches for hypothetical heavy new particles. The challenge in this kinematic regime is to identify those jets that originate from top quark decays and distinguish them from other sources. In order to do so, jet substructure is a crucial tool. Various variables can be constructed that are sensitive to the origin of jets. The jet mass (Section 3.2.1) and measures of the energy distribution within a jet such as the N-subjettiness (Section 3.2.2) are common examples of such observables. Soft drop [57], a popular jet grooming algorithm is introduced in Section 3.2.3. In Sections 3.2.4 and 3.2.5 measurements of substructure observables are presented that are performed using light quark as well as gluon jets and jets initiated by hadronic decays of top quarks, respectively.

3.2.1 Jet mass

The jet mass m_{jet} is defined as the invariant mass of the sum of the momenta p_i of all particle candidates in a jet via

$$m_{\text{jet}} = \sqrt{\left(\sum_i p_i\right)^2}. \tag{3.8}$$

In a typical collision event, all constituents of a jet are stable particles with masses $m_i \ll p_{\text{T},i}$. In this case, the jet mass is dominantly determined by the relative orientation of the constituents and their momenta. Thus, the jet mass in QCD multijet events is mostly generated by the splitting and branching in hadron showers. This leads to the so-called Sudakov peak [58] in the m_{jet} distribution that shifts its position with the jet p_{T}, although the naive expectation would be a falling spectrum with a maximum close to 0 GeV, which is roughly the invariant mass of a light quark or gluon. In an experimental environment such as the LHC, the jet mass is further influenced by additional particles from pileup and underlying event as well as initial and final state radiation.

The jet mass of large-radius jets that include the hadronic decay of Lorentz-boosted heavy particles is sensitive to the initial particle's mass. Thus, the jet mass can be used in order to distinguish light quark and gluon jets from those that include all decays products of a hadronic top quark decay. Furthermore, a measurement of the jet mass in decays of boosted top quarks is sensitive to the top quark mass itself and offers the possibility of the extraction of this fundamental SM parameter.

In addition, the jet mass is an observable that can be calculated from first principles, which would enable the extraction of the top quark mass from analytical predictions in a well defined mass scheme. For a long time, these calculations [59] of m_{jet} were only feasible for electron-positron collisions, where the process $\text{e}^+\text{e}^- \to \text{t}\bar{\text{t}}$ is divided in two hemispheres, and the jet mass is defined as the invariant mass of all particles in one hemisphere. Consequently, the differential $\text{t}\bar{\text{t}}$ production cross section as a function of the jet mass can be calculated in soft-collinear effective field theory (SCET) [60, 61] for processes at large scales $Q \gg m_{\text{jet}}$. The calculation at hadron colliders introduces the necessity to treat color states in the initial state, which makes the color connection between initial and final state non-trivial. However, recently a first calculation of m_{jet} in proton-proton collisions has been performed in Ref. [62], where effects from non-perturbative QCD could be avoided by employing the soft drop algorithm [57], which is detailed in Section 3.2.3. Figure 3.4 shows the resulting distribution in m_{jet}, which is compared to the spectrum obtained with PYTHIA. For the first time, this calculation shows

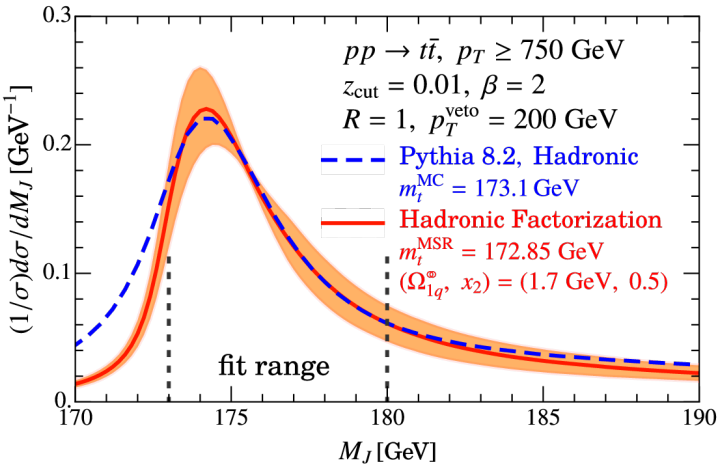

Figure 3.4: Distribution in m_{jet} obtained from simulation (blue dashed line) and analytical calculation (red solid line). The spectrum is obtained from lightly groomed jets using the soft drop algorithm. Taken from Ref. [62].

the possibility of extracting a well defined top quark mass from a spectrum of the jet mass in boosted top quark decays at a hadron collider.

3.2.2 N-subjettiness

Similar to the N-jettiness defined in Section 3.1.3, the N-subjettiness τ_N [63] is a measure of the compatibility of a jet with a hypothesis that it contains at most N subjets. This directly targets the separation of the expected three-prong structure of top quark decays from one-prong structures in jets originating from single gluons or light quarks. It is defined as

$$\tau_N = \frac{1}{d_0} \sum_k p_{\text{T},k} \min\left(\Delta R_{1,k}, \Delta R_{2,k}, ..., \Delta R_{\text{N},k}\right), \tag{3.9}$$

where $p_{\text{T},k}$ is the transverse momentum of a particle candidate k inside the jet, $\Delta R_{i,k}$ indicates the angular distance between a subjet candidate i and the particle candidate k, and d_0 is a normalization factor in order to obtain values for τ_N between 0 and 1. If all particles inside a jet are aligned with the axes of the N subjet candidates, the value of τ_N becomes small. Nevertheless, Figure 3.5 (left) shows that the variable τ_3 is not enough to distinguish jets from top quark decays from those originating from light quarks and gluons (referred to as QCD jets). However, the ratio $\tau_{32} = \tau_3/\tau_2$ (Figure 3.5, right) is sensitive to the difference between jets containing a top quark decay and those that do not. Although the ratio τ_{32} – in contrast to τ_3 – is not IRC safe, it can be calculated analytically in perturbative QCD since it fulfills the

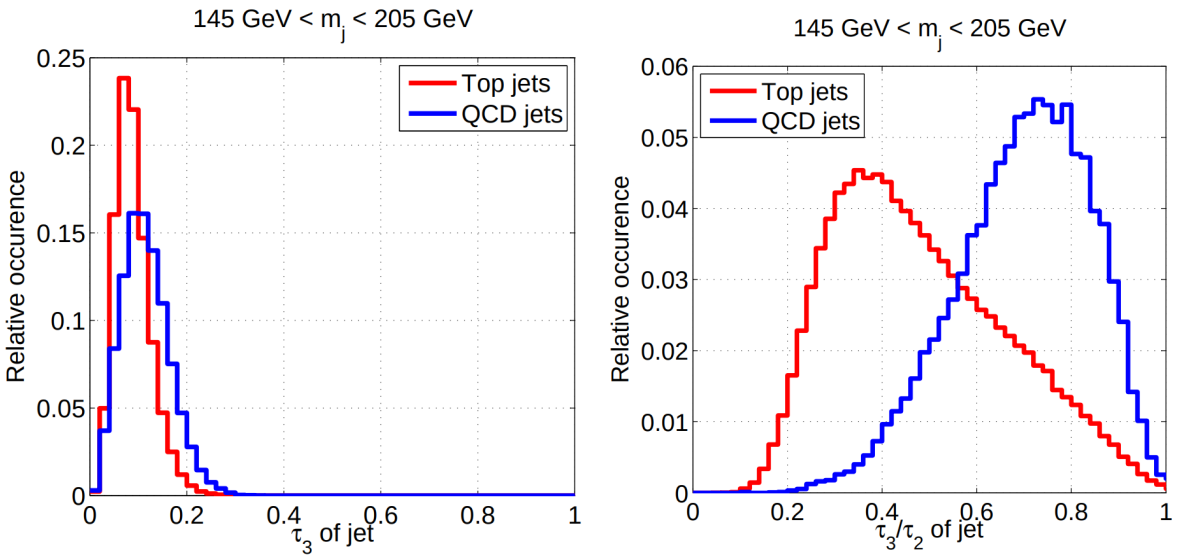

Figure 3.5: The distributions in τ_3 (left) and $\tau_{32} = \tau_3/\tau_2$ (right) for jets containing a hadronic top quark decay (red) and for jets originating from light quarks or gluons (blue). While τ_3 does not show a high sensitivity on the origin of the jet, the ratio τ_{32} does. Taken from Ref. [63].

requirements of Sudakov safety [64].

3.2.3 Soft drop

A large-radius jet is likely to contain contributions from pileup, underlying event, and low-energy radiation, which significantly change its substructure and complicate identifying its origin. Grooming techniques have been developed that aim at removing additional low-energy and wide angle radiation from the jet. The cleaned jet then allows for a more precise inference of the properties of the initiating particle. One of the most frequently used grooming techniques is the soft drop algorithm [57], which is a generalization of the modified MassDrop Tagger [58]. In order to apply the algorithm, all constituents of a jet are reclustered using the CA algorithm. Afterwards, the last iteration of the clustering procedure, where the remaining two pseudojets were added to form the final jet, is reversed. Now, the soft drop condition,

$$\frac{\min\left(p_{\mathrm{T},1}, p_{\mathrm{T},2}\right)}{p_{\mathrm{T},1} + p_{\mathrm{T},2}} > z_{\mathrm{cut}} \left(\frac{\Delta R_{12}}{R}\right)^{\beta} \tag{3.10}$$

is tested. Here, $p_{\mathrm{T},1}$ and $p_{\mathrm{T},2}$ are the transverse momenta of the two pseudojets, ΔR_{12} is their angular separation, and R the distance parameter of the jet under consideration. The threshold parameter z_{cut} and exponent β control the strength and angular dependence of the grooming

procedure, respectively. If the condition does not hold, the jet is redefined to be the pseudojet with larger p_{T}, and the condition is checked again for the previous clustering step. Once the condition holds, the jet is declared to be the final jet, and the soft drop algorithm stops. Thus, the two parameters z_{cut} and β directly control which contributions to a jet are rejected. A value of $\beta > 0$ preferably suppresses wide angle radiation while the case of $\beta = 0$ removes the angular dependence from the soft drop condition. Negative values of β are possible as well but are usually not relevant for the experimental case. The strength z_{cut} controls the threshold on the transverse momenta of the pseudojets and decides which pseudojets are kept. Within analyses carried out by the CMS Collaboration the default values $z_{\mathrm{cut}} = 0.1$ and $\beta = 0$ (corresponding to the modified MassDrop Tagger) are chosen.

In the identification of hadronic decays of heavy particles, the soft drop jet mass m_{SD} plays a crucial role and is an important observable in most jet identification – or tagging – algorithms, since a jet reconstructing the full decay is expected to have a jet mass close to the mass of the original particle. Figure 3.6 shows the soft drop jet mass distribution for jets originating from a top quark decay and those initiated by light quarks and gluons in QCD multijet events. In the top quark sample, three categories of jets can be identified. Ideally, all decay products of the top quark lay inside the jet and produce a jet mass close to the top quark mass. If the b quark decay is not captured inside the jet, the jet mass is shifted towards the W boson mass. Jets with masses between the W boson mass and top quark mass are likely to include the b quark but only one of the two W boson decay products. Even higher masses at $m_{\mathrm{SD}} > m_{\mathrm{t}}$ are generated if additional particles enter a jet that already includes all top quark decay products. Nevertheless, the spectrum obtained with the top quark sample is very different from the falling spectrum for light quark and gluon jets. This makes the jet mass a powerful observable for the identification of jets, and measurements of m_{jet} or m_{SD} provide crucial input for the understanding and modeling of jet substructure.

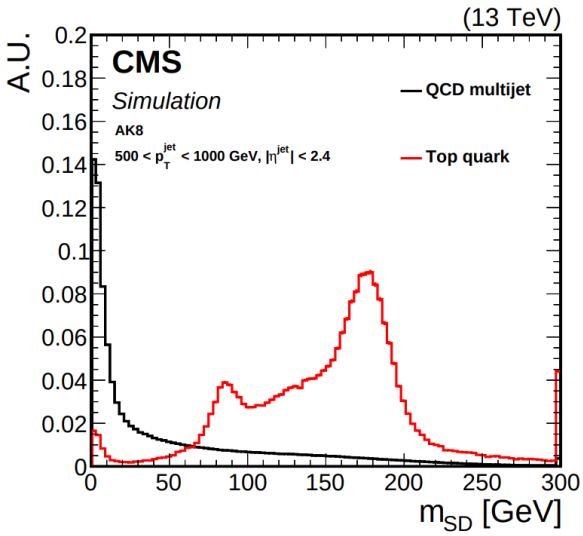

Figure 3.6: Normalized distribution of the soft drop groomed jet mass for $t\bar{t}$ (red line) and QCD multijet simulation (black line). Only jets clustered with anti-k_T and $R = 0.8$ fulfilling $p_T > 500$ are considered. Taken from Ref. [9].

3.2.4 Measurements of light quark and gluon jets

The jet mass has been measured by the CMS Collaboration in QCD dijet events at $\sqrt{s} =$ 13 TeV [65], using AK8 jets. The differential jet production cross section extracted from this measurement as a function of both the ungroomed jet mass without and groomed jet mass with applying the soft drop algorithm is shown in Figure 3.7. Furthermore, m_{jet} is measured in various bins of jet p_T, spanning an extensive range from 200 GeV up to 1300 GeV. The grooming clearly suppresses the Sudakov peak. After applying the soft drop algorithm, the jet mass spectrum is a purely falling spectrum as one would naively expect from light quarks and gluons. Over the full kinematic range of the measurement, the data agree with the prediction obtained with various event generators. In addition, analytical calculations are available for the soft drop jet mass and agree with the measurement as well. Similarly, the ATLAS Collaboration performed a measurement of the soft drop jet mass [66] at $\sqrt{s} = 13$ TeV. The resulting normalized cross section measurement using anti-k_T jets and a radius parameter of $R = 0.8$ is shown in Figure 3.8 and compared to analytical calculations.

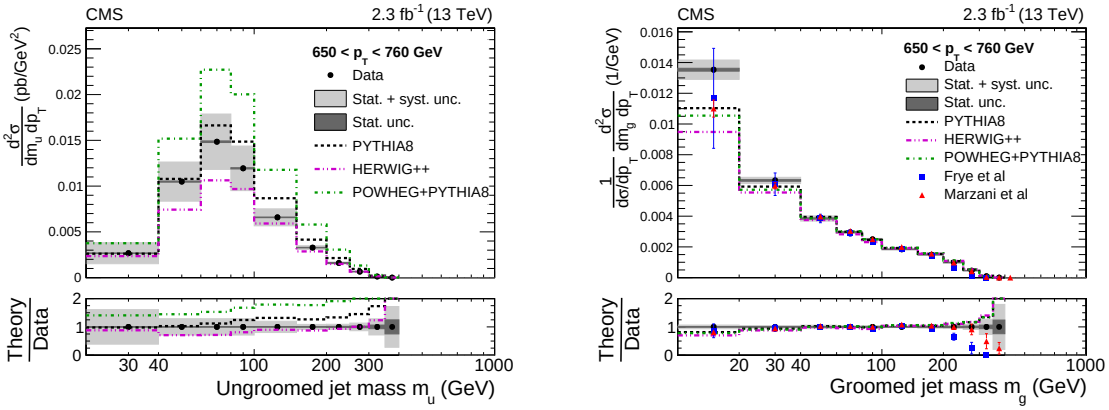

Figure 3.7: Normalized differential jet production cross section as a function of the ungroomed (left) and groomed jet mass (right) in QCD dijet events. The differential cross section is measured in bins of jet p_{T} ranging from 200 GeV to 1300 GeV, where the bin with $650 < p_{\mathrm{T}} < 760$ GeV is selected for display. The measured data (black markers) are compared to simulations obtained with PYTHIA, POWHEG and HERWIG (lines) and analytical calculations (colored markers). Statistical and total uncertainties in the measurement are displayed as dark and light grey areas. Uncertainties in the calculations are displayed as vertical bars. The lower panel shows the ratio of prediction to data. Taken from Ref. [65].

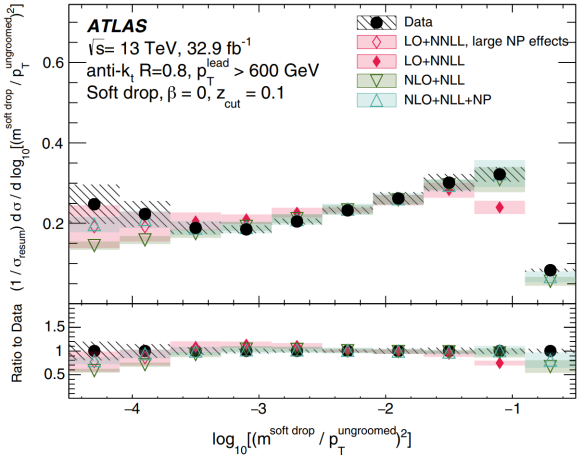

Figure 3.8: Normalized differential cross section as a function of $\log[(m_{\mathrm{SD}}/p_{\mathrm{T}})^2]$ in QCD dijet events for jets with $p_{\mathrm{T}} > 600$ GeV that are clustered with the anti-k_{T} algorithm and a radius parameter of $R = 0.8$. Data (black markers) are compared to analytical calculations (colored markers), uncertainties are displayed as hatched and filled areas. In the bottom panel, the ratio of calculations to data is shown. Taken from Ref. [66].

3.2.5 Measurements in hadronic top quark decays

A first measurement of the jet mass [1] in boosted top quark decays was carried out by the CMS Collaboration using data collected at a center-of-mass energy of $\sqrt{s} = 8$ TeV. The differential

$t\bar{t}$ production cross section was measured as a function of the ungroomed jet mass in hadronic decays of boosted top quarks. The measurement was performed in the lepton+jets channel, where the hadronic top quark decay is reconstructed using a single large-radius jet. The lepton acts as a tag and provides a good selection efficiency while it enables the selection of a very pure $t\bar{t}$ sample. The large jets were clustered using the Cambridge-Aachen algorithm with a distance parameter of $R = 1.2$. Boosted top quarks were selected by requiring at least one jet to have $p_T > 400$ GeV. The result of the differential cross section measurement is shown in Figure 3.9 (left). This measurement alone provides crucial input for the tuning of $t\bar{t}$ simulations and especially provides constraints on the parton shower modeling. In addition, the normalized cross section (Figure 3.9, right) is sensitive to the value of the top quark mass. Using simulated templates for different values of m_t, the top quark mass has been measured to be

$$m_t = 170.8 \pm 6.0\,(\text{stat}) \pm 2.8\,(\text{syst}) \pm 4.6\,(\text{model}) \pm 4.0\,(\text{theo})\ \text{GeV} \quad (3.11)$$

$$m_t = 170.8 \pm 9.0\ \text{GeV}. \quad (3.12)$$

While the statistical uncertainty is dominant, other large contributions from the jet energy scale and jet mass scale as well as parton shower modeling are observed. These uncertainties can be reduced using a larger data set with increased statistical precision as well as smaller jets reducing the effects from pileup and underlying event and therefore improving the jet calibration. Despite the large uncertainty in the extraction of the top quark mass, this analysis acts as a proof of concept that such a measurement is experimentally feasible. Furthermore, it shows the importance of the jet mass not only in tagging algorithms and for parton shower modeling but also in the extraction of fundamental SM parameters.

The N-subjettiness ratio τ_{32} has been measured by both ATLAS [67] and CMS [68] in $t\bar{t}$ events. ATLAS performed the measurement in the boosted regime, where the top quark decay is reconstructed with a single anti-k_T jet with $R = 1.0$ and $p_T > 350$ GeV. Jets that contain all top quark decay products contribute to the peak at small values of τ_{32} in Figure 3.10 (left). Conversely, CMS selects $t\bar{t}$ events with energies close to threshold production and measures τ_{32} using anti-k_T jets with $R = 0.4$. Thus, the CMS measurement does not aim at the three-prong structure of a top quark decay but rather uses the selection of a $t\bar{t}$ sample in order to select jets originating from light quarks and suppressing the contribution from gluon jets. As expected, the small AK4 jets do not include the full three-prong structure of the boosted top quark decay and result in a distribution (Figure 3.10, right) similar to the expectation for QCD multijet events. In contrast to the ATLAS measurement, which focuses on the description of top quark decays, this measurement mostly aims at a general validation of the substructure description

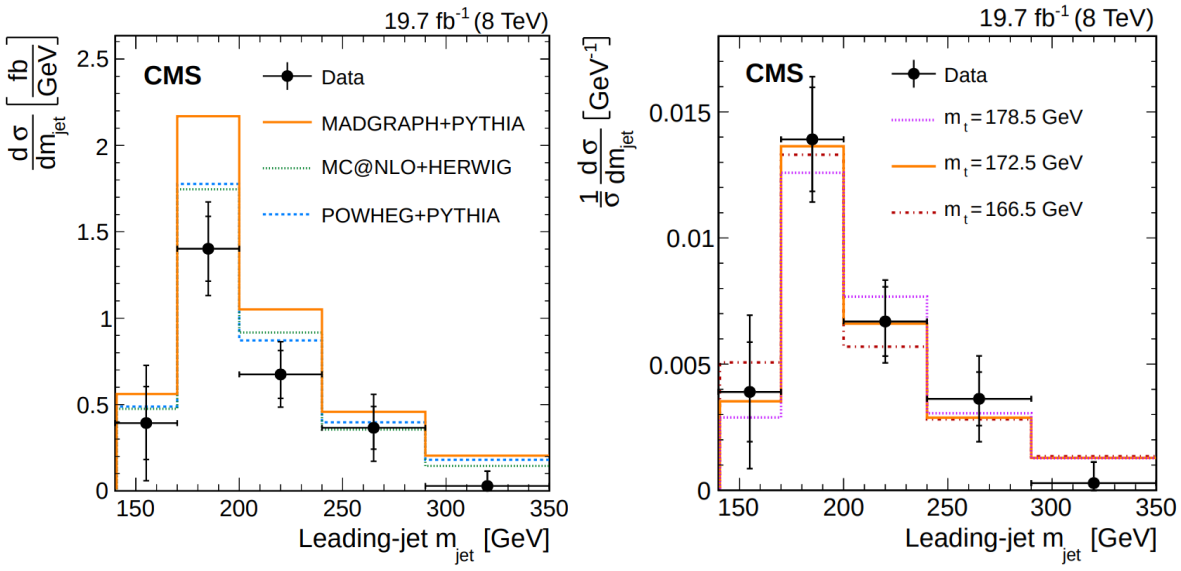

Figure 3.9: Differential cross section (left) and normalized differential cross section (right) as a function of m_{jet} from a measurement performed at $\sqrt{s} = 8$ TeV in hadronic decays of boosted top quarks. The left graph compares data (markers) to three predictions from simulation (lines). On the right, the normalized measurement in data (markers) is compared to three predictions for different values of m_{t} (lines). The vertical lines on the data points show the total (outer bars) and statistical (inner bars) uncertainties. The horizontal bars indicate the bin width. Taken from Ref. [1].

obtained from MC generators. Both measurements indicate shape differences between data and simulation – especially for POWHEG. Since jet tagging techniques rely on the substructure of jets it is crucial to measure and understand differences between simulation and data. The measurement of top tagging efficiencies presented in Chapter 8 aims at the estimation and correction for differences in selection efficiencies due to imperfect modeling of substructure observables in simulation.

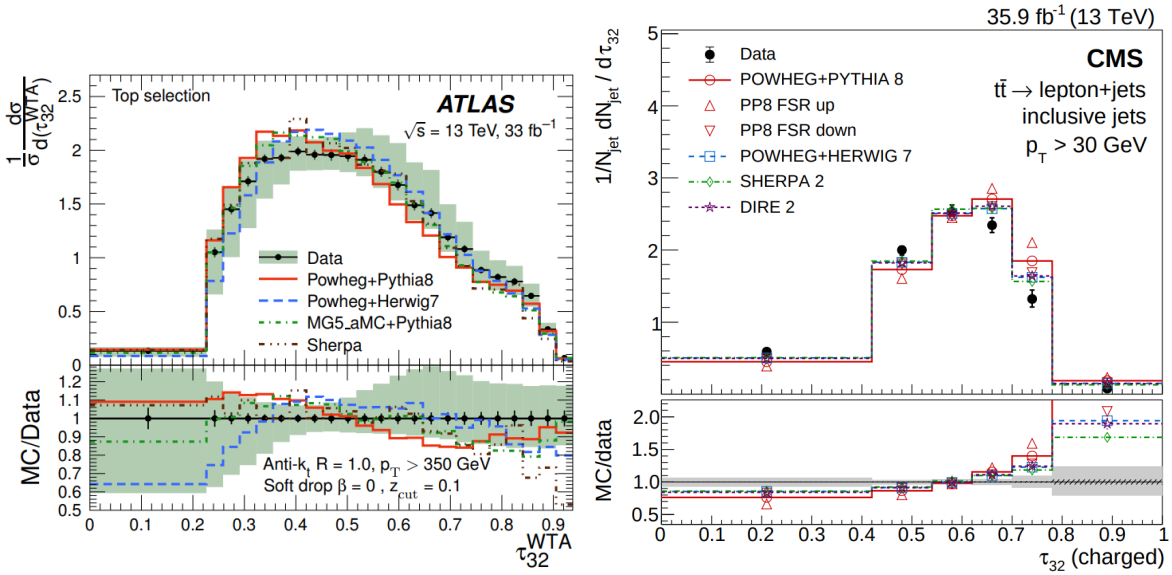

Figure 3.10: Measurements of the N-subjettiness ratio τ_{32} performed by ATLAS (left) and CMS (right) in hadronic top quark decays. ATLAS measures large radius jets with $R = 1.0$ and soft drop applied in the boosted regime targeting fully-merged top quark decays while CMS selects smaller jets with $R = 0.4$ targeting resolved top quark decays. Data (black markers) are compared to predictions by several MC generators (lines). In the bottom panels, the ratio of predictions to data is shown. Uncertainties are displayed as filled area (left) and vertical bars (right). Taken from Refs. [67] and [68].

4 Experimental setup

The analyses presented in this thesis investigate proton-proton collision data collected by the CMS experiment at the Large Hadron Collider. The abundant production of top quarks at the LHC makes it an ideal laboratory for precision measurements of top quark properties. Electrons, muons, photons, and hadrons produced in proton-proton collisions are reconstructed using the CMS detector. The particle collider LHC and all components of the CMS detector are discussed in the following.

4.1 Large Hadron Collider

The LHC is a proton-proton (and heavy ion) particle accelerator and collider and the world's largest of its kind. It is located at the European Organization for Nuclear Research (CERN) facility and operated at a center-of-mass energy of $\sqrt{s} = 13$ TeV in the years 2016, 2017, and 2018. In order to obtain a beam of protons, electrons are removed from hydrogen atoms in the very first stage of the accelerator complex via a strong electromagnetic field. The protons are accelerated by a variety of linear and circular accelerators to increasingly high energies before they are injected into the LHC ring, where superconducting cavities accelerate the protons to an energy of 6.5 TeV. Figure 4.1 shows CERN's accelerator complex and displays the path of the protons. Within the LHC two proton beams circulate in opposite directions and are brought to collision at dedicated interaction points, where the detectors of the experiments ALICE [1], ATLAS [2], CMS, and LHCb [3] are located. While ALTAS and CMS are multi-purpose detectors aiming at a wide range of physics analyses, LHCb focuses on physics involving bottom quarks, and ALICE targets analyzing heavy ion collisions.

The beams are subdivided in 2808 bunches each consisting of about 10^{11} protons. Superconducting dipole magnets bend the proton trajectory into a circular shape through the LHC ring while quadrupole and higher order magnets focus the beam. Every 25 ns, two bunches of opposite beams collide at the interaction points. Due to the high number of protons within a

[1] A Large Ion Collider Experiment
[2] A Toroidal LHC Apparatus
[3] Large-Hadron-Collider-beauty-Experiment

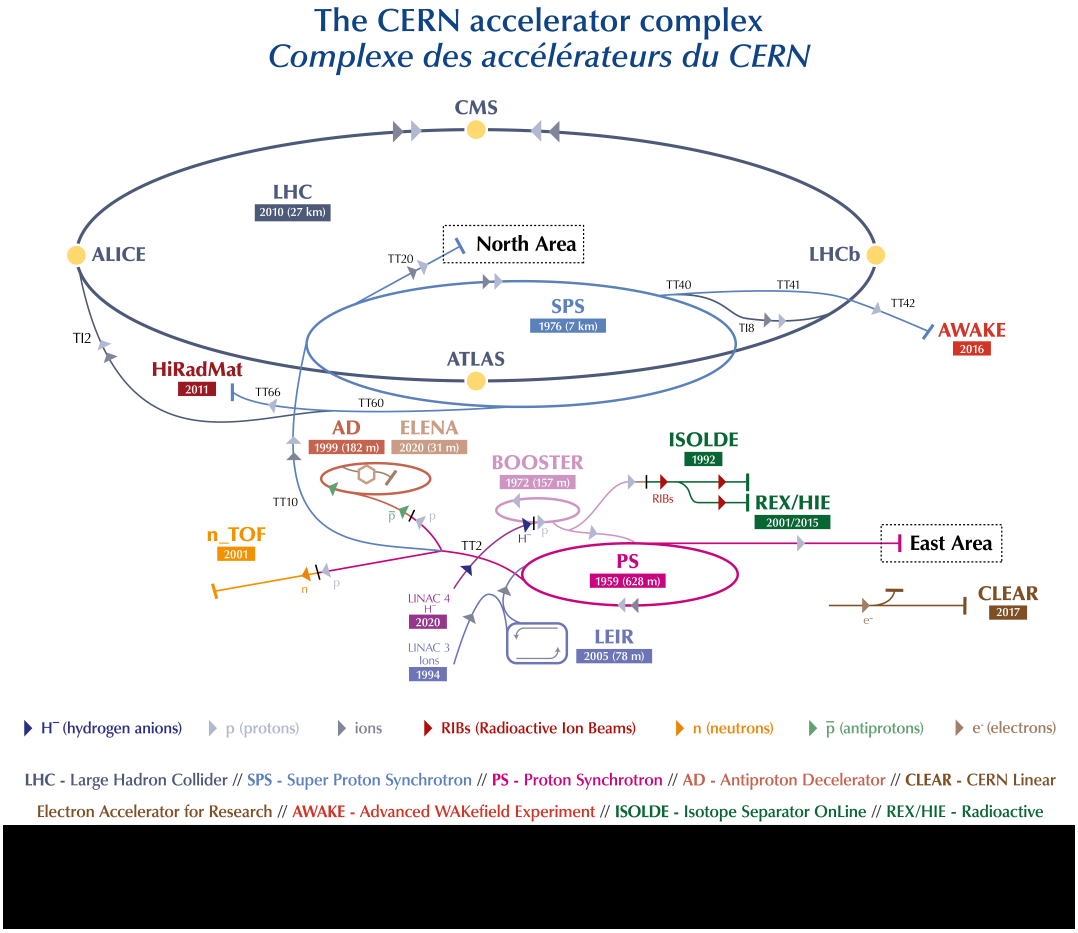

Figure 4.1: Sketch of the CERN accelerator complex. The paths of various particle types through the accelerators are indicated by arrows of different colors. The positions of the four main experiments at the LHC are also displayed. Taken from Ref. [69].

bunch, multiple collisions take place simultaneously. Depending on the spontaneous luminosity, which changes between the data taking periods of 2016, 2017, and 2018, the average number of simultaneous collisions per bunch crossing lies between 25 and 40. The spontaneous luminosity L is an important parameter of a particle collider and is defined as

$$L = \frac{nN_1N_2f}{4\pi\sigma_x\sigma_y}, \tag{4.1}$$

where n is the number of bunches, N_1 and N_2 are the number of protons inside the two colliding bunches, f is the orbit frequency, and σ_x and σ_y are the beam widths in x and y direction, respectively. The LHC was designed to reach a luminosity of $L = 10^{34}\,\mathrm{cm}^{-2}\,\mathrm{s}^{-1}$, which was already achieved in 2016. The size of a data set is usually given as luminosity integrated over time L_{int}. From this, the expected number of events N from a certain process can be easily

calculated using the cross section σ of this very process via

$$N = \sigma L_{\text{int}}. \tag{4.2}$$

4.2 Compact Muon Solenoid experiment

The CMS detector is a multi-purpose detector located at the LHC. It was designed to maximize the sensitivity to new physics and enable the discovery of the Higgs boson. Nevertheless, it offers the feasibility for a wide range of particle physics analyses. The CMS detector has a cylindrical shape with a length of almost 30 m, diameter of 15 m and mass of 14000 t. The CMS experiment defines a right-handed coordinate system with its origin in the interaction point. The x-axis points towards the center of the LHC ring, the y-axis points upwards, and the z-axis is parallel to the beam axis. The radial distance to the z-axis is referred to as r. The observables θ (and with it the pseudorapidity η) as well as ϕ indicate the angle from the beam axis and the angle in the x-y-plane, respectively. The detector consists of various specialized subdetectors that are arranged in a layered structure. As depicted in Figure 4.2, the subdetectors – from the inside out – are: tracker, electromagnetic calorimeter (ECAL), hadronic calorimeter (HCAL), solenoid magnet, and muon system. Another crucial part of the CMS experiment is the trigger system, which is used to reduce the event rate to values that can be stored permanently for further analysis. All components are described in the following. Further details can be found in Ref. [70].

4.2.1 Solenoid magnet

With an inner diameter of 6 m, length of 13 m and providing a magnetic field of 3.8 T on the inside, the superconducting solenoid magnet is a central part of the CMS detector. Its purpose is to bend the trajectories of charged particles inside the tracker and muon system in order to enable a measurement of their momenta. The strong magnetic field of 3.8 T ensures bent trajectories also at high momenta and subsequently enables a precise determination of the particle momentum at large energies. In addition, the solenoid design provides a homogeneous magnetic field inside the tracking systems but also limits the size of all subdetectors that are located within the magnet.

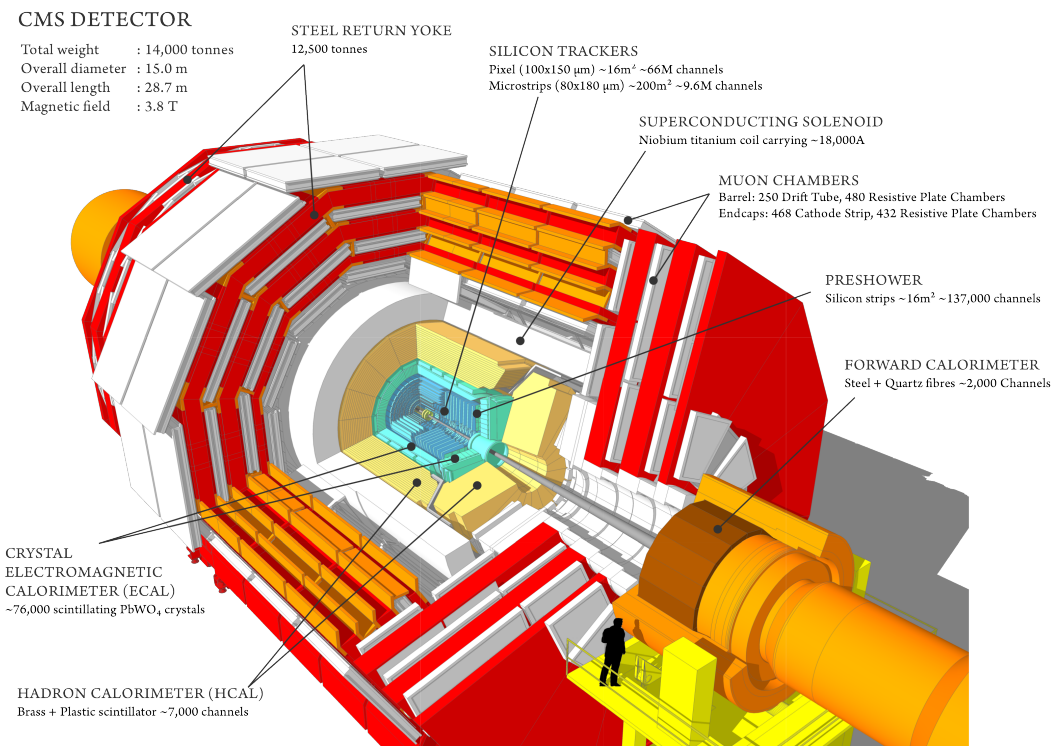

Figure 4.2: Sketch of the full CMS detector showing all layers of the detector with various subdetectors. Taken from Ref. [71].

4.2.2 Tracker

The tracking system is the innermost subsystem of the CMS detector and itself consists of various subsystems each containing multiple layers. All components of the tracking system are built mainly from silicon, which is used as radiation hard semiconducting material. Whenever a charged particle hits the detector material, it produces electrons that travel towards an electrode and induce a signal. From such hits in multiple layers, a track can be reconstructed. In combination with the strong magnetic field provided by the solenoid magnet, the momentum and sign of the electromagnetic charge can be measured from the radius and direction of curvature, respectively. The full tracker covers the region up to $|\eta| < 2.5$ and is subdivided into the pixel detector, the tracker inner barrel (TIB), tracker inner disks (TIDs), tracker outer barrel (TOB), and tracker outer disks (TODs). A schematic view of the components of the tracking system is shown in Figure 4.3. During the 2016 data taking period, the pixel detector consisted of three and two layers in the barrel and endcap regions, respectively. Between the data taking periods of 2016 and 2017, a new pixel detector was installed, which features an additional layer in the barrel and endcap part. Not only does the track reconstruction improve with an

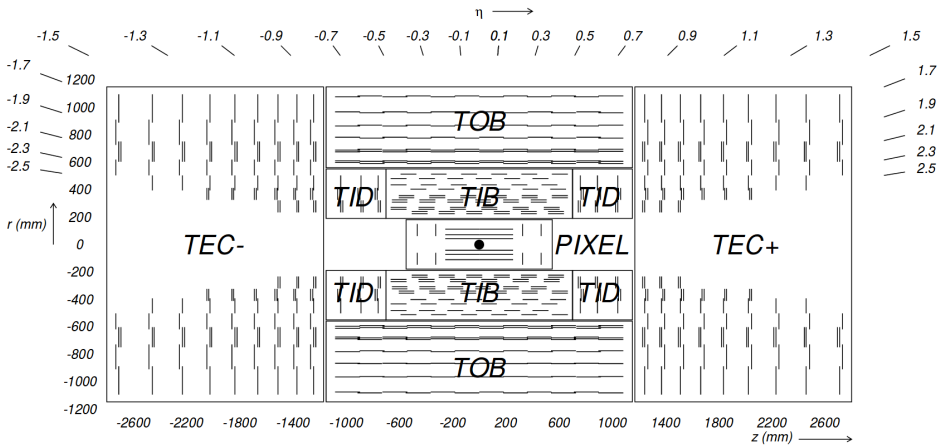

Figure 4.3: Schematic display of subsystems of the CMS tracking detector during the 2016 data taking period in the r-z-plane. The coverage of every subsystem is shown in pseudorapidity η and radial distance r from the beam axis. Taken from Ref. [70].

additional layer, but also is the innermost layer now installed closer to the beam, helping in the reconstruction of secondary vertices, which is crucial for the identification of jets originating from b quarks (see Section 5.2). All layers of the pixel detector contain pixels with a size of 100 µm $\times$ 150 µm, which results in an excellent spatial resolution. The surrounding subsystems of the inner tracker feature strip modules, which have a reduced resolution but cover a larger area. With additional four layers in the TIB, three disks in the TID, six layers in the TOB, and nine disks in the TEC, a charged particle can be followed precisely through the tracking system. The design of the CMS tracking system enables a spatial resolution down to 9.4 µm for a single hit in the pixel detector. Because the measurement of momenta relies on the determination of the bending radius of curved paths, the resolution worsens for increasing momenta when the tracks are barely curved.

4.2.3 Calorimeters

The calorimeters of the CMS detector are installed around the tracker but inside the solenoid magnet. In addition to the measurement of momenta in the tracking system, calorimeters aim at absorbing and measuring the energy of a particle. Within CMS, two types of calorimeters are installed: the ECAL and the HCAL. Both work with the same underlying principle and use scintillating material in order to convert the energy of traversing particles into light. The signal of emitted photons is then amplified with photo multipliers and recorded with photo detectors. Since the intensity of emitted photons is proportional to the energy deposited in the

calorimeter, it can be used as a measure for the deposited energy. In contrast to the tracker, the relative precision of energy measurements increases with the energy of incoming particles. Furthermore, neutral hadrons or photons can only be detected in calorimeters, which makes them crucial for analyses targeting jets at high momenta. Important parameters for the material used in calorimeters are the radiation length X_0 as well as the nuclear interaction length λ_n, which define the distance after which the energy of an incoming electron or hadron is reduced to $1/\mathrm{e}$ of its initial energy. In general, the energy resolution σ_E of calorimeters can be displayed as the quadratic sum of three terms, each of which parameterizing different contributions. The relative energy resolution depends on the stochastic term a, a noise term b that consists of electronic and pileup noise, and a constant term c, which includes inhomogeneities and miscalibration of the calorimeter as well as undetected energy leakage:

$$\frac{\sigma_E}{E} = \frac{a}{\sqrt{E/\,\mathrm{GeV}}} \oplus \frac{b}{E/\,\mathrm{GeV}} \oplus c. \tag{4.3}$$

With increasing energy, the relative energy resolution improves until the constant term is dominant. As a consequence, proper calibrations of the calorimeters are crucial at high energies, in order to keep the constant term under control. CMS uses two specialized calorimeters that are further described below.

The ECAL is installed directly outside the tracker, covers a range up to $|\eta| < 3.0$, and is divided into a barrel part ($|\eta| < 1.479$) and endcaps ($1.479 < |\eta| < 3.0$). Its purpose is to absorb and measure the energy of photons and electrons. The highly segmented ECAL consists of lead tungstate crystals that have an area of 22 mm $\times$ 22 mm facing towards the interaction point, corresponding to 0.0174×0.0174 in the η-ϕ-plane. The crystals are 23 cm long, which corresponds to 25.8 X_0. Additional preshower detectors that help to distinguish prompt photons from those originating from π^0 decays and improve the determination of the photon direction are installed on the inside of the endcaps. No specialized absorber layers are installed, which makes the ECAL of CMS a homogeneous calorimeter. This design lacks of a segmentation in the radial direction but in turn drastically improves the energy resolution of the ECAL, which was measured using an electron beam [72] to be

$$\frac{\sigma_E}{E} = \frac{2.8\%}{\sqrt{E/\,\mathrm{GeV}}} \oplus \frac{12\%}{E/\,\mathrm{GeV}} \oplus 0.3\%. \tag{4.4}$$

The design of the ECAL was driven by the potential discovery of the Higgs boson decaying into two photons, which was achieved in 2012 [17, 18]. Crucial for the reconstruction of the

two-photon final state is not only a good energy resolution but also a spatial separation of nearby showers, which is attained by both the small-area and homogeneous lead tungstate crystals. Furthermore, the material used emits the photons from scintillation in a very short time, which is crucial to assign the signal in the detector to the correct collision and makes calorimeter signals a suitable input for the trigger system.

The HCAL is installed outside the ECAL, in a distance $1.77 < r < 2.95$ m to the z-axis and aims at absorbing and measuring the energy of hadrons that have not been stopped in the ECAL. In contrast to the ECAL, the HCAL is a sampling calorimeter, meaning it is built up from alternating layers of absorber and active material. In CMS, the materials were chosen to be brass plates and a plastic scintillator. The HCAL consists of a barrel part covering the range $|\eta| < 1.3$, endcaps covering $1.3 < |\eta| < 3.0$ and a forward calorimeter located 11.1 m in both z-directions from the interaction point to cover the range $3.0 < |\eta| < 5.0$. Additional layers are placed outside the solenoid magnet in order to detect the tails of showers that were not fully absorbed in the main part of the HCAL. The energy resolution of the combination of ECAL and HCAL was measured in a test beam using pions [73] and can be parameterized as

$$\frac{\sigma_E}{E} = \frac{110\%}{\sqrt{E/\,\mathrm{GeV}}} \oplus 9\%. \tag{4.5}$$

4.2.4 Muon system

On the very outside of the CMS detector and embedded in the return yoke of the solenoid magnet the muon system is located. While the precision of measurements of small muon momenta is still dominated by the inner tracker because of multiple scatterings before the muon system, muons with high momenta traverse the calorimeters with small energy loss and are precisely measured in the muon system. Furthermore, this design reduces the rate of particle candidates being misidentified as muons since particles other than muons and neutrinos are likely to be stopped in the calorimeters. This ensures the excellent reconstruction also for non-isolated muons. Three different detector types are used for specific ranges in η. Drift tubes are installed in the barrel region inside $|\eta| < 1.2$ and contain cells filled with a gas that is ionized by an energetic muon. As a result of the ionization, electrons and ions drift to anode and cathode wires and induce an electric signal, which is interpreted as a hit of a muon. Cathode strip chambers are placed in the endcaps between $0.9 < |\eta| < 2.4$ and work very analogously to drift tubes but with multiple wires tensioned inside a chamber, which helps to cope with

higher muon rates in this region. Additionally, resistive plate chambers are used in both barrel and endcap region up to $|\eta| < 1.6$. Because of their fast readout speed they are heavily used in order to fire dedicated muon triggers.

4.2.5 Trigger system

At the interaction point inside the CMS detector, proton bunches cross with a rate of roughly 40 MHz, resulting in about 10^9 collisions per second. In order to treat this vast amount of data and be able to store the collision data, the event rate has to be reduced to a few 100 Hz. In this process, the challenge is to keep relevant and rare collision data while rejecting known and common processes such as low-energy QCD multijet production. Multiple trigger paths are aiming for specific final states, for example selecting events containing high energy muons or jets. This is achieved with a two-stage trigger system consisting of a hardware based level-1 (L1) trigger [74] and a software based high-level trigger (HLT) [75]. The L1 trigger reduces the event rate to about 100 kHz using information from detector components that enable fast readout such as the calorimeters and muon system. The L1 trigger is capable of making the decision if a collision event is kept or regarded within a few microseconds. The HLT can make use of more complex observables that include information from all detector subsystems and further reduce the event rate to the required few 100 Hz. In order to pass the HLT, an event has to fulfill multiple selection steps that are designed for a dedicated trigger path. Within the CMS Collaboration a variety of trigger paths can be used that require a specific object in the final state or a combination of objects. In this thesis, three dedicated trigger paths are used that aim for a single electron, photon, or muon with high transverse momentum.

5 Object reconstruction and calibration

Electric signals in detector subsystems are converted into hits in the inner tracker and muon system as well as energy clusters in the calorimeters. From those, physics objects are reconstructed following the particle-flow (PF) algorithm [76]. It includes information from various subsystems in the reconstruction of single objects instead of relying on specialized components only. In this chapter, the PF algorithm is described in Section 5.1, followed by an introduction to the identification of jets that originate from the hadronization of b quarks and missing transverse momentum in Sections 5.2 and 5.3, respectively. The calibration of jets prior to the data analysis in summarized in Section 5.4.

5.1 Particle-flow reconstruction

The PF algorithm aims at following particle candidates through the detector and combines information from various subdetectors in order to reconstruct and identify particles as photons, electrons, muons, charged hadrons, or neutral hadrons. This method exploits the fact that different subsystems are superior to others in specific energy regions and combines all available information in the reconstruction of particle candidates. Thus, the measurement can be combined such that the highest possible precision is achieved. Figure 5.1 shows the different signatures created by different particles in the subsystems of the CMS detector. While electrons produce hits in the tracker and an electromagnetic shower in the ECAL, photons only produce a shower in the ECAL. Charged hadrons are visible in the tracker and HCAL, neutral hadrons are visible only in the HCAL and muons produce hits in the inner tracker as well as the muon system. The PF algorithm relies on two central objects that are reconstructed from detector signals: tracks and energy clusters. Hits in the inner tracker and muons system are combined to form tracks using an iterative algorithm. In every subsequent step, quality criteria are lowered in order to reconstruct even tracks not originating from the primary vertex. In this way, a high reconstruction efficiency is ensured while retaining a low mistag rate. In the calorimeters, energy deposits are combined to form clusters. For each particle type implemented in the PF

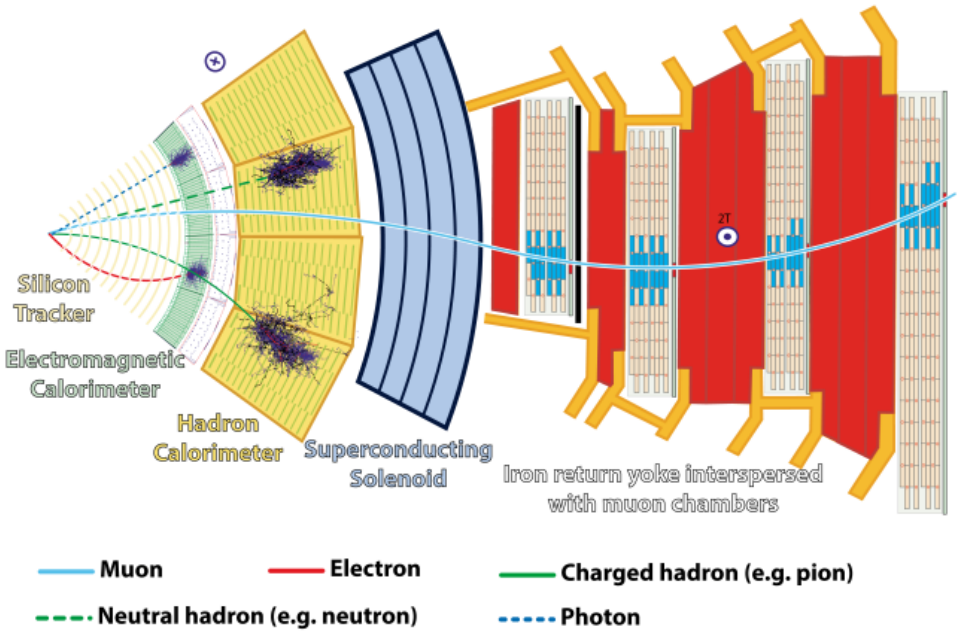

Figure 5.1: Slice of the CMS detector displaying the signature of different particle types in all subdetectors. The proton-proton interaction point is on the left, and particle traverse the detector from the inside out. Taken from Ref. [77].

algorithm a dedicated combination of track and cluster information is used in order to ensure high efficiency and excellent momentum resolution. The step-by-step reconstruction performed by the PF algorithm is described below.

Primary vertices are reconstructed from track intersections with more than two tracks close to the nominal interaction point within the CMS detector. The primary-vertex candidate with the highest sum of quadratic momenta p_{T}^2 of assigned tracks is considered to be the primary vertex of an event.

Muons are reconstructed from signals in the muon system and the inner tracker. Tracks in the tracking system are extrapolated and matched to those in the muon system. Since other particles – except neutrinos – are stopped within the calorimeters, the muon system ensures a very high identification rate while the precise momentum measurement of the inner tracking system can be exploited. Within the PF algorithm, three types of muons are identified. A standalone muon refers to a muon that is reconstructed from information of the muon system only. Global muons are reconstructed from matched tracks in both the inner tracker and muons system, and tracker muons are reconstructed from a track that is extrapolated from the inner

tracker to a hit in one segment of the muon system. Due to the excellent efficiency of the inner tracker and muon system, 99% of the muons are identified either as global or tracker muons [76]. Especially at low momenta, muons might not pass through the whole muon system due to multiple scattering, and the identification efficiency relies on the definition of tracker muons rather than global muons. In general, for muons with $20 < p_{\mathrm{T}} < 100$ GeV a momentum resolution between 1.3% and 2.0% is reached in the barrel region [78]. All tracks connected to identified muons are removed from the input of the PF algorithm.

Electrons leave a track in the inner tracker and energy clusters in the ECAL. The tracks are extrapolated to entries in the ECAL, also taking possible photons from Bremsstrahlung into account. The energy of an electron candidate is determined using a combination of the energy measurement in the ECAL, the track information and the energy clusters assigned to photons from Bremsstrahlung. The reconstruction results in a momentum resolution as low as 1.7% for electrons in the barrel region [79]. All tracks and energy clusters that have been used in the measurement of an identified electron candidate are removed from the input list.

Charged hadrons have a similar signature as electrons but with additional energy clusters in the HCAL. Again, tracks in the inner tracker are connected to clusters in the calorimeters. All information is used in a combined measurement ensuring a stable reconstruction performance over a large energy range. Especially for this analysis that heavily relies on the precise measurement of jet properties, the reconstruction of charged hadrons – which typically contribute to about 65% of the jet energy – is crucial. After charged hadrons are identified, tracks and clusters are removed from the input list if they were used in the reconstruction.

Photons are reconstructed from energy clusters in the ECAL that cannot be assigned to a track extrapolated from the inner tracker. Furthermore, the shape of energy clusters can help to distinguish between photons and electrons. A good resolution of both energy and direction of flight is achieved by the design of the ECAL. Because photons contribute up to 25% to the energy of jets, a precise reconstruction is crucial not only for analyses that target photons in the final state but also all analyses using jets. All clusters used in the reconstruction are removed from the input.

Neutral hadrons do not leave a track in the inner tracker and are therefore reconstructed only from energy clusters in the ECAL and HCAL that are not matched to any track in the inner

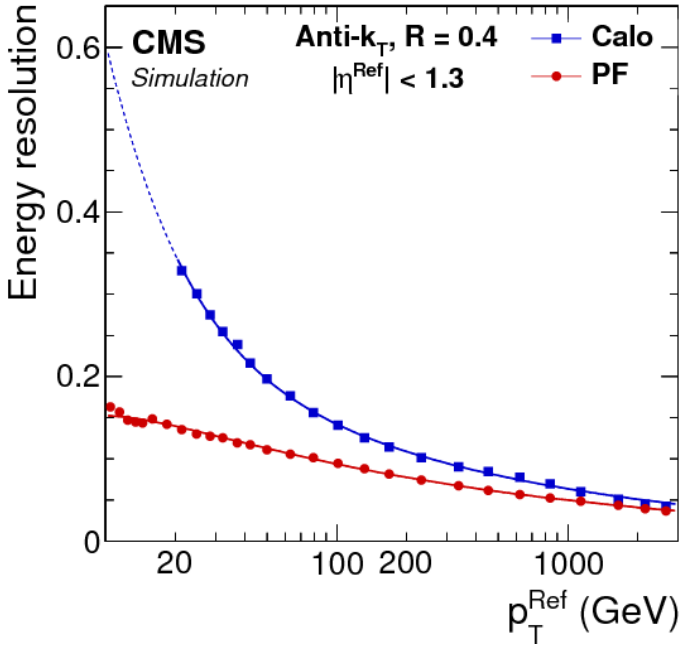

Figure 5.2: Jet energy resolution as a function of jet p_T for jets reconstructed from calorimeter clusters only (blue) and the particle flow algorithm (red). The study is performed in simulated events, and jets are clustered using the anti-k_T algorithm with a radius parameter of $R = 0.4$. Taken from Ref. [76].

tracker. Nevertheless, is is crucial to identify and measure the energy from neutral hadrons since they contribute roughly 10% to the typical jet energy at the LHC. The combined energy resolution of jets that consist of charged hadrons, neutral hadrons, and photons is shown in Figure 5.2. In contrast to jets that are reconstructed from calorimeter clusters only, the energy resolution of jets that are clustered from PF candidates is better than 20% over the whole range of jet p_T.

5.2 Identification of b jets

Properties of the b quark and the hadrons it forms make it possible to identify jets that originate from b quarks. Within CMS, mainly three algorithms are commonly used: the combined secondary vertex v2 (CSVv2) [80, 81], DeepCSV [80, 81], and DeepJet (or DeepFlavor) [81] algorithms. All of those algorithms make use of the fact that b hadrons have a rather long lifetime and travel several 100 µm inside the detector before their decay. This leads to a well-separated secondary vertex inside the tracker that can be identified by following the paths of

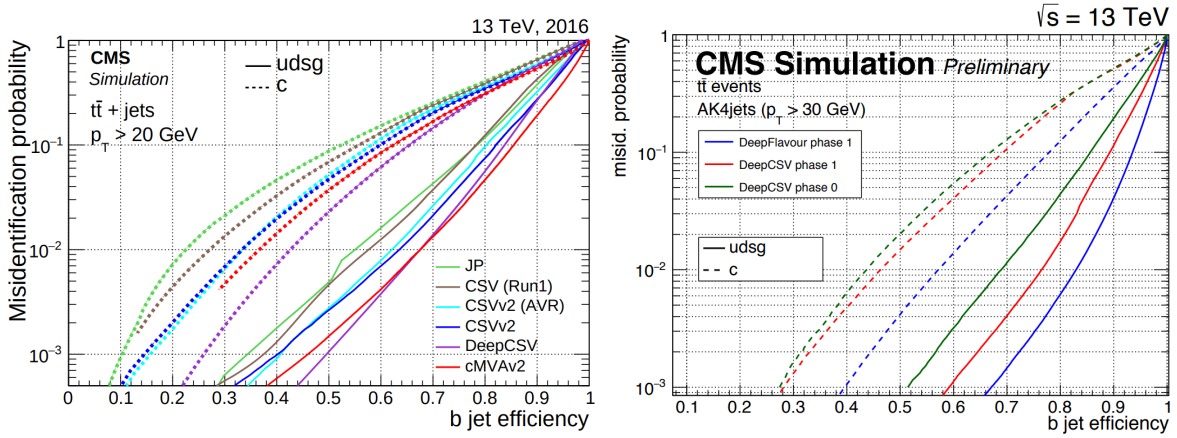

Figure 5.3: The b-tagging misidentification rates as a function of b-tagging efficiencies for different algorithms used in CMS. The left plot compares CSVv2 (blue) and DeepCSV (purple) among other taggers. On the right, the performance of DeepCSV (green) is compared with DeepJet (DeepFlavor, blue). Both studies were performed using simulated $\mathrm{t\bar{t}}$ events. Taken from Refs. [80] and [81].

particle candidates. In addition, the large mass of the b quark of about 5 GeV is exploited. The algorithms return a value between 0 and 1 per jet, where large values indicate a high probability of the jet originating from a b quark. While the CSVv2 algorithm follows a multivariate approach based on the reconstruction of a secondary vertex and track information, DeepCSV uses the same inputs fed to a neural network. Furthermore, a few additional inputs containing tracker information are used in the DeepCSV approach. The DeepJet algorithm is based on a deep neural network and was developed not only to identify b jets but also classify jets originating from various flavors. Its inputs include many different variables of charged and neutral PF candidates but the algorithm also mostly relies on information from the tracking system of CMS. At a misidentification rate of 1%, the b-tagging efficiencies for jets with $p_\mathrm{T} > 20$ GeV were measured to be 63% and 68% [80] for the CSVv2 and DeepCSV algorithms, respectively. DeepJet further improves the b-tagging efficiency to more than 80% [81] at the same misidentification rate for jets with $p_\mathrm{T} > 30$ GeV. The misidentification rates as a function of the b-tagging efficiencies are shown in Figure 5.3 in detail.

5.3 Missing transverse momentum

The initial state of a collision at the LHC has negligible momentum in the transverse plane. Therefore, the sum of the transverse momenta of all final-state particles in an event is expected to be zero as well. However, mismeasurements and undetected particles can lead to a non-zero

value of the negative sum of all transverse momenta, which is referred to as missing transverse momentum. It is defined as

$$p_{\mathrm{T}}^{\mathrm{miss}} = \left| -\sum_i \vec{p}_{\mathrm{T},i} \right|, \tag{5.1}$$

where the sum runs over all PF candidates i. All changes of momenta due to jet energy corrections are propagated to $p_{\mathrm{T}}^{\mathrm{miss}}$ by replacing the PF candidates with the calibrated jet momenta they are clustered into. The missing transverse momentum is commonly used as a measure of the undetected activity in a collision event. Especially in events with a single neutrino in the final state, the missing transverse momentum can be used to infer the neutrino's p_{T}.

5.4 Jet calibration

Jets are an important part of the object reconstruction within CMS and especially for the analyses presented here. It is crucial that jets are not only carefully calibrated and corrected but also that effects from pileup and underlying event are suppressed.

5.4.1 Pileup mitigation techniques

Particles originating from pileup vertices result in additional energy deposits in the detector that are erroneously clustered into jets assigned to the leading vertex. There are various methods reducing this effect, two of which are used in this thesis.

Charged hadron subtraction (CHS) aims at using the tracking information of charged particles and assigning them to the leading vertex or a pileup vertex [82]. If a charged particle is assigned to a pileup vertex, it is removed from the input list of the jet clustering. With this method, only the charged fraction of the additional energy deposits can be addressed. Nevertheless, this makes up a considerable part of the particles from pileup and reduces the dependency of jet observables on the number of pileup interactions significantly. Jets that were clustered after removing particles with CHS are referred to as CHS jets.

The pileup per particle algorithm (PUPPI) improves upon the CHS technique and additionally targets the reduction of the neutral pileup component [83, 84]. This is done by

assigning a weight that scales down the magnitude of the four-momentum of each particle candidate. The weight represents the probability of a given particle to originate from the primary vertex and takes values between 1 and 0. Similar to the CHS algorithm, charged particles are unambiguously assigned to the primary or a pileup vertex and get a weight of exactly 1 or 0, respectively. A variable α is defined as a measure for the energy deposited in the vicinity of that particle and depends on the distance to and transverse momentum of neighboring particle candidates. Subsequently, the distribution of α is measured individually for charged particles from primary and pileup vertices and shows sensitivity to the particle's origin. Thus, the probability of a particle originating from a primary vertex is directly related to α, and a PUPPI weight can be assigned to neutral particles based on the observable α. Jets that are clustered from particle candidates which were weighted with the PUPPI algorithm are referred to as PUPPI jets.

5.4.2 Jet energy corrections

All jets in simulation are corrected [85, 86] such that their momentum at the detector level matches the momentum of the same jet at the particle level. Differences can be introduced by a variety of effects e.g. additional energy deposits because of pileup, non-linearities in the detector response, or faulty measurements in one of the subdetectors. With the help of simulated collision events and the GEANT4 detector model, jets at the detector level are calibrated such that they match their true energy at the particle level. First, L1 offset corrections reduce the energy of a reconstructed jet as a function of its area in η and ϕ, energy density in the event as well as p_{T} and η of the jet in order to mitigate the effects from pileup. This step is not needed for PUPPI jets since the effects of pileup are already sufficiently removed from the particle candidates itself. The detector response is corrected by the L2 relative and L3 absolute corrections. The L2 correction targets a uniform detector response and is applied as a function of reconstructed p_{T} and η of a jet. The L3 correction aims at matching the momentum of a jet at the detector level to its momentum at the particle level. All corrections are applied to jets in data as well. Further detector effects which are not covered by the GEANT4 model are measured in data. The η-dependence is targeted using dijet events, where one jet is well measured in the barrel region, and the second jet is used to probe the response as a function of η. A similar approach is used in γ/Z+jets events, where a probe jet is calibrated to balance a well-measured photon or reconstructed Z boson decaying into leptons. The resulting corrections are applied as small residual corrections to jets in data only. Additionally, flavor dependent corrections can be derived in order to correct for the different responses of jets originating from

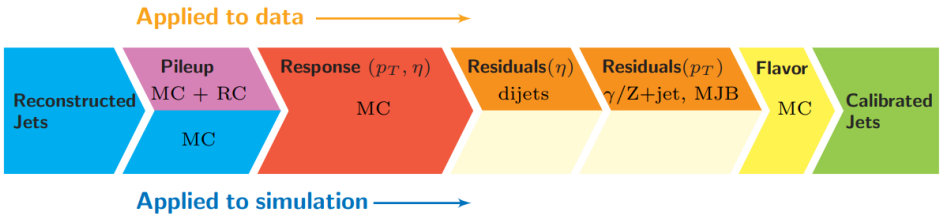

Figure 5.4: A sketch of the subsequent steps of jet energy corrections that are applied to data (top) and simulation (bottom). Taken from Ref. [85].

gluons, light quarks, and bottom quarks. However, this procedure is not yet a standard in CMS analyses and is studied individually in appropriate final states. The full chain of jet energy corrections is shown in Figure 5.4. The uncertainty in the estimation of the jet energy scale was estimated to be below 3% at a center-of-mass energy of 8 TeV [85] and remains comparable also at 13 TeV [86]. After the jet energy scale is calibrated, the energy resolution is corrected in simulation to match the resolution observed in data. The jet energy resolution is defined as the width of the distribution of the ratio of measured and true jet transverse momenta. In data and simulation, the true jet p_{T} is estimated by probing a jet that recoils against a well-measured γ or Z boson. Correction factors as a function of η and p_{T} are applied to jets in simulation to correct for differences in comparison to data. At 8 TeV, the jet energy resolution was measured to be 5–20% [85], where the resolution improves with increasing jet momenta. Again, comparable results are obtained at 13 TeV [86].

5.4.3 Additional jet corrections for XCone

In the jet mass measurement presented in Chapter 7 of this thesis, XCone jets with a distance parameter of $R = 0.4$ are used. While isolated XCone jets behave very similar to isolated anti-k_{T} jets, this changes drastically in the boosted regime when jets are very close to their neighbors and particles are not unambiguously assigned to a single jet. As described in Sections 3.1.1 and 3.1.3, the boundary between those XCone jets is always a straight line and not a circular jet in the center with a crescent moon shape around it as in the anti-k_{T} case. Since these non-isolated jets play an important role in the boosted regime, the XCone jets are further calibrated after applying the jet corrections derived with anti-k_{T} jets (as described in Section 5.4.2). Especially for low-p_{T} XCone jets, a deviation of the reconstruction-level jet from the same jet at the particle level is observed. In this scope it is verified by matching jets to partons in simulation that this does not depend on the origin of the jet but is only caused by clustering the jets with XCone instead of the anti-k_{T} algorithm. In the jet mass measurement

presented in Chapter 7, the XCone algorithm is used to reconstruct the $\mathrm{t\bar{t}}$ process, and an additional correction is derived from $\mathrm{t\bar{t}}$ events simulated with POWHEG in the all-jets final state, where both top quarks decay via $\mathrm{t} \to \mathrm{Wb} \to \mathrm{q\bar{q}'b}$. This correction is applied as a multiplicative factor to the four-momenta of all XCone jets in data and simulation. At first, XCone jets at the particle level are matched to a corresponding jet at the detector level via their smallest angular distance. If a match is found within $\Delta R < 0.2$, the jet is categorized by its particle-level momentum $p_{\mathrm{T}}^{\mathrm{gen}}$ and η, where the η bins are compatible with those in the anti-k_{T} jet correction procedure. For each region in $p_{\mathrm{T}}^{\mathrm{gen}}$ and η, the ratio of transverse momenta at the particle and detector level, $r = p_{\mathrm{T}}^{\mathrm{rec}} / p_{\mathrm{T}}^{\mathrm{gen}}$, as well as the reconstructed transverse momentum $p_{\mathrm{T}}^{\mathrm{rec}}$ are filled into histograms (see Figure 5.5). The means $\langle r \rangle$ and $\langle p_{\mathrm{T}}^{\mathrm{rec}} \rangle$ of the distributions of r and $p_{\mathrm{T}}^{\mathrm{rec}}$ are extracted via a Gaussian fit and a simple mean calculation, respectively. Both mean values are used to determine a correction factor $f = [\langle r \rangle]^{-1}$ for certain values of $p_{\mathrm{T}}^{\mathrm{rec}}$ in a given bin of η. Thus, the corrected jet four-momentum is $p^{\mathrm{rec,corrected}} = f \cdot p^{\mathrm{rec}}$. In order to obtain a smooth function $f(p_{\mathrm{T}}^{\mathrm{rec}})$, a fit is performed in each η region using a second-order polynomial. An example of such a fit is displayed in Figure 5.6, where the markers indicate the extraction of f from the mean values, and the red line shows the fit. Since the second-order polynomial is not physically motivated and a subjective choice, the fit is performed again using higher orders of polynomials. The envelope of all fits is interpreted as the systematic uncertainty arising from the choice of the fit function.

The additional correction is validated in the all-jets $\mathrm{t\bar{t}}$ simulation as displayed in Figure 5.7 (left). The relative difference between particle level and detector level p_{T} is shown in bins of $p_{\mathrm{T}}^{\mathrm{gen}}$ for uncorrected jets (orange), jets with the anti-k_{T} correction applied (blue) and after the additional XCone correction (red). For the latter, the distribution is flat and shows deviations well below 1%. Nevertheless, the non-closure is added to the total systematic uncertainty arising from this correction method. Figure 5.7 (right) shows the same cross check in an independent sample of tW simulation. Within the systematic uncertainty, the jets at the detector level are well in agreement with those at the particle level. In the scope of the analysis presented in Chapter 7 it is further verified that simulation and data are in agreement after applying the corrections presented here. In the selected phase space of the analysis presented in Chapter 7, the additional correction has an average size of 2% and average uncertainty of 0.3%.

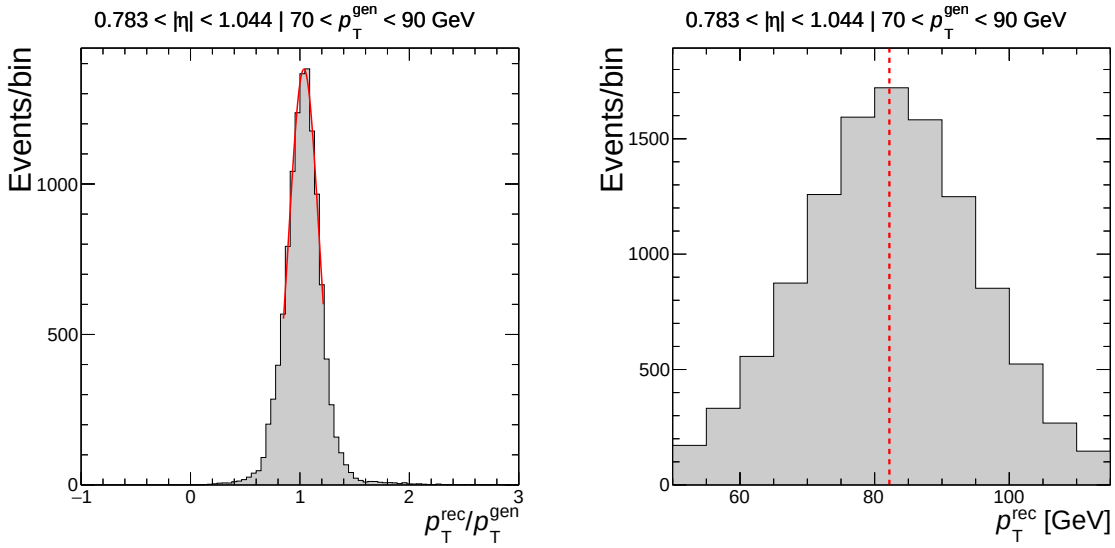

Figure 5.5: Distributions in p_T^{rec}/p_T^{gen} (left) and p_T^{rec} (right) obtained from a sample of simulated $t\bar{t}$ events. The extraction of the mean values $\langle p_T^{rec}/p_T^{gen}\rangle$ and $\langle p_T^{rec}\rangle$ from the corresponding distributions is indicated by the red lines. On the left, a Gaussian is fit to extract the mean while on the right the mean is calculated directly. The two distributions correspond to a specific region in η and p_T^{gen}.

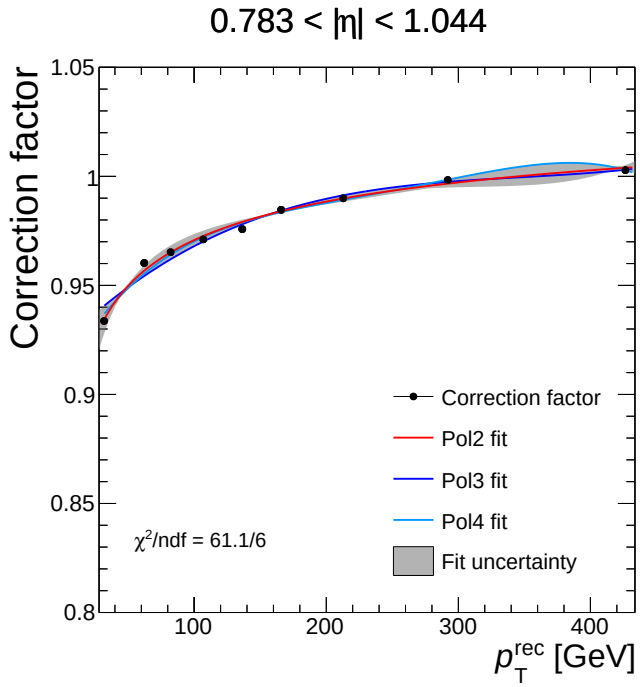

Figure 5.6: Additional XCone jet correction factor as a function of jet p_T. An example of the fit (red line) for a specific η region is presented. The points show the extracted pairs of values $\left(\frac{1}{\langle p_T^{rec}/p_T^{gen}\rangle}, \langle p_T^{rec}\rangle\right)$. The higher order polynomial functions are fit in order to estimate the systematic uncertainty connected to a potential bias due to the choice of the fit function.

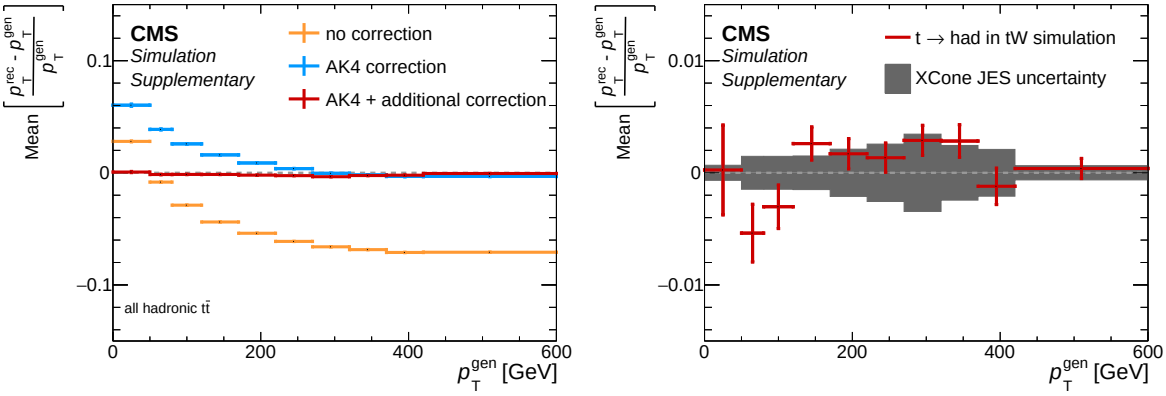

Figure 5.7: Relative deviation of the reconstructed jet p_T from its particle level value. The validation of the additional XCone correction performed in $t\bar{t}$ simulation (left) and an independent sample containing simulated tW events (right). The three lines on the left show the relative p_T difference between particle and detector level and correspond to three scenarios: without any correction applied (orange), only AK4 corrections applied (blue), and AK4 corrections and additional XCone correction applied (red). On the right, the latter case is shown in a tW sample, also displaying the systematic uncertainty originating from the additional correction. Published in the supplementary material [12] of Ref. [3].

6 Data and simulated samples

In this thesis, two analyses are presented. While the measurement of the jet mass distribution (discussed in Chapter 7) is carried out using data collected by the CMS detector in 2016, the measurement of top tagging efficiencies (see Chapter 8) relies on all three data taking periods of LHC's Run 2, which corresponds to the years 2016, 2017, and 2018. In this chapter the data and simulated samples used in both analyses are summarized. Especially, the properties of the data sets as well as underlying generators and parton shower models of simulated samples are discussed.

6.1 Data

The data analyzed in this thesis have been recorded in three separate periods in the years 2016, 2017, and 2018, corresponding to a total integrated luminosity of more than 137 fb^{-1}. Figure 6.1 (left) shows the total delivered integrated luminosity over time for all data taking periods at the LHC. But not only does the data set size vary between the years but also the properties of the recorded data are different. The number of interactions per bunch crossing, shown in Figure 6.1 (right), is one of the major changes between the years. While during the 2016 data taking period a mean number of 27 simultaneous interactions was reached, this number was increased up to 38 in 2017. It is also visible that in 2017, and 2018 a large fraction of the integrated luminosity was recorded with well above 40 interactions per bunch crossing, which was barely reached in 2016. This increase is a direct consequence of a higher instantaneous luminosity, which results in the possibility to collect more data in the same time period, but on the other hand introduces harsher conditions on the experimental side. The larger number of simultaneous interactions in turn leads to larger contamination with pileup. Especially the analyses presented in this thesis, which depend on the use of jets and jet substructure, have to adjust to the larger impact from pileup.

In addition to changes of the run conditions, the detector changes over time. This begins at upgrades, such as the additional layer of the pixel detector, which was installed after the 2016 data taking period (see Section 4.2.2), but also includes ongoing calibrations of subsystems as

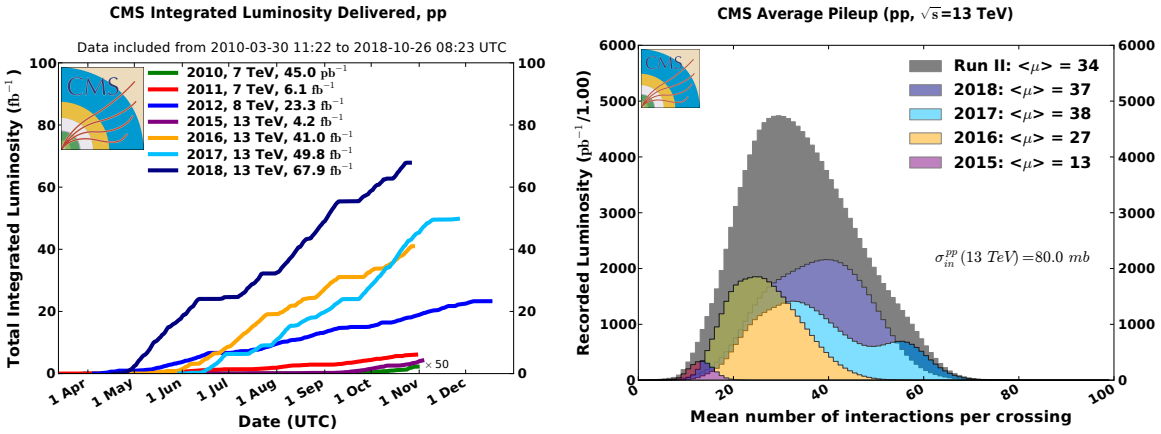

Figure 6.1: Integrated luminosity delivered by the LHC as a function of time for all data taking periods until the year 2018 (left) and recorded luminosity as a function of the number of interactions per bunch crossing (left). It is displayed separately and cumulated for the years 2015–2018. Furthermore, the mean number of interactions $< \mu >$ is specified. Taken from Ref. [87].

well as damaged detector parts. The tracker upgrade mostly improves the reconstruction of secondary vertices and enables a more efficient b tagging. In the analyses presented in the following, b tagging is indeed used in the respective event selections. Nevertheless, the improved b-tagging efficiency only has a small impact on the precision of the measurements themselves. The overall detector performance was stable over the three year period, but calibrations are derived for each year individually, since detector parts are suffering from radiation damage, outages, or changes in the detector alignment. Furthermore, time periods where the quality of the data cannot be ensured are identified and excluded from data analysis.

6.2 Simulated samples

For each year, samples of a wide variety of collision processes are generated. For the analyses presented in this thesis a certain set of processes is considered, aiming at a full description of the data in the targeted phase space. The signal in both measurements, the $\mathrm{t\bar{t}}$ process, is simulated at next-to-leading order (NLO) using the POWHEG generator. For the measurement of the jet mass, an alternative $\mathrm{t\bar{t}}$ sample is generated at NLO using MADGRAPH5_aMC@NLO, which provides a test of the generator dependence of the measurement. The largest background contributions of singly produced top quarks and the W+jets process are generated at NLO using POWHEG and MADGRAPH5_aMC@NLO, respectively. Contributions from Z+jets production are simulated at leading order (LO) and are normalized to the cross section obtained with NLO [88]. The

production of two heavy gauge bosons with additional jets and the contribution from QCD multijet events are simulated at LO using PYTHIA. In all processes, the hadronization and parton shower is simulated using PYTHIA. The matrix element calculations of samples simulated in MADGRAPH5_aMC@NLO are matched to parton showers using the FxFx [89] and MLM [90] algorithms for NLO and LO, respectively. The simulation of the parton shower relies on the tune, which represents a certain choice of free modeling parameters. These parameters include the energy scales for initial state and final state radiation as well as the scale of the parton shower matching in POWHEG, which is controlled by the parameter h_{damp}. During the 2016 data taking period, the CUETP8M2T4 tune [91] is used for both the simulation of $\mathrm{t\bar{t}}$ and single top quark production in the t-channel. Other channels of single top quark, W+jets, Z+jets, and QCD multijet production are simulated using the CUETP8M1 [92, 93] tune. In the measurement of the top tagging efficiencies (discussed in Chapter 8), also the t-channel of single top quark production makes use of the CUETP8M1 tune. In contrast, the samples generated for the data taking campaigns of 2017 and 2018 all use the newly introduced CP5 [91] tune. It introduces changes of the parameter h_{damp} and those parameters connected to initial and final state radiation. As presented in the measurement of top tagging efficiencies, a large difference in the description of jet substructure variables is observed. As an example, Figure 6.2 shows a comparison in the angular distance ΔR_g between two groomed subjets of various tunes – including CUETP8M1 and CP5 – to data. A large difference between the tunes is observed, which stresses the importance of a careful study of the underlying parton shower model parameters.

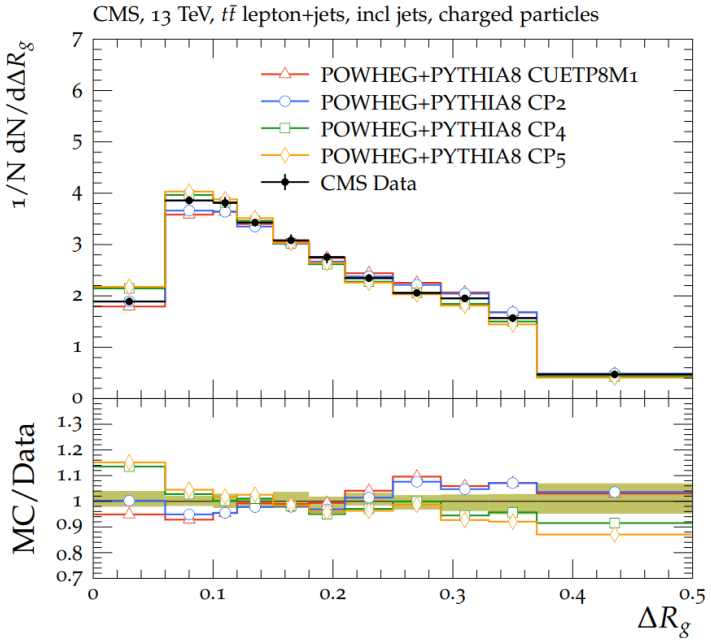

Figure 6.2: The angular distance between two groomed subjets ΔR_g for different tunes in $\mathrm{t\bar{t}}$ (colored) and data (black markers). The bottom panel shows the ratio of all simulated samples to the data. The total experimental uncertainty is shown by the shaded band. Taken from Ref. [91].

7 | Measurement of the top quark mass and jet mass distribution

In this chapter, the measurement of the differential $t\bar{t}$ production cross section as a function of the jet mass is presented. The measurement probes hadronic decays of top quarks with high transverse momenta. The normalized cross section shows high sensitivity to the top quark mass. The benefit of this measurement is the possibility to calculate the distribution in the jet mass from first principles. This makes the jet mass a suitable candidate for a measurement of the top quark mass that does not rely on ambiguities in the simulation of parton showers. While these calculations are not available so far for the phase space presented here, they will provide important input in the future. In the meantime, the extraction of the top quark mass from simulation acts as an orthogonal measurement in a kinematic regime very different from direct measurements and demonstrates the sensitivity of this measurement, which is the first of its kind at a center-of-mass energy of 13 TeV. Furthermore, the data provide crucial information for the modeling of jet substructure in simulation. This chapter is structured as follows: An introduction to the kinematic phase space of boosted top quarks, and the connected strategy of the jet mass measurement are given in Section 7.1. The following Section 7.2 introduces the event selection and presents studies on the choice of a suitable jet clustering algorithm at the particle level. The event selection and performance at the detector level as well as corrections applied to simulation and data are discussed in Section 7.3. Afterwards, Section 7.4 introduces the unfolding procedure, which enables a measurement at the particle level by measuring and correcting for detector and pileup effects. The treatment of statistical and systematic uncertainties is detailed in Section 7.5. The results of the differential cross section measurement and the extraction of the top quark mass are presented in Sections 7.6 and 7.7, respectively. Pioneering studies towards an improved precision of the measurement are detailed in Section 7.8.

7.1 The boosted regime in precision measurements

In contrast to most precision measurements of the SM, this analysis aims at reconstructing the decay products of boosted top quarks. In order to achieve high sensitivity and enable analytical calculations, all decay products of the hadronic top quark decay have to be reconstructed with a single jet. This introduces the challenge of selecting a suitable jet clustering algorithm in combination with an experimentally feasible selection of top quarks with high momenta. The lepton+jets channel of the $t\bar{t}$ process allows for the selection of a pure $t\bar{t}$ sample with small contributions from background processes. By requiring a high-p_T lepton, the leptonic leg of the $t\bar{t}$ system acts as a tag while the measurement is performed using a large-radius jet reconstructing the hadronic top quark decay. If those criteria are met, the jet mass distribution should have a narrow peak close to the top quark mass, which enables a precise extraction of m_t in the boosted regime. Almost all conventional precision measurements of the top quark mass select objects with an energy threshold as low as possible in order to retain a high statistical precision. Consequently, these measurements are dominated by low energy scales. Performing the measurement at high energies acts not only as a cross check in a different kinematic region but also introduces new possibilities. A large disadvantage of hadron colliders is that the initial partons carry color charge themselves. Subsequently, all colored particles that are produced during a collision are connected to the initial state particles or remnants of the initial state via color strings. This does not only introduce large uncertainties in the modeling of these processes but also makes analytical calculations more complex and often even impossible. However, these effects can be reduced in the boosted regime. Figure 7.1 shows a sketch of the production and decay of a low-p_T (left) and high-p_T (right) $t\bar{t}$ pair with additional radiation in the all-jets final state. Compared to the low-p_T case, the boosted top quarks are well separated, and particle trajectories from opposite top quark decays do not overlap. A single jet including a top quark decay can be considered isolated from the initial state as well as other color states in the event and makes this kinematic region valuable for precision measurements and calculations. Not only are uncertainties very different from those in analyses dominated by threshold production but also comparisons to analytical calculations become possible, enabling a top quark measurement in a well-defined mass scheme.

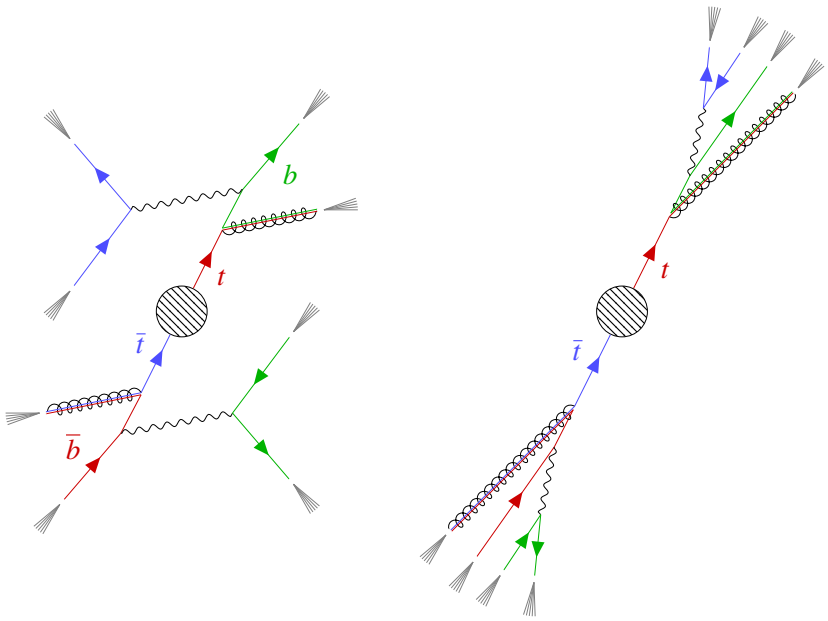

Figure 7.1: Sketch of the production and decay of a low-p_{T} (left) and high-p_{T} (right) top quark pair. All displayed top quarks decay via $\mathrm{t} \to \mathrm{Wb} \to \mathrm{q\bar{q}'b}$ and radiate a gluon. The flow of color charge is indicated by the colored lines. Created with TikZ [42].

7.2 Studies at particle level

The particle level phase space defines the kinematic region in which the measurement is performed. Since data are unfolded to the particle level, the selection criteria at the particle level are designed such that a similar phase space can be achieved at the detector level. Moreover, various jet clustering algorithms are studied at the particle level with the goal to select a jet definition that benefits the precision of this measurement.

7.2.1 Jet definition

The measurement of the jet mass mass relies on the jet definition. As a first step, suitable jet clustering algorithms are studied. For this purpose, the resulting jet mass distribution is studied at the particle level in $\mathrm{t\bar{t}}$ simulation. Selection criteria are applied such that a large fraction of top quark decays are entirely reconstructed with a single jet. The $\mathrm{t\bar{t}}$ sample is divided into fully merged and not merged fractions, where the former category contains events in which all three partons of the hadronic top quark decay lie within $\Delta R < R$ to the jet, where R is the distance parameter in the jet clustering. Unless specified otherwise, the p_{T}-leading jet is considered to be the measurement jet. In order to ensure boosted topologies, only events with a measurement

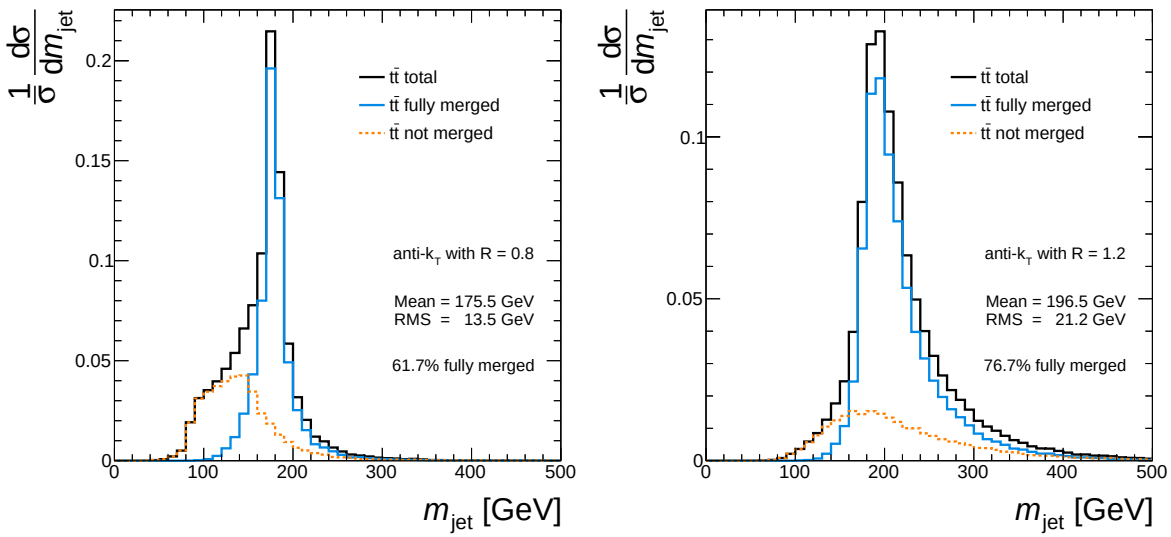

Figure 7.2: The m_{jet} distributions in $t\bar{t}$ simulation at the particle level for jets clustered with the anti-k_{T} algorithm and a distance parameter of $R = 0.8$ (left) as well as $R = 1.2$ (right). The distributions are separately shown for the contributions from fully merged and not merged top quark decays.

jet with $p_{\text{T}} > 400$ GeV are considered. In addition, the jet mass of the jet that acts as the measurement jet has to be greater than the invariant mass of the system containing a second jet and the lepton. The latter requirement helps to select fully merged events without introducing a bias to the m_{jet} distribution. If the measurement jet contains the full top quark decay, the mass requirement should always hold since the neutrino from the leptonic top quark decay is undetected. The event selection is based on a previous measurement [1, 2]. The jet mass distribution should ideally feature a narrow peak close to the the top quark mass because this will directly benefit the sensitivity to the top quark mass.

As a starting point, jets clustered with the anti-k_{T} algorithm [13] are studied. The resulting jet mass distributions for distance parameters of $R = 0.8$ and $R = 1.2$ are displayed in Figure 7.2 at the particle level. The simulated $t\bar{t}$ events are divided into fully merged and not merged contributions. In order to quantify the performance of the jet clustering, a Gaussian is fit to the peak region evaluating the mean and width of the distribution. Furthermore, the fraction of fully merged events is estimated. If a jet has a larger area, it is more likely to catch the full top quark decay but also includes more additional particles from the underlying event. This causes the jet mass distribution to be smeared and shifted to values above the top quark mass for jets clustered with a large value of R. On the other hand, a shoulder at masses around 100 GeV appears when using jets clustered with $R = 0.8$. This is mostly due to events in which one of

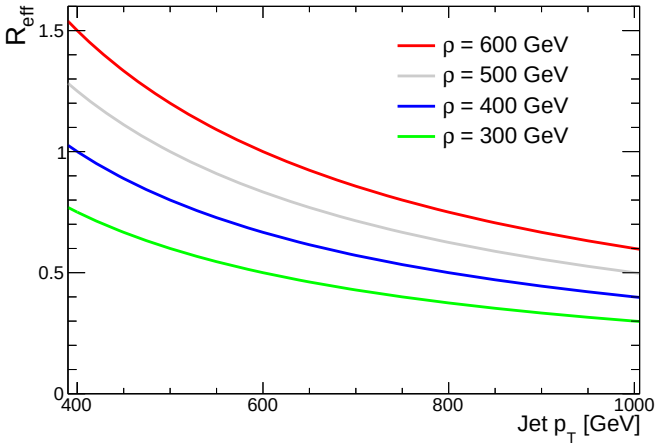

Figure 7.3: The effective distance parameter R_{eff} of the HOTVR algorithm as a function of the jet p_{T} for different values of the slope parameter ρ.

the two partons of the W boson decay or the b quark is not included in the jet. Furthermore, the selection efficiency increases with the jet area. Jets with large areas are more likely to pass the p_{T} requirement, and especially in these extreme kinematic regions it can be crucial to retain as many events as possible. In a previous analysis [1] this was one of the driving reasons for the choice of Cambridge-Aachen jets clustered with $R = 1.2$.

A possible solution is a jet clustering algorithm with a variable cone size such as the HOTVR algorithm [14]. First, the influence of the parameter ρ is studied, which steers the p_{T}-dependence of the distance parameter via $R_{\text{eff}} = \rho / p_{\text{T}}$. Figure 7.3 shows the p_{T}-dependence of R_{eff} for different values of ρ. Not only does the slope of R_{eff} change but especially the effective maximum of the distance parameter of selected jets with $p_{\text{T}} > 400$ GeV decreases with smaller values for ρ. Thus, tuning the ρ parameter has a very similar impact as changing the fixed distance parameter in the anti-k_{T} algorithm. Nevertheless, other properties of the HOTVR jet clustering show up when studying the resulting jet mass distributions. Figure 7.4 shows those distributions for four different choices of ρ, starting from the default value of $\rho = 600$ GeV down to $\rho = 300$ GeV in steps of 100 GeV. The mass jump criterion implemented in the HOTVR algorithm results in a two-peak structure exhibiting a peak around the W boson mass, since additional soft radiation is rejected. For larger values of ρ, the tail to higher masses is more pronounced due to jets that include the full top quark decay as well as additional energy. For small ρ, the distribution falls steeply from the peak to higher masses but includes a larger fraction of events in which only the W decay lies within the jet. A choice of $\rho = 400$ GeV would combine the advantages of both a steeply falling distribution after the peak as well as a large fraction of fully merged events.

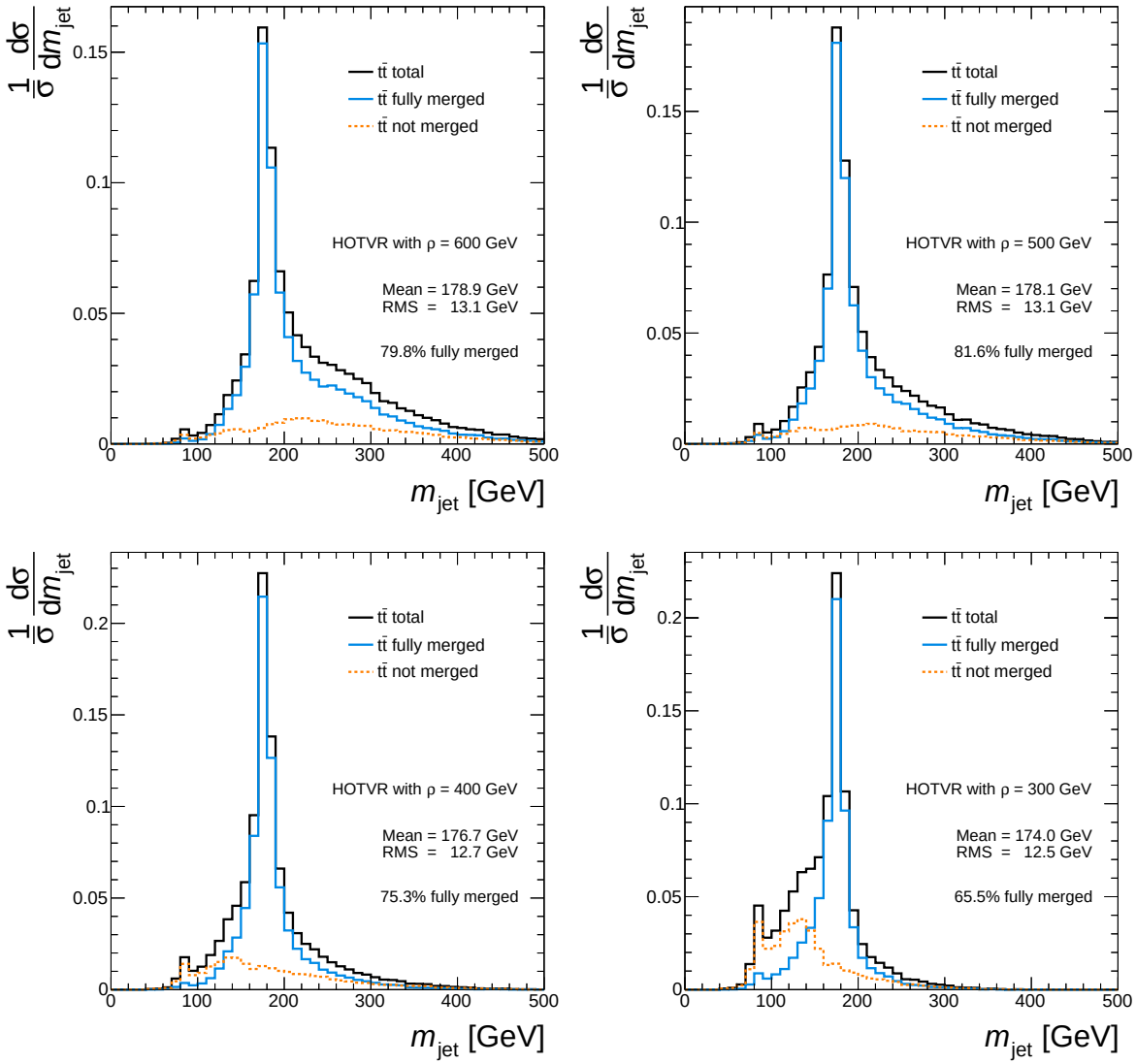

Figure 7.4: The m_{jet} distribution in $\text{t}\bar{\text{t}}$ simulation at the particle level for jets clustered with the HOTVR algorithm and different values for ρ in steps of 100 GeV between 600 GeV (upper left) and 300 GeV (lower right). The distributions are separately shown for the contributions from fully merged and not merged top quark decays.

A third approach is studied with the XCone clustering algorithm [56]. As suggested in Ref. [94], the signature of $\text{t}\bar{\text{t}}$ events can be resolved using a two-step clustering approach. First, XCone is run requesting two large-radius jets. This is designed to reconstruct one top quark decay per jet. Since this analysis selects the lepton+jets channel of $\text{t}\bar{\text{t}}$, the jet including the hadronic top quark decay is identified by the large angular distance to the prompt lepton. Subsequently, all particle candidates inside the jets reconstructing the hadronic and leptonic leg are used in clustering three and two XCone subjets, respectively. The choice of the number of subjets is made such

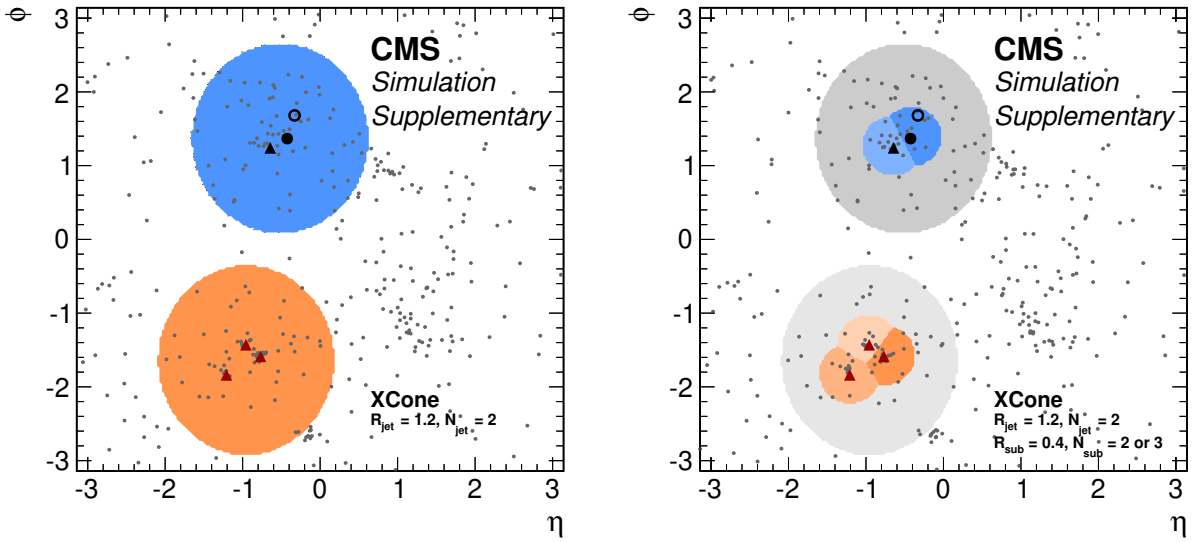

Figure 7.5: Shapes of jets clustered with the two-step clustering procedure using the XCone algorithm in the η-ϕ-plane. All grey dots represent the locations of stable particles at the particle level. The locations of the decay partons of the top quarks are highlighted with triangles and larger circles. The quarks from the decay $t \to bq\bar{q}'$ are shown as red triangles, the b quark (black triangle), charged lepton (black circle), and neutrino (black open circle) from the leptonic decay are also shown. The orange and blue areas in the left graph show the jet area of the two large-radius jets of the first clustering step with $R = 1.2$. The subjets after the second clustering step are shown as blue and orange areas in the right graph. In this example, the hadronic jet has $p_T = 688$ GeV and $m_{jet} = 191$ GeV. Published in the supplementary material [12] of Ref. [3].

that the three-prong hadronic decay is reconstructed. On the leptonic leg the neutrino is not detected, which makes this effectively a two-prong decay. The radius of the subjets is chosen to be $R_{sub} = 0.4$, which is consistent with the CMS standard of anti-k_T jets with the same distance parameter. Figure 7.5 shows the two-step clustering procedure for one selected event. The left graph shows the two large-radius XCone jets as colored areas. The colored areas in the right graph depict the subjets. The feature of nearby XCone jets having a straight separation is clearly visible. Furthermore, all partons of the top quark decay lie within the subjets. The measurement is performed using the combination of the subjets only, rejecting all particles that are clustered to the large-radius jet but are not clustered into subjets.

While the distance parameter of the subjets is designed to coincide with the standard jet distance parameter in CMS, a suitable choice for R_{jet} of the large-radius jet is studied. Figure 7.6 shows the jet mass distribution at the particle level for the previously described two-step XCone clustering method using four different choices of R_{jet} for the first clustering step. As opposed to the behavior when increasing R for anti-k_T jets, the peak position is stable for all scenarios with

XCone jets. A small change is visible at the peak close to the W boson mass, which is more pronounced for small R_{jet} since the b quark is missed in the reconstruction more frequently. Nevertheless, a large effect of R_{jet} is visible in the tails of the distributions with jet masses above 300 GeV. For choices of a large distance parameter, the tail is almost constant and reaches values of jet masses above 500 GeV. As opposed to the tails in the distributions of anti-k_{T} and HOTVR jets, those are not events, where the full top quark decay plus additional radiation is clustered. In XCone, the tails mostly consist of not merged decays, and the invariant mass of the combination of subjets is dominated by their angular distance. Because of an increase of events in the tail, the fraction of fully merged top quark decays decreases with increasing R_{jet}. Again, the most suitable R_{jet} is chosen as a compromise between a small tail, a less pronounced W boson peak and an overall large fraction of fully merged events. For this analysis it is chosen to be $R_{\text{jet}} = 1.2$.

At the reconstruction level, the clustering procedure, which relies on the identification of the prompt lepton before clustering the subjets, is impractical. Since the second jet is only used for the criterion of m_{jet} being larger than the invariant mass of the system containing a second jet and a lepton, it was found that a clustering with three subjets in each large-radius jet and later identifying the jet including the hadronic top quark decay gives similar results. The effect of the third subjet on the leptonic side is found to be negligible as Figure 7.7 shows.

For each of the three jet clustering algorithms – anti-k_{T}, HOTVR and XCone – a suitable setup was found. Figure 7.8 shows the jet mass distributions of the three selected options. Overall, XCone shows the best performance with a less pronounced W peak and the best resolution, while retaining a large fraction of fully merged events. Thus, the two-step clustering procedure using XCone with $R_{\text{jet}} = 1.2$ and $R_{\text{sub}} = 0.4$ and three subjets in both large-radius jets is chosen for the measurement of the jet mass distribution. Furthermore, XCone is not an iterative clustering algorithm but is defined through axes obtained by the N-jettiness algorithm [95], which simplifies analytical calculations. This makes XCone a well fitting choice for this measurement.

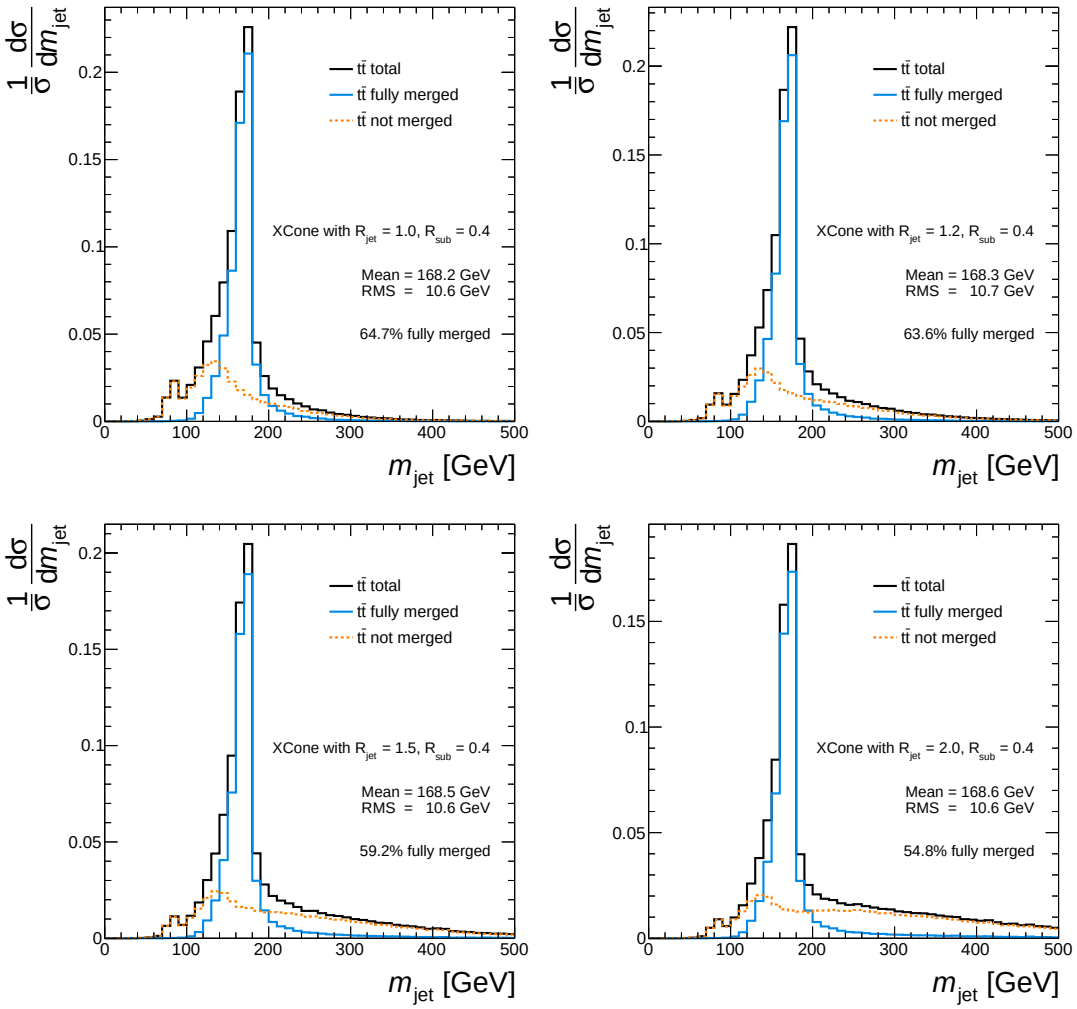

Figure 7.6: The m_{jet} distributions in $t\bar{t}$ simulation at the particle level for jets clustered with the two-step clustering using XCone and $R_{\text{jet}} = 1.0$ (upper left), $R_{\text{jet}} = 1.2$ (upper right), $R_{\text{jet}} = 1.5$ (lower left), as well as $R_{\text{jet}} = 2.0$ (lower right). The distributions are separately shown for the contributions from fully merged and not merged top quark decays.

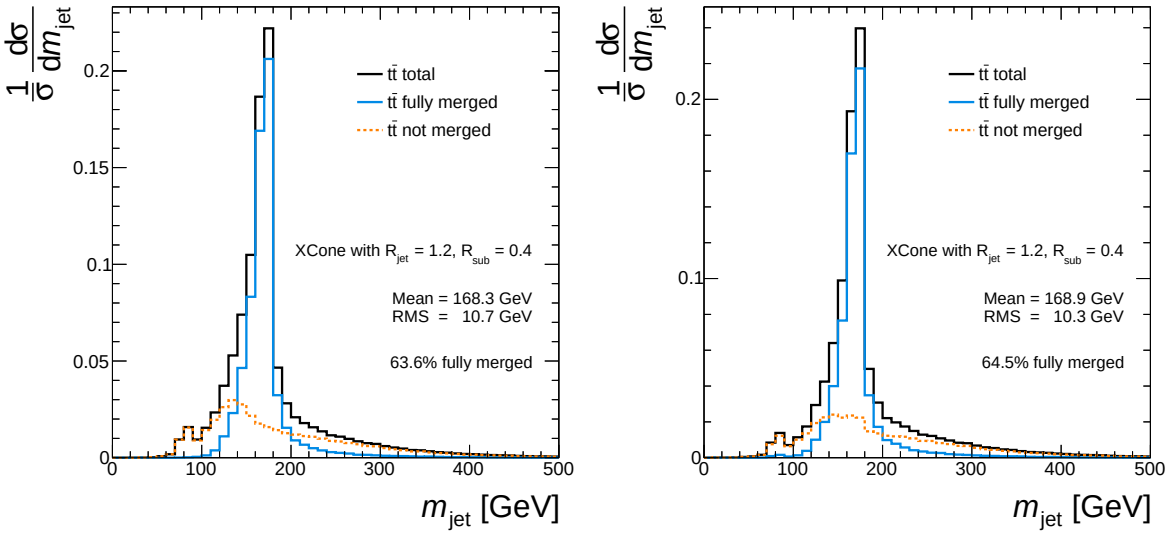

Figure 7.7: The jet mass distributions in $t\bar{t}$ simulation at the particle level for jets clustered with the two-step clustering using XCone and the option of requesting 2 (left) or 3 (right) subjets on the leptonic leg of the $t\bar{t}$ decay. The distributions are separately shown for the contributions from fully merged and not merged top quark decays.

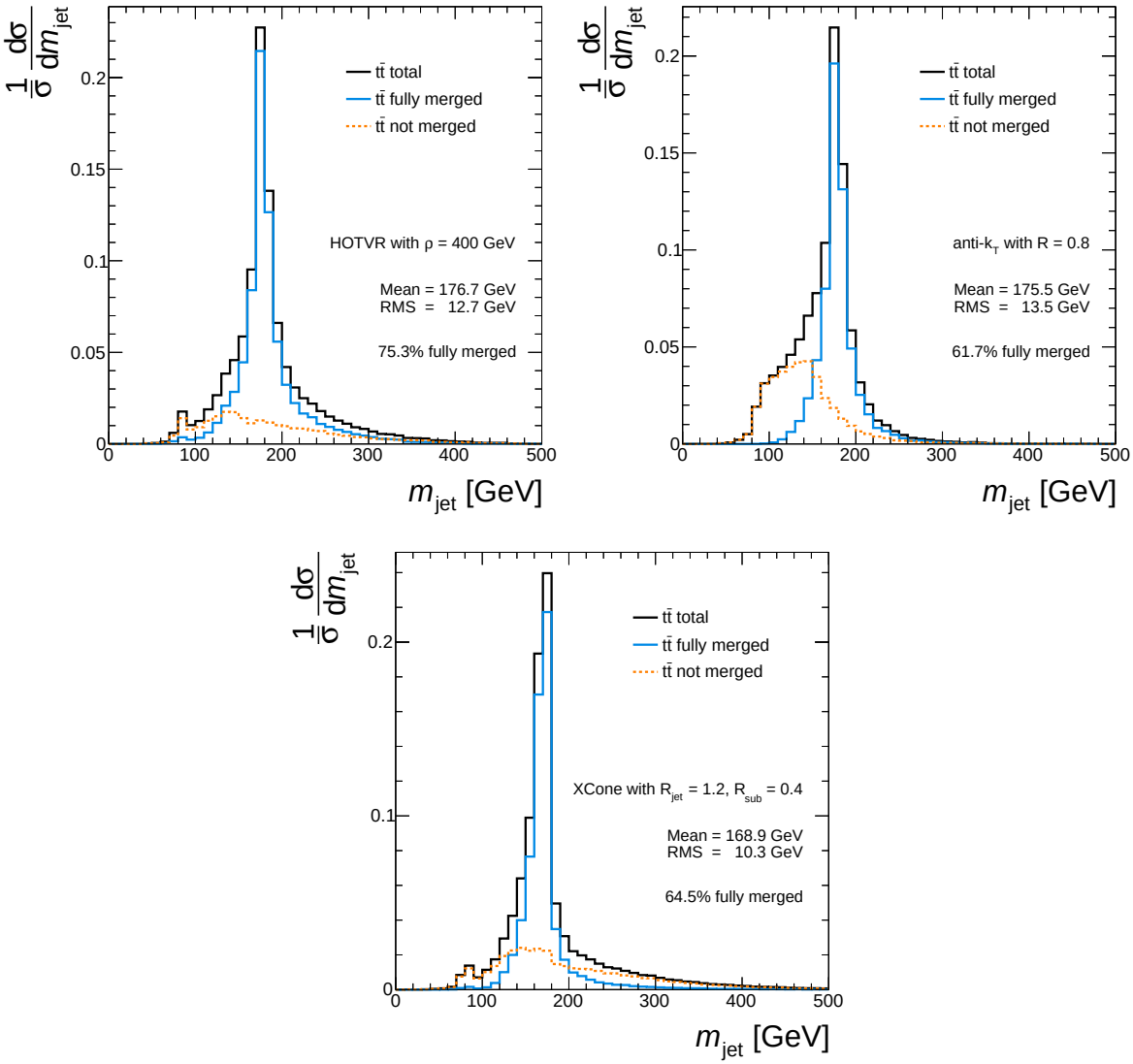

Figure 7.8: The m_{jet} distributions in $t\bar{t}$ simulation at the particle level for jets clustered with the HOTVR (upper left), anti-k_{T} (upper right), and XCone (lower) algorithms. In all plots the distribution is separately shown for the contributions from fully merged and not merged top quark decays.

7.2.2 Phase space definition

The measurement is performed in the lepton+jets channel of the $t\bar{t}$ process. Thus, events are selected that contain exactly one prompt lepton (muon or electron) originating from a W boson decay. Decays into τ leptons are not considered part of the signal and are treated as background. Furthermore, the lepton is required to have $p_T > 60$ GeV. This value is designed to match the requirements of the detector level selection, which requires a high-p_T lepton in order to be selected by the trigger. The XCone jet has to fulfill $p_T > 400$ GeV with each of its subjets fulfilling $p_T > 30$ GeV and $|\eta| < 2.4$. In addition, the mass of the XCone jet has to be larger than the invariant mass of the combination of the second jet and lepton. Here, the second jet is defined as the sum of its three subjets after removing the overlapping lepton. An event is rejected if the second jet has $p_T < 10$ GeV, in order to ensure a decent reconstruction of the leptonic top quark decay.

7.2.3 Results at particle level

The jet mass distribution using the previously discussed two-step clustering procedure is displayed in Figure 7.9 (left) after the full particle level selection. A peak close to the top quark mass is visible, which consists of about 75% fully merged events. The shape of the fully merged contribution is compared to a similar distribution from a previous analysis [1] (Figure 7.9, right). Despite the same distance parameter of 1.2, the two-step XCone clustering results in a much narrower peak region, where the peak is not shifted towards high values compared to the Cambridge-Aachen reconstruction. The width of the peak is reduced by a factor of two, which already hints at a higher sensitivity to the top quark mass. Furthermore, the reduced tail displays a smaller influence of additional energy deposits e.g. from the underlying event, which is one of the limiting factors in Ref. [1]. Especially large pileup effects are hard to handle since they always lead to large migrations towards higher masses from the particle level to the detector level. Thus, not only the sensitivity is expected to drastically increase, but also effects from pileup and underlying event can be reduced using the novel XCone jet reconstruction. This, together with higher statistical precision due to the larger data set, directly targets the limiting factors in precision of the previous analysis.

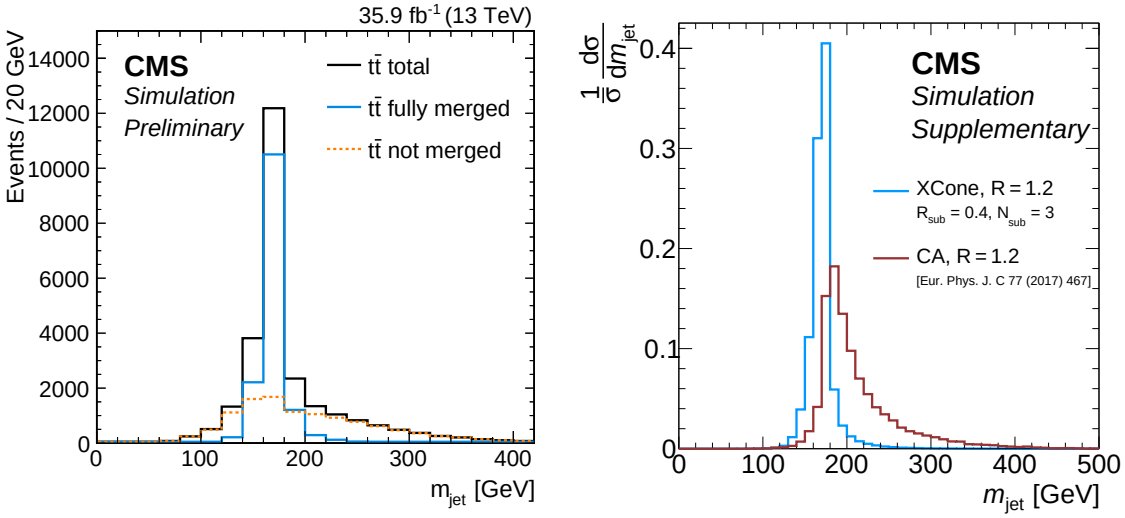

Figure 7.9: The m_{jet} distribution at the particle level after applying the full selection. The left graph shows $\mathrm{t\bar{t}}$ simulation scaled to 35.9 fb^{-1} (black solid), also separately for the contributions of fully merged (blue solid) and not merged (orange dotted) events. The right graph shows the fully merged distribution but normalized to unit area (blue) and compared to the m_{jet} distribution from a previous analysis using Cambridge-Aachen jets with $R = 1.2$ (red). Published in Ref. [96] and in the supplementary material [12] of Ref. [3].

7.3 Studies at detector level

At the detector level a phase space similar to the definition at the particle level is selected in order to ensure minimal migrations into and out of the measurement phase space. In addition, a pure $\mathrm{t\bar{t}}$ sample has to be selected, suppressing events from background processes.

7.3.1 Phase space definition

The goal of the detector level selection is to obtain a phase space similar to the particle level while suppressing events from background processes. A first step towards a pure $\mathrm{t\bar{t}}$ sample is the choice of the lepton+jets channel since it allows to use the lepton in the final state as a tag while measuring the jet on the hadronic leg of the $\mathrm{t\bar{t}}$ system.

The analyzed data were recorded in 2016 and correspond to an integrated luminosity of 35.9 fb^{-1}. Two separate trigger paths are used for the final state containing either a muon or an

electron, respectively. Events containing one muon are selected with a single muon trigger[1] that requires one muon candidate with $p_T > 50$ GeV. The e+jets channel is selected using a combination of triggers[2] requiring one isolated electron candidate with $p_T > 27$ GeV, an electron candidate without an isolation requirement but with $p_T > 115$ GeV, or at least one photon candidate with $p_T > 175$ GeV. The photon trigger ensures a high selection efficiency at high electron momenta since the trigger selects candidates with reduced quality criteria. The trigger requirements are also applied to simulated events. Event weights in simulation are adjusted as a function of lepton p_T and η in order to match the trigger efficiency observed in data [97, 98, 99]. The correction factors for the electron triggers are measured within the scope of this analysis and are presented in Appendix A. Also the pileup profile in simulation is adjusted via event weights in order to match the profile in data.

Leptons are required to pass quality criteria provided by the CMS Collaboration [78, 99], also known as lepton IDs. Those criteria include the number of hits used to reconstruct the candidate track in certain subsystems of the detector, the χ^2 value of a global track fit for muons, the spatial expansion of the showers used to identify electrons, and the ratio of energy of an electron candidate deposited in the HCAL and ECAL. Again, these criteria are applied to simulation as well as to data and scale factors as a function of lepton p_T and η are centrally derived by the CMS Collaboration, correcting for different efficiencies compared to data. Only events are considered in this analysis containing exactly one muon or one electron candidate with $p_T > 60$ GeV and $|\eta| < 2.4$. Every selected event contains exactly one muon and no electrons or one electron and no muons. Because of the detector geometry, electron candidates in the range $1.44 < |\eta| < 1.57$ are rejected.

In addition to the quality criteria, leptons are required to pass an isolation requirement in order to suppress QCD multijet events that include a lepton. Since leptons in the targeted $\mathrm{t\bar{t}}$ event topology also tend to overlap with a jet originating from a b quark, the isolation criterion has to be carefully adjusted. Two useful observables are the angular distance ΔR between the lepton and the closest AK4 jet as well as the lepton p_T relative to the axis of the closest AK4 jet, p_T^{rel}. For both observables, all AK4 jets with $p_T > 15$ GeV are considered. Figure 7.10 shows the p_T^{rel}-ΔR-plane for QCD (left) and $\mathrm{t\bar{t}}$ (right) events in simulation. While the events in the QCD sample accumulate at low values of both observables, $\mathrm{t\bar{t}}$ events spread out over the whole plane. In order to suppress the contribution from multijet events, events with $\Delta R < 0.4$ and $p_T^{rel} < 40$ GeV are not considered in this analysis.

[1] HLT_Mu50 and HLT_TkMu50

[2] HLT_Ele27_WPTight_Gsf, HLT_Ele115_CaloIdVT_GsfTrkIdT and HLT_Photon175

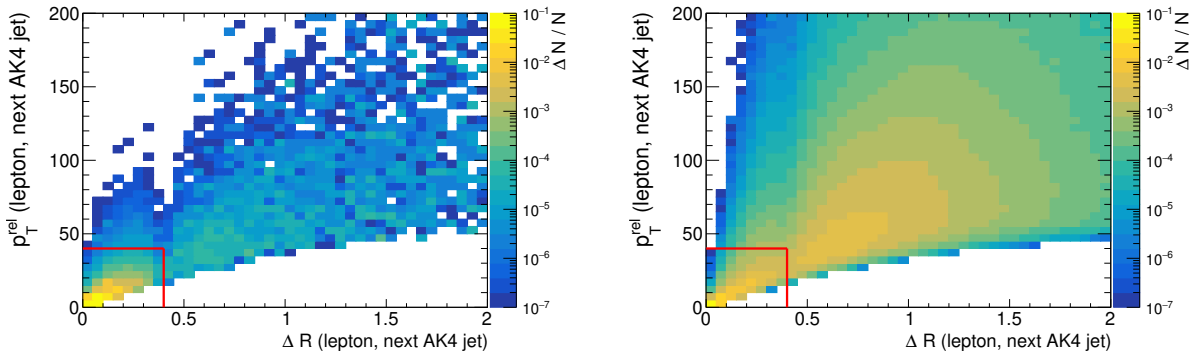

Figure 7.10: The $p_{\mathrm{T}}^{\mathrm{rel}}$-$\Delta R$-plane for multijet QCD production (left) and $\mathrm{t\bar{t}}$ events (right), normalized to an integral of unity. The red lines indicate the window which is cut out using the customized lepton isolation.

Since the lepton+jets channel includes a neutrino in the final state, $p_{\mathrm{T}}^{\mathrm{miss}}$ is required to exceed 50 GeV. With the selection criteria discussed above, almost all contributions from Z+jets, diboson, and QCD multijet production are eliminated, leaving W+jets as the dominant background. A major difference in the final states of $\mathrm{t\bar{t}}$ and W+jets processes is the presence of two b quarks in $\mathrm{t\bar{t}}$ that can be identified using b tagging. All AK4 jets with $p_{\mathrm{T}} > 30$ GeV and $|\eta| < 2.4$ are considered. The AK4 jet with the highest discriminator value of the CSVv2 algorithm [80, 81] is required to have a value greater than 0.9535, corresponding to a tagging efficiency and mistag rate of 68% an 0.1%, respectively. The tagging efficiency in simulation is corrected to match the corresponding efficiency in data by applying a reweighting procedure depending on a jet's p_{T}, η, CSV value, and generator information. Figure 7.11 shows the distribution of the CSV discriminator in data and simulation for the AK4 jet with the highest discriminator value before (left) and after (right) the reweighting procedure. The agreement between data and simulation drastically improves and ensures a comparable efficiency. Furthermore, it can be observed that after selecting those events located at high values, most of the contribution from W+jets is rejected.

After the baseline selection introduced above, the selected sample contains mostly events from $\mathrm{t\bar{t}}$ production with minor contributions from single top quark production and W+jets events. Distributions of muon p_{T} and η, electron p_{T} and η as well as $p_{\mathrm{T}}^{\mathrm{miss}}$ and AK4 jet p_{T} are shown in Figure 7.12. Data are compared to simulation only including statistical uncertainties. Despite a trend at high jet p_{T} and $p_{\mathrm{T}}^{\mathrm{miss}}$, which can be explained with the observed mismodeling of the top quark p_{T} in simulation [100, 101, 102, 103, 1], data and the simulated prediction agree well.

After the baseline selection, requirements similar to the ones applied at the particle level are

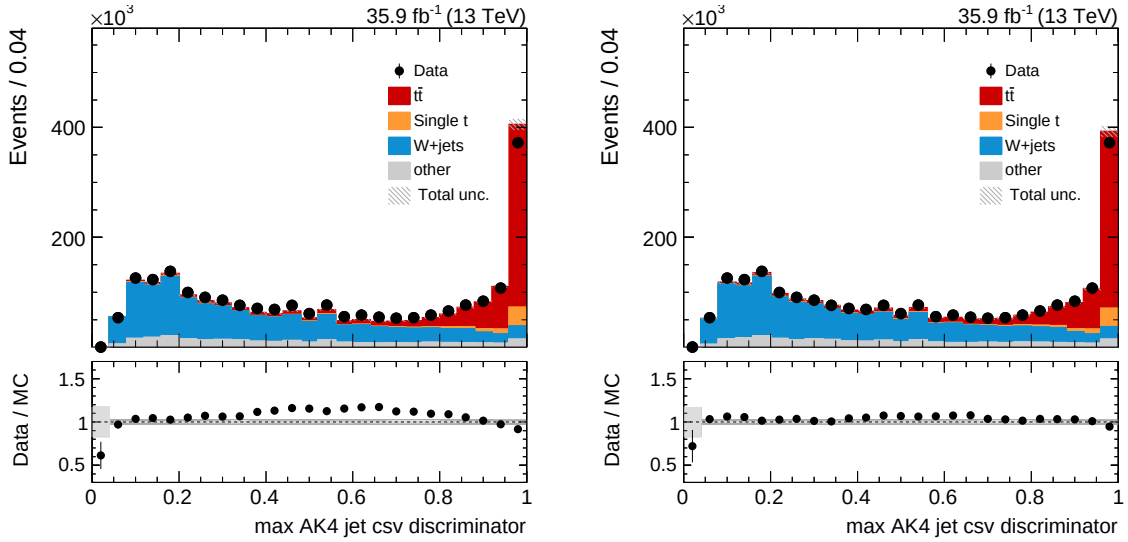

Figure 7.11: The CSV discriminator for the AK4 jet with the highest CSV value in the event before (left) and after (right) the CSV correction. Data (markers) are compared to simulation (filled areas) in the upper panels while the lower panels show their ratio. The hatched and solid areas in the upper and lower panels show the statistical uncertainties. Events that are expected to contain at least one jet originating from a b quark show large values of the CSV discriminator.

imposed, and XCone jets are equally reconstructed using the two-step clustering procedure. Charged hadrons that are identified as originating from pileup vertices are removed from the particle list before the jet clustering using the CHS algorithm [82] (see Section 5.4). Events must contain an XCone jet identified as containing the hadronic top quark decay with $p_{\mathrm{T,jet}} > 400$ GeV with its subjets all carrying $p_{\mathrm{T}} > 30$ GeV and being inside $|\eta| < 2.4$. Also, the XCone-jet mass must be greater than the invariant mass of the system constructed from the second jet and the lepton. The XCone subjet distributions in p_{T} and η are displayed in Figure 7.13 after the XCone-jet corrections (presented in Section 5.4.3), including statistical and experimental systematic uncertainties. A full description of all uncertainties considered can be found in Section 7.5. In order to match the cross section observed in data for displaying purposes, the $\mathrm{t\bar{t}}$ contribution is scaled with a constant factor of 0.85. The hadronic W boson decay can be reconstructed from subjets of the XCone jet by combining the two subjets with the smallest pairwise jet mass m_{ij}. Also, this distribution (see Figure 7.14) shows a good agreement between data and simulation. In combination with the spectra in Figure 7.13 this confirms a valid calibration of the XCone subjets in both simulation and data.

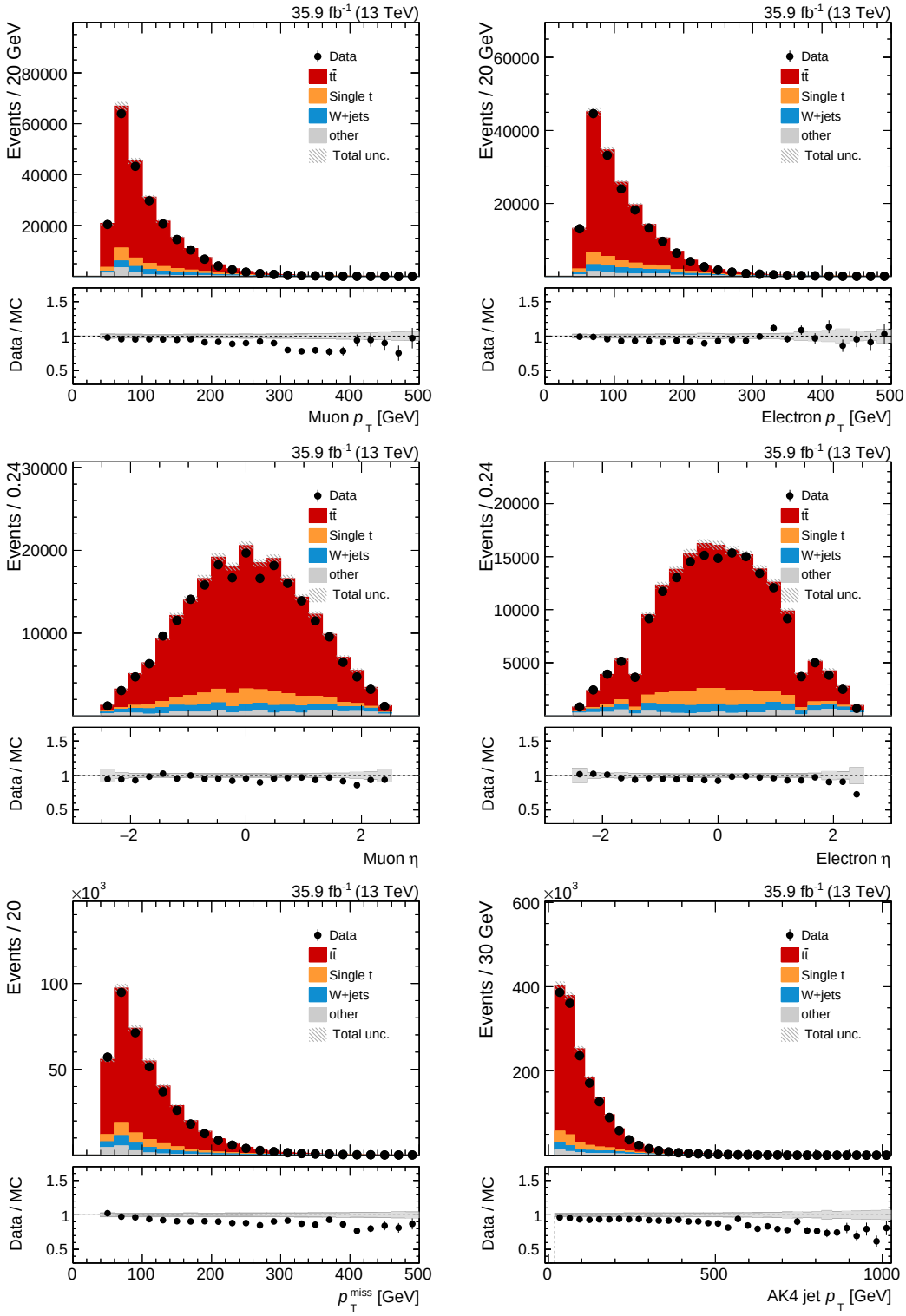

Figure 7.12: Distributions of muon p_{T} (upper left), electron p_{T} (upper right), muon η (middle left), electron η (middle right), missing transverse energy (lower left), and AK4 jet p_{T} (lower right) after the baseline selection. Data (markers) are compared to simulation (filled areas) in the upper panels while the lower panels show their ratio. The hatched and solid areas in the upper and lower panels show the statistical uncertainties.

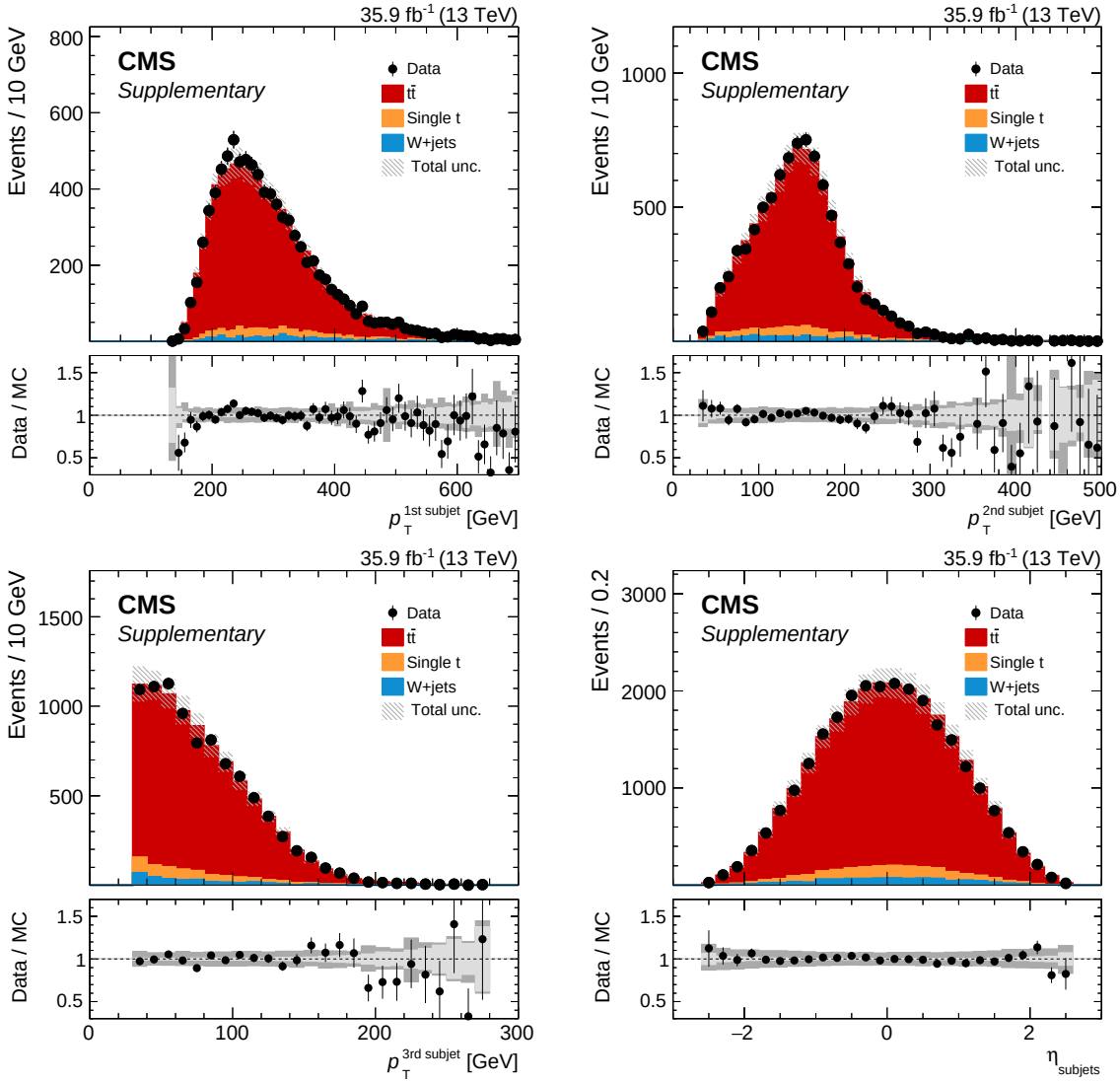

Figure 7.13: Event distributions after applying the additional jet correction in p_{T} of the leading (upper left), second (upper right), and third (lower left) XCone subjet from the measurement jet ordered in p_{T} after the full event selection. The bottom right graph shows the η of all three subjets. Data (markers) are compared to simulation (filled areas), and a good agreement is observed after scaling the $\mathrm{t\bar{t}}$ contribution to match the fiducial cross section in data. The hatched areas in the upper panels show the total uncertainty. The lower panels show the ratio of data to simulation and the statistical (light grey) and total uncertainties (dark grey). Only statistical and experimental systematic uncertainties are considered. Published in the supplementary material [12] of Ref. [3].

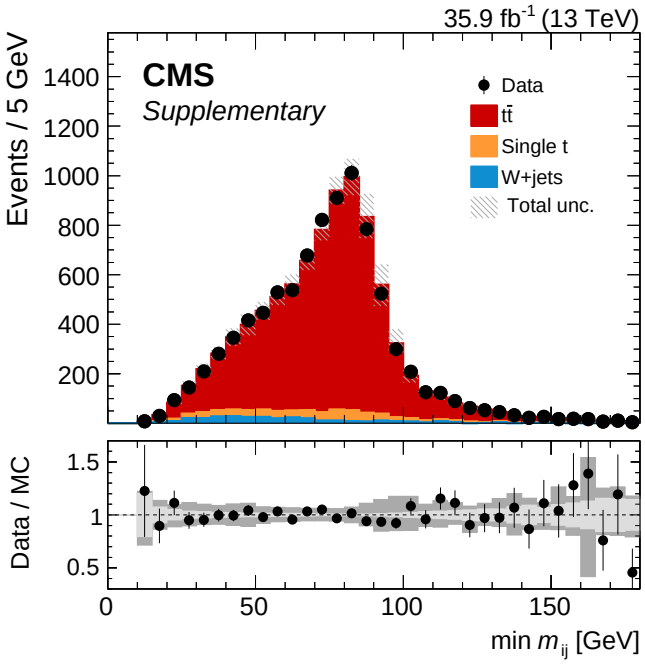

Figure 7.14: The reconstructed minimum pairwise mass m_{ij} is compared between simulation (filled areas) and data (markers) after the full selection. The hatched areas in the upper panels show the total uncertainty. The lower panels show the ratio of data to simulation and the statistical (light grey) and total uncertainties (dark grey). Only statistical and experimental systematic uncertainties are considered. Published in the supplementary material [12] of Ref. [3].

7.3.2 Results at detector level

The distributions of p_T and η of the XCone jet after the full selection are displayed in Figure 7.15. Both show a very good agreement between data and simulation within uncertainties after adjusting the $t\bar{t}$ cross section to match the one observed in data. Jets are observed up to a transverse momentum of 1000 GeV, but the selected events are clearly dominated by the region around 400 GeV. The jet mass distribution of the XCone jet containing the hadronic top quark decay is shown in Figure 7.16 for the muon channel (left), electron channel (right), and the combination of both (lower). Both channels show a consistent shape with a few more events in the muon channel due to a more efficient reconstruction. Data are in good agreement with the prediction, and the $t\bar{t}$ contribution is again scaled to match the observed cross section in data. All m_{jet} distributions show a narrow peak close to the top quark mass with no visible peak at the W mass and steeply falling tails. The performance of the XCone-jet reconstruction is studied in terms of jet mass resolution and stability against pileup. Figure 7.17 (left) shows the XCone-jet mass resolution for different pileup scenarios obtained from $t\bar{t}$ simulation. With very little influence from pileup and values of 6–7% over the whole p_T range, XCone shows a stable performance especially compared to a resolution of approximately 14% achieved

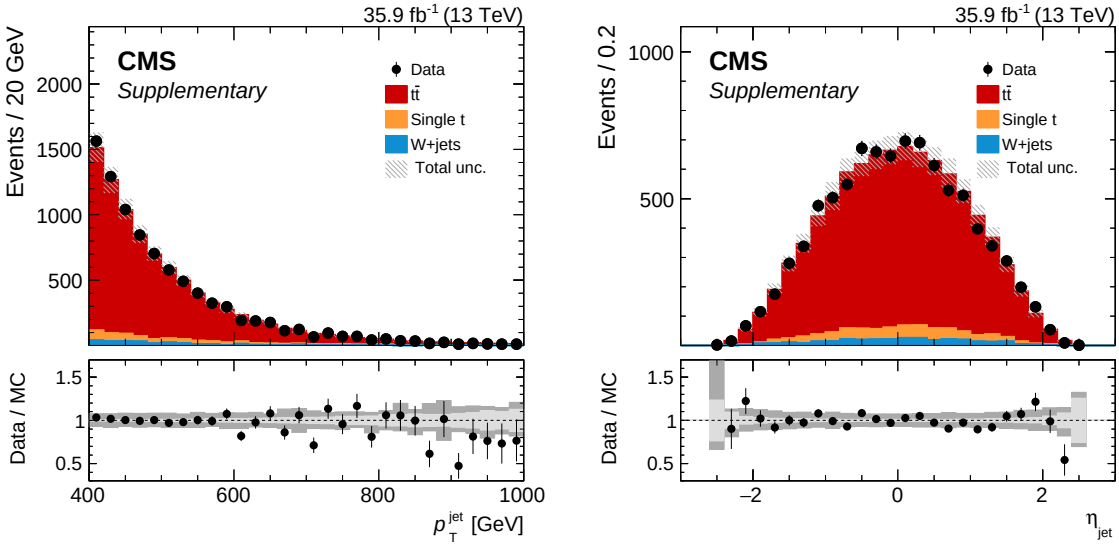

Figure 7.15: The distributions in XCone-jet p_T (left) and η (right) are compared between simulation (filled areas) and data (markers) after the full selection. The hatched areas in the upper panels show the total uncertainty. The lower panels show the ratio of data to simulation and the statistical (light grey) and total uncertainties (dark grey). Only statistical and experimental systematic uncertainties are considered. Published in the supplementary material [12] of Ref. [3].

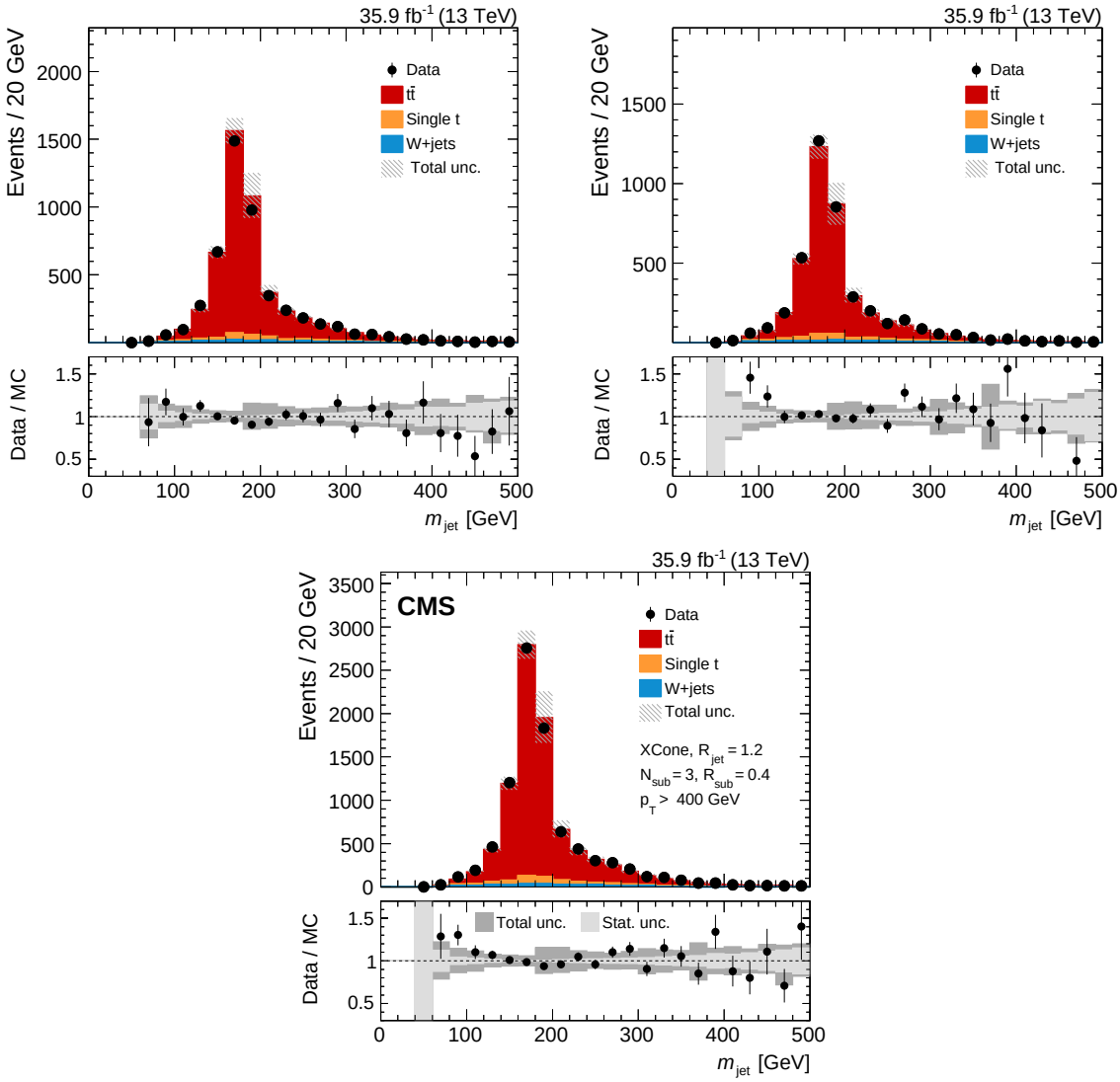

Figure 7.16: Detector level distribution of m_{jet} in the μ+jets channel (upper left), e+jets channel (upper right), and the combined lepton+jets channel (lower) after the full selection. Data (markers) are compared to simulation (filled areas), and a good agreement is observed after scaling the $\text{t}\bar{\text{t}}$ contribution to match the fiducial cross section in data. The hatched areas in the upper panels show the total uncertainty. The lower panels show the ratio of data to simulation and the statistical (light grey) and total uncertainties (dark grey). Only statistical and experimental systematic uncertainties are considered. Lower plot published in Ref. [3].

with Cambridge-Aachen jets with $R = 1.2$ in Ref. [1]. Furthermore, the peak position of the XCone-jet mass is observed to be very stable against pileup as Figure 7.17 (right) suggests. Both the mean of the m_{jet} distribution and the reconstructed W mass are not only stable against the number of primary vertices but also agree between data and simulation. Since the two-step jet clustering procedure acts as a grooming algorithm by removing all particles that are not

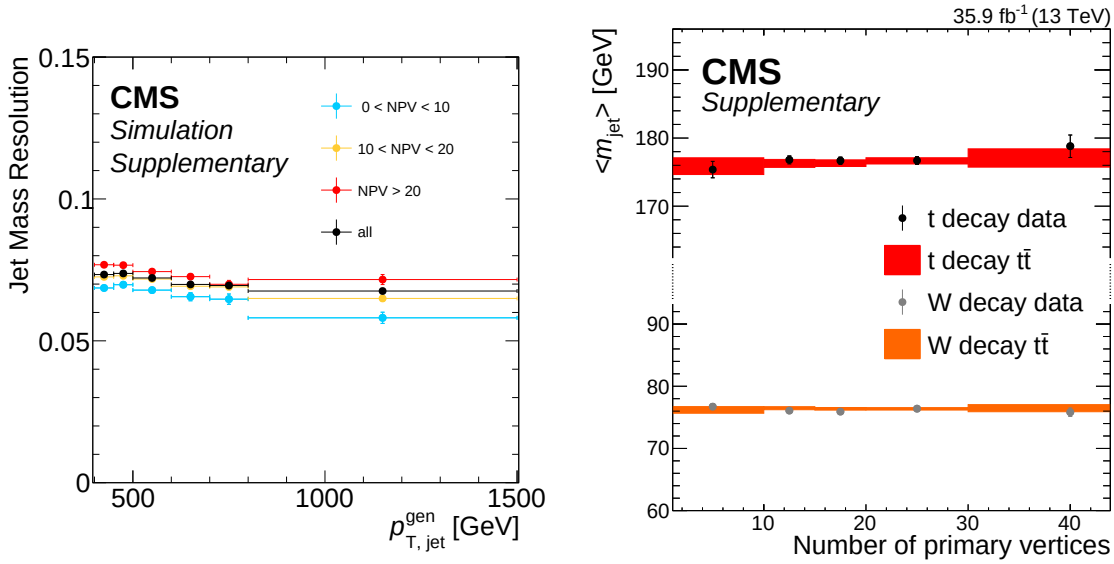

Figure 7.17: Jet mass resolution of XCone jets as a function of the particle level jet p_T for different pileup scenarios (left) and the mean of the m_{jet} distribution as well as the reconstructed W mass compared between simulation (filed areas) and data (markers) as a function of the number of primary vertices (right). Published in the supplementary material [12] of Ref. [3].

part of any of the XCone subjets, a comparison to the widely used soft drop algorithm can be made. In Figure 7.18, the result of the two-step clustering (left) is contrasted to the jet mass distribution obtained by applying the soft drop algorithm to the large-radius jets after the first clustering step (right). The distributions are shown after the full event selection and after combining the muon and electron channels. It is observed that the two-step procedure results in a narrower peak and more steeply falling tail. This study emphasizes the performance of the two-step jet clustering even in comparison to well-established grooming algorithms.

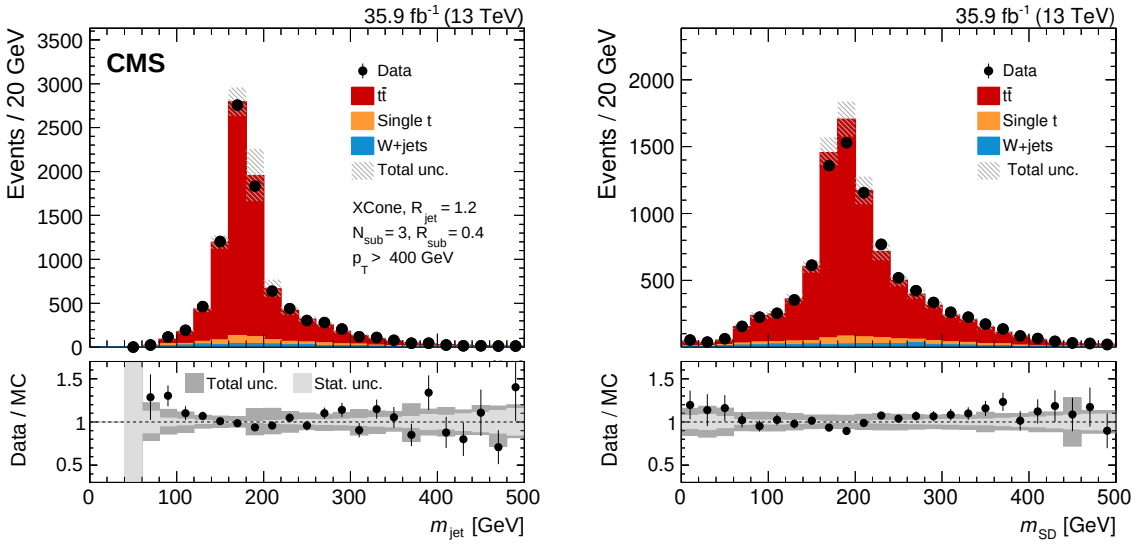

Figure 7.18: Detector level distribution of the jet mass obtained with the two-step XCone clustering (left) and by applying the soft drop algorithm to the large-radius XCone jets (right). Data (markers) are compared to simulation (filled areas), and a good agreement is observed after scaling the $t\bar{t}$ contribution to match the fiducial cross section in data. The hatched areas in the upper panels show the total uncertainty. The lower panels show the ratio of data to simulation and the statistical (light grey) and total uncertainties (dark grey). Only statistical and experimental systematic uncertainties are considered. Left plot published in Ref. [3].

7.4 Unfolding procedure

In order to measure the $t\bar{t}$ production cross section, the detector level distribution has to be corrected for detector and pileup effects. This procedure is referred to as unfolding. The muon and electron channels are combined prior the unfolding, which ensures high statistical precision. Nevertheless, both channels are unfolded separately with the same setup in order to provide a consistency check. In this context, the transformation from the detector level to particle level is obtained from $t\bar{t}$ simulation and then applied to events measured in data. The unfolding setup is described in detail in the following.

A matrix with entries A_{ij} is constructed from the $t\bar{t}$ event simulation and contains migrations from a bin x_i at the particle level to a bin y_j at the detector level. Thus, the inverse of A describes the transfer from the detector-level distribution to a distribution at the particle level. However, simply inverting the matrix would lead to an amplification of small fluctuations. This is due to the fact that large variations at the particle level usually lead to smaller variations at the detector level because of the finite detector resolution. Therefore, small fluctuations at the detector level can drastically change the distribution at the particle level. In order to be able

to unfold data distributions with finite statistical precision, statistical fluctuations are damped using a regularization term. In this analysis, the unfolding is carried out using the TUnfold framework [104], which provides a regularized and multidimensional unfolding method. Within TUnfold, the unfolding translates into a minimization of a Lagrangian $\mathscr{L}$ composed of three terms $\mathscr{L} = \mathscr{L}_1 + \mathscr{L}_2 + \mathscr{L}_3$, which are defined as

$$\mathscr{L}_1 = (\vec{y} - A\vec{x})^{\mathsf{T}} V_{yy}^{-1} (\vec{y} - A\vec{x}), \tag{7.1}$$

$$\mathscr{L}_2 = \tau^2 (\vec{x} - f_b \vec{x}_0)^{\mathsf{T}} L^{\mathsf{T}} L (\vec{x} - f_b \vec{x}_0) \quad \text{and} \tag{7.2}$$

$$\mathscr{L}_3 = \lambda (Y - \vec{e}^{\mathsf{T}} \vec{x}) \quad \text{with } Y = \sum_i y_i \text{ and } e_j = \sum_i A_{ij}. \tag{7.3}$$

The first term contains a standard calculation of the least squares taking into account the unfolding result $\vec{x}$, detector-level distribution $\vec{y}$, the migration matrix A, and the covariance matrix V containing uncertainties of $\vec{y}$. The regularization term is described in $\mathscr{L}_2$ and contains the regularization strength τ, which damps deviations of the unfolded result from $f_b \vec{x}_0$. In this analysis f_b is set to the ratio of event yields in simulation used to determine A and the distribution which is unfolded and accounts for normalization differences. The bias distribution $\vec{x}_0$ is set to be the particle-level distribution of the simulation used to create A. In this analysis the optimal value of τ is estimated via minimizing the global correlation coefficient ρ, which is defined as

$$\rho = \sum_i \frac{1}{n} \sqrt{1 - \frac{1}{\left(V_{xx}^{-1}\right)_{ii} (V_{xx})_{ii}}}, \tag{7.4}$$

where V_{xx} is the covariance matrix of the unfolded distribution $\vec{x}$, which has dimension n. The scan for various values of τ and the final choice for τ are displayed in Figure 7.19. The matrix L determines the regularization condition. It can be chosen such that the size, derivative, or second derivative (curvature) of $\vec{x}$ is regularized. All options were studied in this analysis and the curvature mode was selected. The third term $\mathscr{L}_3$ represents an additional area constraint, which forces normalization of $\vec{x}$ corrected for the efficiency $\vec{e}$ to match the event count Y at the detector level. The area constraint is not used in this analysis.

The migration matrix is constructed from a $\mathrm{t\bar{t}}$ sample simulated with POWHEG. A crucial part of the unfolding procedure is the choice of the exact bin ranges for both detector level and particle level. At the detector level, the bins of the m_{jet} distribution are chosen such that every bin contains sufficient events ensuring a good statistical precision over the full range of the selected phase space. The bin sizes of the particle-level distribution are motivated by the jet mass resolution such that every bin spans twice the resolution. With values of m_{jet} around 170 GeV and a resolution of about 6%, this translates into a bin size of roughly 20 GeV,

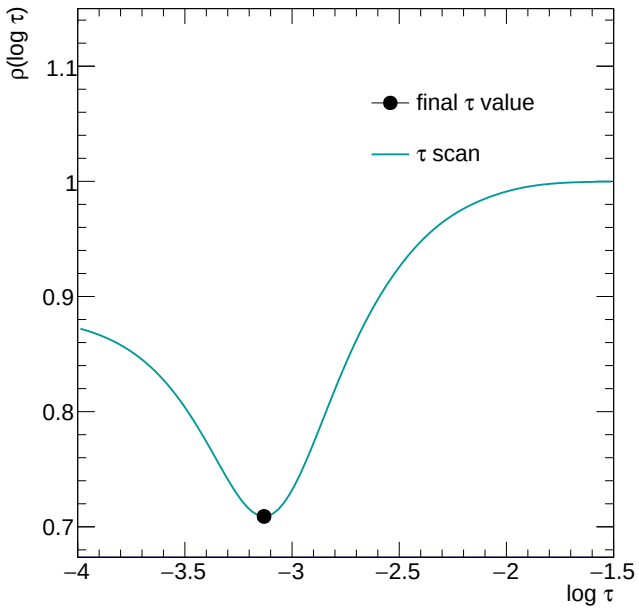

Figure 7.19: Scan of the global correlation coefficient ρ as a function of the regularization strength τ (line). The point indicates the final choice of τ, which corresponds to the minimum value of ρ.

slightly increasing towards higher values of m_{jet} resulting in the binning displayed in Table 7.1. Underflow and overflow bins are used below 112 GeV and above 232 GeV, which do not add sensitivity to the measurement but contribute to the correct estimation of the normalization. Furthermore, bins 2 and 3 are subdivided into bins with 10 GeV during the unfolding procedure and recombined afterwards. This adds granularity to the migration matrix and makes the unfolding framework more sensitive to subtle model differences in the $\mathrm{t\bar{t}}$ simulation and thus less model dependent. A measure of the migrations between particle level and detector level is given by the stability and purity. The stability is defined as the fraction of events that are reconstructed in the same bin as they are generated. Vice versa, purity quantifies the fraction of events that are generated in the same bin as they are reconstructed. With this choice of binning, both purity and stability well above 40% are achieved over the full range of m_{jet} (see Figure 7.20).

In addition to the measurement phase space defined in the previous Sections 7.2 and 7.3, sideband regions are included in the unfolding to keep track of migrations into and out of the measurement phase space. Five of those sideband regions are defined at the detector level, each loosening one of the selection requirements used in the measurement phase space. One region targets leptons with smaller transverse momentum $55 < p_{\text{T}} < 60$ GeV, another one

Table 7.1: Summary of the bins used for the particle-level distributions in the unfolding. Underflow and overflow bins are not shown. Bins 2 and 3 are subdivided into two 10 GeV bins each during the unfolding procedure but recombined afterwards.

Bin number	Range in m_{jet} [GeV]	Bin Width [GeV]
1	112–132	20
2	132–152	20
3	152–172	20
4	172–192	20
5	192–232	40

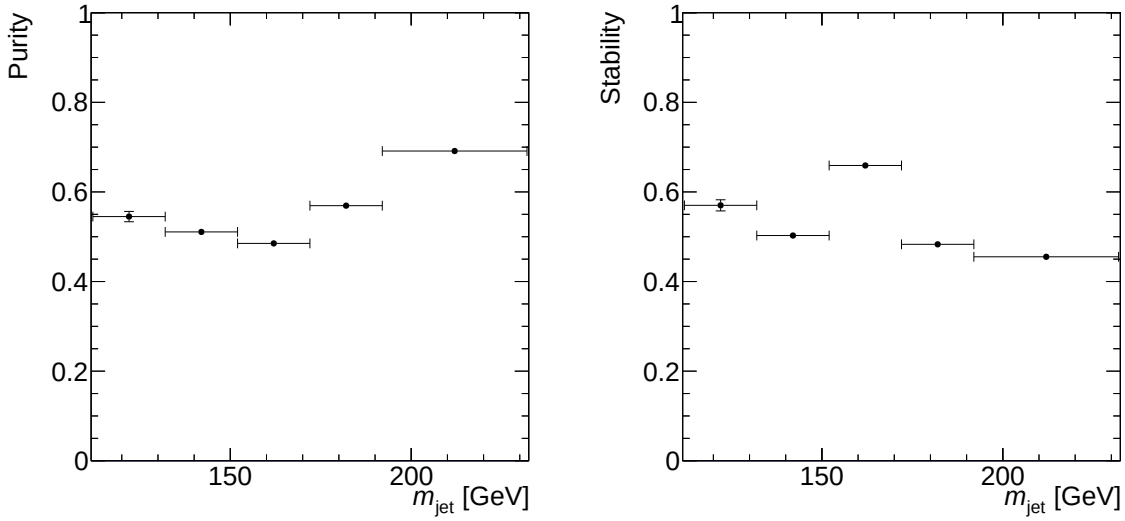

Figure 7.20: Purity and stability for the combined lepton+jets channel in the final binning. Both are well above 0.4 over the full range of m_{jet}.

XCone jets with $350 < p_{\text{T}} < 400$ GeV. The third and fourth regions allow XCone subjets with $p_{\text{T}} < 30$ GeV and m_{jet} being smaller than the mass of the second XCone jet and lepton, respectively. The last sideband consists of events where an AK4 jet passes a looser b tagging requirement while not fulfilling the b tagging requirement of the measurement phase space. At the particle level the same regions are defined except for the last region targeting a looser b tag. Two regions – with lower p_{T} threshold and inverted mass criterion – that especially change the shape of the jet mass distribution are displayed in Figure 7.21 at the detector level. Despite the different kinematics, the data are well described by the simulation after correcting the $\text{t}\bar{\text{t}}$ normalization. Because the shape of m_{jet} changes, and bins at smaller values are more populated, the binning in m_{jet} is adjusted accordingly for each sideband.

In addition, the measurement region and the sideband including XCone jets with $350 < p_{\text{T}} < 400$ GeV are subdivided into bins of XCone-jet p_{T} during the unfolding. This provides a high

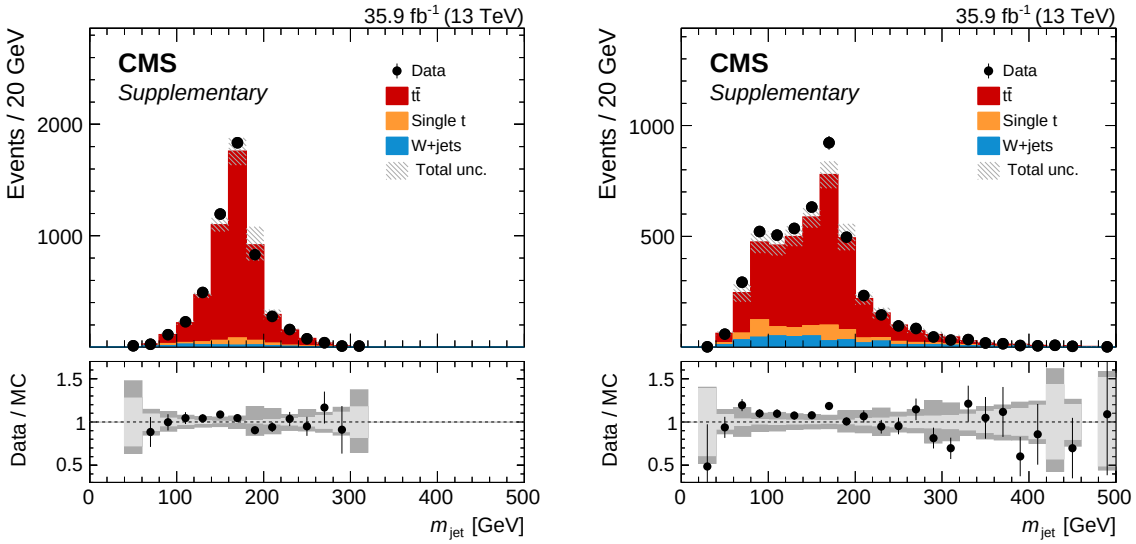

Figure 7.21: The detector level distribution in m_{jet} in the sideband which requires the XCone jet to have $350 < p_{\text{T}} < 400$ GeV (left) and in the sideband containing events with m_{jet} being smaller than the combined mass of second jet and lepton (right). Data (markers) are compared to simulation (filled areas), and a good agreement is observed after scaling the $\text{t}\bar{\text{t}}$ contribution to match the fiducial cross section in data. The hatched areas in the upper panels show the total uncertainty. The lower panels show the ratio of data to simulation and the statistical (light grey) and total uncertainties (dark grey). Only statistical and experimental systematic uncertainties are considered. Published in the supplementary material [12] of Ref. [3].

granularity and increases the sensitivity to p_{T} dependent effects. All bins in p_{T} are combined after the unfolding. A scheme of the full migration matrix with all sideband regions and subdivisions into p_{T} regions is displayed in Figure 7.22. In total, the matrix consists of 200 bins at the detector level and 72 bins at the particle level. Prior to the unfolding of data, the contribution from background processes is estimated from simulation and subtracted. However, uncertainties arising from the statistical precision of the simulation or the production cross section of those background processes are considered.

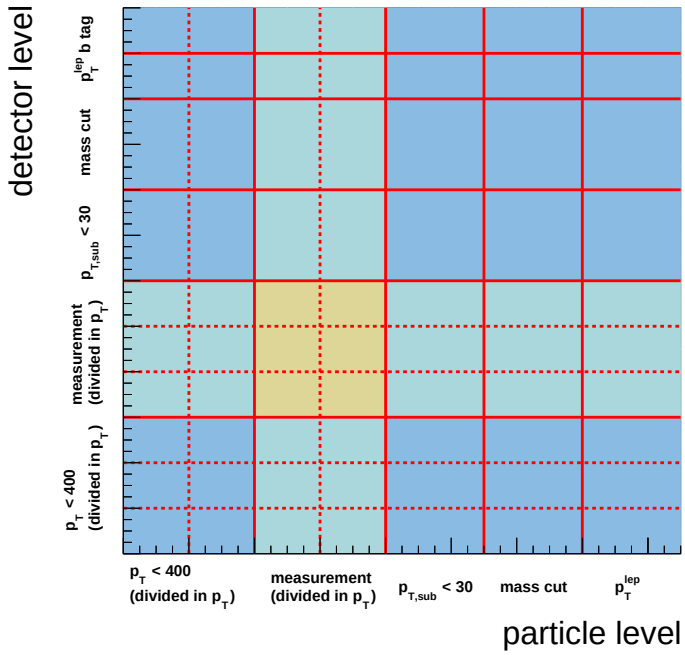

Figure 7.22: Schematic display of the response matrix used in the unfolding procedure. Solid lines divide the full phase space into several sideband regions and the measurement phase space (yellow). Dashed lines indicate separate $p_{\mathrm{T,jet}}$ regions inside the sideband region with $p_{\mathrm{T,jet}} < 400$ GeV as well as the measurement region.

7.5 Uncertainties

All uncertainties that are considered in this measurement are evaluated as their impact on the five output bins of the unfolding procedure. For each uncertainty source, one covariance matrix is created, which contains not only the contribution to each output bin but also correlations between bins. In this analysis, three types of uncertainties are considered for the measurement: statistical uncertainties, uncertainties originating from experimental calibrations and those originating from model dependencies in the unfolding procedure. If a source of uncertainty is not explicitly connected to a background process, it is estimated using the $\mathrm{t\bar{t}}$ contribution only. This is sufficient because the almost negligible background contribution is subtracted from data prior to the unfolding. Even an uncertainty of 100% on the production cross section of background processes is found to be negligible in this measurement. Which sources of uncertainties are considered and how they are estimated is detailed in the following.

7.5.1 Statistical uncertainties

Finite statistical precision does not only concern the collected data but also all simulated samples that are used in the unfolding process. However, only the statistical uncertainty related to the data is considered as statistical uncertainty. The uncertainties arising from the limited number of simulated events in the $\mathrm{t\bar{t}}$ sample used to create the migration matrix and all background processes are added to the experimental uncertainties. Nevertheless, the procedure to obtain a covariance matrix containing the uncertainties is identical for all sources. All statistical uncertainties are handled within TUnfold and simply propagated through the whole unfolding process. The statistical precision of data only contributes noticeably to the first two and last bin of the unfolded distribution while it only contributes 6–7% in the peak region. Uncertainties due to statistical precision in simulated event samples are negligible.

7.5.2 Experimental systematic uncertainties

Multiple experimental uncertainties are considered, most of which originate from corrections and calibrations of physics objects prior to the unfolding. This includes the uncertainties in efficiency correction factors of the trigger, lepton identification and b tagging as well as uncertainties connected to the jet energy scale and resolution, additional XCone-jet correction, modeling of the pile up profile, and luminosity measurement. For each source, the change in the migration matrix, corresponding to a variation of one standard deviation, is estimated in $\mathrm{t\bar{t}}$ simulation, and an alternative migration matrix A' is constructed. Here, A' can be written as a variation of A as $A' = A + \delta A$. The shift of the unfolded distribution due to δA is calculated and results in a shift Δ_i in bin i. In each bin the average shift taking into account the positive and negative variations of each uncertainty source is calculated. From the variation with largest total shift $\sum_i |\Delta_i|$ it is estimated if the correlation between bins is positive or negative. Using the shifts Δ_i and the correlations $\rho_{ij} = \pm 1$ between bins i and j, one covariance matrix is constructed for every uncertainty source. The largest impact is observed in uncertainties connected to the jet energy scale since those shift the jet mass spectrum significantly. The jet energy scale correction delivers the dominant experimental uncertainty with up to 31% in the peak region. Corrections of the jet energy resolution and the additional XCone correction contribute with 7–13% and 2–8%, respectively. Other uncertainties connected to the reweighting of the pileup profile, trigger scale factors, lepton identification scale factors, and instantaneous luminosity are also considered but found to be negligible. Uncertainties arising from the production cross sections of background processes are estimated similarly. Rate uncertainties of 19% for W+jets, 23%

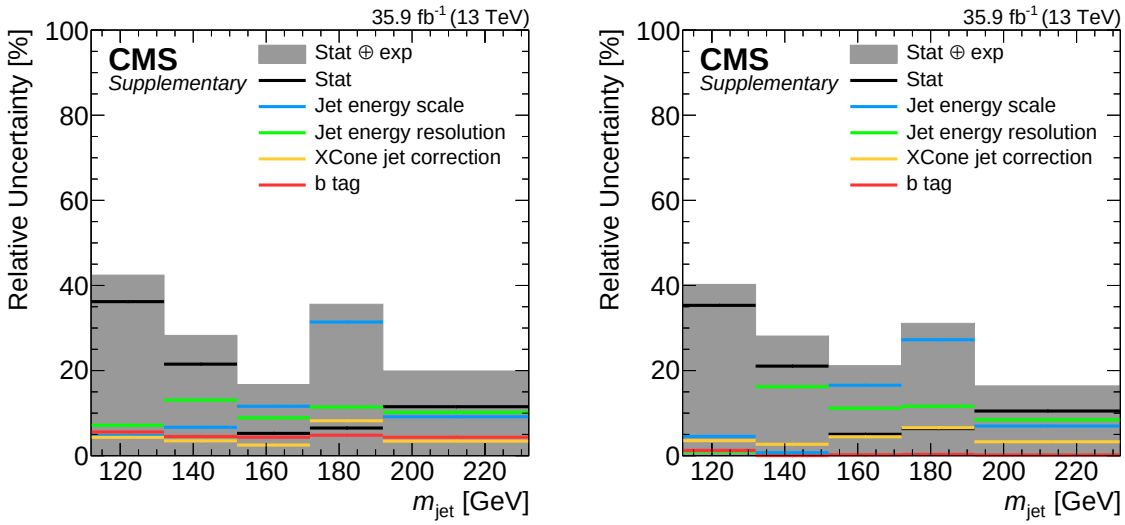

Figure 7.23: Contributions of experimental uncertainties to each bin of the unfolded distribution as relative component for the differential cross section (left) and normalized differential cross section (right). Only relevant uncertainty sources are displayed. The filled areas correspond to all experimental uncertainties and the statistical uncertainty added in quadrature. Published in the supplementary material [12] of Ref. [3].

for single top production and 100% for all other contributions are considered but are negligible after the unfolding. Figure 7.23 shows a summary of all relevant experimental uncertainties and compares them to the statistical uncertainty. The summary is provided for the differential cross section measurement (left) and the normalized differential cross section (right). For the latter, the respective covariance matrix is normalized using error propagation. Also, the total experimental uncertainty, which is calculated by adding all covariance matrices, is displayed. In the peak region, especially the uncertainty caused by the jet energy scale surpasses the statistical uncertainty, which was dominant in every bin of the previous analysis [1].

7.5.3 Modeling systematic uncertainties

Since the unfolding is performed using a sample of simulated $\mathrm{t\bar{t}}$ events with specific modeling assumptions, it has to be verified that also different models can be unfolded with the same setup. This is tested by unfolding $\mathrm{t\bar{t}}$ samples with varied modeling parameters using the nominal migration matrix and validating if the unfolded result is compatible with the true particle level distribution of the given variation. As an example, Figure 7.24 shows the unfolded result of a $\mathrm{t\bar{t}}$ sample where the factorization and renormalization scales μ_f and μ_r are multiplied with 0.5. The result is compared to its own particle level truth and the particle level truth of the nominal

sample, which defines the migration matrix. The difference Δ_i between truth and unfolded distribution in a bin i is then treated analogously as in the case of experimental uncertainties. Conversely, the correlations are taken not from the variation with the largest total shift but from the variation which introduces the largest shift of the mean of the particle-level m_{jet} distribution with respect to the nominal $\mathrm{t\bar{t}}$ sample. Because only the central values of the true particle-level distribution and of the unfolded result enter the calculation, statistical fluctuations are absorbed into the modeling uncertainties. Especially if a sample is statistically limited, this can lead to an overestimation of the model dependence. However, it is verified that this procedure leads to similar results compared to varying the migration matrix, as done for experimental uncertainties. For the uncertainty arising from the choice of the PDFs, 100 variations of the NNPDF set [105] are unfolded, each resulting in a negligible uncertainty. The uncertainty due to the factorization and renormalization scales μ_f and μ_r is estimated by changing both scales either coherently or individually by factors of 2. The scales of final- and initial-state radiation (FSR and ISR) are varied with a factor of 2 [91]. The matching between matrix element and parton shower is controlled by the parameter $h_{\text{damp}} = 1.58^{+0.66}_{-0.59}$ [91] and varied within its uncertainties. The dependence on the color reconnection (CR) model is checked by unfolding three different models which are a gluon-move scheme [106], a QCD-inspired scheme [107], and an MPI-based scheme allowing early resonance decays [108]. The underlying event tune CUETP8M2T4, which is used to generate the nominal $\mathrm{t\bar{t}}$ sample, is varied within uncertainties. Uncertainties related to the invisible fraction of semileptonic b-hadron decays were also studied but found to be negligible and are not included. Furthermore, an uncertainty originating from the choice of the top quark mass for the nominal $\mathrm{t\bar{t}}$ sample is evaluated by unfolding various m_{t} hypotheses, extrapolating the shifts $\Delta_i(m_{\text{t}})$ with a linear fit in each bin i and evaluating the uncertainty at ± 3 GeV with respect to the nominal value of 172.5 GeV. In addition, a $\mathrm{t\bar{t}}$ sample generated with MADGRAPH5_aMC@NLO is used to check the generator dependence of the measurement. The unfolded result was found to be consistent with its true particle level distribution within statistical uncertainties. Thus, no uncertainty connected to the choice of the event generator is assigned. All modeling uncertainties are summarized in Figure 7.25 for the differential cross section (left) and normalized differential cross section (right). Similarly to the experimental uncertainties, all uncertainty sources are compared to the statistical uncertainty. The dominating modeling uncertainties are connected to the modeling of the parton shower, where the largest contribution comes from the FSR with up to 18% in the peak region. All model uncertainties except the choice of m_{t} are also considered as theoretical uncertainties, which contribute to the prediction of the jet mass distribution by particle-level event generators. Here, simply the variations at the particle level determine the uncertainties.

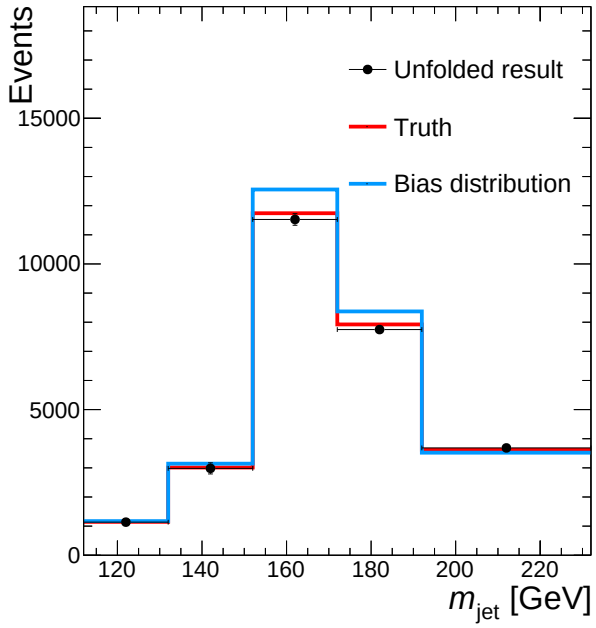

Figure 7.24: Unfolded distribution of a $t\bar{t}$ sample where the factorization and renormalization scales are coherently reduced by a factor of 2. The unfolded distribution (markers) is compared to its true particle level distribution (red) and the particle level distribution obtained with the nominal $t\bar{t}$ sample, which was used to create the migration matrix (blue). Only statistical uncertainties are considered in the unfolding procedure.

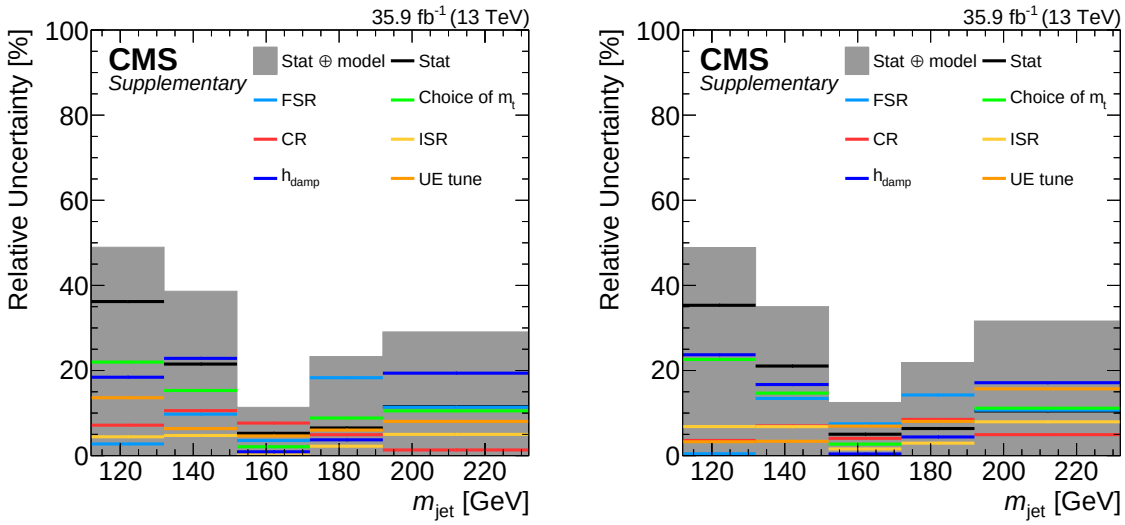

Figure 7.25: Contributions of modeling uncertainties to each bin of the unfolded distribution as relative component for the differential cross section (left) and normalized differential cross section (right). The filled areas represent all modeling uncertainties and the statistical uncertainty added in quadrature. Published in the supplementary material [12] of Ref. [3].

7.6 Differential cross section measurement

The measured differential cross section as a function of the jet mass in the lepton+jets channel is displayed in Figure 7.26 and compared to the predictions from POWHEG and MADGRAPH5_aMC@NLO. The observed fiducial $t\bar{t}$ production cross section in the range $112 < m_{\text{jet}} < 240$ GeV is

$$\sigma = 527 \pm 15\,(\text{stat}) \pm 39\,(\text{exp}) \pm 29\,(\text{model})\ \text{fb}. \tag{7.5}$$

Here, the uncertainties are estimated by calculating the sum of all entries in the respective covariance matrix. With this, the observed cross section is smaller than the cross section of 680 ± 109 fb predicted by POWHEG. This discrepancy is in agreement with previous measurements of boosted top quarks [1, 100, 101, 102, 103]. Table 7.2 shows the total covariance matrix of the measurement, which includes all statistical, experimental, and modeling uncertainties. A large anti-correlation between the two peak bins 3 and 4 is observed. The exact values of the differential cross section measurement and the contributions of all uncertainties to each bin are listed in detail in Table 7.3.

Furthermore, the differential cross section measurement is repeated independently for the electron and muon channel. The measurements are displayed in Figure 7.27 showing well-compatible results already within statistical uncertainties. The measurement of m_{jet} provides crucial input for the modeling of jet substructure in simulation and can be used as a test on analytical calculations. But not only future modeling of $t\bar{t}$ simulation can profit from this result. Also, the measurement can be used to verify analytical calculations of the jet mass in boosted top quark decays.

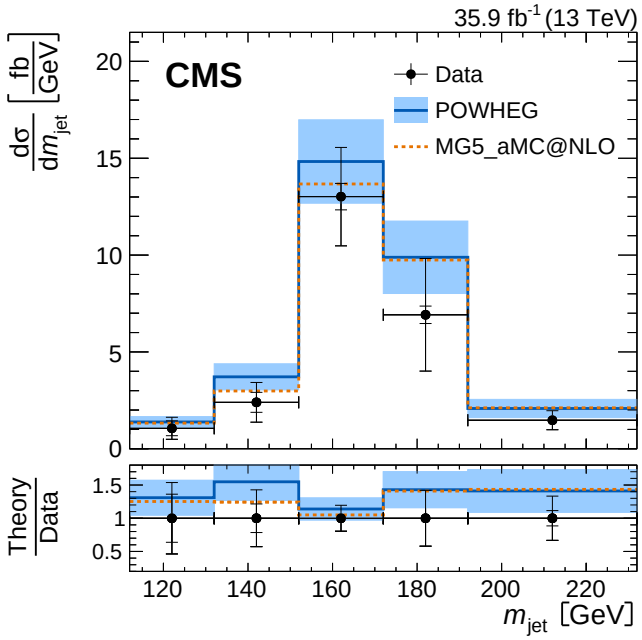

Figure 7.26: The differential cross section as a function of m_{jet} measured in data (markers) and compared to the prediction obtained with POWHEG (blue solid line) and MADGRAPH5_aMC@NLO (orange dotted line). The vertical error bars indicate the statistical (inner) and total (outer) uncertainty in the measurement, horizontal bars indicate the bin width. The blue area around the POWHEG prediction shows the theoretical uncertainty. In the lower panel, the ratio of prediction and data is displayed. Published in Ref. [3].

Table 7.2: All entries of the covariance matrix of the differential cross section measurement. Anti-correlations between neighboring bins – especially bins 3 and 4 – are observed. The presented covariance matrix contains contributions from all statistical, experimental, and modeling uncertainties. All entries are given in units of $\left[\text{fb}^2\right]$. Published in the supplementary material [12] of Ref. [3].

Bin	1	2	3	4	5
1	129.16	-86.46	55.30	-30.72	159.08
2		420.67	-125.51	282.49	-311.68
3			2582.99	-2229.32	-815.00
4				3379.63	888.49
5					385.34

Table 7.3: List of measured differential cross section as a function of the jet mass and individual uncertainties. All uncertainty contributions are listed as relative values in percent. Published in the supplementary material [12] of Ref. [3].

Range in m_{jet} [GeV]	112–132	132–152	152–172	172–192	192–232
Integrated cross section [fb]	21	48	260	138	59
Statistical uncertainty [%]	36.2	21.5	5.2	6.5	11.5
Experimental uncertainty [%]	22.1	18.4	15.9	35.0	16.2
Jet energy scale	4.7	6.7	11.6	31.4	9.1
Jet energy resolution	7.2	13.1	8.9	11.4	10.2
XCone jet correction	4.3	3.5	2.5	8.2	3.4
b tag	5.6	4.5	4.3	4.8	4.3
MC stat.	18.5	8.8	1.9	2.4	5.6
Luminosity	2.5	2.5	2.5	2.5	2.5
Background	3.8	1.1	< 1	< 1	2.2
Pileup	1.1	1.2	< 1	< 1	< 1
MuID	1.1	< 1	< 1	1.1	< 1
MuTrigger	< 1	< 1	< 1	1.0	< 1
ElID	< 1	< 1	< 1	< 1	< 1
ElTrigger	< 1	< 1	< 1	< 1	< 1
ElReco	< 1	< 1	< 1	< 1	< 1
Model uncertainty [%]	33.0	32.1	10.1	22.4	26.7
FSR	2.8	9.8	3.6	18.3	11.4
Choice of m_t	22.0	15.3	2.1	8.8	10.5
CR	7.2	10.6	7.7	4.9	1.3
UE tune	13.6	6.3	4.6	6.0	8.1
ISR	4.4	4.7	< 1	2.2	5.0
h_{damp}	18.4	22.9	< 1	3.7	19.4
Scale	1.1	1.7	1.7	2.7	2.2
PDF	< 1	< 1	< 1	< 1	< 1
Total Uncertainty [%]	53.8	42.8	19.5	42.0	33.3

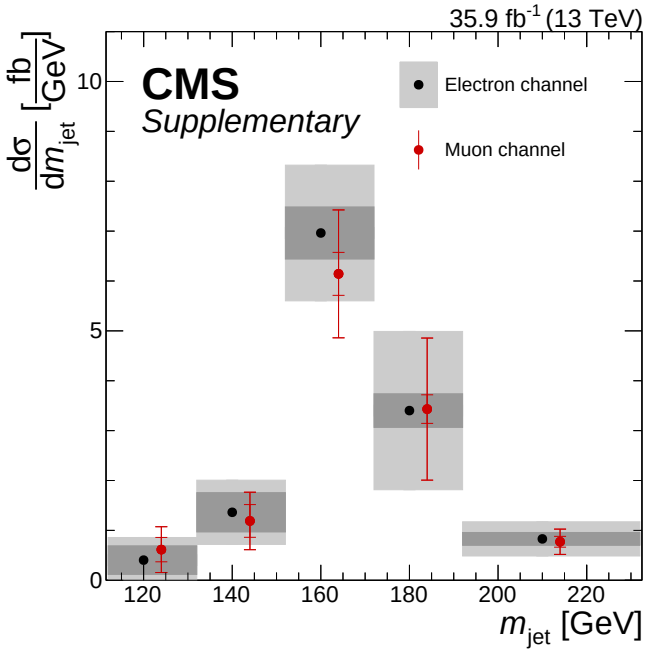

Figure 7.27: The differential cross section as a function of m_{jet} measured independently in the e+jets (area with black markers) and μ+jets channel (red markers). Statistical uncertainties are displayed by the inner areas and inner vertical bars, respectively. The outer areas and vertical bars indicate the total uncertainty in both measurements. Published in the supplementary material [12] of Ref. [3].

7.7 Extraction of the top quark mass

The normalized differential cross section is displayed in Figure 7.28 and is compared to multiple m_t hypotheses obtained with POWHEG. All distributions are normalized to their observed fiducial cross section in the range $112 < m_{jet} < 240$ GeV. Especially in the peak region, the data are sensitive to the value of m_t and can be used to extract the top quark mass. The normalized distribution is chosen for the mass extraction in order to evaluate the compatibility of the measurement to hypotheses of m_t based on shape information without taking the total cross section into account. Since analytical calculations are not available for the selected phase space yet, the top quark mass is extracted using predictions from particle-level event generators. This of course does not solve the ambiguities in the definition of m_t but acts as an alternative measurement to those at $t\bar{t}$ threshold production with very different systematic uncertainties. Furthermore, the expected sensitivity of the m_t extraction is studied and can be compared to a previous measurement [1].

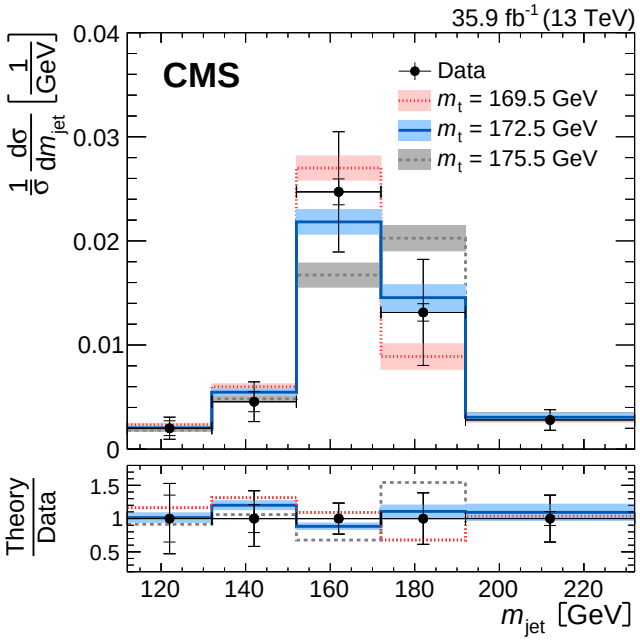

Figure 7.28: The normalized differential cross section as a function of m_{jet} measured in data (markers) and compared to the prediction obtained with POWHEG for three hypothesis of m_t (lines). The vertical error bars indicate the statistical (inner) and total (outer) uncertainty in the measurement, horizontal bars indicate the bin width. The areas around the predictions show the theoretical uncertainty. In the lower panel, the ratio of prediction and data is displayed. Published in Ref. [3].

The top quark mass is extracted via a χ^2 method, where the χ^2 is defined as

$$\chi^2 = d^T V^{-1} d \tag{7.6}$$

with the differences d between the normalized cross section measurement and the predicted m_t hypothesis. The normalized covariance matrix V includes all statistical, experimental, modeling, and theoretical uncertainties. The uncertainties of the measured data are listed in detail in Table 7.4. The normalized covariance matrix is displayed in Table 7.5 and shows large anti-correlations between bins 3 and 4 as already observed in the cross section measurement. In addition to the predictions for top quark masses with values of 169.5 GeV, 171.5 GeV, 172.5 GeV, 173.5 GeV, and 175.5 GeV the content of each output bin is interpolated in order to obtain an even finer grid of χ^2 values for top mass hypotheses in steps of 0.5 GeV. For every value of m_t, a χ^2 is evaluated, indicating the compatibility of the individual prediction with the measurement in data. Figure 7.29 shows the obtained values of χ^2 and the fit with a second order polynomial function. The position of the minimum of the fit represents the extracted m_t value while the values where χ^2 increased by 1 indicate the uncertainty corresponding to one standard deviation. It is verified that a higher order polynomial produces the same result. Furthermore, removing the interpolated m_t points does not change the result. Also, the influences of different types of uncertainties is studied. The statistical component is obtained by repeating the fit where the covariance matrix V only contains statistical uncertainties. The individual influences of experimental, modeling, and theoretical uncertainties are studied by removing the according components and comparing to the total uncertainty. The overall method to measure m_t is verified in simulation, where POWHEG samples with different values of m_t are unfolded. The resulting distributions are used to determine values of m_t, which are compared to the true values used in the simulation. The results are displayed in Figure 7.30, where only statistical uncertainties and the uncertainty due to the choice of m_t are considered. Within uncertainties, all extracted values of m_t are in very good agreement with the respective true value. This does not only demonstrate a stable extraction but also verifies the reasonable size of the uncertainty connected to the choice of m_t.

In data, the top quark mass is measured to be

$$m_t = 172.6 \pm 0.4\,(\text{stat}) \pm 1.6\,(\text{exp}) \pm 1.5\,(\text{model}) \pm 1.0\,(\text{theo})\ \text{GeV} \tag{7.7}$$

$$m_t = 172.6 \pm 2.5\ \text{GeV}. \tag{7.8}$$

The detailed contribution of every uncertainty source is displayed in Table 7.6. Again, dominating uncertainties are connected to the parton shower modeling – especially FSR – and the jet

Table 7.4: Full list of the normalized differential cross section measurement as a function of the jet mass and individual uncertainties. All uncertainty contributions are listed as relative values in percent. Published in the supplementary material [12] of Ref. [3].

Range in m_{jet} [GeV]	112–132	132–152	152–172	172–192	192–232
Integrated normalized cross section	0.04	0.09	0.49	0.26	0.11
Statistical uncertainty [%]	35.3	21.1	5.0	6.4	10.5
Experimental uncertainty [%]	19.3	18.6	20.6	30.4	12.6
Jet energy scale	4.5	< 1	16.6	27.2	7.0
Jet energy resolution	< 1	16.2	11.1	11.6	8.4
XCone jet correction	3.5	2.7	4.5	6.6	3.3
b tag	1.2	< 1	< 1	< 1	< 1
MC stat.	18.0	8.6	1.9	2.4	5.0
Luminosity	< 1	< 1	< 1	< 1	< 1
Background	3.2	< 1	< 1	< 1	1.4
Pileup	1.3	1.6	< 1	< 1	1.1
MuID	< 1	< 1	< 1	< 1	< 1
MuTrigger	< 1	< 1	< 1	< 1	< 1
ElID	< 1	< 1	< 1	< 1	< 1
ElTrigger	< 1	< 1	< 1	< 1	< 1
ElReco	< 1	< 1	< 1	< 1	< 1
Model uncertainty [%]	33.8	28.0	11.4	20.9	29.8
FSR	< 1	13.4	7.5	14.2	10.7
Choice of m_t	22.6	14.7	2.7	8.2	11.1
CR	3.6	7.0	4.1	8.5	4.9
UE tune	3.3	3.4	6.9	8.0	15.7
ISR	6.8	6.8	1.6	2.9	7.9
h_{damp}	23.7	16.7	< 1	4.4	17.1
Scale	< 1	< 1	< 1	1.6	4.9
PDF	< 1	< 1	< 1	< 1	< 1
Total Uncertainty [%]	52.9	41.9	23.4	38.8	35.3

energy scale.

The measured value of m_{t} is in agreement with the direct measurements of m_{t} performed at very different energy scales. Furthermore, the sensitivity of 2.5 GeV corresponds to a factor of 3.6 improved precision compared to the result obtained at a center-of-mass energy of 8 TeV [1]. This is achieved by the novel jet reconstruction technique using XCone, which drastically improves the jet resolution on both detector and particle level. Also, the larger data set allows for a more granular migration matrix, which mitigates the model dependence of this measurement. With this result, the determination of a fundamental parameter of the SM is demonstrated in the boosted regime, with a relative precision better than 1.5%.

Table 7.5: All entries of the covariance matrix of the normalized differential cross section measurement. Anti-correlations between neighboring bins – especially bins 3 and 4 – are observed. The presented covariance matrix contains contributions from all statistical, experimental, and modeling uncertainties. All entries are given in units of 10^{-4}. Published in the supplementary material [12] of Ref. [3].

Bin	1	2	3	4	5
1	4.51	-3.49	1.54	-4.82	4.51
2		14.58	-6.02	2.03	-14.19
3			133.49	-109.63	-38.77
4				103.82	17.21
5					15.62

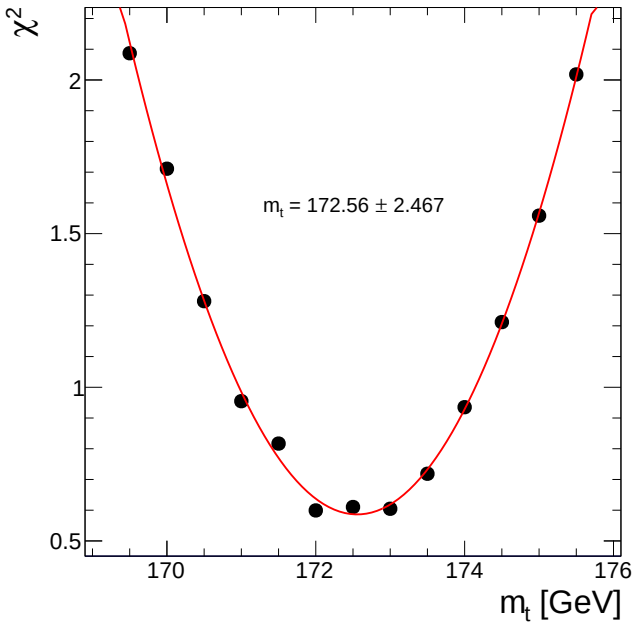

Figure 7.29: A second order polynomial function (red line) fit to the χ^2 values of various hypotheses of the top quark mass obtained with POWHEG (markers). All points other than the values 169.5 GeV, 171.5 GeV, 172.5 GeV, 173.5 GeV, and 175.5 GeV for m_t are obtained by interpolation. The minimum of the fit indicates the measured m_t, the uncertainties corresponding to one standard deviation are evaluated at the points where χ^2 increased by 1.

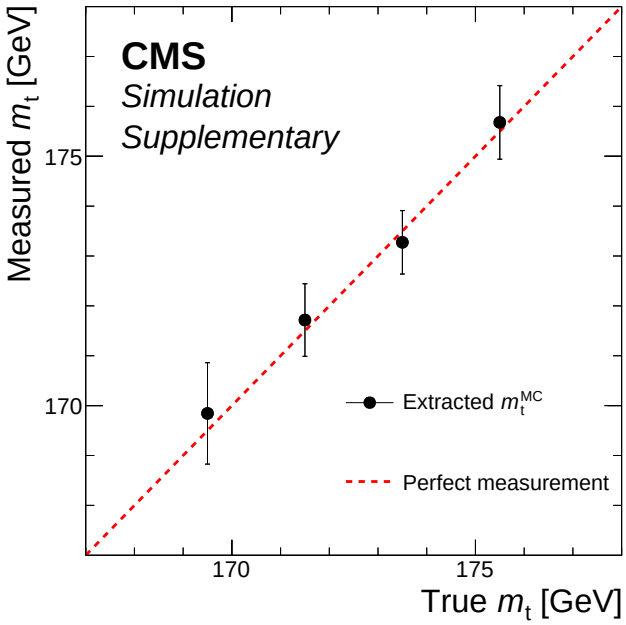

Figure 7.30: The top quark mass is extracted from different POWHEG hypotheses and compared to its true value (markers). The dashed line represents a perfect agreement. Only statistical precision and the uncertainty due to the choice of m_t are considered. Published in the supplementary material [12] of Ref. [3].

Table 7.6: Uncertainties in the top quark mass extraction split by each source considered. Despite the statistical uncertainty, all contributions are estimated by performing the extraction excluding the given source. The statistical uncertainty is determined by extracting the mass only including the statistical uncertainty. Published in the supplementary material [12] of Ref. [3].

Source	Uncertainty [GeV]
Total uncertainty	2.47
Statistical uncertainty	0.41
Experimental uncertainty	1.58
Jet energy scale	1.47
Jet energy resolution	0.45
XCone jet correction	0.45
MC stat.	0.15
Pileup	0.05
b tag	0.02
Background	0.02
MuTrigger	0.01
MuID	< 0.01
ElTrigger	< 0.01
ElID	< 0.01
ElReco	< 0.01
Luminosity	< 0.01
Model uncertainty	1.55
FSR	1.17
CR	0.66
UE tune	0.51
Choice of m_{t}	0.48
Scale	0.15
ISR	0.10
PDF	0.01
h_{damp}	< 0.01
Theoretical uncertainty	1.02
CR	0.74
FSR	0.51
Scale	0.42
ISR	0.14
UE tune	0.12
h_{damp}	0.08

7.8 Towards higher precision

This measurement has made a large step towards the precision obtained in direct measurements of the top quark mass. However, some aspects of the measurement can be improved to further increase the sensitivity to m_{t}. At first, a larger data set became available with the data taking periods of 2017 and 2018, which increases the event yield by a factor of four. Despite harsher pileup conditions in the years 2017 and 2018, the vast amount of data allows for higher statistical precision in the measurement. With more data, also more simulated samples are available and improve the statistical precision of the migration matrix, which enables an unfolding setup with smaller bin sizes, more sideband regions and differential in other observables such as jet p_{T}. While a more granular unfolding setup already helps in the understanding of systematic uncertainties, dedicated measurements can use data to constrain those and increase the precision in the extraction of m_{t}. In the following, studies that can constrain the dominant model and experimental uncertainties – FSR and jet energy scale – are presented. The studies were made in the scope of two Master's theses [7, 6] that have been supervised by the author of this work and in collaboration with another PhD project [8].

7.8.1 Constraining the final state radiation modeling

The dominant modeling uncertainty in the measurement is connected to the parton shower parameter, which steers the final state radiation in the simulation. A dedicated measurement of jet substructure observables can provide constraints on the size of this uncertainty. Especially distributions related to the localized energy density in jets, such as the N-subjettiness ratio τ_{32}, are sensitive to the amount of final state radiation, which smears the expected three-prong decay towards a four-prong decay. In Ref. [7] a measurement of the differential $\mathrm{t\bar{t}}$ production cross section as a function of τ_{32} in decays of boosted top quarks is performed at 13 TeV, using anti-k_{T} jets with a radius parameter of $R = 0.8$. Similar to the analysis presented in this chapter, jets are selected such that they contain the top quark decay into hadrons and are required to have $p_{\mathrm{T}} > 400$ GeV. The result of the measurement of τ_{32} is shown in Figure 7.31. Especially at low values of τ_{32}, high sensitivity to the exact value of the FSR parameter is observed, which can be used as a constraint on this very uncertainty.

A similar measurement of τ_{32} using the XCone two-step jet clustering procedure as presented above has been performed in Ref. [6], where the τ_{32} distribution is studied at the detector level. A phase space similar to that of the measurement of the jet mass is selected. Figure 7.32

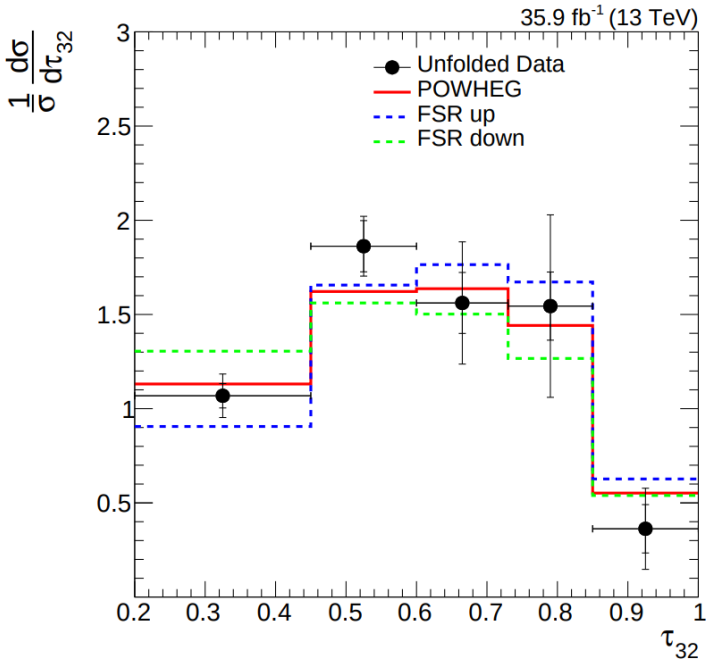

Figure 7.31: Normalized differential $\mathrm{t\bar{t}}$ production cross section as a function of τ_{32}. Jets clustered with the anti-k_T algorithm and a radius parameter of $R = 0.8$ are selected and required to have $p_\mathrm{T} > 400$ GeV. Data (markers) are compared to the prediction obtained with POWHEG for the nominal final state radiation parameter (red line) and the variations of the FSR scale by a factor of 2 (blue and green line). The horizontal error bars indicate the bin widths and vertical lines the statistical (inner) and total (outer) uncertainties. Taken from Ref. [7].

shows the normalized τ_{32} distribution of the anti-k_T jet with $R = 0.8$ closest in ΔR to the corresponding XCone jet at the detector level. In this study, the N-subjettiness is not available for XCone jets, but since both jet algorithms cluster the same set of particles, those jets are expected to be similar. Data are compared to $\mathrm{t\bar{t}}$ events simulated with POWHEG for different scenarios of the FSR parameter in the parton shower modeling. Contributions from background processes are estimated from simulation and subtracted from data. Due to different underlying event tunes in 2016 with respect to the data taking periods of 2017 and 2018, the study was performed individually for 2016 (left) and the combination of 2017 and 2018 (right). The data are compared to the variations of the FSR parameter by a factor of 2 for 2016 and factors of $\sqrt{2}$, 2, and 4 in the combination of 2017 and 2018. In order to obtain predictions for intermediate values of the FSR parameter, the bin contents are parameterized as a function of a multiplicative factor f^FSR using a logarithmic fit, reflecting the fact that the cross section depends on higher orders of the FSR parameter. Similar to the extraction of the top quark mass (Section 7.7), a χ^2 test results in a best fit value of the multiplicative factor f^FSR of the FSR parameter in POWHEG.

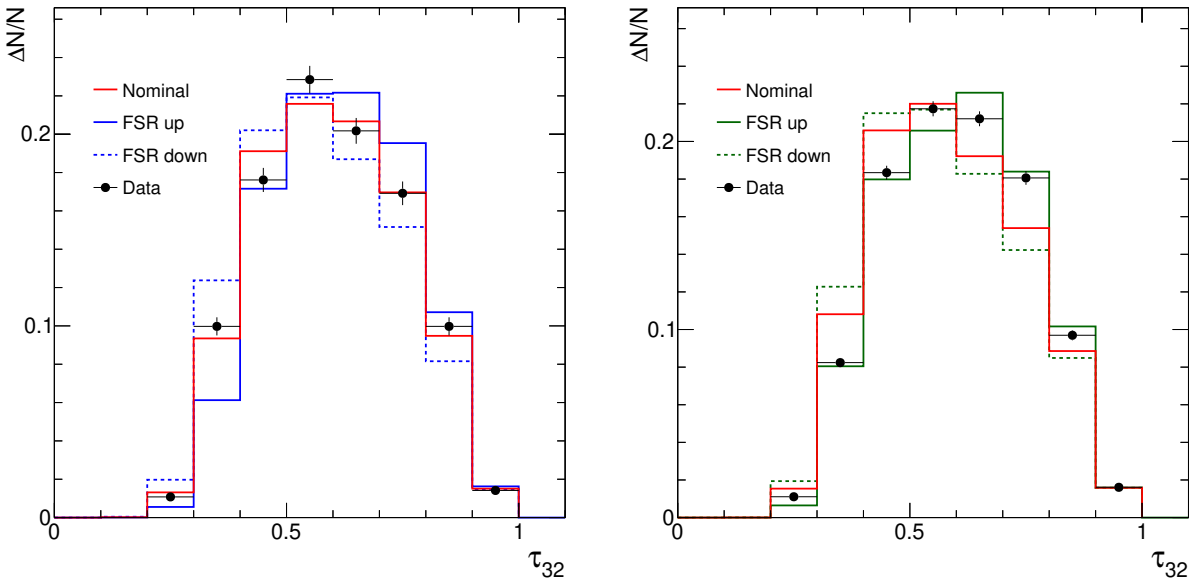

Figure 7.32: Normalized distribution of τ_{32} comparing background subtracted data (markers) to the nominal $\mathrm{t\bar{t}}$ sample and variations of the final state radiation parameter. It is individually shown for the 2016 data taking period (left) and combination of 2017 and 2018 (right), where the FSR parameter is varied by factors of 2 and 4, respectively. Taken from Ref. [6].

Taking only statistical uncertainties into account, best fit values were found at

$$f^{\mathrm{FSR}}_{2016} = 1.0 \pm 0.1 \quad \text{and} \tag{7.9}$$

$$f^{\mathrm{FSR}}_{2017,2018} = 5.7 \pm 0.7, \tag{7.10}$$

respectively. These resulting values of f^{FSR} hint at a better description of data using the parton shower model that was used in 2016, where f^{FSR}_{2016} is compatible with unity. With the new tune that was used in 2017 and 2018, the factor $f^{\mathrm{FSR}}_{2017,2018}$ shows a deviation from the nominal value of the FSR parameter. Similar to the estimation of the uncertainty in the choice of m_{t}, the unfolded result in every m_{jet} bin is parameterized as a function of the factor f^{FSR} using a logarithmic fit. Thus, the uncertainty in FSR in each bin is evaluated as the difference between the unfolded result at f^{FSR} and its variations. In a comparison of the m_{t} extractions with 2016 data, the uncertainty in the modeling of FSR can be reduced from $\Delta m_{\mathrm{t}} = 1.2$ GeV to 0.2 GeV.

7.8.2 Constraining the jet energy scale

The dominating experimental uncertainty is connected to the jet energy scale. The corresponding corrections are applied as multiplicative factors to the jet four-momenta. This directly impacts the jet mass, even though the correction factors are determined as a function of jet p_{T}. This can lead to large uncertainties since the jet mass depends on the angular distribution of individual particles inside a jet and not only its total energy. In Ref. [6] a dedicated calibration of m_{jet} is studied by taking the jet energy scale and additional XCone jet corrections into account. In order to calibrate m_{jet} independently from the measurement of the top quark mass, only the two XCone subjets containing the W decay are selected, and the corresponding jet mass $m_{\mathrm{jet}}^{\mathrm{W}}$ is studied.

The $m_{\mathrm{jet}}^{\mathrm{W}}$ distribution is measured in four independent regions, split by momentum $p_{\mathrm{T}}^{\mathrm{W}}$ of the reconstructed W boson and the momentum fraction of the p_{T} leading subjet $p_{\mathrm{T}}^{\text{leading subjet}}/p_{\mathrm{T}}^{\mathrm{W}}$. Since the anti-$k_{\mathrm{T}}$ jet corrections and additional XCone corrections have a similar effect on the jet mass, both corrections are studied simultaneously. In each bin of the four $m_{\mathrm{jet}}^{\mathrm{W}}$ distributions, a fit is performed that describes the bin content as a function of both corrections. A two-dimensional χ^2 distribution is calculated, which tests the compatibility with the observed data and results in best fit values of multiplicative factors f^{JEC} and f^{XCone}. The factors are constructed such that values of 0 and ± 1 correspond to the nominal corrections and variations by one standard deviation. The factors c^{JEC} and c^{XCone} that are applied to the jet momentum then read

$$c^{\mathrm{JEC}} = c_{\mathrm{nominal}}^{\mathrm{JEC}} + f^{\mathrm{JEC}} |c_{\mathrm{up}}^{\mathrm{JEC}} - c_{\mathrm{nominal}}^{\mathrm{JEC}}| \quad \text{and} \tag{7.11}$$

$$c^{\mathrm{XCone}} = c_{\mathrm{nominal}}^{\mathrm{XCone}} + f^{\mathrm{XCone}} |c_{\mathrm{up}}^{\mathrm{XCone}} - c_{\mathrm{nominal}}^{\mathrm{XCone}}|, \tag{7.12}$$

where $c_{\mathrm{nominal}}^{\mathrm{JEC}}$ and $c_{\mathrm{nominal}}^{\mathrm{XCone}}$ as well as $c_{\mathrm{up}}^{\mathrm{JEC}}$ and $c_{\mathrm{up}}^{\mathrm{XCone}}$ are the correction factors that correspond to the original corrections and positive variations of one standard deviation. The corrected jet mass $m_{\mathrm{jet}}^{\mathrm{corrected}}$ is calculated from the uncorrected jet mass $m_{\mathrm{jet}}^{\mathrm{raw}}$ via

$$m_{\mathrm{jet}}^{\mathrm{corrected}} = c^{\mathrm{JEC}} c^{\mathrm{XCone}} m_{\mathrm{jet}}^{\mathrm{raw}}. \tag{7.13}$$

Figure 7.33 (left) shows the normalized $m_{\mathrm{jet}}^{\mathrm{W}}$ distribution for data, the nominal, and varied jet energy correction factors in the region of high $p_{\mathrm{T}}^{\mathrm{W}}$ and small $p_{\mathrm{T}}^{\text{leading subjet}}/p_{\mathrm{T}}^{\mathrm{W}}$. The resulting ellipse representing the region of 68% confidence level is presented in Figure 7.33 (right). In the unfolding, the best fit value and four extreme points of the ellipse of the jet calibration are considered in the calculation of m_{jet}. The original jet corrections are adjusted to only change

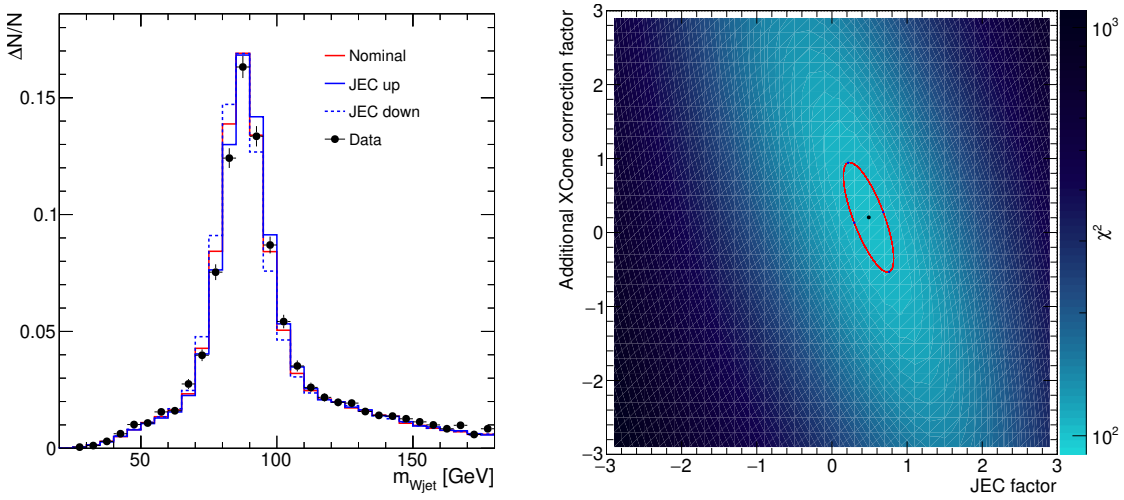

Figure 7.33: Normalized jet mass distribution of the two subjets reconstructing the W boson (left) and χ^2 distribution as a function of the jet energy correction factor and additional XCone correction (right). On the left, data (markers) are compared to simulated $\mathrm{t\bar{t}}$ events for different variations of the jet energy scale (lines). The region of in the region of high $p_{\mathrm{T}}^{\mathrm{W}}$ and small $p_{\mathrm{T}}^{\text{leading subjet}}/p_{\mathrm{T}}^{\mathrm{W}}$ is selected for display. On the right, the ellipse indicates the resulting region of 68% confidence level. The four extreme points of the ellipse represent the considered variations that are used to estimate the uncertainty in the jet mass scale. Taken from Ref. [6].

the momentum of the jet while leaving its mass unchanged. With this, the uncertainty in the jet energy scale can be studied independently from the jet mass scale. In a preliminary comparison of the m_{t} extractions with 2016 data, the uncertainty due to the jet energy scale can be reduced from $\Delta m_{\mathrm{t}} = 1.5$ GeV to 0.4 GeV. The additional jet mass scale contributes with 0.4 GeV, and the combination of jet energy scale and jet mass scale uncertainty amounts to 0.6 GeV.

A step towards an even more precise calibration of the jet mass would be a full calibration of particle flow candidates, based on a fit to the W boson mass. Pioneering studies in this direction have been done using data recorded in 2017, where the jet mass distributions in hadronic decays of high-momentum top quarks and W bosons were investigated. A first step towards a calibration is the categorization of jet constituents into groups of charged hadrons, neutral hadrons, photons and everything else. The fractional energy of every category is displayed in Figure 7.34 as a function of the PF candidate's η. The momenta of PF candidates of different categories are individually varied by 1%. For each of these variations, a nuisance parameter is constructed, and the simulation is fit to the data using the combine tool [109], which was developed for the combination of ATLAS and CMS searches for the Higgs boson.

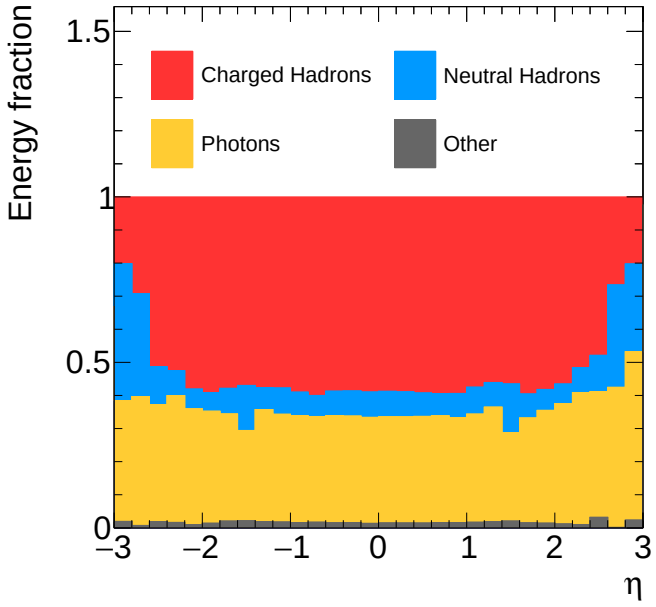

Figure 7.34: Energy fraction of individual PF categories as a function of the candidate's η. The energy in an event is split into contributions from charged hadrons, neutral hadrons, photons, and other particles and displayed individually as fractions.

In addition, three regions are constructed, aiming at a fully merged W boson decay, a merged top quark decay, and not merged contributions. Also, the $\mathrm{t\bar{t}}$ simulation is split into its contributions where a AK8 jet contains all top quark decay partons (fully merged), only the W boson decay (merged W), the b quark and one of the W boson decay partons (merged QB), or at most one decay parton (not merged). All regions are fit simultaneously and result in a best fit value for the energy scales of every category of jet constituents. By including both a top quark and W boson enriched region, differences in the jet mass modeling of both decays – for example opposite jet mass shifts in simulation – can be resolved. In a first study, the merged top region is defined as all events passing $\tau_{32} < 0.5$ while merged W events must satisfy $\tau_{32} > 0.5$ and $\tau_{21} < 45$. In addition, the regions are split into bins of jet p_{T}. Furthermore, the fit can adjust the normalization of all backgrounds and $\mathrm{t\bar{t}}$ contributions individually. Figure 7.35 shows all regions for jets with $400 < p_{\mathrm{T}} < 500$ GeV before (left) and after (right) a fit to pseudo data obtained from simulation, where the momenta of all charged hadrons is increased. The fit is able to find the correct nuisance parameter and adjust the simulation accordingly, which results in an almost perfect agreement with the pseudo data. This test has been performed with all nuisance parameters for each PF category, and it is verified that the correct nuisance parameter is identified and correctly adjusted by the fit. Similarly, the simulated samples are

fit to data. Figure 7.36 presents all regions before (left) and after (right) a fit to data for jets with $400 < p_{\mathrm{T}} < 500$ GeV. This study can be extended to include even more signatures such as the hadronic Z boson decay. With the precisely measured masses of the W and Z bosons, the jet mass can be calibrated by adjusting the energy scales of all PF candidates. Also, this measurement could be extended to observables such as the energy density in the neighborhood of particles, which further influence the PF reconstruction and its calibration. Especially for a measurement that relies on the resolution and modeling of the jet mass, this calibration would lead to significant improvements by decreasing the uncertainty in the jet mass scale.

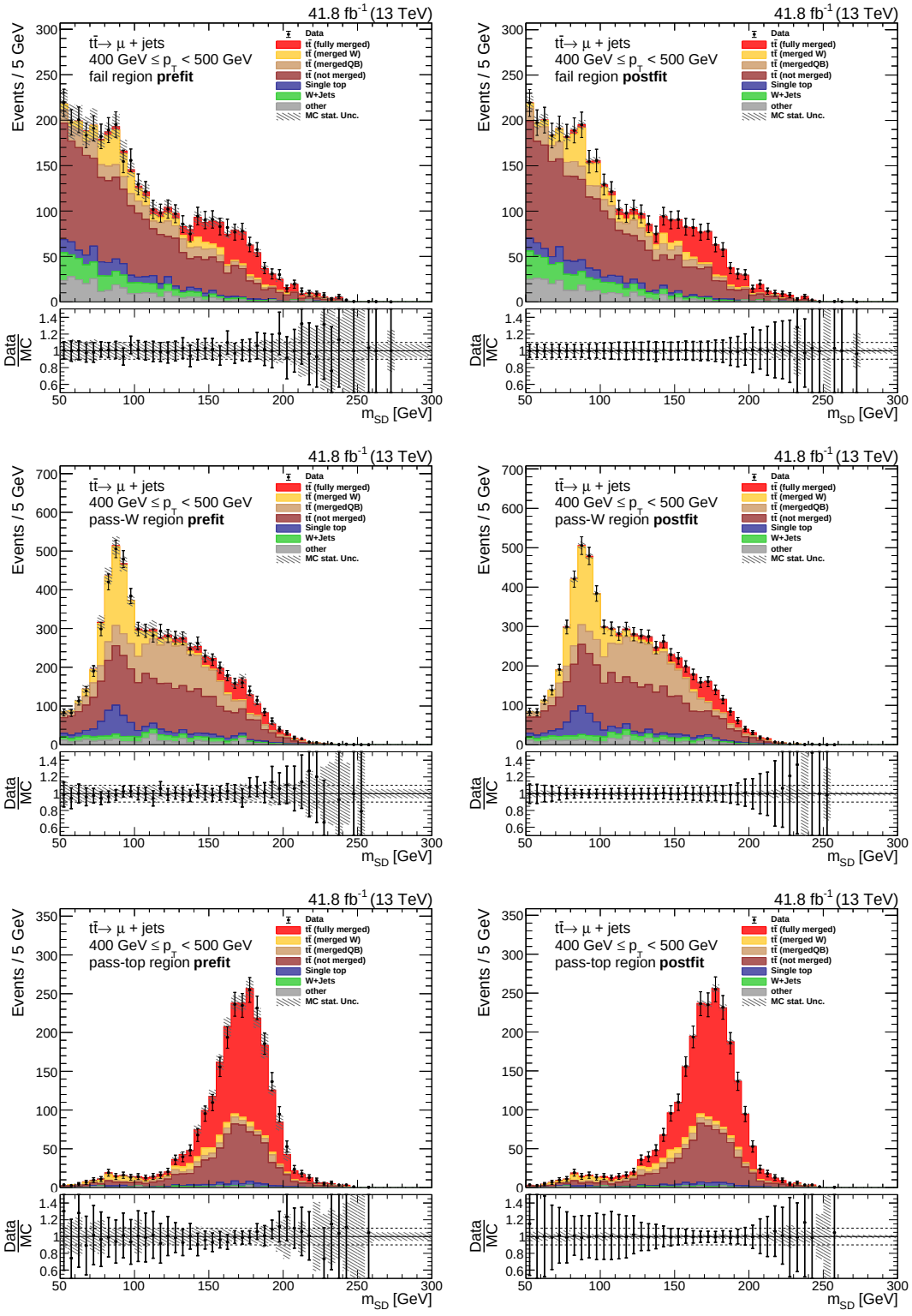

Figure 7.35: Comparison of pseudo data (marker) with simulation (filled areas) in the fail (upper), merged W (middle), and merged top (lower) regions before (left) and after (right) the fit for jets with $400 < p_{\mathrm{T}} < 500$ GeV. The pseudo data correspond to the simulation with increased momenta for all charged hadrons. In the bottom panels, the ratio of pseudo data and simulation is displayed. Uncertainties are indicated by the hashed areas and contain statistical uncertainties as well as the uncertainties due to changes in the PF candidate momenta. Taken from Ref. [8].

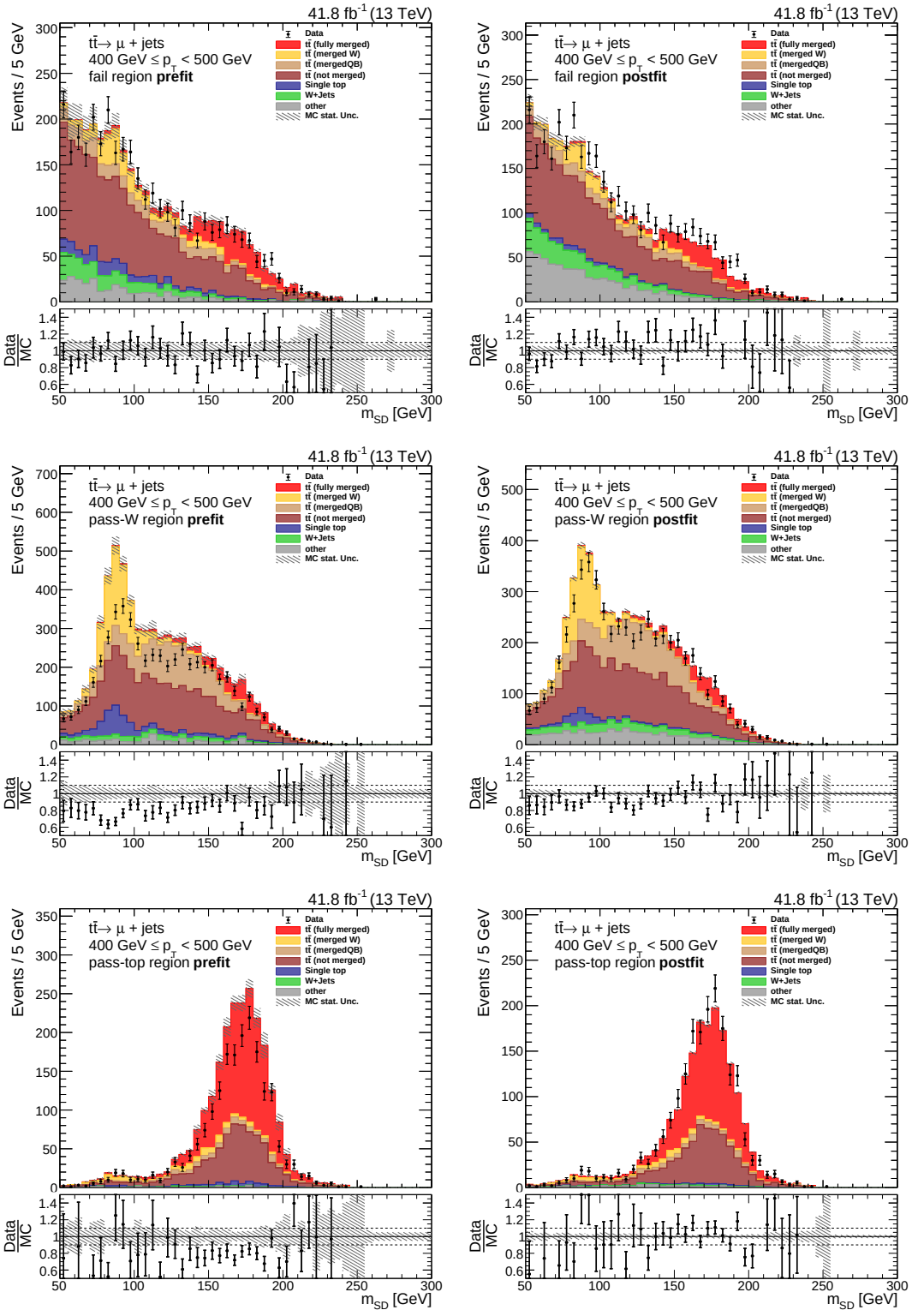

Figure 7.36: Comparison of data (marker) with simulation (filled areas) in the fail (upper), merged W (middle), and merged top (lower) regions before (left) and after (right) the fit for jets with $400 < p_{\mathrm{T}} < 500$ GeV. In the bottom panels, the ratio of data and simulation is displayed. Uncertainties are indicated by the hashed areas and contain statistical uncertainties as well as the uncertainties due to changes in the PF candidate momenta. Taken from Ref. [8].

8 | Measurement of top tagging efficiencies

For many measurements and searches for new physics top quarks with high transverse momenta are crucial. At high Lorentz-boosts, the products of a hadronic top quark decay merge into a single large-radius jet. In order to identify those jets that originate from top quark decays, tagging algorithms that make use of jet substructure information are developed. Because of non-perturbative effects in the modeling of parton showers, the jet substructure observables used in those algorithms often introduce differences between data and simulation. Thus, analyses using top tagging algorithms rely on corrections that are applied to simulation in order to match the tagging efficiency observed in data. The analysis presented here aims at a measurement of those top tagging efficiencies in data as well as simulation and results in correction factors for simulation. The measurement is performed separately for all three data taking periods of LHC's Run 2 corresponding to integrated luminosities of 35.9 fb^{-1}, 41.5 fb^{-1}, and 59.7 fb^{-1} recorded with the CMS detector in the years 2016, 2017, and 2018, respectively. Sections 8.1 and 8.2 introduce the analysis strategy and the top tagging algorithms that are studied in this thesis. Section 8.3 describes the event selection. Systematic uncertainties are discussed in Section 8.4. The substructure observables which are used in the top tagging algorithms studied in this thesis, are detailed and their modeling in simulated events is validated with data in Section 8.5. The tagging efficiencies are measured using a template fit method, which is detailed in Section 8.6. The results and final correction factors for simulation are presented in Section 8.7.

8.1 Analysis strategy

In this analysis, the top tagging efficiencies are measured in simulation and data. The efficiencies are measured using a tag-and-probe method, where a high-p_{T} muon and a b-tagged jet in the same hemisphere act as tags of a $\text{t}\bar{\text{t}}$ event in the μ+jets channel. In all tagged events, the p_{T}-leading large-radius jet in the opposite hemisphere is defined as the probe (see Figure 8.1). Top tagging algorithms are applied to this jet, where the tagging efficiency is defined as the fraction of jets passing all tagging criteria. The efficiencies in data are extracted using template

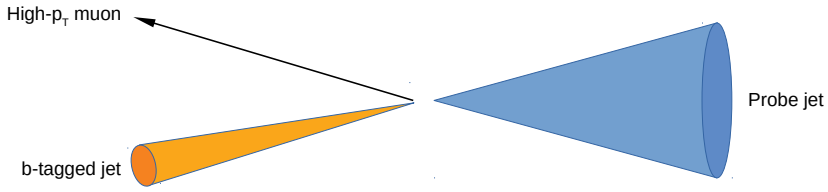

Figure 8.1: Sketch of a $t\bar{t}$ event in the μ+jets channel. The event is tagged with a high-p_T muon and a b-tagged jet in the same hemisphere. A large-radius jet in the opposite hemisphere acts as probe. The neutrino leaves the detector undetected and is not shown.

fits. Correction factors are derived, which can be applied to simulation in order to match the top tagging efficiency in data.

8.2 Identification of top jets

In this thesis, top tagging methods are studied for jets clustered with the anti-k_T [13] algorithm using $R = 0.8$ (AK8) and jets clustered with the HOTVR algorithm [14]. As an input, both jet collections use the list of PF particle candidates after applying the PUPPI algorithm [83, 84]. Both tagging algorithms are a sequence of selection steps based on jet substructure observables. If a jet fulfills all of those, it is considered top-tagged.

For AK8 jets, there are two main criteria. A jet has to have a soft drop [57] mass close to the top quark mass within the range $105 < m_{SD} < 210$ GeV and an N-subjettiness ratio $\tau_{32} < \tau_{cut}$. The latter criterion targets three-prong decays and defines five working points for different values of τ_{cut} (see Table 8.1), corresponding to different top tagging efficiencies. In addition, subjet b tagging can be used for the top jet identification. Here, the DeepCSV algorithm [80, 81] is applied to the subjets obtained from the soft drop algorithm. Any differences in b tagging efficiencies between data and simulation are absorbed into the corresponding top tagging correction factor. The algorithm using AK8 jets is also referred to as CMSTopTagger v2 PUPPI.

Table 8.1: The five working points of the AK8 top tagger are defined as the criterion $\tau_{32} < \tau_{\text{cut}}$ with different values of τ_{cut}. The efficiency of the top tagging increases with increasing τ_{cut}.

Working point	τ_{cut}
1	0.40
2	0.46
3	0.54
4	0.65
5	0.80

In addition, top tagging is performed using jets clustered with the HOTVR algorithm. Compared to the CMSTopTagger v2 PUPPI, more substructure-related criteria have to be fulfilled for a jet to be considered top-tagged. At first, the jet mass has to be inside a range $140 < m_{\text{jet}} < 220\,\text{GeV}$ and $\tau_{32} < 0.56$ is required. In addition, the HOTVR jet has to consist of a minimum of three subjets, where the p_{T}-leading subjet carries a fraction $f < 0.8$ of the transverse momentum of the large-radius jet. This aims at the expected three-prong structure of top quark decays while the QCD multijet background should result in one subjet carrying almost all the energy of the large-radius probe jet. Targeting the W boson of the top quark decay, the minimum pairwise mass of two of the leading three subjets m_{ij} has to be larger than 50 GeV. For HOTVR, only one working point is defined.

8.3 Event selection of the tag

The top tagging efficiencies are measured using a tag-and-probe method, in which the $\text{t}\bar{\text{t}}$ process in the lepton+jets channel is tagged by requiring a high-p_{T} muon and a b-tagged jet in the same hemisphere. Additional selection criteria are applied in order to obtain a pure $\text{t}\bar{\text{t}}$ sample with small contributions from background processes. Data are selected that pass a single muon trigger[1] requiring at least one muon with $p_{\text{T}} > 50\,\text{GeV}$. In addition, the muon candidate must pass an offline requirement of $p_{\text{T}} > 55\,\text{GeV}$ and $|\eta| < 2.4$, which ensures a constant and high trigger efficiency. Every selected event must contain exactly one muon and no electrons. Quality criteria [78] such as the number of hits in the muon and tracking system and the goodness of the track fit secure the selection of a reliable muon candidate. Correction factors as a function of muon p_{T} and η are applied to simulation, correcting the efficiencies of the trigger and muon selection to be equivalent to those observed in data [97]. Furthermore, the customized isolation for muons is applied as described above in Section 7.3.1 and Figure 7.10.

[1] HLT_Mu50 and HLT_TkMu50

All events are discarded where the muon fulfills $\Delta R < 0.4$ and $p_{\mathrm{T}}^{\mathrm{rel}} < 25$ GeV with respect to the closest AK4 jet, where all AK4 jets with $p_{\mathrm{T}} > 30$ GeV are considered. Since a neutrino is expected in the final state, every event is required to have $p_{\mathrm{T}}^{\mathrm{miss}} > 50$ GeV. Furthermore, the transverse momentum of the W boson decaying into muon and neutrino is reconstructed from the p_{T} and ϕ of the muon as well as $\vec{p}_{\mathrm{T}}^{\mathrm{miss}}$ and has to be greater than 150 GeV. For every event the existence of a b-tagged AK4 jet in the leptonic hemisphere is required. The leptonic hemisphere is defined as the area within $\Delta R < 2\pi/3$ around the selected muon. The medium b tagging working point of the DeepJet algorithm [81] is checked for all AK4 jets with $p_{\mathrm{T}} > 30$ GeV and $|\eta| < 2.4$ that are inside the leptonic hemisphere. An event is kept if at least one jet passes the DeepJet requirements. The b tagging efficiency of simulated events is again corrected to match the efficiency observed in data. Due to a failure of a section of the HCAL in 2018, all events in data that were recorded during the outage are rejected if they contain an electron or jet with $\eta < -1.3$ and $-1.57 < \phi < -0.87$. This effect is corrected in simulation by randomly rejecting the same proportion of events that contain jets or electrons pointing in the respective angular section. The pileup profile is reweighted in simulation such that it matches the profile measured in data. Figure 8.2 shows the distributions in muon p_{T} (left) and $p_{\mathrm{T}}^{\mathrm{miss}}$ (right) for the three data taking periods in 2016, 2017, and 2018 for data and simulation. Only statistical uncertainties are considered. After the selection a rather pure $\mathrm{t\bar{t}}$ sample is obtained with small contributions from background processes. In 2016, a normalization offset is observed but both observables are overall well described by the simulation.

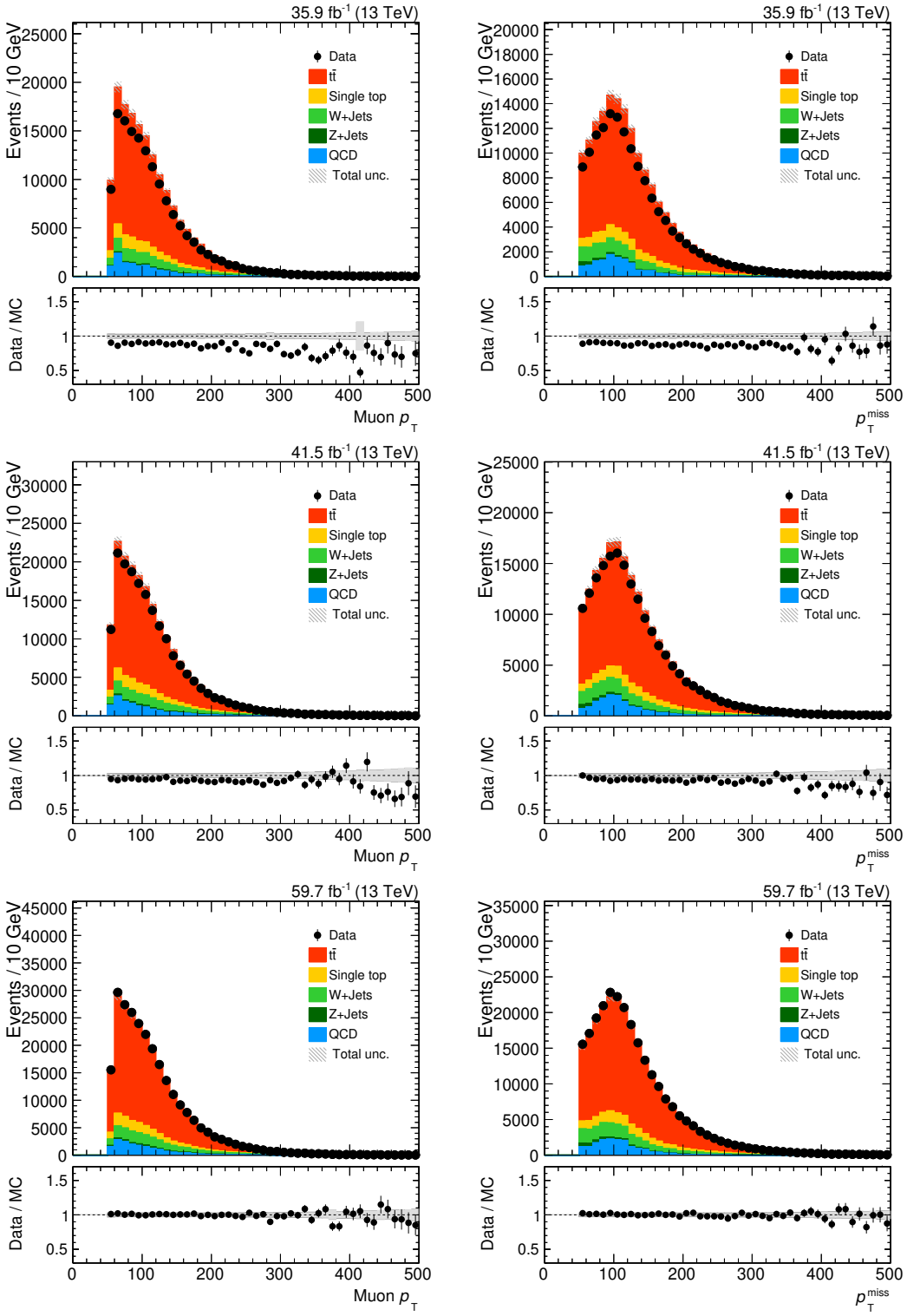

Figure 8.2: Distributions in muon p_{T} (left) and $p_{\mathrm{T}}^{\mathrm{miss}}$ (right) obtained for the 2016 (upper), 2017 (middle), and 2018 (lower) data taking periods after the event selection. Data (markers) are compared to simulation (filled areas). The bottom panels show the ratio of data to simulation. Only statistical uncertainties are considered and displayed as hashed areas in the top panels or grey filled areas in the bottom panels.

8.4 Systematic uncertainties

Various sources of systematic uncertainties are taken into account for the estimation of the top tagging efficiencies. However, only uncertainties that contribute to a non-negligible amount are considered in the template fit, which is discussed below in Section 8.6. For each uncertainty source, two samples corresponding to the variations of one positive and negative standard deviation are produced for each physics process. These samples are later used to extract one nuisance parameter per uncertainty source. The variations connected to the correction factors regarding the muon trigger and identification efficiencies are estimated by changing the correction factors within its uncertainties. Similarly, samples corresponding to the uncertainties connected to the correction of b tagging efficiencies, corrections of the jet energy scale and jet energy resolution as well as the reweighting of the pileup profile are estimated. A total of 100 variations of the NNPDF3.0 set [105] are used to estimate the uncertainty due to the choice of the PDFs. In each bin of a distribution, the difference of the nominal simulation with respect to the standard deviation calculated from all 100 variations is considered the uncertainty. The renormalization, factorization and final state radiation scales are individually changed by factors of 0.5 and 2. All mentioned uncertainty sources are studied but only the variations connected to the jet energy scale and resolution, final state radiation, renormalization scale, and factorization scale are considered to be non-negligible and enter the template fit as well as the distributions presented in the following.

8.5 Modeling of substructure observables

After the event selection, the description of substructure variables is studied by comparing the prediction obtained from simulation to data. Probe jets are considered with $p_{\mathrm{T}} > 300$ GeV if AK8 jets are used. Below this threshold, the jets are unlikely to contain all decay products of the hadronic top quark decay, and top tagging is not applicable any more. In contrast, HOTVR jets cover a larger area at low p_{T} due to the variable radius approach and are considered down to $p_{\mathrm{T}} > 200$ GeV.

In the following, the contributions from $\mathrm{t\bar{t}}$ and single produced top quarks in simulation are divided into their merged, semimerged, and unmerged fractions. Here, a merged event is an event where all three partons from the hadronic top quark decay have an angular distance to the probe jet smaller than the jet radius. The radius is taken to be 0.8 for AK8 jets. For HOTVR

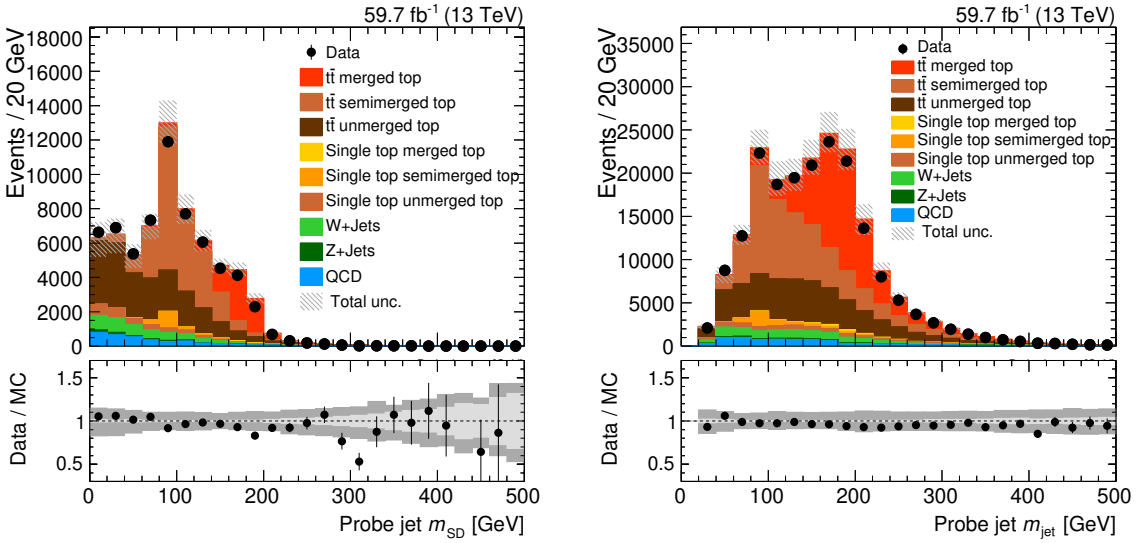

Figure 8.3: Distributions of the AK8 soft drop mass m_{SD} (left) and HOTVR jet mass m_{jet} (right) obtained in the 2018 data taking period after the event selection. Data (markers) are compared to simulation (filled areas). The bottom panels display the ratio of events observed in data and predicted by simulation. In the upper panels, the total uncertainty is shown as hatched area, in the bottom panels the statistical uncertainty (inner area) and total uncertainty (outer area) are shown individually. Only AK8 jets with $p_{\mathrm{T}} > 300$ GeV and HOTVR jets with $p_{\mathrm{T}} > 200$ GeV are considered. The distributions of the years 2016 and 2017 are presented in Figure B.1 of Appendix B.

the effective radius is calculated via $R_{\mathrm{eff}} = 600\,\mathrm{GeV}/p_{\mathrm{T}}$, where p_{T} refers to the jet p_{T} before applying jet energy corrections. If not all three but only two of the top quark decay partons are inside the probe jet, an event is classified as semimerged. Events where only one or none of the top quark decay partons can be matched to the probe jet are classified as unmerged.

Figure 8.3 shows the m_{SD} and m_{jet} distributions of AK8 and HOTVR jets for the 2018 data taking period. In the case of HOTVR jets, a larger fraction of merged events is visible, which is a direct result of an overall larger jet area. As expected, the merged contribution accumulates close to the top quark mass while unmerged events have small masses. The semimerged events show a peak close to the W boson mass. Since this category also includes events where the b quark and one of the W decay partons are clustered into the jet, the peak close to the W boson mass is smeared out towards larger masses.

The p_{T} spectra of AK8 jets in 2016 and 2018 are displayed in Figure 8.4, and data are compared to simulation. In the 2016 data taking period (Figure 8.4, left), a spectrum shifted to smaller momenta is observed in data compared to simulation. As a result of the selection of high-p_{T} jets, also a normalization difference in data and simulation in observed. This effect is due to the

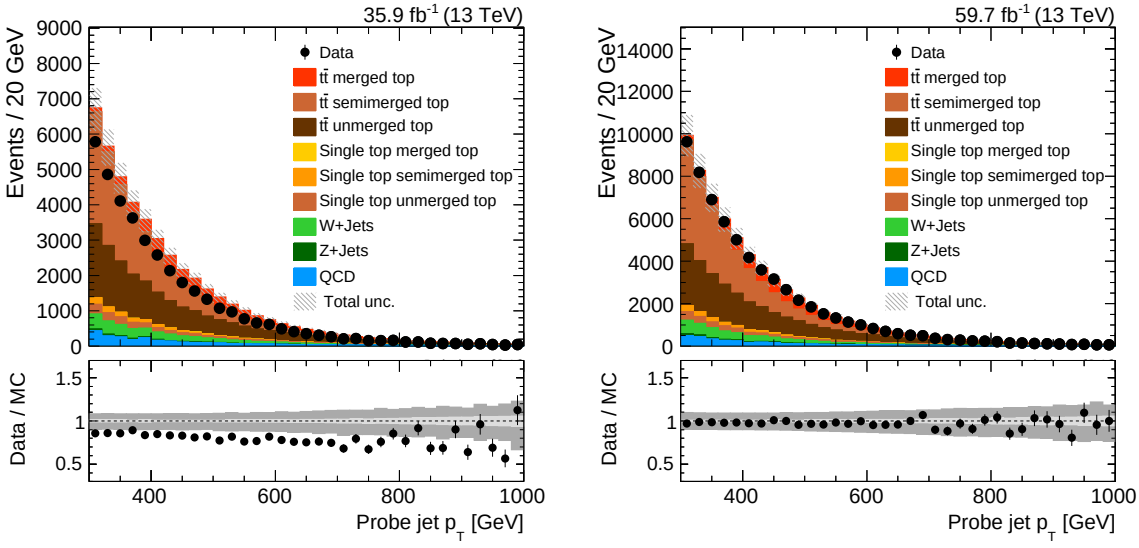

Figure 8.4: Probe jet p_{T} distributions obtained in the 2016 (left) and 2018 (right) data taking periods for AK8 jets after the event selection. Data (markers) are compared to simulation (filled areas). The bottom panels display the ratio of events observed in data and predicted by simulation. In the upper panels, the total uncertainty is shown as hatched area, in the bottom panels the statistical uncertainty (inner area) and total uncertainty (outer area) are shown individually. The distributions of 2017 and for HOTVR jets are displayed in Figure B.2 of Appendix B.

modeling of the top quark p_{T} spectrum and has been discussed in the measurement of the jet mass distribution (Chapter 7) and several other analyses [100, 101, 102, 103, 1]. The transition from the CUETP8M2T4 tune to CP5 in $\mathrm{t\bar{t}}$ simulation corrects for this effect and leads to a good modeling of the probe jet p_{T} in the data taking period of 2018 (Figure 8.4, right). Because of the same tune, the distribution from 2017 is very similar to 2018 (see Appendix B, Figure B.2). The same behavior is observed with HOTVR jets (see Appendix B, Figure B.2).

Although the top quark p_{T} modeling improved with the CP5 tune, the description of the N-subjettiness ratio τ_{32} did not. As shown in Figure 8.5, the observed τ_{32} distribution was mostly described well by simulation during 2016 (left), taking into account the difference in normalization already discussed above. In 2018 (right) however, a discrepancy between data and simulation is observed, especially for small values of τ_{32}. Nevertheless, all distributions show the discriminating power of τ_{32}. Events categorized as merged tend to accumulate at small values while other top quark contributions and background are dominant at large values. Figure 8.6 shows a direct comparison of the normalized τ_{32} distributions between the three data taking periods. The comparison is presented for data (left) and $\mathrm{t\bar{t}}$ simulation (right) for AK8 jets. Data taken in all three years agree well while simulation is different in 2016 compared to 2017

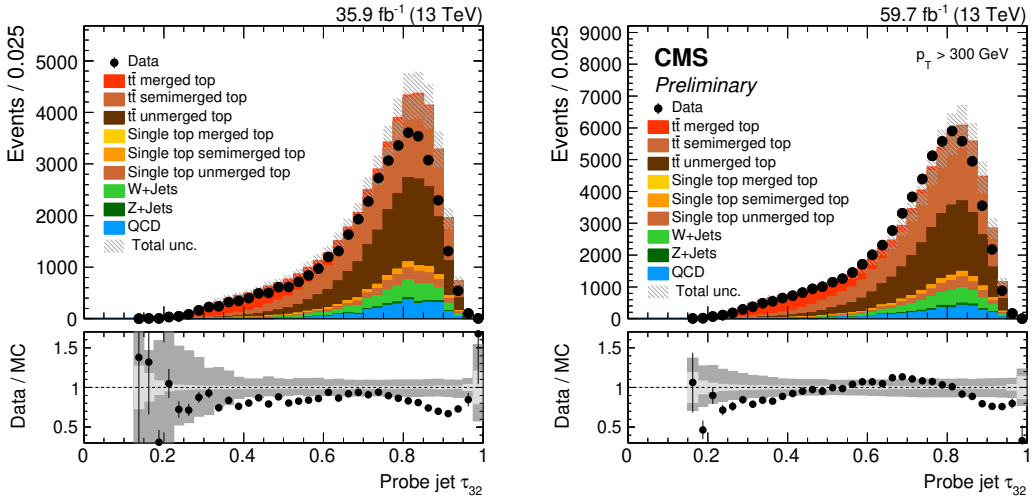

Figure 8.5: Distributions in the N-subjettiness ratio τ_{32} obtained in the 2016 (left) and 2018 (right) data taking periods for AK8 jets after the event selection. Data (markers) are compared to simulation (filled areas). The bottom panels display the ratio of events observed in data and predicted by simulation. In the upper panels, the total uncertainty is shown as hatched area, in the bottom panels the statistical uncertainty (inner area) and total uncertainty (outer area) are shown individually. The distributions of 2017 and for HOTVR jets are displayed in Figure B.3 of Appendix B. The right plot was published in Ref. [10].

and 2018, especially for small values of τ_{32}. This again demonstrates the stability of the data taking and indicates that the modeling of $t\bar{t}$ events causes the discrepancies in data to simulation comparisons. The behavior of HOTVR jets is similar (see Appendix B, Figure B.4).

In addition to the N-subjettiness, certain working points of the AK8 tagger make use of subjet b tagging. Here, the AK8 jet must contain at least one subjet that satisfies the medium working point of the DeepCSV algorithm. The distribution of the highest DeepCSV value inside an AK8 jet is shown in Figure 8.7 for 2018. Although there are dedicated correction factors for efficiency differences of the DeepCSV algorithm, those are not applied and absorbed into the top tagging efficiency itself. In this way uncertainties in the b tagging correction factors are avoided, which might not be valid in the dense environment inside an AK8 jet.

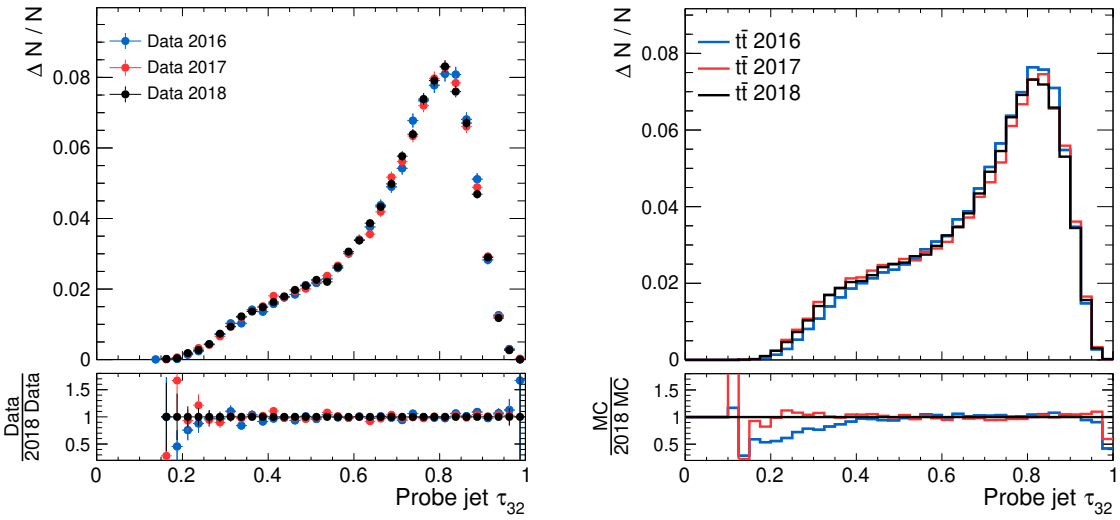

Figure 8.6: The normalized distributions of the N-subjettiness ratio τ_{32} compared between the three data taking periods for data (left) and $t\bar{t}$ simulation (right) for AK8 jets after the event selection. Only probe jets with $p_T > 400$ GeV are considered. The bottom panels show the relative difference to data collected in 2018 (left) or to the prediction from the 2018 simulation (right). The distributions of HOTVR jets are displayed in Figure B.4 of Appendix B.

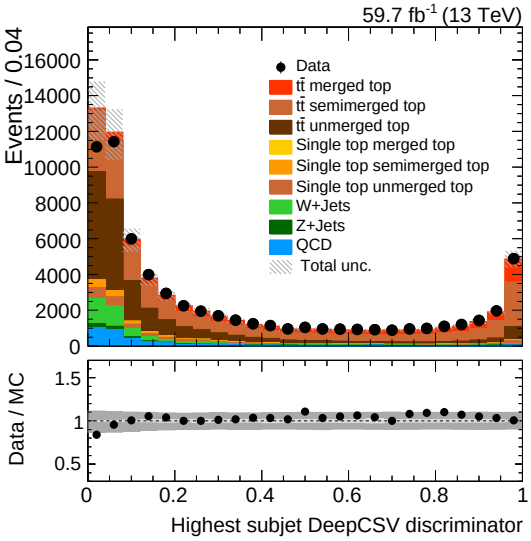

Figure 8.7: Distribution of highest DeepCSV discriminator value of a subjet inside an AK8 probe jet obtained 2018. Data (markers) are compared to simulation (filled areas). The bottom panel displays the ratio of events observed in data and predicted by simulation. In the upper panel, the total uncertainty is shown as hatched area, in the bottom panel the statistical uncertainty (inner area) and total uncertainty (outer area) are shown individually. The distributions of 2016 and 2017 are displayed in Figure B.5 of Appendix B.

The HOTVR algorithm does not only make use of the observables m_{jet} and τ_{32} but further requires a minimum of three subjets, a minimum pairwise subjet mass of $m_{ij} > 50$ GeV, and the p_{T} ratio of the p_{T} leading subjet and probe jet to be $f < 0.8$. The distributions of m_{ij} and f in 2018 are presented in Figure 8.8. Data is compared to simulation and an overall good modeling is observed, also in all other years (see Appendix B, Figure B.6). Furthermore, the sensitivity of the variables is visible. Merged events tend to have a minimum pairwise mass around 80 GeV since this variable aims to reconstruct the W boson of the top quark decay. Also, the three-prong structure of merged events leads to a rather evenly distributed momentum fraction of all three subjets and small values of f.

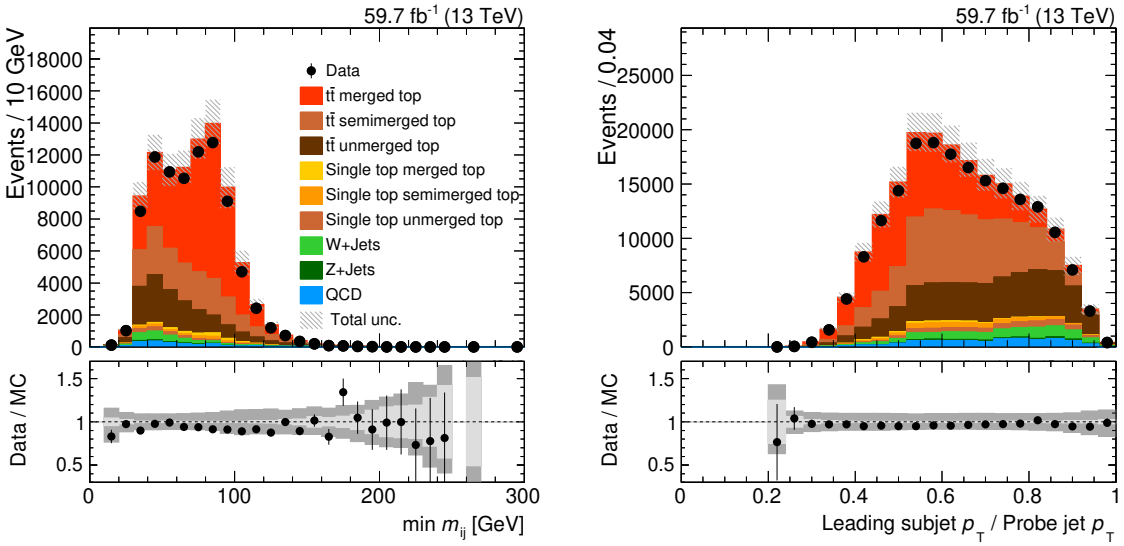

Figure 8.8: Distributions of additional substructure observables used in the HOTVR algorithm for 2018. Namely, the minimum pairwise mass of two subjets m_{ij} (left) and the ratio of the leading subjet p_{T} and probe jet p_{T} (right) are shown for data (markers) and simulation (filled areas). The bottom panels display the ratio of events observed in data and predicted by simulation. In the upper panels, the total uncertainty is shown as hatched area, in the bottom panels the statistical uncertainty (inner area) and total uncertainty (outer area) are shown individually. The distributions of 2016 and 2017 are displayed in Figure B.6 of Appendix B.

8.6 Template fit

The top tagging efficiencies for all presented working points of the taggers using AK8 and HOTVR jets are extracted independently for the merged, semimerged, and unmerged contributions of all $t\bar{t}$ events. This makes the resulting correction factors valid for any phase space, also those with a very different composition of these three categories. In order to obtain the efficiencies for those categories from a data sample, the simulation is fit to data using a maximum likelihood procedure. The fits are performed simultaneously for events passing and failing the respective top tagging working point using the distributions of the soft drop mass m_{SD} and plain jet mass m_{jet} for AK8 and HOTVR jets, respectively. Also, the merged, semimerged, and unmerged contributions of $t\bar{t}$ are allowed to float independently in the fit. This makes the fits stable for all regions of probe jet p_{T}, despite the very different shapes in m_{jet}. The mass requirements $105 < m_{\mathrm{SD}} < 210\,\mathrm{GeV}$ and $140 < m_{\mathrm{jet}} < 220\,\mathrm{GeV}$ are applied after performing the fits, which allows to fit a physically reasonable mass spectrum and includes the full shape information in the fits. This especially improves the handle on the semimerged, and unmerged events since those mostly lie outside the selected mass windows. Figures 8.9 and 8.10 show the m_{SD} and m_{jet} distributions, divided into pass and fail regions, in 2018 for AK8 and HOTVR jets, respectively. In the case of AK8 jets, the working point requiring $\tau_{32} > 0.46$ is selected for display. The pass regions show a very pure sample of merged $t\bar{t}$ events as aimed for. While the fail region shows a good agreement between data and simulation, some differences are observed in the pass region. This is mostly caused by the description of substructure variables used to define top-tagged jets and directly motivates the derivation of dedicated correction factors.

Since the probability of a probe jet containing all decay products of the top quark is strongly correlated with the initial momentum of the top quark itself and the resulting Lorentz boost, the shapes in m_{SD} and m_{jet} change with p_{T}. Therefore, the top tagging efficiencies strongly depend on the p_{T} of the probe jet. To account for this effect, the template fit is performed separately in bins of the probe jet p_{T}. Figure 8.11 shows the shape of the m_{jet} distribution for different bins of jet p_{T} for AK8 and HOTVR jets. For AK8 jets, the position of the peak shifts towards larger values with increasing p_{T}. With that, also the peak is narrower at larger momenta. In contrast, the HOTVR peak position is rather constant due to the adjustable jet size but the tail at high m_{jet} increases with p_{T}. The p_{T} windows that are chosen for the efficiency measurement are summarized in Table 8.2. The AK8 tagger – due to its constant radius – is very inefficient for probe jets with $p_{\mathrm{T}} < 300\,\mathrm{GeV}$. Thus, lower p_{T} bins are only considered for HOTVR jets.

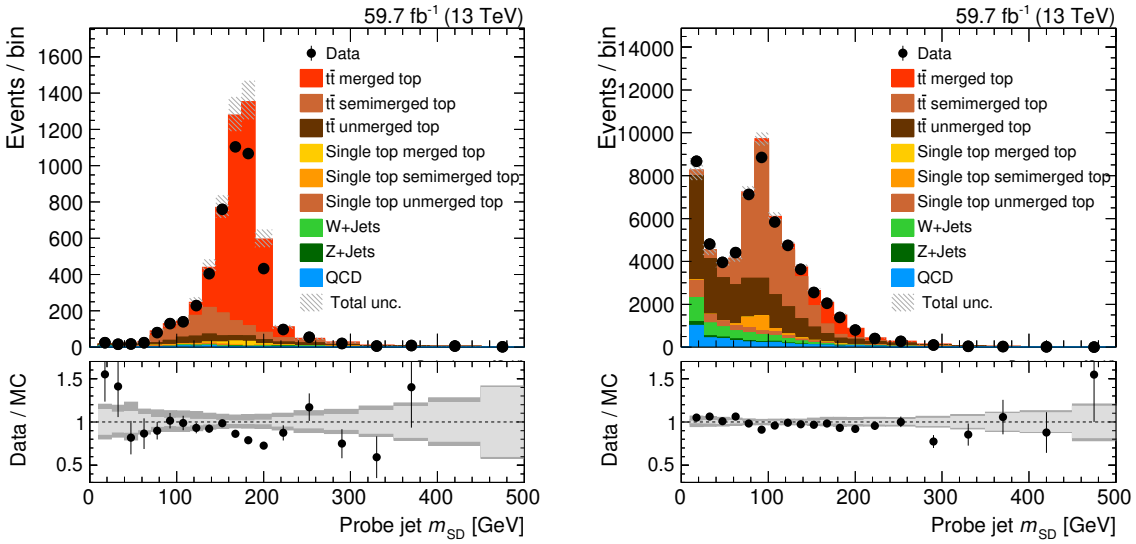

Figure 8.9: Distributions of the AK8 soft drop mass m_{SD} obtained in the 2018 data taking period divided into passing (left) and failing (right) the requirement $\tau_{32} < 0.46$. Data (markers) are compared to simulation (filled areas). The bottom panels display the ratio of events observed in data and predicted by simulation. In the upper panels, the total uncertainty is shown as hatched area, in the bottom panels the statistical uncertainty (inner area) and total uncertainty (outer area) are shown individually. Only probe jets with $p_T > 300$ GeV are considered. The distributions of 2016 and 2017 are displayed in Figure B.7 of Appendix B.

The bin sizes are chosen such that the p_T dependent effect is captured while retaining sufficient statistical precision.

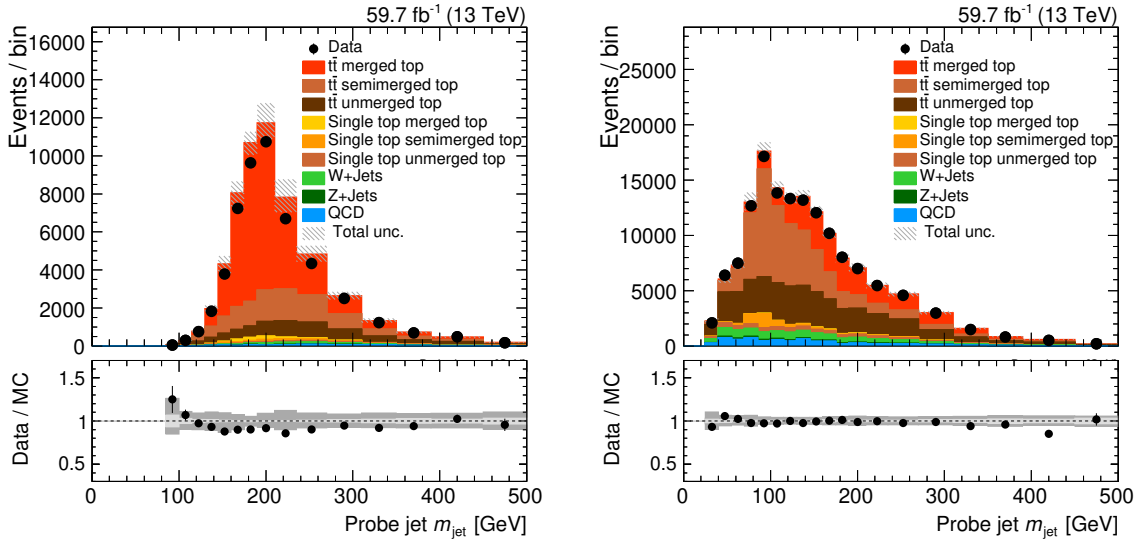

Figure 8.10: Distributions of the HOTVR jet mass m_{jet} obtained in the 2018 data taking period divided into passing (left) and failing (right) HOTVR top tagging requirements. Data (markers) are compared to simulation (filled areas). The bottom panels display the ratio of events observed in data and predicted by simulation. In the upper panels, the total uncertainty is shown as hatched area, in the bottom panels the statistical uncertainty (inner area) and total uncertainty (outer area) are shown individually. Only probe jets with $p_{\text{T}} > 200$ GeV are considered. The distributions of 2016 and 2017 are displayed in Figure B.8 of Appendix B.

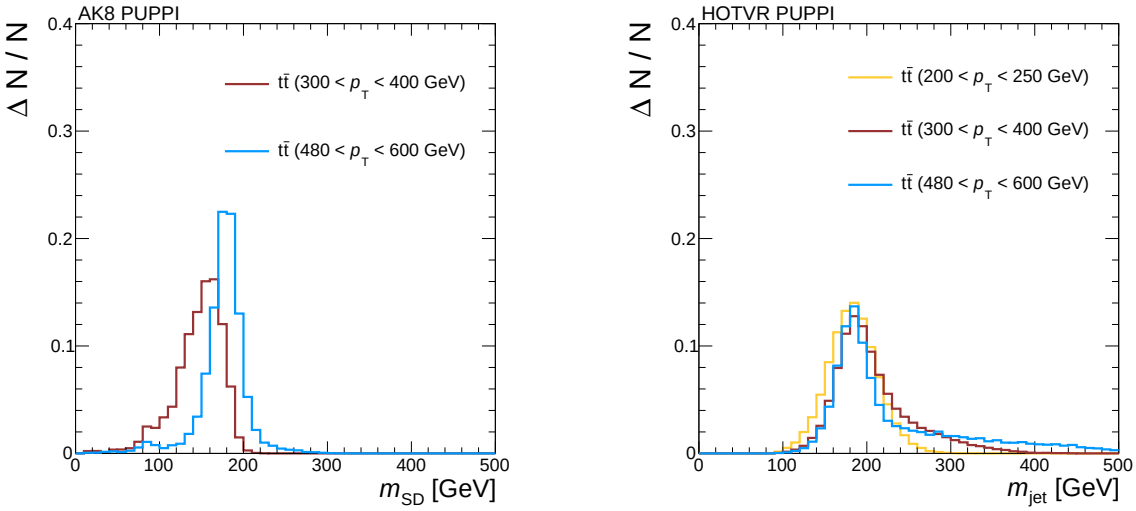

Figure 8.11: The m_{SD} and m_{jet} distributions in various ranges of the probe jet p_{T} for AK8 (left) and HOTVR (right) jets using $\text{t}\bar{\text{t}}$ simulation corresponding to the 2018 data taking period. All distributions are normalized to an integral of unity.

The template fits are performed using the THETA framework [110]. It allows to introduce nuisance parameters representing systematic uncertainties, which can be constrained by the observed distributions in data. The nuisance parameters are created within THETA via template morphing using the positive and negative variations by one standard deviation of each systematic uncertainty. Furthermore, the uncertainties in the rates of all processes are introduced as nuisance parameters allowing the fit to increase or decrease the contribution of each process. Here, the merged, semimerged, and unmerged contributions of $\mathrm{t\bar{t}}$ and single top events can be varied independently. Three additional nuisance parameters are constructed that increase or decrease the number of events in the pass region while simultaneously decreasing or increasing the event yield in the fail region. Each of those three parameters only acts on three-prong (merged $\mathrm{t\bar{t}}$ and merged single top), two-prong (semimerged $\mathrm{t\bar{t}}$ and semimerged single top), or one-prong events (unmerged $\mathrm{t\bar{t}}$, unmerged single top, and all backgrounds). This makes it possible to adjust for varying top tagging efficiencies without changing the total event yield and is a crucial improvement with respect to a previous measurement of the top tagging efficiencies in 2016 [9]. This also prevents large correlations of the extracted efficiencies with the uncertainties in the production cross sections of background processes and helps reducing the systematic uncertainties in the measurement. An example is presented in Figure 8.12, where the pass and fail regions are presented before and after the template fit. Shown is the fit in the region $480 < p_\mathrm{T} < 600$ GeV using AK8 jets and a top tagging criterion of $\tau_{32} < 0.46$. Overall, the agreement between data and simulation improves after the fit as expected. Also, the data can constrain some of the uncertainties, which is especially visible in the peak bins of the pass region. The nuisance parameters after the fit are shown in Figure 8.13 and compared to the parameters before the fit. It is observed that some parameters, e.g. rates of single top, W+jets, or Z+jets production cannot be constrained by the fit. Others, including uncertainties connected to jet energy corrections or the parton shower modeling, can drastically change the shape and normalization of the m_SD distributions and can thus be constrained by the data. A correlation

Table 8.2: Summary of the p_T regions in which the template fit is performed. The two regions with $p_\mathrm{T} < 300$ GeV are used for HOTVR jets only.

Bin number	Range in probe jet p_T [GeV]	Jet collection
1	200–250	HOTVR
2	250–300	HOTVR
3	300–400	AK8, HOTVR
4	400–480	AK8, HOTVR
5	480–600	AK8, HOTVR
6	>600	AK8, HOTVR

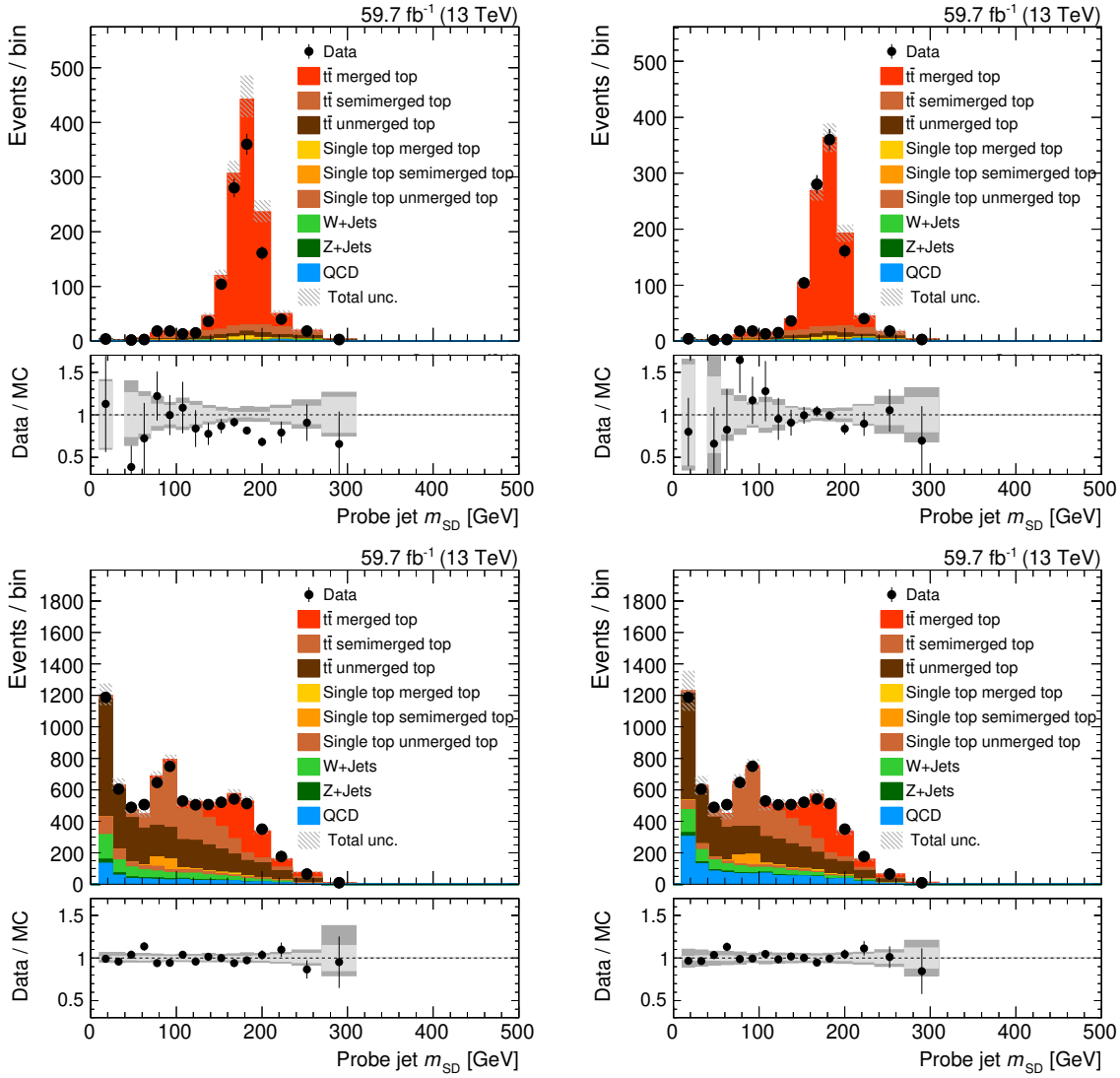

Figure 8.12: AK8 soft drop mass m_{SD} distributions in 2018 before (left) and after (right) performing the template fit for probe jets with $480 < p_T < 600$ GeV. The distributions are divided into events that pass (upper) or fail (lower) the requirement $\tau_{32} < 0.46$. Data (markers) are compared to simulation (filled areas). The bottom panels display the ratio of events observed in data and predicted by simulation. In the upper panels, the total uncertainty is shown as hatched area, in the bottom panels the statistical uncertainty (inner area) and total uncertainty (outer area) are shown individually.

matrix (see Figure 8.14) is created, and no correlations larger than 0.6 are observed between nuisance parameters.

Figures 8.15 and 8.16 show the m_{SD} and m_{jet} distributions of 2018 after the fit for AK8 and HOTVR jets, respectively. Again, the distributions are divided into pass (left) and fail regions (right). For AK8, the working point $\tau_{32} < 0.46$ is chosen for display. In those plots,

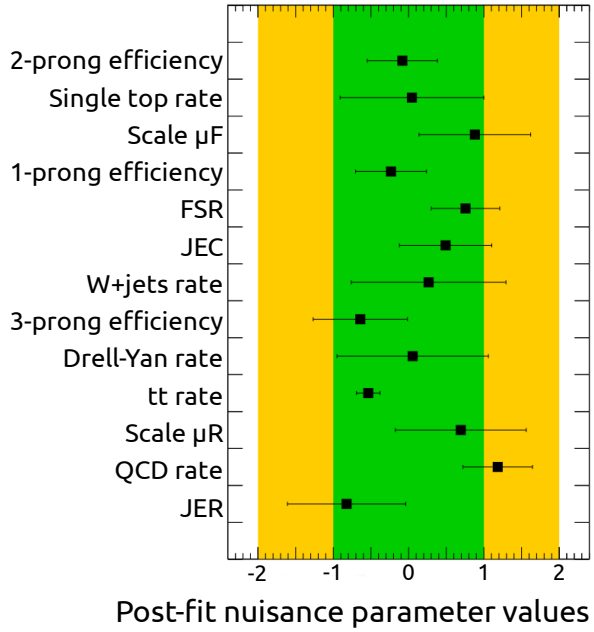

Figure 8.13: Nuisance parameters (markers) with uncertainties (horizontal bars), corresponding to one standard deviation after the fit and the variations of one (inner band) and two (outer band) standard deviations of the parameters prior to the fit. Shown is the result for a fit using AK8 jets in 2018 with $480 < p_{\mathrm{T}} < 600$ GeV passing and failing $\tau_{32} < 0.46$.

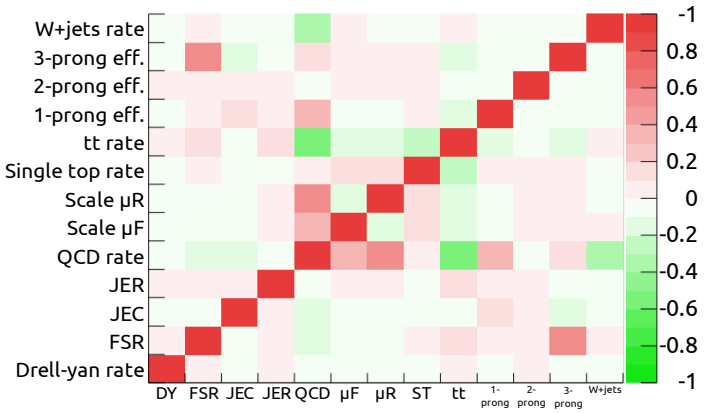

Figure 8.14: Correlation matrix of nuisance parameters. Shown is the result for a fit using AK8 jets in 2018 with $480 < p_{\mathrm{T}} < 600$ GeV passing and failing $\tau_{32} < 0.46$.

all p_{T} bins are combined after the fit. Overall, the data are described well by simulations over the full range of m_{SD} and m_{jet}, which is also observed in 2016 and 2017 (see Appendix B, Figures B.9 and B.10).

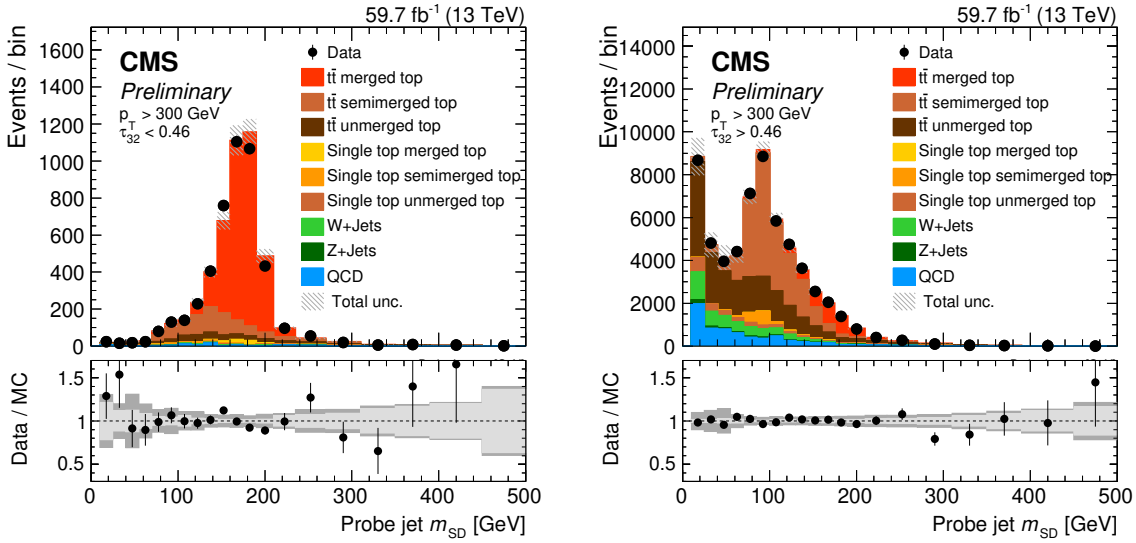

Figure 8.15: Distributions in the AK8 soft drop mass m_{SD} after the template fit obtained in the 2018 data taking period divided into passing (left) and failing (right) the requirement $\tau_{32} < 0.46$. Data (markers) are compared to simulation (filled areas). The bottom panels display the ratio of events observed in data and predicted by simulation. In the upper panels, the total uncertainty is shown as hatched area, in the bottom panels the statistical uncertainty (inner area) and total uncertainty (outer area) are shown individually. The distributions of 2016 and 2017 are displayed in Figure B.9 of Appendix B. Published in Ref. [10].

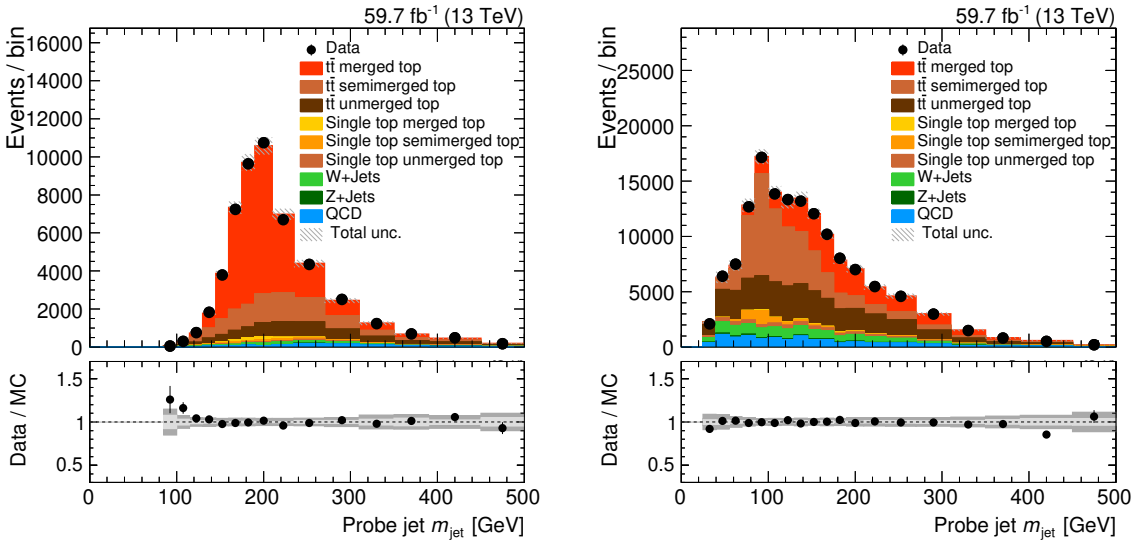

Figure 8.16: Distributions in the HOTVR jet mass m_{jet} after the template fit obtained in the 2018 data taking period divided into passing (left) and failing (right) HOTVR top tagging requirements. Data (markers) are compared to simulation (filled areas). The bottom panels display the ratio of events observed in data and predicted by simulation. In the upper panels, the total uncertainty is shown as hatched area, in the bottom panels the statistical uncertainty (inner area) and total uncertainty (outer area) are shown individually. The distributions of 2016 and 2017 are displayed in Figure B.10 of Appendix B.

8.7 Measurement of data-to-simulation scale factors

In order to obtain correction factors for the $t\bar{t}$ simulation, the top tagging efficiencies have to be measured in both data and simulation. Because the mass window is not applied in the template fits, the top tagging efficiency ε^{tot} is calculated as the product of two individual terms: the efficiency of the mass window $\varepsilon^{\text{mass}}$ and the efficiency ε of all other requirements – such as τ_{32} – that define the pass and fail regions above. The latter efficiency is defined as

$$\varepsilon = \frac{N_{\text{pass}}}{N_{\text{pass}} + N_{\text{fail}}}, \tag{8.1}$$

where N_{pass} and N_{fail} correspond to the number of events in the pass and fail regions, respectively. In simulation, the event yields are estimated from the $t\bar{t}$ prediction prior to the fit. The efficiency in data, however, is calculated using the event yields observed in simulation after performing the template fit. This enables to extract independent correction factors for the three categories merged, semimerged, and unmerged. The sum of all entries of the covariance matrix containing the correlations and uncertainties of all nuisance parameters determines the uncertainty of the corresponding event yields. The efficiency due to the jet mass window is calculated directly in simulation and data before the fit via

$$\varepsilon^{\text{mass}} = \frac{N_{\text{inside mass window}}}{N_{\text{inside mass window}} + N_{\text{outside mass window}}}, \tag{8.2}$$

where the events are counted inside and outside the applied mass window. The combined efficiency of the top tagger then simply is

$$\varepsilon^{\text{tot}} = \varepsilon \cdot \varepsilon^{\text{mass}}, \tag{8.3}$$

where ε and $\varepsilon^{\text{mass}}$ are treated as uncorrelated, and the normal propagation of uncertainties is used.

Figure 8.17 presents an example for the AK8 working point requiring $\tau_{32} < 0.46$ and the HOTVR tagger showing the efficiencies ε, $\varepsilon^{\text{mass}}$, and ε^{tot} in all p_{T} bins calculated from the distributions before and after the template fit for the merged contribution of $t\bar{t}$ in 2018. The efficiencies are calculated independently for each year, jet selection, $t\bar{t}$ category and top tagging working point. The efficiency decrease of $\varepsilon^{\text{mass}}$ for large jet p_{T} is caused by the change of the m_{SD} and m_{jet} distributions as a function of p_{T} (see Figure 8.17, middle). For very high p_{T} the jet is likely to include additional radiation, and the jet mass is more likely to be shifted towards

higher masses and out of the mass window. Also, additional radiation leads to a decreasing efficiency of the τ_{32} requirement for AK8 jets. In contrast, the tagging efficiency of HOTVR jets is very stable over the whole p_{T} range before applying the mass window. The overall efficiency decreases with increasing p_{T} because large shifts in m_{jet} appear, and probe jets are more likely to be pushed out of the mass window.

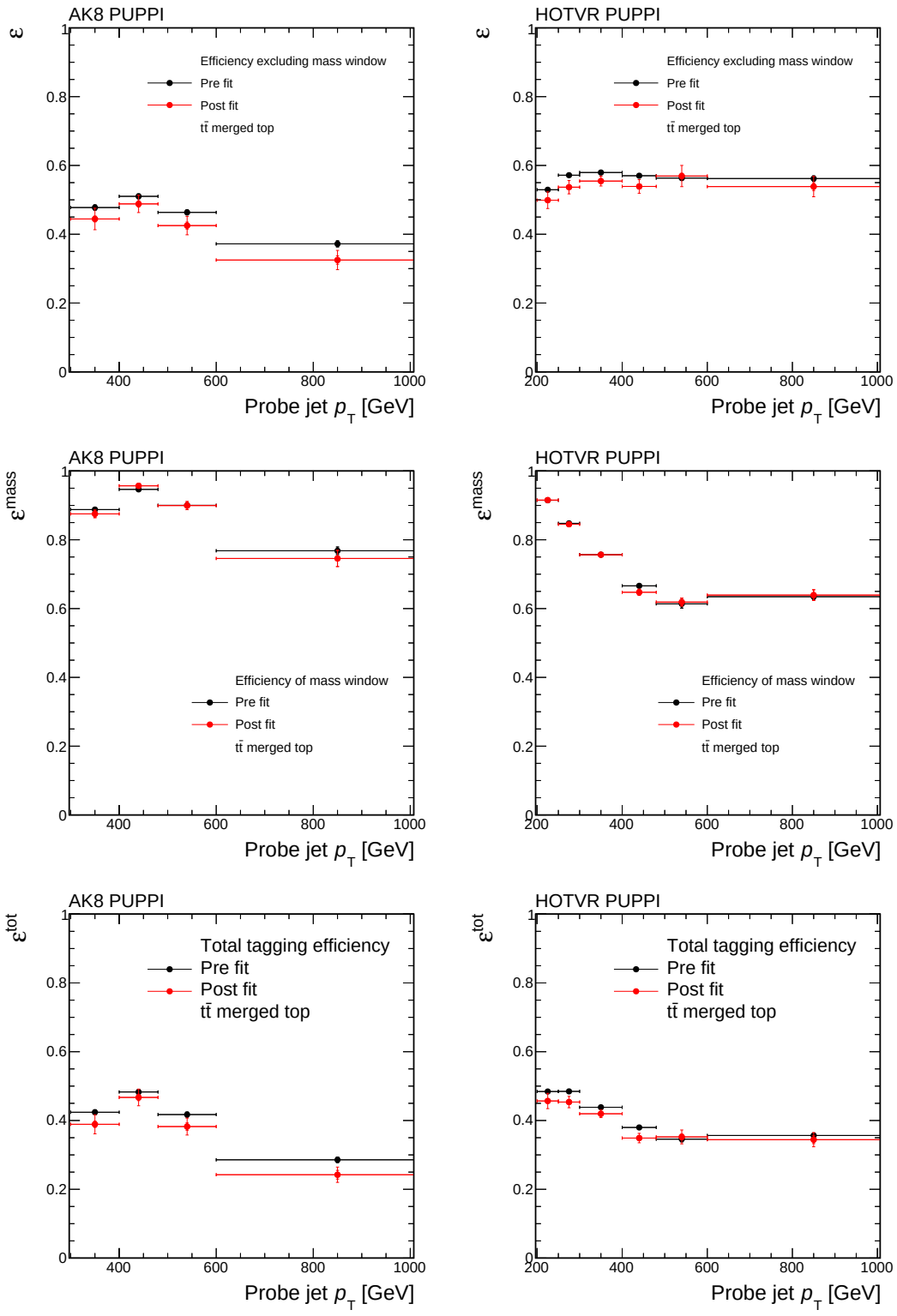

Figure 8.17: Efficiencies measured in the 2018 data taking periods before (black markers) and after (red markers) the template fit for AK8 (left) and HOTVR jets (right). Displayed are the tagging efficiencies in the merged category excluding the mass requirement (upper), the mass window alone (middle), and the total tagging efficiency (lower) as the product of those. The error bars show the total uncertainty of the efficiency measurement. For AK8 jets, the working point $\tau_{32} < 0.46$ is chosen for display.

Table 8.3 summarizes the efficiencies for signal and background measured in simulation. Here, probe jets with $480 < p_T < 600$ GeV are considered, which are clustered within $\Delta R < 0.6$ to a generated top quark (signal) or in QCD multijet events (background). This definition was already used and studied in Ref. [9] and found to provide a fair comparison between jet algorithms that rely on different jet sizes. The numbers give a comparison between the working points, but in a specific analysis, the efficiencies can differ from these numbers due to the different contribution of merged, semimerged, and unmerged events. The additional subjet b tag decreases the signal efficiency but at the same time helps rejecting contributions from background processes.

From the total efficiency ε^{tot} a corrective scale factor (SF) is calculated via

$$\text{SF} = \frac{\varepsilon^{\text{tot}}_{\text{data}}}{\varepsilon^{\text{tot}}_{\text{MC}}}, \tag{8.4}$$

with $\varepsilon^{\text{tot}}_{\text{data}}$ and $\varepsilon^{\text{tot}}_{\text{MC}}$ being the efficiencies obtained for data and simulation from the distributions after and before the fit, respectively.

Figure 8.18 shows the resulting scale factors of the two example working points of AK8 and HOTVR for the merged, semimerged, and unmerged contributions in $\mathrm{t\bar{t}}$. Statistical and total uncertainties are shown as inner and outer bands. In general, the fit shows more ability to constrain the uncertainties for merged events than for the other categories.

Table 8.3: Signal and background tagging efficiencies for all working points studied in this analysis using simulated samples corresponding to the 2018 data taking period. The efficiencies for signal and background are measured in simulated $\mathrm{t\bar{t}}$ events where the generated top quark is within $\Delta R < 0.6$ to the probe jet and QCD multijet simulation, respectively. Only events are considered where the probe jet fulfills $480 < p_T < 600$ GeV. Published in Ref. [10].

Tagger	Working point	Signal efficiency [%]	Background efficiency [%]
AK8 PUPPI	$\tau_{32} < 0.40$	17	0.2
	$\tau_{32} < 0.46$	26	0.5
	$\tau_{32} < 0.54$	37	1.7
	$\tau_{32} < 0.65$	49	5.1
	$\tau_{32} < 0.80$	62	15.9
AK8 PUPPI + subjet btag	$\tau_{32} < 0.40$	16	0.1
	$\tau_{32} < 0.46$	23	0.3
	$\tau_{32} < 0.54$	33	0.6
	$\tau_{32} < 0.65$	43	1.8
	$\tau_{32} < 0.80$	53	5.3
HOTVR PUPPI	$\tau_{32} < 0.56$	37	2.6

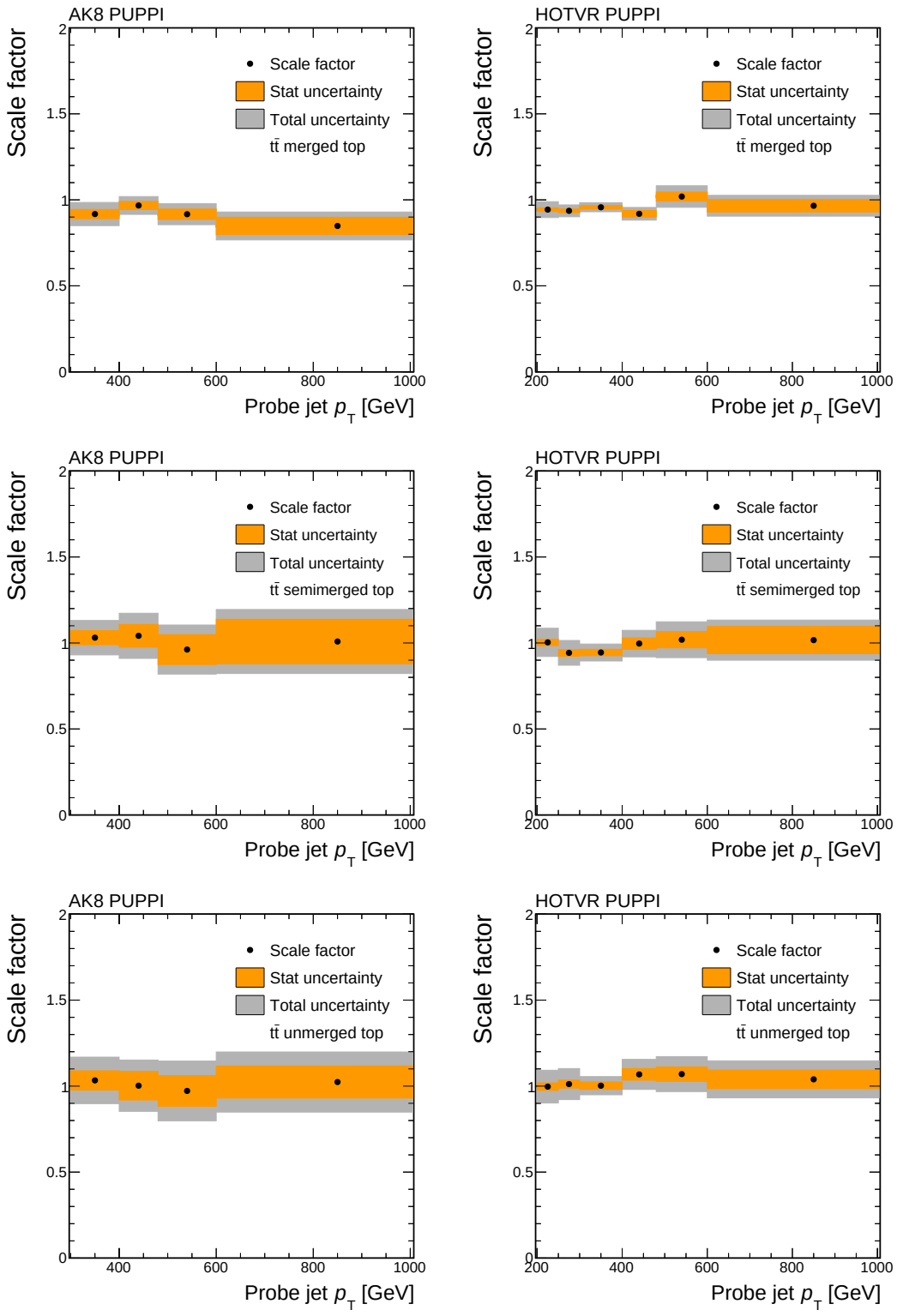

Figure 8.18: Scale factors obtained from the total tagging efficiencies in 2018 for AK8 (left) and HOTVR jets (right) for $t\bar{t}$ events in the categories merged (upper), semimerged (middle), and unmerged (lower). The inner bands represent the statistical component of the total uncertainty, which is displayed in the outer bands. The working point $\tau_{32} < 0.46$ is displayed representing AK8 jet tagging.

Figure 8.19 shows the results from 2016 compared to a previous iteration of the measurement [9]. The measurement in this thesis shows results compatible with the old iteration for all working points of 2016. The new fit setup helps constraining the uncertainties also for the semimerged, and unmerged categories and prevents the scale factor values from fluctuating. The same holds for all scale factors obtained for the 2017 data taking period, which are presented in Ref. [2] and obtained with the same setup as used in Ref. [9]. This improvement was achieved with the introduction of new nuisance parameters that prevent large correlations between the extracted efficiencies and uncertainties in the production cross section of background processes. Since the uncertainties are dominated from contributions in the pass region, where semimerged, and unmerged contributions are suppressed, the improvement in precision is most visible in those categories. The fit also improves the precision in the merged contribution of $\mathrm{t\bar{t}}$. In addition, the analysis presented here extended the measurement to include HOTVR jets with $200 < p_\mathrm{T} < 300$ GeV, which have not been considered so far. The scale factors measured in this thesis supersede those extracted in Refs. [9] and [2] as the official correction factors for the use in CMS analyses.

The scale factors for all years and all working points are presented in Figures 8.20 and 8.21 for PUPPI and HOTVR, respectively. Figure 8.20 also includes the scale factors obtained with additional subjet b tagging. For AK8, slightly smaller scale factors are observed for all working points in the merged $\mathrm{t\bar{t}}$ category in 2017 and 2018 with respect to 2016. This is due to the difference in the modeling of τ_{32} as described above. In general, uncertainties decrease with a rising value of τ_cut because the fit uncertainty is dominated by the pass region, which is limited in statistical precision for small tagging efficiencies. This is especially visible for semimerged, and unmerged events. The scale factors for AK8 jets are close to unity and stable over the whole range in p_T. For the HOTVR algorithm, the scale factors are close to unity for all years and show consistently small uncertainties. Again, a trend to larger deviations from unity in 2017 and 2018 with respect to 2016 is observed for merged $\mathrm{t\bar{t}}$ events.

The provided scale factors are crucial for all analyses that rely on top tagging. With this analysis, a total of 414 scale factors are obtained, which are split into three event categories, three data taking periods, four p_T regions and ten working points for AK8 jets as well as six p_T regions for HOTVR jets. With the newly set up template fit, the uncertainties are largely reduced with respect to the previous measurement. All scale factors provided in this analysis supersede those extracted before and are endorsed by the CMS Collaboration for the use in analyses.

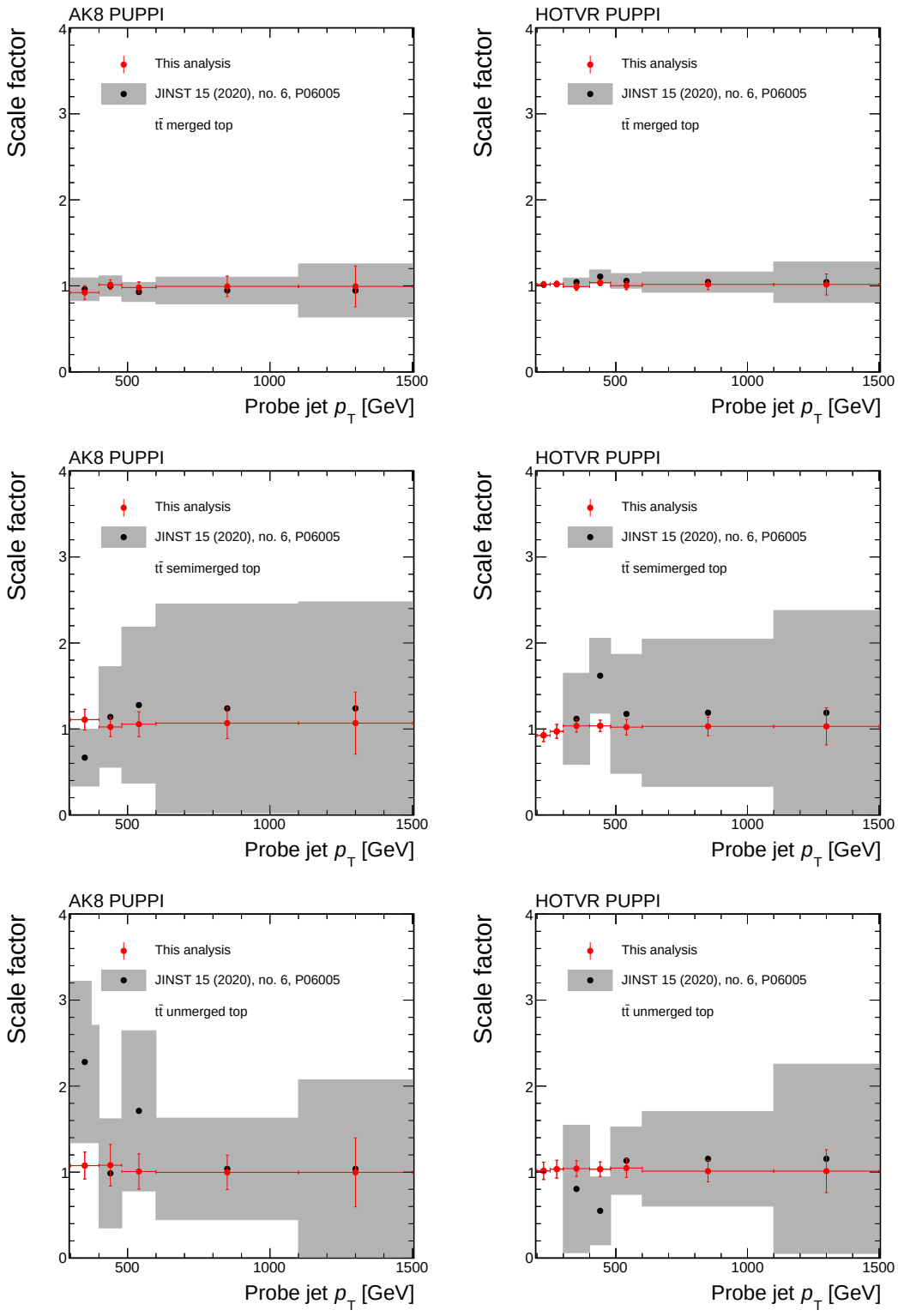

Figure 8.19: Comparison of the 2016 scale factors measured in this analysis (red markers) to those obtained in Ref. [9] (black markers) for AK8 (left) and HOTVR jets (right). The total uncertainties are presented as vertical error bars and filled areas. All three categories of $t\bar{t}$ events – merged (upper), semimerged (middle), and unmerged (lower) – are presented.

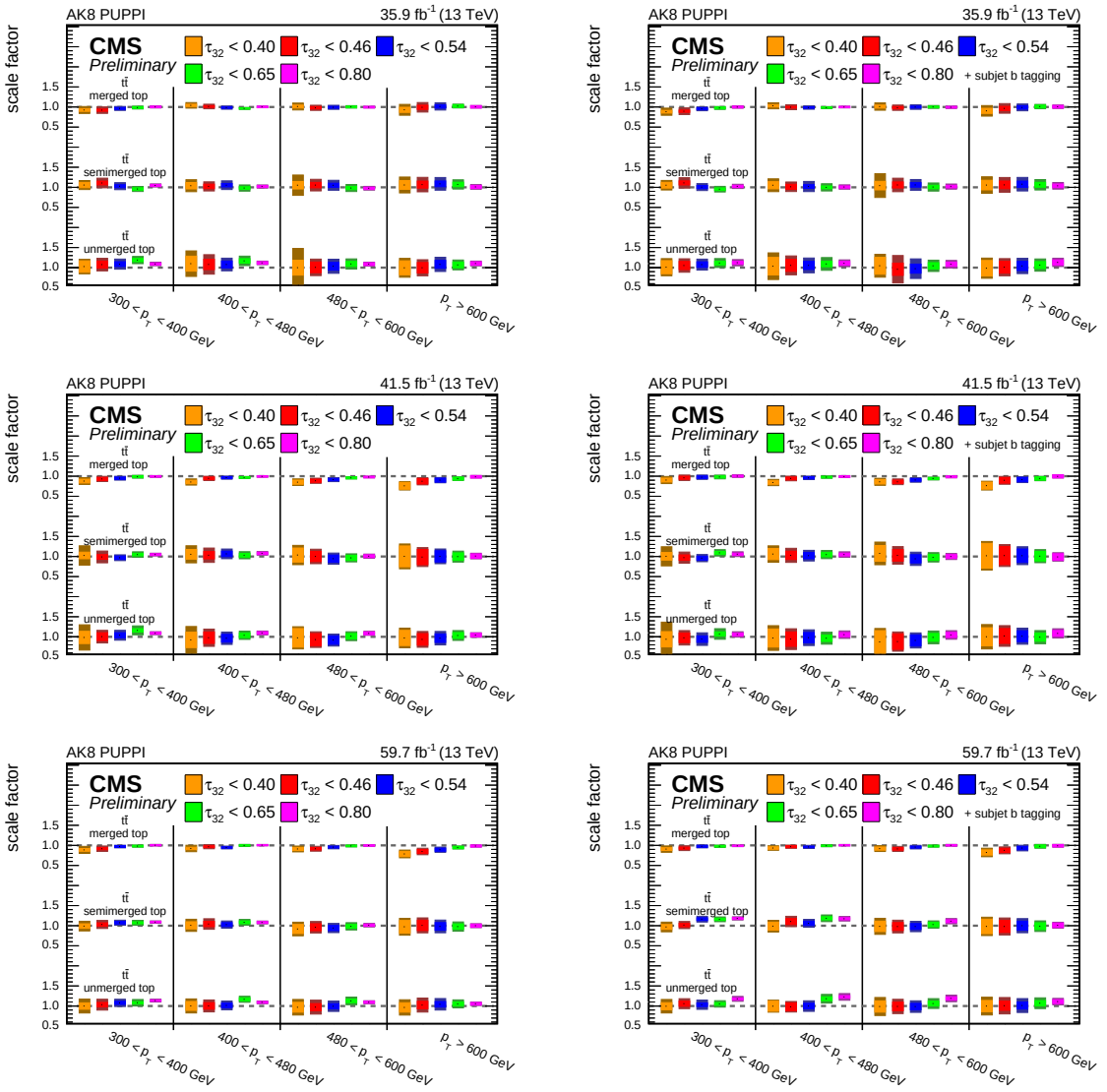

Figure 8.20: Summary of all top tagging scale factors for different working points with (right) and without (left) additional subjet b tagging for 2016 (upper), 2017 (middle), and 2018 (lower) using AK8 PUPPI jets. The scale factors are measured for the merged, semimerged, and unmerged contributions of $t\bar{t}$ events. The inner areas display the statistical uncertainties, the outer areas show the total uncertainties. Published in Ref. [10].

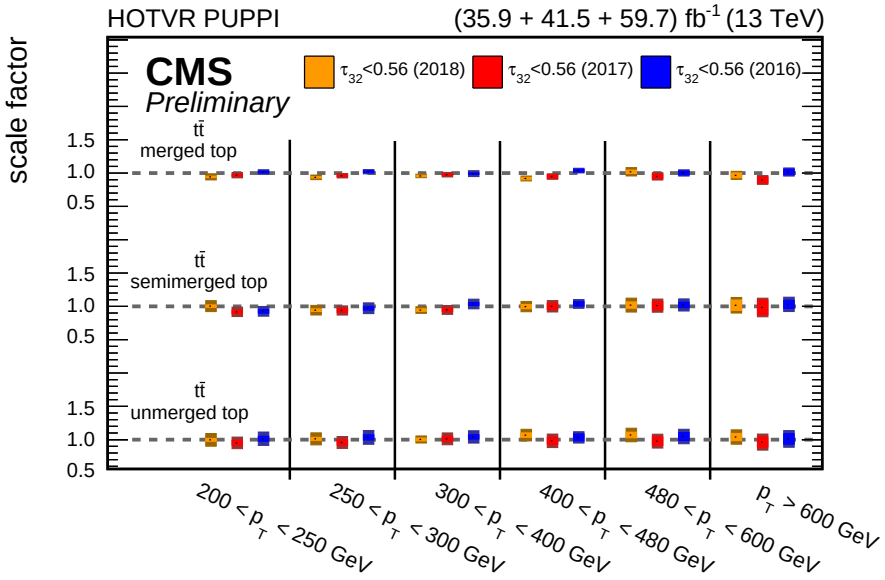

Figure 8.21: Summary of top tagging scale factors for 2016 (blue), 2017 (red), and 2018 (orange) using HOTVR PUPPI jets. The outer areas show the total uncertainty and inner areas indicate the contribution of the statistical uncertainty. The scale factors are measured for the merged, semimerged, and unmerged contributions of $t\bar{t}$ events. Published in Ref. [10].

9 | Conclusions

At the LHC, top quarks with high transverse momenta are abundantly produced, and a detailed understanding of their decay is crucial for many measurements and searches for new physics. In this thesis, two analyses focusing on hadronic decays of boosted top quarks have been presented.

First, a measurement of the jet mass distribution and top quark mass was carried out analyzing data collected by the CMS detector in 2016 and corresponding to an integrated luminosity of 35.9 fb^{-1}. Events were selected in the lepton+jets channel of the $\mathrm{t\bar{t}}$ process, where the hadronic top quark decay was reconstructed with a single jet that satisfies $p_{\mathrm{T}} > 400\,\text{GeV}$. With a novel 2-step jet clustering procedure using the XCone algorithm, the jet mass resolution was improved by a factor of 2 in both the m_{jet} width at particle level and the experimental resolution in comparison to a similar measurement at a center-of-mass energy of 8 TeV [1]. In addition, a more granular unfolding setup led to reduced modeling uncertainties. As a result, the differential $\mathrm{t\bar{t}}$ production cross section was measured as a function of the jet mass, providing important input and constraints on the modeling of jet substructure. Furthermore, the kinematic regime of collimated top quark decays allows for analytic calculations in the future. The extraction of the top quark mass of $m_{\mathrm{t}} = 172.6 \pm 2.5\,\text{GeV}$ was performed using simulated templates but can be extended to a comparison with calculations once those become available. With these calculations, this measurement promises an extraction of the top quark mass in a well-defined mass scheme to resolve ambiguities in the top quark mass definition in direct measurements. Already now, this analysis shows the potential of the boosted regime in the precise extraction of fundamental standard model parameters. Compared to direct mass measurements, the sensitivity starts to become competitive and offers an important consistency check in a kinematic region with very different systematic uncertainties than at threshold production. With a few improvements – especially constraining the jet mass scale and uncertainties in the modeling of final state radiation – this measurement could reach a sensitivity below 2 GeV with the data already recorded.

For many searches and measurements, top tagging is an important tool for the identification of jets that originate from top quarks with high momenta, and tagging algorithms have to be validated and understood. In the second analysis discussed in this thesis, a measurement of

top tagging efficiencies was presented using data collected with the CMS detector in the years 2016, 2017, and 2018, corresponding to integrated luminosities of 35.9 fb^{-1}, 41.5 fb^{-1}, and 59.7 fb^{-1}, respectively. For the analysis, the μ+jets channel of the $\text{t}\bar{\text{t}}$ process was selected by requiring a high-p_{T} muon and a b-tagged jet in the same hemisphere. A probe jet was reconstructed in the opposite hemisphere, enabling a measurement of top tagging efficiencies using a tag-and-probe method. For all three data taking periods, several tagging working points and jets clustered with the HOTVR and anti-k_{T} algorithms, the top tagging efficiencies were measured as a function of jet p_{T}. Using template fits, the efficiencies were determined for the merged, semimerged, and unmerged contributions of $\text{t}\bar{\text{t}}$ in both data and simulation. Consequently, correction factors were derived for simulation, which account for differences in tagging efficiencies compared to data. Within uncertainties all scale factors were found to be compatible with unity. In total, 414 correction factors are provided and have been endorsed by the CMS Collaboration for the use in analyses.

APPENDIX

A Measurement of electron trigger efficiencies

In the scope of the jet mass measurement and extraction of the top quark mass, the efficiencies of the combination of single electron and photon triggers are measured in data and simulation. The measurement is performed using a tag-and-probe method. Here, an event is tagged by fulfilling the single muon trigger with a p_{T} threshold of 50 GeV and the muon selection used in the measurement. An additional electron in the event acts as a probe. Scale factors f are derived which correct the efficiency in simulation to match the one observed in data. They are defined as

$$f = \frac{\varepsilon_{\mathrm{Data}}}{\varepsilon_{\mathrm{MC}}}, \tag{A.1}$$

where $\varepsilon_{\mathrm{Data}}$ and $\varepsilon_{\mathrm{MC}}$ indicate the efficiencies measured in data and simulation. The efficiencies and scale factors are measured in regions of low and high electron p_{T}, since the isolation criterion is different for electrons with p_{T} above and below 120 GeV. In addition, the measurement is performed in bins of electron η. Figure A.1 shows the trigger efficiencies measured in bins of electron η in data and simulation. For electrons with $p_{\mathrm{T}} < 120$ GeV the efficiencies in data are observed to be smaller than in simulation.

The resulting scale factors are displayed in Figure A.2. While the scale factor is compatible with unity for electrons with high p_{T}, the low-p_{T} and high-η bins show smaller values.

A closure test is presented in Figure A.3, where the scale factors are applied to simulation, and the procedure is repeated. If the scale factor does correct for all differences in tagging efficiencies the scale factors should now be compatible with unity. As expected, the closure test as a function of electron η results in scale factors of exactly unity. Also, the closure test as a function of electron p_{T} is compatible with 1.

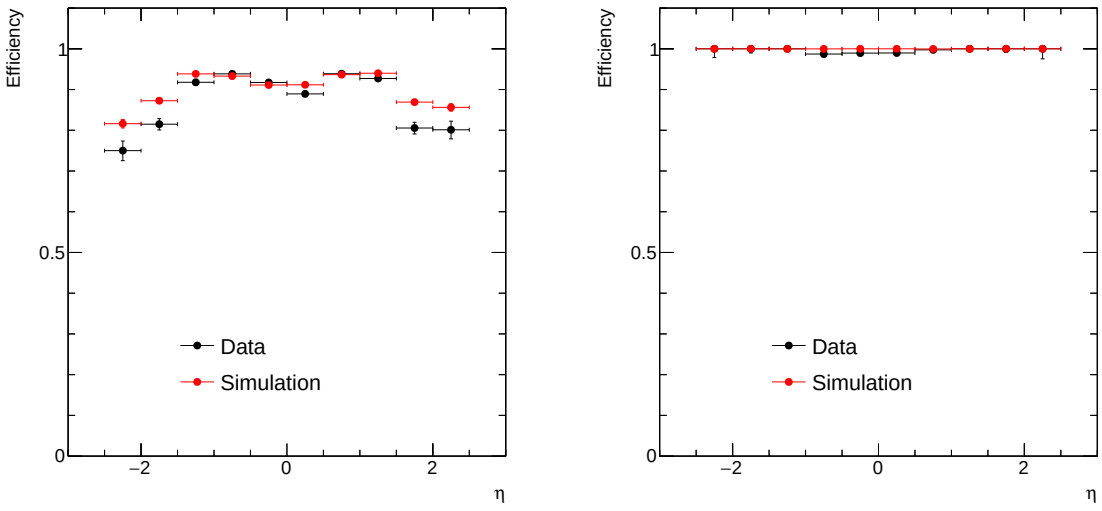

Figure A.1: Single electron trigger efficiencies in data and simulation for electrons with $p_{\mathrm{T}} < 120$ GeV (left) and $p_{\mathrm{T}} > 120$ GeV (right) as a function of η.

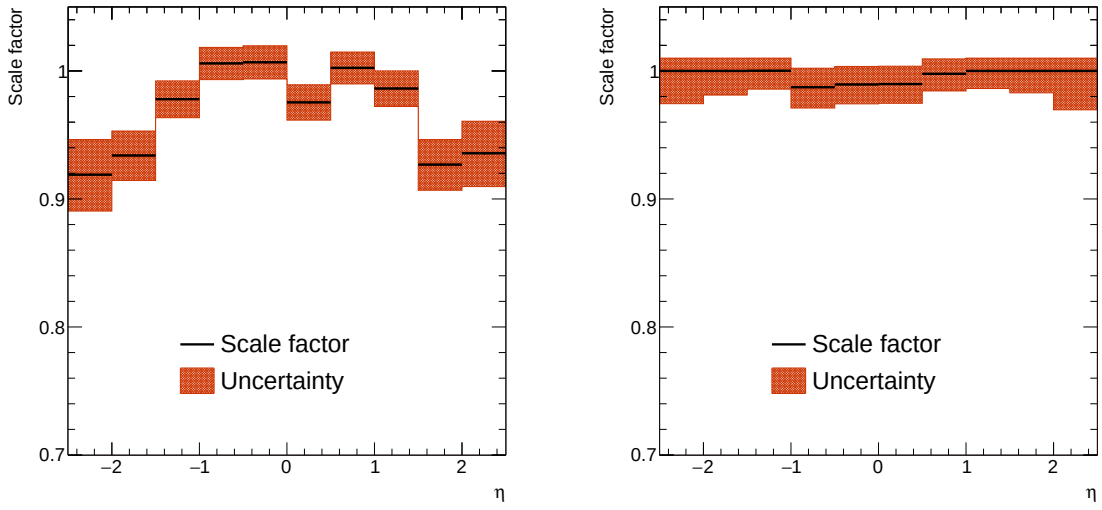

Figure A.2: Measured electron trigger scale factors for electrons with $p_{\mathrm{T}} < 120$ GeV (left) and $p_{\mathrm{T}} > 120$ GeV (right) as a function of η.

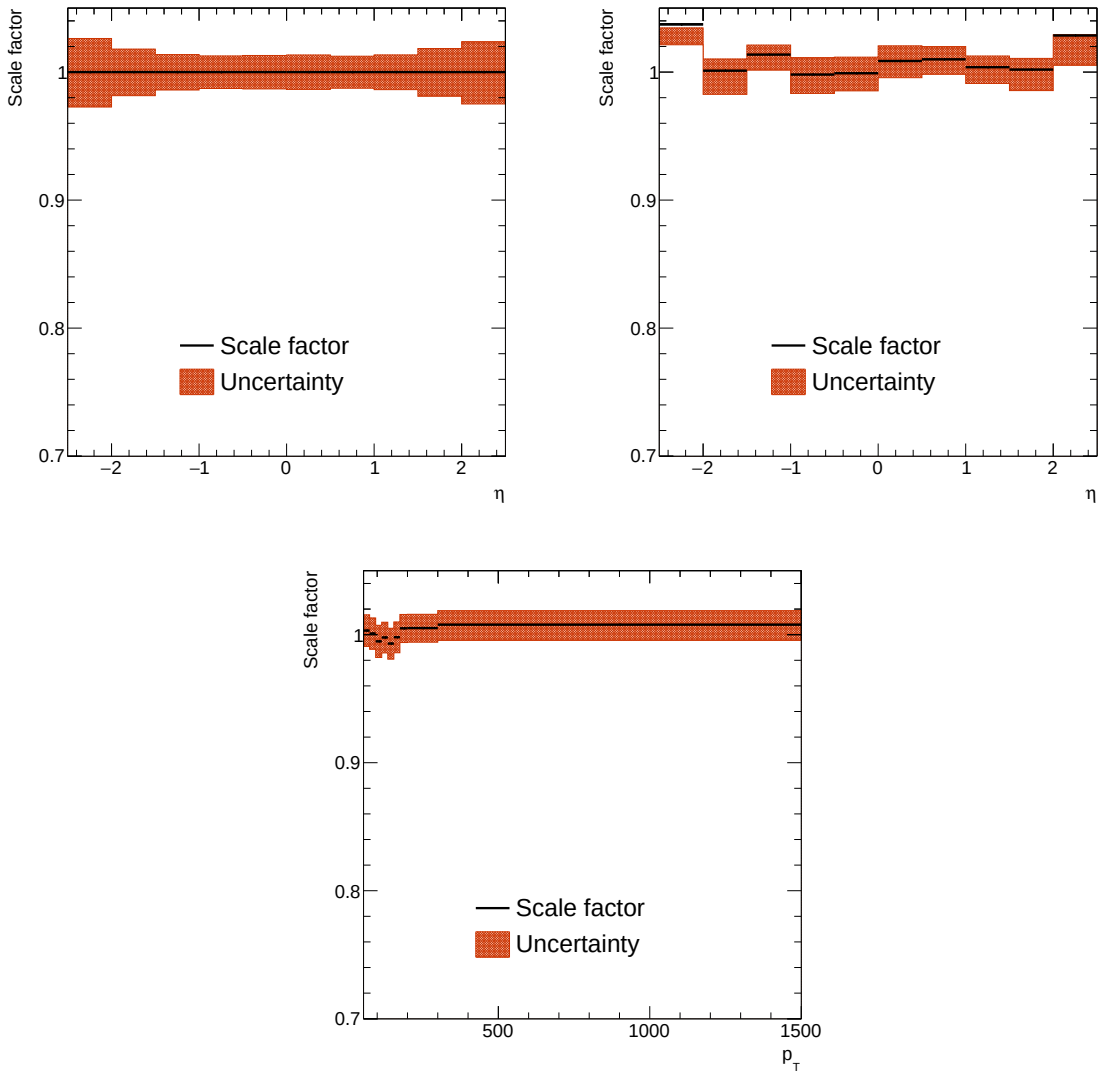

Figure A.3: Closure test after applying the scale factors for electrons with $p_{\mathrm{T}} < 120$ GeV (left) and $p_{\mathrm{T}} > 120$ GeV (right) as a function of η and as a function of electron p_{T} (lower).

B | Additional figures for the measurement of top tagging efficiencies

In this appendix, additional figures from the measurement of top tagging efficiencies are presented. Due to similar behaviors in many distributions of different data taking periods or jet clustering algorithms, not all years and jets are presented in Chapter 8. Here, the distributions of all years and jet collections are shown – also those presented in Chapter 8 – in order to enable a comparison between all three years of data taking.

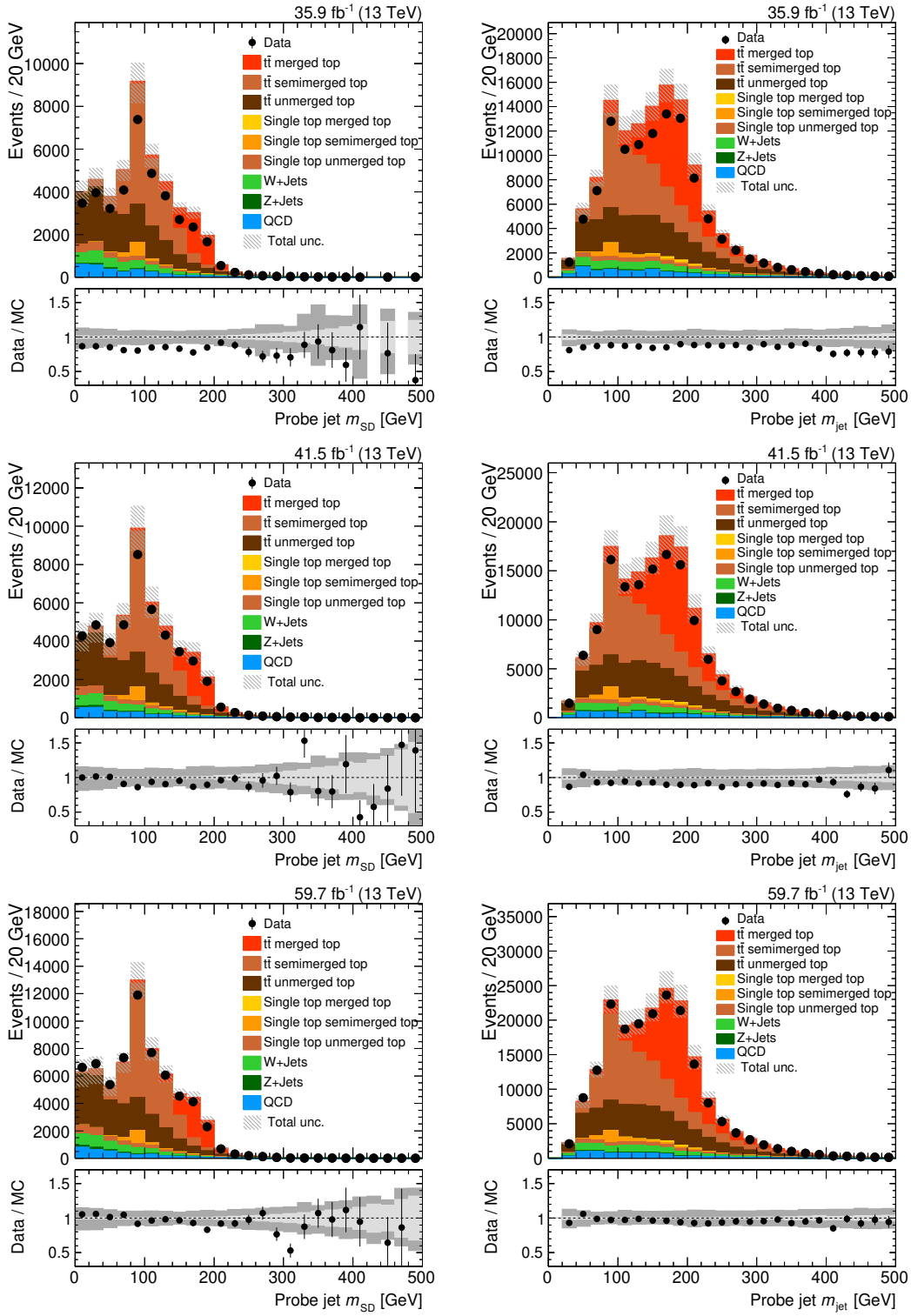

Figure B.1: Distributions of the AK8 soft drop mass m_{SD} (left) and HOTVR jet mass m_{jet} (right) obtained in the 2016 (upper), 2017 (middle), and 2018 (lower) data taking periods after the event selection. Data (markers) are compared to simulation (filled areas). The bottom panels display the ratio of events observed in data and predicted by simulation. In the upper panels, the total uncertainty is shown as hatched area, in the bottom panels the statistical uncertainty (inner area) and total uncertainty (outer area) are shown individually. Only AK8 jets with $p_T > 300$ GeV and HOTVR jets with $p_T > 200$ GeV are considered.

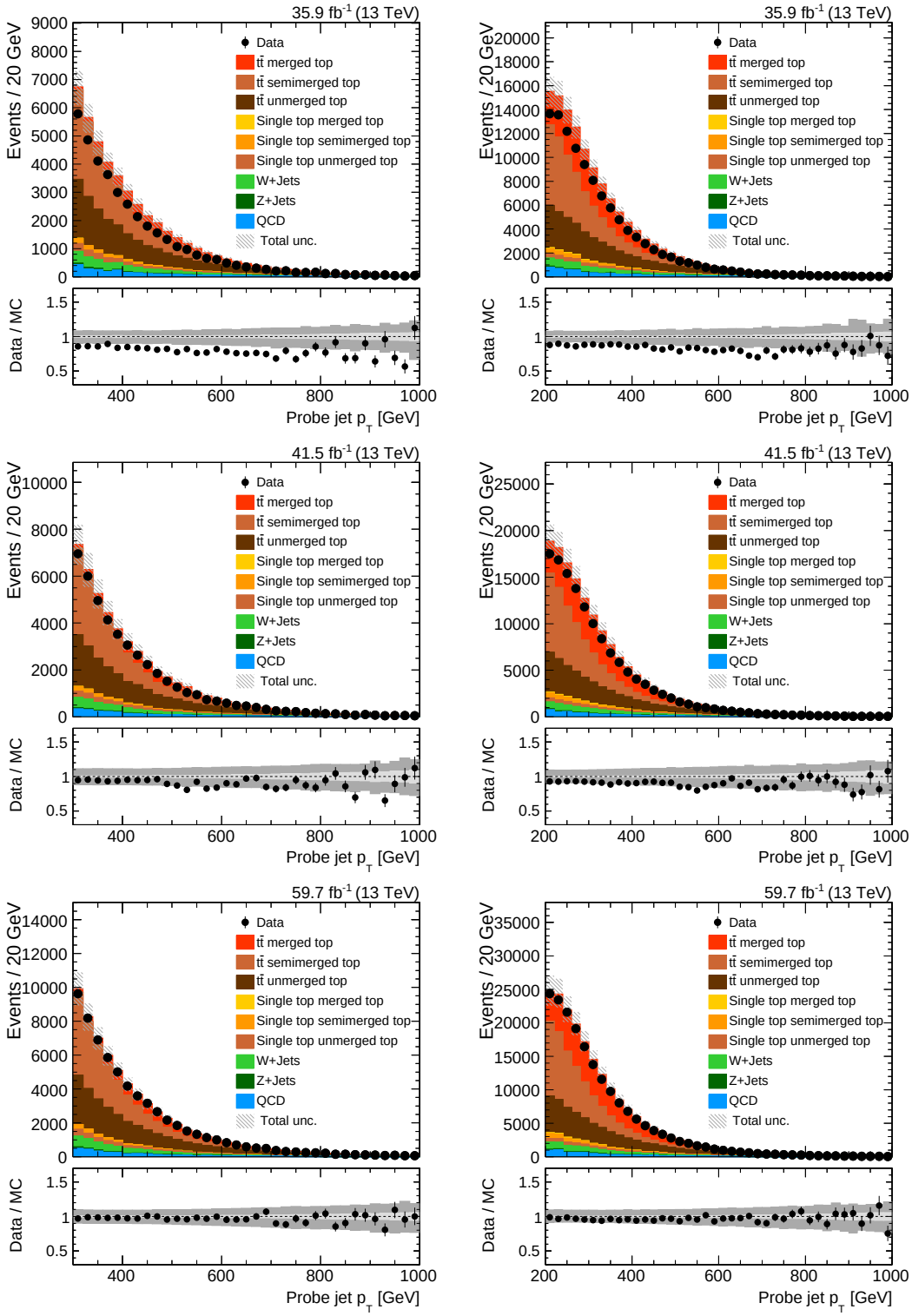

Figure B.2: Probe jet p_T distributions obtained in the 2016 (upper), 2017 (middle) and, 2018 (lower) data taking periods for AK8 (left) and HOTVR (right) jets after the event selection. Data (markers) are compared to simulation (filled areas). The bottom panels display the ratio of events observed in data and predicted by simulation. In the upper panels, the total uncertainty is shown as hatched area, in the bottom panels the statistical uncertainty (inner area) and total uncertainty (outer area) are shown individually.

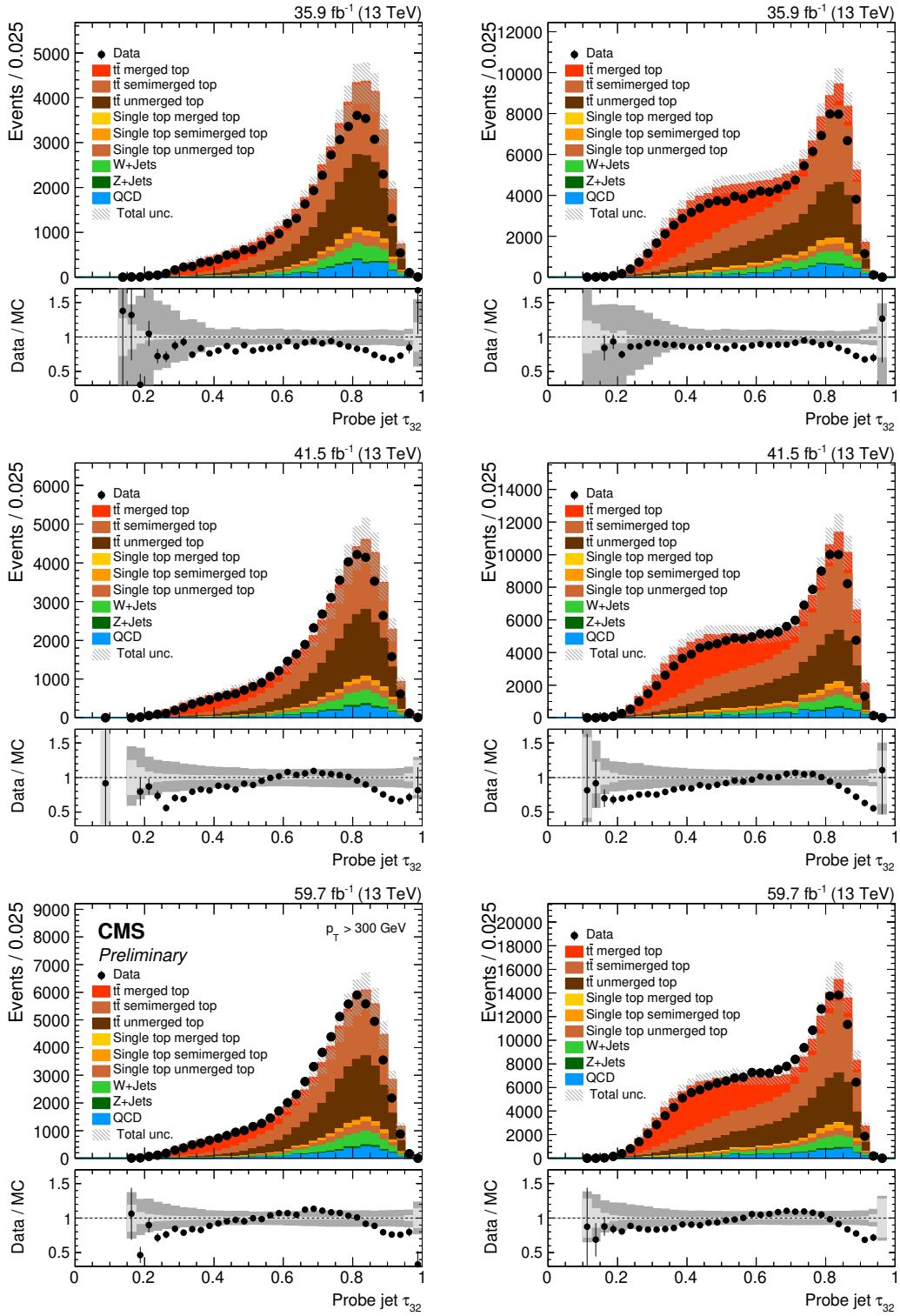

Figure B.3: Distributions in the N-subjettiness ratio τ_{32} obtained in the 2016 (upper), 2017 (middle), and 2018 (lower) data taking periods for AK8 (left) and HOTVR (right) jets after the event selection. Data (markers) are compared to simulation (filled areas). The bottom panels display the ratio of events observed in data and predicted by simulation. In the upper panels, the total uncertainty is shown as hatched area, in the bottom panels the statistical uncertainty (inner area) and total uncertainty (outer area) are shown individually. The lower left plot was published in Ref. [10].

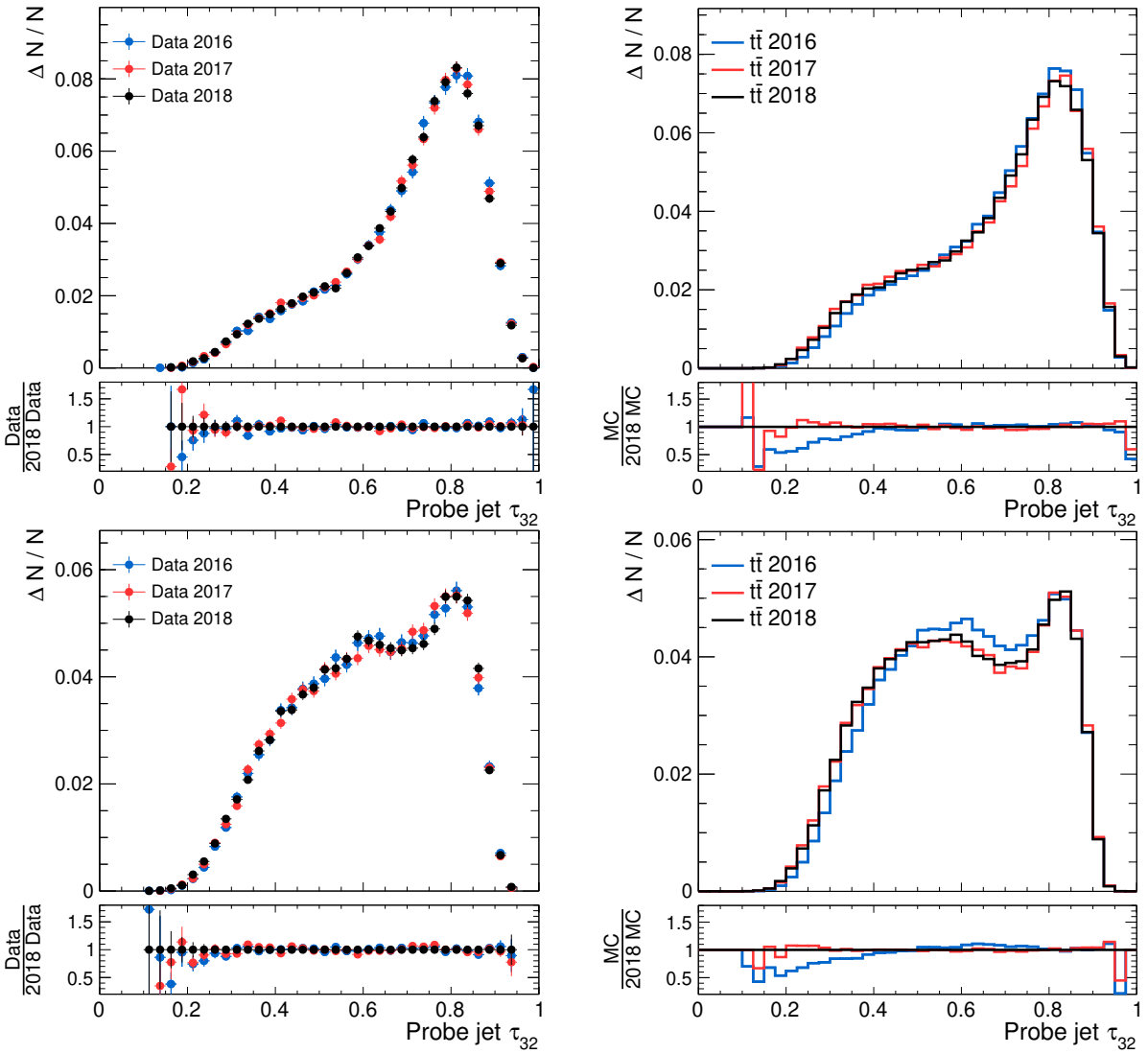

Figure B.4: The normalized distributions of the N-subjettiness ratio τ_{32} compared between the three data taking periods for data (left) and $t\bar{t}$ simulation (right) as well as for AK8 (upper) and HOTVR jets (lower) after the event selection. Only probe jets with $p_T > 400$ GeV are considered. The bottom panels show the relative difference to data collected in 2018 (left) or to the prediction from the 2018 simulation (right).

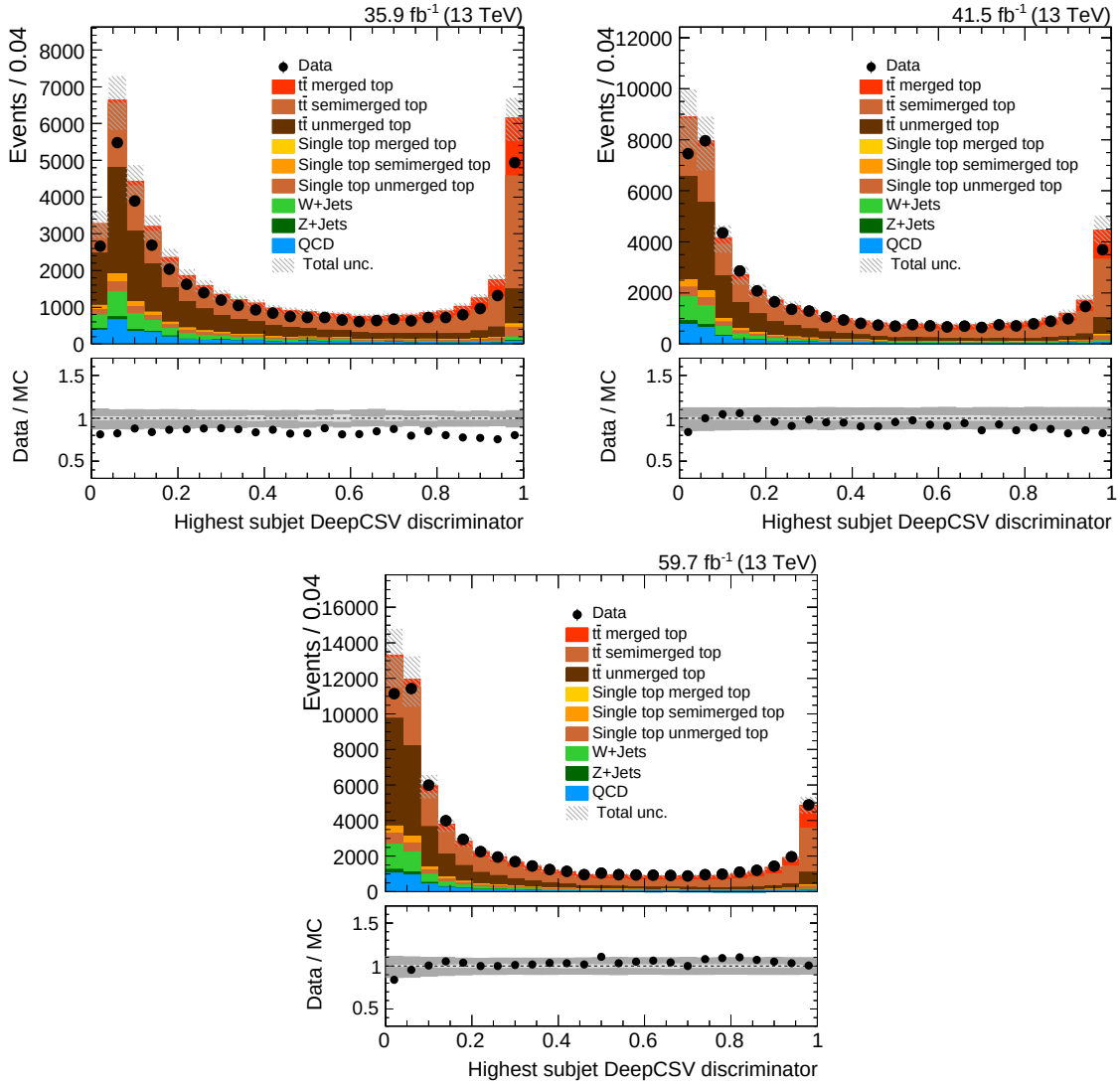

Figure B.5: Distribution of highest DeepCSV discriminator value of a subjet inside an AK8 probe jet obtained in 2016 (left), 2017 (right), and 2018 (lower). Data (markers) are compared to simulation (filled areas). The bottom panels display the ratio of events observed in data and predicted by simulation. In the upper panels, the total uncertainty is shown as hatched area, in the bottom panels the statistical uncertainty (inner area) and total uncertainty (outer area) are shown individually.

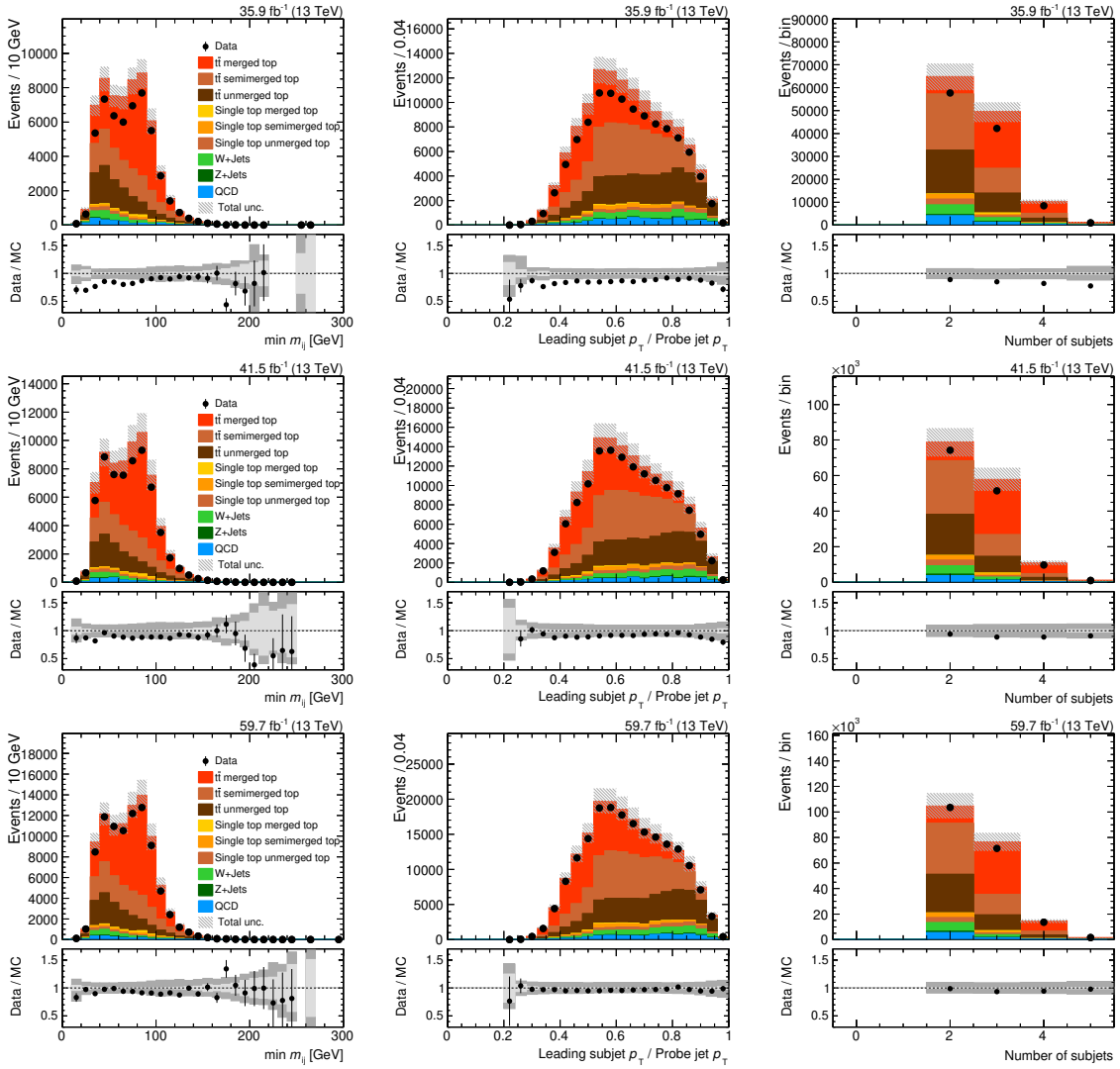

Figure B.6: Distributions of additional substructure observables used in the HOTVR algorithm for 2016 (upper), 2017 (middle), and 2018 (lower). Namely, the minimum pairwise mass of two subjets m_{ij} (left), the ratio of the leading subjet p_T and probe jet p_T (middle), as well as the number of subjets found by the HOTVR algorithm (right) are shown for data (markers) and simulation (filled areas). The bottom panels display the ratio of events observed in data and predicted by simulation. In the upper panels, the total uncertainty is shown as hatched area, in the bottom panels the statistical uncertainty (inner area) and total uncertainty (outer area) are shown individually.

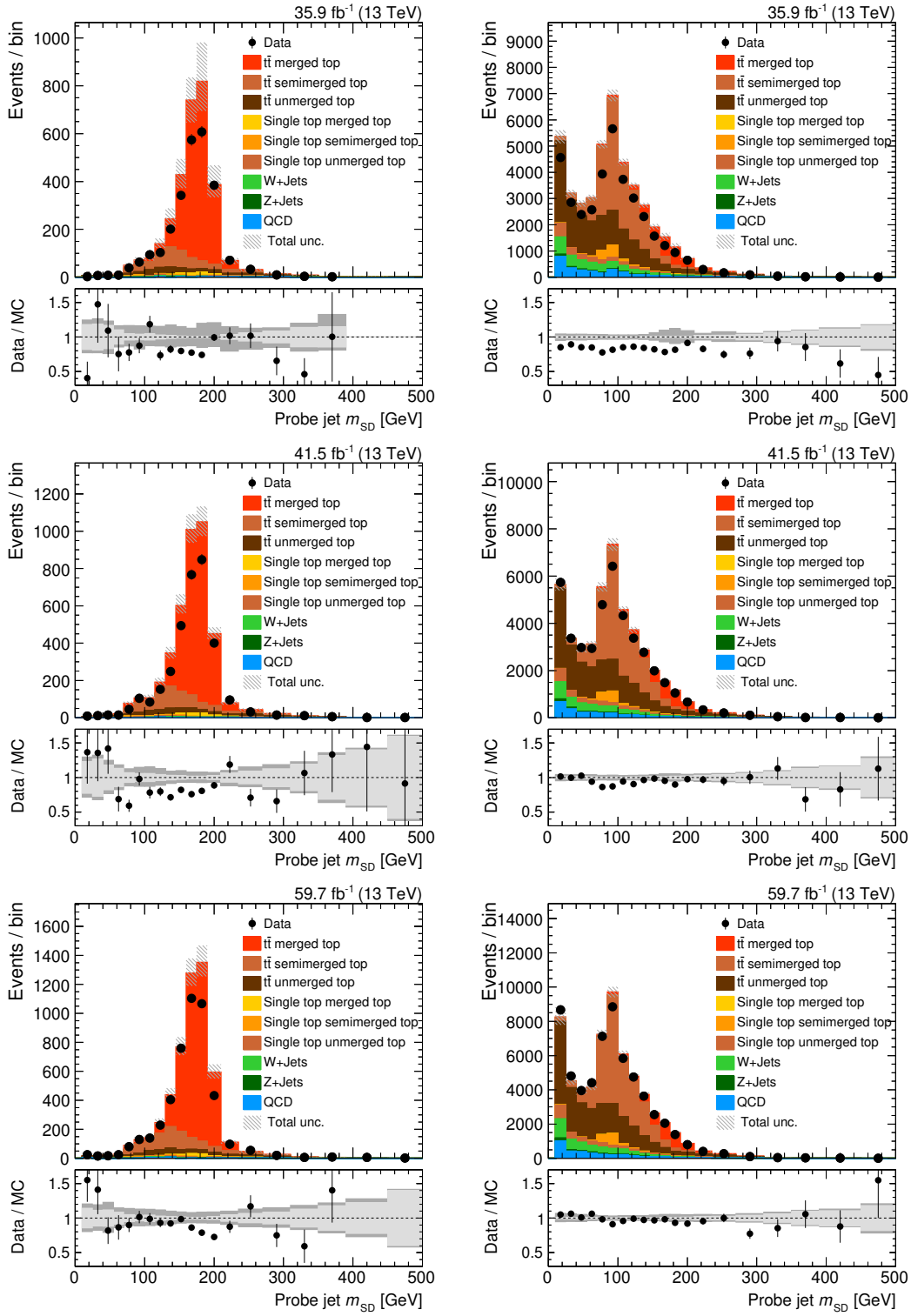

Figure B.7: Distributions of the AK8 soft drop mass m_{SD} obtained in the 2016 (upper), 2017 (middle), and 2018 (lower) data taking periods divided into passing (left) and failing (right) the requirement $\tau_{32} < 0.46$. Data (markers) are compared to simulation (filled areas). The bottom panels display the ratio of events observed in data and predicted by simulation. In the upper panels, the total uncertainty is shown as hatched area, in the bottom panels the statistical uncertainty (inner area) and total uncertainty (outer area) are shown individually. Only probe jets with $p_T > 300$ GeV are considered.

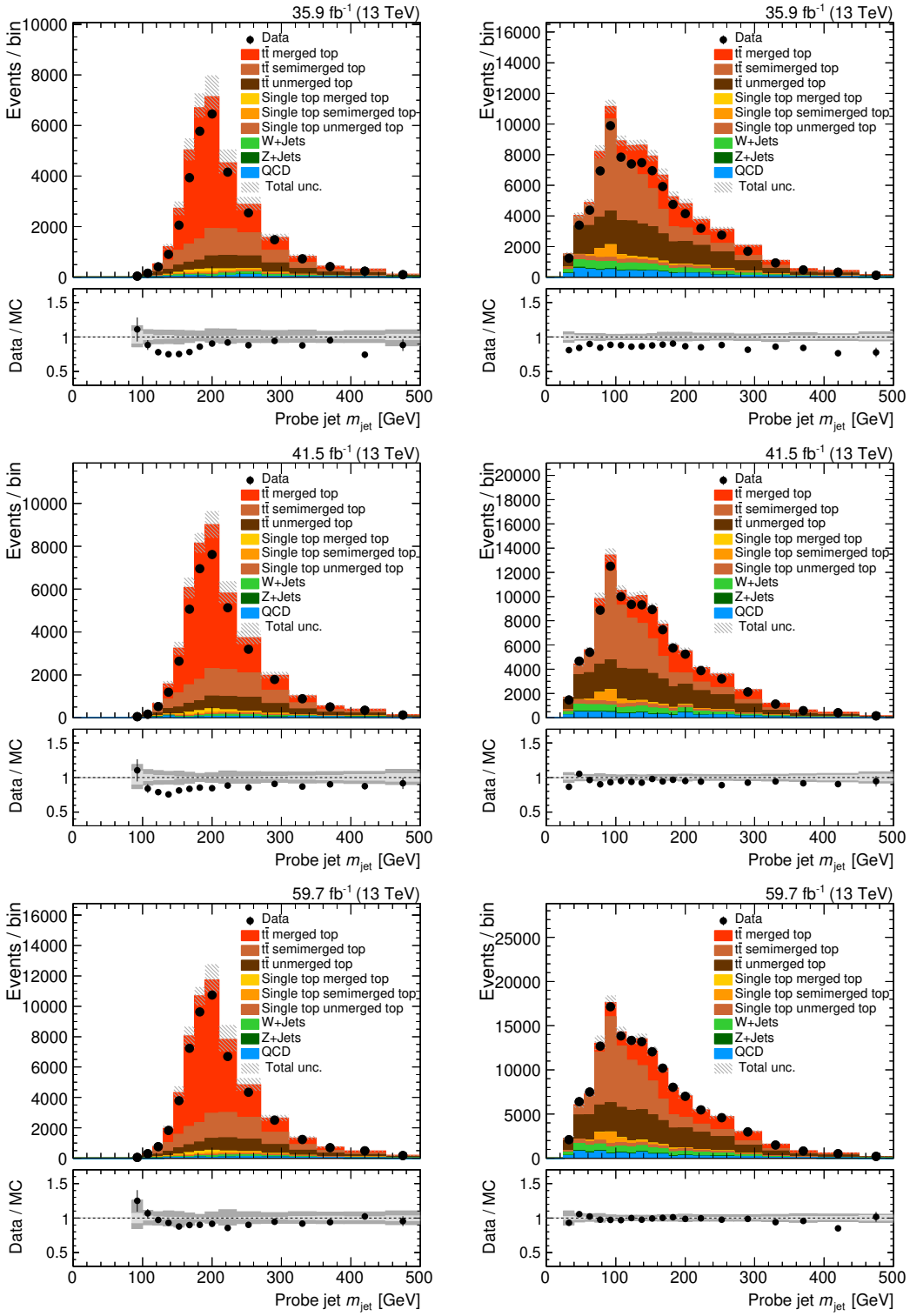

Figure B.8: Distributions of the HOTVR jet mass m_{jet} obtained in the 2016 (upper), 2017 (middle), and 2018 (lower) data taking periods divided into passing (left) and failing (right) HOTVR top tagging requirements. Data (markers) are compared to simulation (filled areas). The bottom panels display the ratio of events observed in data and predicted by simulation. In the upper panels, the total uncertainty is shown as hatched area, in the bottom panels the statistical uncertainty (inner area) and total uncertainty (outer area) are shown individually. Only probe jets with $p_{\text{T}} > 200$ GeV are considered.

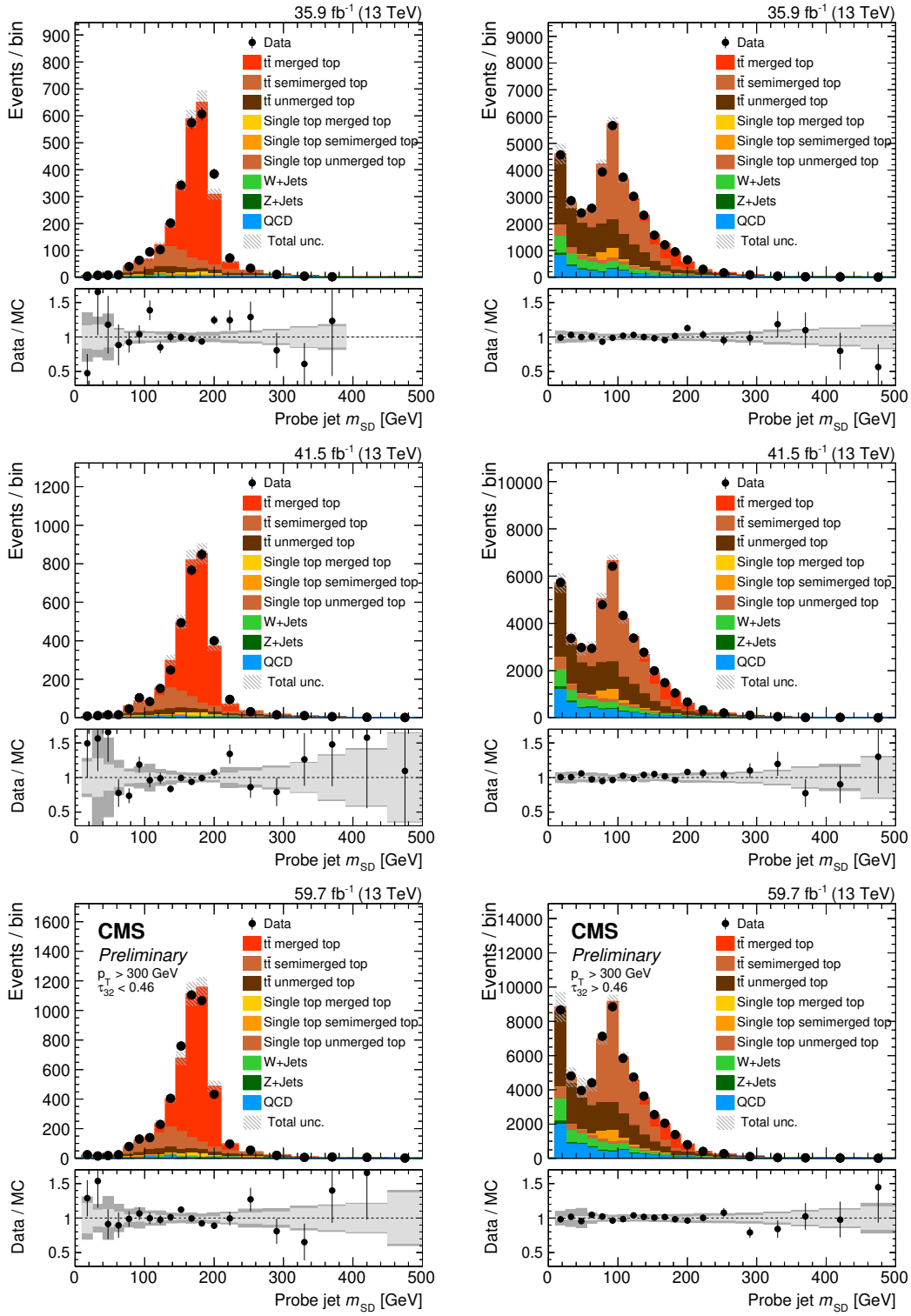

Figure B.9: Distributions in the AK8 soft drop mass m_{SD} after the template fit obtained in the 2016 (upper), 2017 (middle), and 2018 (lower) data taking periods divided into passing (left) and failing (right) the requirement $\tau_{32} < 0.46$. Data (markers) are compared to simulation (filled areas). The bottom panels display the ratio of events observed in data and predicted by simulation. In the upper panels, the total uncertainty is shown as hatched area, in the bottom panels the statistical uncertainty (inner area) and total uncertainty (outer area) are shown individually. The lower plots were published in Ref. [10].

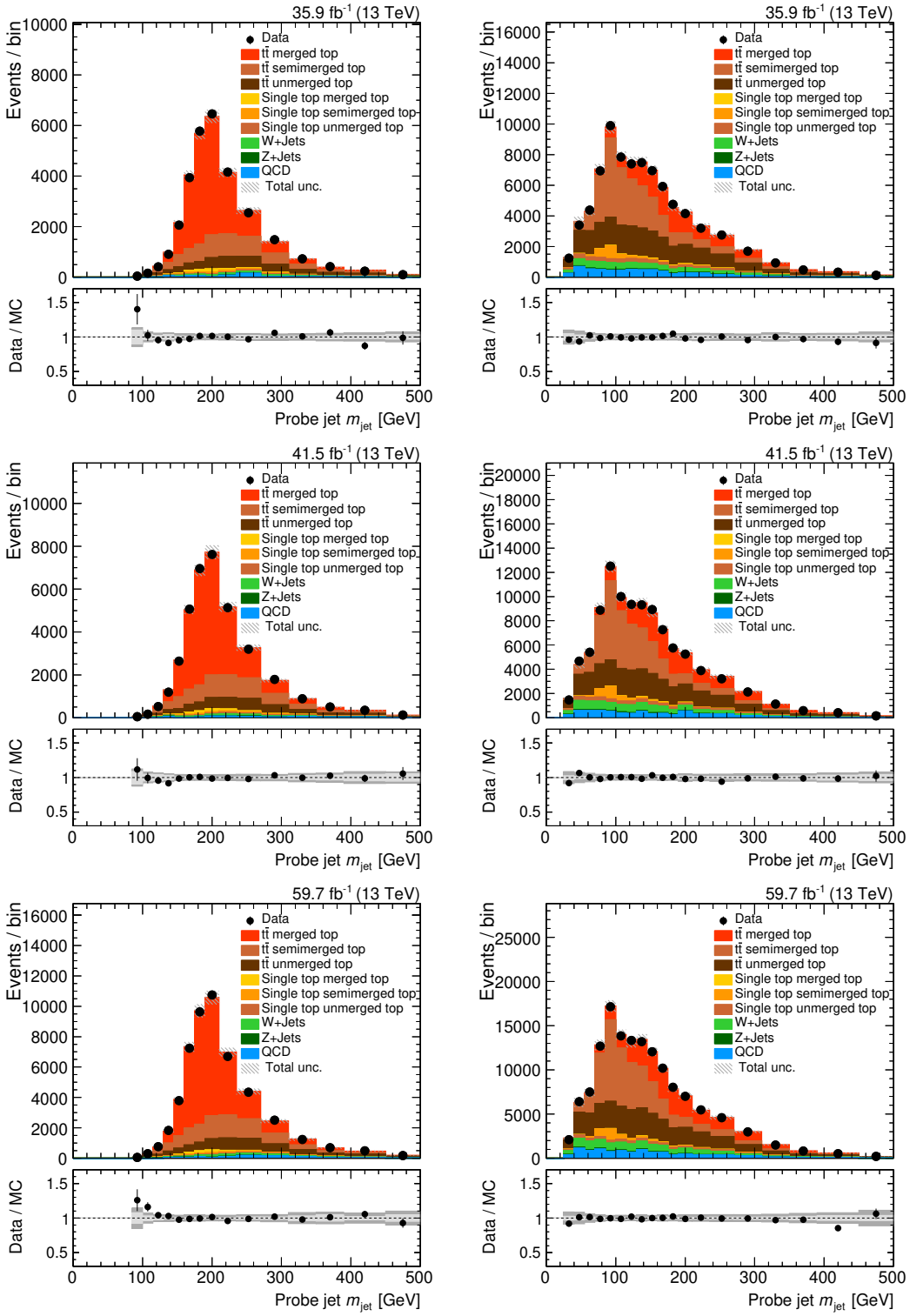

Figure B.10: Distributions in the HOTVR jet mass m_{jet} after the template fit obtained in the 2016 (upper), 2017 (middle), and 2018 (lower) data taking periods divided into passing (left) and failing (right) HOTVR top tagging requirements. Data (markers) are compared to simulation (filled areas). The bottom panels display the ratio of events observed in data and predicted by simulation. In the upper panels, the total uncertainty is shown as hatched area, in the bottom panels the statistical uncertainty (inner area) and total uncertainty (outer area) are shown individually.

Bibliography

[1] CMS Collaboration, *Measurement of the jet mass in highly boosted* $\mathrm{t\bar{t}}$ *events from pp collisions at* $\sqrt{s} = 8$ *TeV*, *Eur. Phys. J.* **C77** (2017), no. 7, 467, doi: 10.1140/epjc/s10052-017-5030-3, arXiv:1703.06330.

[2] T. Dreyer, *First measurement of the jet mass in events with highly boosted top quarks and studies with top tagging at CMS*, PhD thesis, Universität Hamburg, 2019.

[3] CMS Collaboration, *Measurement of the jet mass distribution and top quark mass in hadronic decays of boosted top quarks in pp collisions at* $\sqrt{s} = 13$ *TeV*, *Phys. Rev. Lett.* **124** (2020) 202001, doi: 10.1103/PhysRevLett.124.202001, arXiv:1911.03800.

[4] CMS Collaboration, *Boosting top-quark measurements*, *CERN Courier* **March/April** (2020).

[5] A. Paasch, *Improving the Jet Mass Reconstruction in Highly Boosted Top Quark Decays*, Bachelor's Thesis, Universität Hamburg, 2018.

[6] A. Paasch, *Towards an Improved Precision of Jet Mass Measurements in Decays of Boosted Top Quarks at CMS*, Master's thesis, Universität Hamburg, 2020.

[7] J. Skottke, *Measurement of Jet Substructure in Boosted Top Quark Decays at CMS*, Master's thesis, Universität Hamburg, 2019.

[8] S. Albrecht, *in preparation*, PhD thesis, Universität Hamburg.

[9] CMS Collaboration, *Identification of heavy, energetic, hadronically decaying particles using machine-learning techniques*, *JINST* **15** (2020), no. 06, P06005, doi: 10.1088/1748-0221/15/06/P06005, arXiv:2004.08262.

[10] CMS Collaboration, *W and top tagging scale factors for Run 2 data*, CMS Detector Performance Note CMS-DP-2020-025, (2020).

[11] D. Schwarz, *New jet tagging techniques at CMS*, *PoS* **ICHEP2020** (2020) arXiv:2012.06351. Submitted to *PoS*.

[12] CMS Collaboration, *Supplementary Material of CMS-TOP-19-005*, http://cms-results.web.cern.ch/cms-results/public-results/publications/TOP-19-005/index.html.

[13] M. Cacciari, G. P. Salam, and G. Soyez, *The anti-k_t jet clustering algorithm*, *JHEP* **04** (2008) 063, doi: 10.1088/1126-6708/2008/04/063, arXiv:0802.1189.

[14] T. Lapsien, R. Kogler, and J. Haller, *A new tagger for hadronically decaying heavy particles at the LHC*, *Eur. Phys. J.* **C76** (2016), no. 11, 600, doi: 10.1140/epjc/s10052-016-4443-8, arXiv:1606.04961.

[15] M. Thomson, *Modern particle physics*, Cambridge University Press, New York, 2013.

[16] Particle Data Group, M. Tanabashi, et al., *Review of particle physics*, *Phys. Rev. D* **98** (2018) 030001, doi: 10.1103/PhysRevD.98.030001.

[17] CMS Collaboration, *Observation of a New Boson at a Mass of 125 GeV with the CMS Experiment at the LHC*, *Phys. Lett.* **B716** (2012) 30–61, doi: 10.1016/j.physletb.2012.08.021, arXiv:1207.7235.

[18] ATLAS Collaboration, *Observation of a new particle in the search for the Standard Model Higgs boson with the ATLAS detector at the LHC*, *Phys. Lett.* **B716** (2012) 1–29, doi: 10.1016/j.physletb.2012.08.020, arXiv:1207.7214.

[19] Super-Kamiokande Collaboration, *Evidence for oscillation of atmospheric neutrinos*, *Phys. Rev. Lett.* **81** (1998) 1562–1567, doi: 10.1103/PhysRevLett.81.1562, arXiv:hep-ex/9807003.

[20] SNO Collaboration, *Measurement of the rate of $\nu_e + d \to p + p + e^-$ interactions produced by ^8B solar neutrinos at the Sudbury Neutrino Observatory*, *Phys. Rev. Lett.* **87** (2001) 071301, doi: 10.1103/PhysRevLett.87.071301, arXiv:nucl-ex/0106015.

[21] N. Cabibbo, *Unitary Symmetry and Leptonic Decays*, *Phys. Rev. Lett.* **10** (1963) 531–533, doi: 10.1103/PhysRevLett.10.531. [,648(1963)].

[22] M. Kobayashi and T. Maskawa, *CP Violation in the Renormalizable Theory of Weak Interaction*, *Prog. Theor. Phys.* **49** (1973) 652–657, doi: 10.1143/PTP.49.652.

[23] J. Ellis, M. K. Gaillard, and D. V. Nanopoulos, *A Historical Profile of the Higgs Boson. An Updated Historical Profile of the Higgs Boson*, doi: 10.1142/9789814733519_0014. Comments: 22 pages, 5 figures, update of arXiv:1201.6045, to be published in the

volume "The Standard Theory of Particle Physics", edited by Luciano Maiani and Gigi Rolandi.

[24] A. Grinbaum, *Which fine-tuning arguments are fine?*, *Found. Phys.* **42** (2012) 615–631, doi: 10.1007/s10701-012-9629-9, arXiv:0903.4055.

[25] CMS Collaboration, *Summaries of CMS cross section measurements*, https://twiki.cern.ch/twiki/bin/view/CMSPublic/PhysicsResultsCombined.

[26] P. Nason, *A New method for combining NLO QCD with shower Monte Carlo algorithms*, *JHEP* **11** (2004) 040, doi: 10.1088/1126-6708/2004/11/040, arXiv:hep-ph/0409146.

[27] S. Frixione, P. Nason, and C. Oleari, *Matching NLO QCD computations with Parton Shower simulations: the POWHEG method*, *JHEP* **11** (2007) 070, doi: 10.1088/1126-6708/2007/11/070, arXiv:0709.2092.

[28] S. Alioli, P. Nason, C. Oleari et al., *A general framework for implementing NLO calculations in shower Monte Carlo programs: the POWHEG BOX*, *JHEP* **06** (2010) 043, doi: 10.1007/JHEP06(2010)043, arXiv:1002.2581.

[29] S. Frixione, P. Nason, and G. Ridolfi, *A Positive-weight next-to-leading-order Monte Carlo for heavy flavour hadroproduction*, *JHEP* **09** (2007) 126, doi: 10.1088/1126-6708/2007/09/126, arXiv:0707.3088.

[30] J. Alwall, R. Frederix, S. Frixione et al., *The automated computation of tree-level and next-to-leading order differential cross sections, and their matching to parton shower simulations*, *JHEP* **07** (2014) 079, doi: 10.1007/JHEP07(2014)079, arXiv:1405.0301.

[31] S. Frixione and B. R. Webber, *Matching NLO QCD computations and parton shower simulations*, *JHEP* **06** (2002) 029, doi: 10.1088/1126-6708/2002/06/029, arXiv:hep-ph/0204244.

[32] T. Sjöstrand, S. Ask, J. R. Christiansen et al., *An Introduction to PYTHIA 8.2*, *Comput. Phys. Commun.* **191** (2015) 159, doi: 10.1016/j.cpc.2015.01.024, arXiv:1410.3012.

[33] G. Corcella, I. G. Knowles, G. Marchesini et al., *HERWIG 6: An Event generator for hadron emission reactions with interfering gluons (including supersymmetric processes)*, *JHEP* **01** (2001) 010, doi: 10.1088/1126-6708/2001/01/010, arXiv:hep-ph/0011363.

[34] GEANT4 Collaboration, GEANT4—*A simulation toolkit*, *Nucl. Instrum. Meth. A* **506** (2003) 250, doi: 10.1016/S0168-9002(03)01368-8.

[35] J. Allison et al., GEANT4 *developments and applications*, *IEEE Trans. Nucl. Sci.* **53** (2006) 270, doi: 10.1109/TNS.2006.869826.

[36] CDF Collaboration, *Observation of top quark production in $\bar{p}p$ collisions*, *Phys. Rev. Lett.* **74** (1995) 2626–2631, doi: 10.1103/PhysRevLett.74.2626, arXiv:hep-ex/9503002.

[37] D0 Collaboration, *Observation of the top quark*, *Phys. Rev. Lett.* **74** (1995) 2632–2637, doi: 10.1103/PhysRevLett.74.2632, arXiv:hep-ex/9503003.

[38] ATLAS Collaboration, *Measurement of the top quark mass in the $t\bar{t} \to$ dilepton channel from $\sqrt{s} = 8$ TeV ATLAS data*, *Phys. Lett. B* **761** (2016) 350–371, doi: 10.1016/j.physletb.2016.08.042, arXiv:1606.02179.

[39] CMS Collaboration, *Measurement of the top quark mass with lepton+jets final states using* p p *collisions at $\sqrt{s} = 13$ TeV*, *Eur. Phys. J. C* **78** (2018), no. 11, 891, doi: 10.1140/epjc/s10052-018-6332-9, arXiv:1805.01428.

[40] ATLAS, CDF, CMS and D0 Collaborations, *First combination of Tevatron and LHC measurements of the top-quark mass*, arXiv:1403.4427.

[41] M. Czakon and A. Mitov, *Top++: A Program for the Calculation of the Top-Pair Cross-Section at Hadron Colliders*, *Comput. Phys. Commun.* **185** (2014) 2930, doi: 10.1016/j.cpc.2014.06.021, arXiv:1112.5675.

[42] J. Ellis, *TikZ-Feynman: Feynman diagrams with TikZ*, *Comput. Phys. Commun.* **210** (2017) 103–123, doi: 10.1016/j.cpc.2016.08.019, arXiv:1601.05437.

[43] LHC Top Physics Working Group, *LHCTopWG Summary Plots*, https://twiki.cern.ch/twiki/bin/view/LHCPhysics/LHCTopWGSummaryPlots.

[44] Gfitter Group Collaboration, *The global electroweak fit at NNLO and prospects for the LHC and ILC*, *Eur. Phys. J.* **C74** (2014) 3046, doi: 10.1140/epjc/s10052-014-3046-5, arXiv:1407.3792.

[45] A. H. Hoang and I. W. Stewart, *Top Mass Measurements from Jets and the Tevatron Top-Quark Mass*, *Nucl. Phys. Proc. Suppl.* **185** (2008) 220–226, doi: 10.1016/j.nuclphysbps.2008.10.028, arXiv:0808.0222.

[46] A. H. Hoang, A. Jain, C. Lepenik et al., *The MSR mass and the $\mathcal{O}(\Lambda_{\rm QCD})$ renormalon sum rule*, *JHEP* **04** (2018) 003, doi: 10.1007/JHEP04(2018)003, arXiv:1704.01580.

[47] A. H. Hoang, *What is the Top Quark Mass?*, doi: 10.1146/annurev-nucl-101918-023530, arXiv:2004.12915.

[48] M. Cacciari, G. P. Salam, and G. Soyez, *FastJet user manual*, *Eur. Phys. J. C* **72** (2012) 1896, doi: 10.1140/epjc/s10052-012-1896-2, arXiv:1111.6097.

[49] S. Catani, Y. L. Dokshitzer, M. Seymour et al., *Longitudinally invariant K_t clustering algorithms for hadron hadron collisions*, *Nucl. Phys. B* **406** (1993) 187–224, doi: 10.1016/0550-3213(93)90166-M.

[50] S. D. Ellis and D. E. Soper, *Successive combination jet algorithm for hadron collisions*, *Phys. Rev. D* **48** (1993) 3160–3166, doi: 10.1103/PhysRevD.48.3160, arXiv:hep-ph/9305266.

[51] Y. L. Dokshitzer, G. D. Leder, S. Moretti et al., *Better jet clustering algorithms*, *JHEP* **08** (1997) 001, doi: 10.1088/1126-6708/1997/08/001, arXiv:hep-ph/9707323.

[52] M. Wobisch and T. Wengler, *Hadronization corrections to jet cross-sections in deep inelastic scattering*, in *Workshop on Monte Carlo Generators for HERA Physics (Plenary Starting Meeting)*, pp. 270–279. 4, 1998. arXiv:hep-ph/9907280.

[53] D. Krohn, J. Thaler, and L.-T. Wang, *Jets with Variable R*, *JHEP* **06** (2009) 059, doi: 10.1088/1126-6708/2009/06/059, arXiv:0903.0392.

[54] M. Stoll, *Vetoed jet clustering: The mass-jump algorithm*, *JHEP* **04** (2015) 111, doi: 10.1007/JHEP04(2015)111, arXiv:1410.4637.

[55] K. Hamaguchi, S. P. Liew, and M. Stoll, *How to decontaminate overlapping fat jets*, *Phys. Rev.* **D92** (2015), no. 1, 015012, doi: 10.1103/PhysRevD.92.015012, arXiv:1505.02930.

[56] I. W. Stewart, F. J. Tackmann, J. Thaler et al., *XCone: N-jettiness as an Exclusive Cone Jet Algorithm*, *JHEP* **11** (2015) 072, doi: 10.1007/JHEP11(2015)072, arXiv:1508.01516.

[57] A. J. Larkoski, S. Marzani, G. Soyez et al., *Soft Drop*, *JHEP* **05** (2014) 146, doi: 10.1007/JHEP05(2014)146, arXiv:1402.2657.

[58] M. Dasgupta, A. Fregoso, S. Marzani et al., *Towards an understanding of jet substructure*, *JHEP* **09** (2013) 029, doi: 10.1007/JHEP09(2013)029, arXiv:1307.0007.

[59] S. Fleming, A. H. Hoang, S. Mantry et al., *Jets from massive unstable particles: Top-mass determination*, *Phys. Rev.* **D77** (2008) 074010, doi: 10.1103/PhysRevD.77.074010, arXiv:hep-ph/0703207.

[60] C. W. Bauer, D. Pirjol, and I. W. Stewart, *Soft collinear factorization in effective field theory*, *Phys. Rev. D* **65** (2002) 054022, doi: 10.1103/PhysRevD.65.054022, arXiv:hep-ph/0109045.

[61] C. W. Bauer and I. W. Stewart, *Invariant operators in collinear effective theory*, *Phys. Lett. B* **516** (2001) 134–142, doi: 10.1016/S0370-2693(01)00902-9, arXiv:hep-ph/0107001.

[62] A. H. Hoang, S. Mantry, A. Pathak et al., *Extracting a short distance top mass with light grooming*, *Phys. Rev. D* **100** (2019) 074021, doi: 10.1103/PhysRevD.100.074021, arXiv:1708.02586.

[63] J. Thaler and K. Van Tilburg, *Identifying Boosted Objects with N-subjettiness*, *JHEP* **03** (2011) 015, doi: 10.1007/JHEP03(2011)015, arXiv:1011.2268.

[64] A. J. Larkoski, S. Marzani, and J. Thaler, *Sudakov Safety in Perturbative QCD*, *Phys. Rev.* **D91** (2015), no. 11, 111501, doi: 10.1103/PhysRevD.91.111501, arXiv:1502.01719.

[65] CMS Collaboration, *Measurements of the differential jet cross section as a function of the jet mass in dijet events from proton-proton collisions at* $\sqrt{s} = 13$ *TeV*, *JHEP* **11** (2018) 113, doi: 10.1007/JHEP11(2018)113, arXiv:1807.05974.

[66] ATLAS Collaboration, *Measurement of the Soft-Drop Jet Mass in pp Collisions at* $\sqrt{s} = 13$ *TeV with the ATLAS Detector*, *Phys. Rev. Lett.* **121** (2018), no. 9, 092001, doi: 10.1103/PhysRevLett.121.092001, arXiv:1711.08341.

[67] ATLAS Collaboration, *Measurement of jet-substructure observables in top quark, W boson and light jet production in proton-proton collisions at* $\sqrt{s} = 13$ *TeV with the ATLAS detector*, *JHEP* **08** (2019) 033, doi: 10.1007/JHEP08(2019)033, arXiv:1903.02942.

[68] CMS Collaboration, *Measurement of jet substructure observables in* $\mathrm{t\bar{t}}$ *events from proton-proton collisions at* $\sqrt{s} = 13TeV$, *Phys. Rev. D* **98** (2018), no. 9, 092014, doi: 10.1103/PhysRevD.98.092014, arXiv:1808.07340.

[69] E. Mobs, *The CERN accelerator complex - 2019. Complexe des accélérateurs du CERN - 2019*, . General Photo.

[70] CMS Collaboration, *The CMS experiment at the CERN LHC*, *JINST* **3** (2008) S08004, doi: 10.1088/1748-0221/3/08/S08004.

[71] CMS Collaboration, *CMS detector design*, http://cms.web.cern.ch/news/cms-detector-design.

[72] P. Adzic et al., *Energy resolution of the barrel of the CMS electromagnetic calorimeter*, *JINST* **2** (2007) P04004, doi: 10.1088/1748-0221/2/04/P04004.

[73] USCMS, ECAL/HCAL Collaboration, *The CMS barrel calorimeter response to particle beams from 2-GeV/c to 350-GeV/c*, *Eur. Phys. J.* **C60** (2009) 359–373, doi: 10.1140/epjc/s10052-009-0959-5,10.1140/epjc/s10052-009-1024-0. [Erratum: Eur. Phys. J.C61,353(2009)].

[74] G. CMS Collaboration (Bayatian, D. Bailey, J. Brooke et al., *The TriDAS Project - Technical Design Report, Volume 1: The Trigger Systems: TDR 6.1*, workingpaper, CMS, (2000).

[75] CMS Collaboration, *CMS The TriDAS Project: Technical Design Report, Volume 2: Data Acquisition and High-Level Trigger. CMS trigger and data-acquisition project*, Technical Design Report CMS, CERN, Geneva, 2002.

[76] CMS Collaboration, *Particle-flow reconstruction and global event description with the CMS detector*, *JINST* **12** (2017) P10003, doi: 10.1088/1748-0221/12/10/P10003, arXiv:1706.04965.

[77] D. Barney, *CMS Detector Slice*, https://cds.cern.ch/record/2120661, 2016.

[78] CMS Collaboration, *Performance of the CMS muon detector and muon reconstruction with proton-proton collisions at* $\sqrt{s} = 13$ *TeV*, *JINST* **13** (2018), no. 06, P06015, doi: 10.1088/1748-0221/13/06/P06015, arXiv:1804.04528.

[79] CMS Collaboration, *Performance of Electron Reconstruction and Selection with the CMS Detector in Proton-Proton Collisions at $\sqrt{s}$ = 8 TeV*, *JINST* **10** (2015), no. 06, P06005, doi: 10.1088/1748-0221/10/06/P06005, arXiv:1502.02701.

[80] CMS Collaboration, *Identification of heavy-flavour jets with the CMS detector in pp collisions at 13 TeV*, *JINST* **13** (2018) P05011, doi: 10.1088/1748-0221/13/05/P05011, arXiv:1712.07158.

[81] CMS Collaboration, *Performance of b tagging algorithms in proton-proton collisions at 13 TeV with Phase 1 CMS detector*, CMS Detector Performance Note CMS-DP-2018-033, (2018).

[82] CMS Collaboration, *Pileup Removal Algorithms*, CMS-PAS-JME-14-001, CERN, Geneva, (2014).

[83] D. Bertolini, P. Harris, M. Low et al., *Pileup Per Particle Identification*, *JHEP* **10** (2014) 059, doi: 10.1007/JHEP10(2014)059, arXiv:1407.6013.

[84] CMS Collaboration, *Pileup mitigation at CMS in 13 TeV data*, *JINST* **15** (2020), no. 09, P09018, doi: 10.1088/1748-0221/15/09/P09018, arXiv:2003.00503.

[85] CMS Collaboration, *Jet energy scale and resolution in the CMS experiment in pp collisions at 8 TeV*, *JINST* **12** (2017) P02014, doi: 10.1088/1748-0221/12/02/P02014, arXiv:1607.03663.

[86] CMS Collaboration, *Jet energy scale and resolution performance with 13 TeV data collected by CMS in 2016-2018*, CMS Detector Performance Note CMS-DP-2020-019, (2020).

[87] CMS Collaboration, *Public CMS luminosity information*, https://twiki.cern.ch/twiki/bin/view/CMSPublic/LumiPublicResults.

[88] Y. Li and F. Petriello, *Combining QCD and electroweak corrections to dilepton production in FEWZ*, *Phys. Rev. D* **86** (2012) 094034, doi: 10.1103/PhysRevD.86.094034, arXiv:1208.5967.

[89] R. Frederix and S. Frixione, *Merging meets matching in MC@NLO*, *JHEP* **12** (2012) 061, doi: 10.1007/JHEP12(2012)061, arXiv:1209.6215.

[90] J. Alwall, H. S., F. Krauss et al., *Comparative study of various algorithms for the merging of parton showers and matrix elements in hadronic collisions*, *Eur. Phys. J. C* **53** (2008) 473, doi: 10.1140/epjc/s10052-007-0490-5, arXiv:0706.2569.

[91] CMS Collaboration, *Extraction and validation of a new set of CMS PYTHIA8 tunes from underlying-event measurements*, *Eur. Phys. J. C* **80** (2020) 4, doi: 10.1140/epjc/s10052-019-7499-4, arXiv:1903.12179.

[92] CMS Collaboration, *Event generator tunes obtained from underlying event and multiparton scattering measurements*, *Eur. Phys. J. C* **76** (2016) 155, doi: 10.1140/epjc/s10052-016-3988-x, arXiv:1512.00815.

[93] P. Skands, S. Carrazza, and J. Rojo, *Tuning PYTHIA 8.1: the Monash 2013 Tune*, *Eur. Phys. J. C* **74** (2014) 3024, doi: 10.1140/epjc/s10052-014-3024-y, arXiv:1404.5630.

[94] J. Thaler and T. F. Wilkason, *Resolving Boosted Jets with XCone*, *JHEP* **12** (2015) 051, doi: 10.1007/JHEP12(2015)051, arXiv:1508.01518.

[95] I. W. Stewart, F. J. Tackmann, and W. J. Waalewijn, *N-Jettiness: An Inclusive Event Shape to Veto Jets*, *Phys. Rev. Lett.* **105** (2010) 092002, doi: 10.1103/PhysRevLett.105.092002, arXiv:1004.2489.

[96] CMS Collaboration, *Measurement of the jet mass distribution in highly boosted top quark decays in pp collisions at* $\sqrt{s} = 13$ *TeV*, CMS-PAS-TOP-19-005, CERN, Geneva, (2019).

[97] CMS Collaboration, *Performance of the CMS muon detector and muon reconstruction with proton-proton collisions at* $\sqrt{s} = 13$ *TeV*, *JINST* **13** (2018), no. 06, P06015, doi: 10.1088/1748-0221/13/06/P06015, arXiv:1804.04528.

[98] CMS Collaboration, *Electron and photon performance in CMS with the full 2016 data sample.*, CMS Detector Performance Note CMS-DP-2017-004, (2017).

[99] CMS Collaboration, *Performance of electron and photon reconstruction in Run 2 with the CMS experiment*, CMS Detector Performance Note CMS-DP-2020-037, (2020).

[100] ATLAS Collaboration, *Measurement of the differential cross-section of highly boosted top quarks as a function of their transverse momentum in* $\sqrt{s} = 8$ *TeV proton-proton collisions using the ATLAS detector*, *Phys. Rev. D* **93** (2016) 032009, doi: 10.1103/PhysRevD.93.032009, arXiv:1510.03818.

[101] ATLAS Collaboration, *Measurements of $t\bar{t}$ differential cross-sections of highly boosted top quarks decaying to all-hadronic final states in pp collisions at $\sqrt{s} = 13$ TeV using the ATLAS detector*, *Phys. Rev. D* **98** (2018) 012003, doi: 10.1103/PhysRevD.98.012003, arXiv:1801.02052.

[102] CMS Collaboration, *Measurement of the integrated and differential $t\bar{t}$ production cross sections for high-p_{T} top quarks in pp collisions at $\sqrt{s} = 8$ TeV*, *Phys. Rev. D* **94** (2016) 072002, doi: 10.1103/PhysRevD.94.072002, arXiv:1605.00116.

[103] CMS Collaboration, *Measurement of differential cross sections for the production of top quark pairs and of additional jets in lepton+jets events from pp collisions at $\sqrt{s} = 13$ TeV*, *Phys. Rev. D* **97** (2018) 112003, doi: 10.1103/PhysRevD.97.112003, arXiv:1803.08856.

[104] S. Schmitt, *TUnfold: an algorithm for correcting migration effects in high energy physics*, *JINST* **7** (2012) T10003, doi: 10.1088/1748-0221/7/10/T10003, arXiv:1205.6201.

[105] NNPDF Collaboration, *Parton distributions for the LHC Run II*, *JHEP* **04** (2015) 040, doi: 10.1007/JHEP04(2015)040, arXiv:1410.8849.

[106] S. Argyropoulos and T. Sjöstrand, *Effects of color reconnection on $t\bar{t}$ final states at the LHC*, *JHEP* **11** (2014) 043, doi: 10.1007/JHEP11(2014)043, arXiv:1407.6653.

[107] J. R. Christiansen and P. Z. Skands, *String formation beyond leading colour*, *JHEP* **08** (2015) 003, doi: 10.1007/JHEP08(2015)003, arXiv:1505.01681.

[108] T. Sjöstrand and M. van Zijl, *A multiple interaction model for the event structure in hadron collisions*, *Phys. Rev. D* **36** (1987) 2019, doi: 10.1103/PhysRevD.36.2019.

[109] ATLAS Collaboration, CMS Collaboration and LHC Higgs Combination Group, *Procedure for the LHC Higgs boson search combination in Summer 2011*, CMS-NOTE-2011-005. ATL-PHYS-PUB-2011-11, (2011).

[110] J. Ott, THETA—*A framework for template-based modeling and inference*, 2010.

Danksagung

Zunächst möchte ich Johannes Haller dafür danken, dass er mich in seine Forschungsgruppe aufgenommen und mir ermöglicht hat, sowohl meine Bachelorarbeit, Masterarbeit als auch Dissertation bei ihm zu schreiben. Am Anfang meines Studiums hätte ich nie gedacht, dass es für mich einmal zum Arbeitsalltag gehören wird, sich Woche für Woche mit Kolleg:innen aus aller Welt auszutauschen und eigene Resultate auf internationalen Konferenzen zu präsentieren. Danke, Johannes, dass du mir diese Möglichkeiten eröffnet hast. Außerdem möchte ich dir für all die anregenden Gespräche, Tipps und Expertisen danken, die mich bei meiner Forschung unterstützt haben.

Ich danke Elisabetta Gallo für die Übernahme des Zweitgutachtens und Günter Sigl, Christian Schwanenberger sowie Peter Schleper für das Komplettieren meiner Prüfungskommission.

Roman Kogler möchte ich für seine umfangreiche Hilfe, lange Gespräche, gute Laune und das Lesen diverser Texte – inklusive dieser Arbeit – danken. Durch unsere Diskussionen habe ich vieles erst richtig verstanden und neu entdeckt. Es war mir eine Freude mit dir über Jets, Top-Quarks, Parton Shower, Fußball und Musik zu sprechen.

I would like to thank all present and past members of our group and especially all of my office colleagues for the good atmosphere, the discussions during lunch breaks, coffee breaks in the kitchen, coffee breaks on the sofa, or a beer after work. A lot of my questions were answered by you all! Also, you made travels to conferences always special and much more fun.

Mareike Meyer, Dominik Nowatschin, Heiner Tholen, Simon Kurz, and Torben Dreyer, thank you for all the help during the end of my Master's and beginning of my PhD. Thank you, Anna Benecke and Anna Albrecht, for the great time in our office. Thanks to my Maria-Laach-colleague and flatmate during DPG, Alexander Fröhlich. Andrea Malara, thank you for all the pizza, pasta and JEC/JER advice. Alexander Paasch and Jan Skottke, it was a pleasure working with you during your Master's projects. An extra special 'Thank you!' goes to you, Arne Reimers, for reading my thesis, many answered questions, and all the good times in and outside the office.

Meiner Familie und Inga möchte ich für die Unterstützung in den letzten Jahren danken. Ihr wart immer für mich da und ich konnte mich auf euch verlassen!

Eidesstattliche Erklärung / Declaration on oath

Hiermit versichere ich an Eides statt, die vorliegende Dissertationsschrift selbst verfasst und keine anderen als die angegebenen Hilfsmittel und Quellen benutzt zu haben. Die eingereichte schriftliche Fassung entspricht der auf dem elektronischen Speichermedium. Die Dissertation wurde in der vorgelegten oder einer ähnlichen Form nicht schon einmal in einem früheren Promotionsverfahren angenommen oder als ungenügend beurteilt.

Ort, Datum Unterschrift